



Dielectric elastomer loudspeakers : models, experiments and optimization

Emil Garnell

► To cite this version:

Emil Garnell. Dielectric elastomer loudspeakers : models, experiments and optimization. Acoustics [physics.class-ph]. Institut Polytechnique de Paris, 2020. English. NNT : 2020IPPAE007 . tel-03014629

HAL Id: tel-03014629

<https://theses.hal.science/tel-03014629>

Submitted on 19 Nov 2020

HAL is a multi-disciplinary open access archive for the deposit and dissemination of scientific research documents, whether they are published or not. The documents may come from teaching and research institutions in France or abroad, or from public or private research centers.

L'archive ouverte pluridisciplinaire **HAL**, est destinée au dépôt et à la diffusion de documents scientifiques de niveau recherche, publiés ou non, émanant des établissements d'enseignement et de recherche français ou étrangers, des laboratoires publics ou privés.

Dielectric elastomer loudspeakers: models, experiments and optimization

Thèse de doctorat de l'Institut Polytechnique de Paris
préparée à l'École nationale supérieure de techniques avancées

École doctorale n°626 de l'Institut Polytechnique de Paris (ED IP Paris)
Spécialité de doctorat : Mécanique des fluides et des solides, acoustique

Thèse présentée et soutenue à Palaiseau, le 6 novembre 2020, par

EMIL GARNELL

Composition du Jury :

Herbert Shea Professeur, EPFL (Soft Transducer Laboratory)	Président
Jean-François Deü Professeur, CNAM (LMSSC)	Rapporteur
Morvan Ouisse Professeur, ENSMM (FEMTO-ST)	Rapporteur
Stéphane Job Maître de conférences, Supméca (Laboratoire Quartz)	Examineur
Laurence Bodelot Professeur assistant, École polytechnique (LMS)	Examineur
Olivier Doaré Professeur, ENSTA Paris (IMSIA)	Directeur de thèse
Corinne Rouby Maître de conférences, ENSTA Paris (IMSIA)	Co-encadrante
Yoachim Horyn Head of Fundamental Research, L-Acoustics	Invité

Emil Garnell

*Dielectric elastomer loudspeakers:
models, experiments and optimization*

November 6, 2020, Version: November 18, 2020

Reviewers: Jean-François Deü and Morvan Ouisse

Supervisors: Olivier Doaré and Corinne Rouby

ENSTA Paris, Institut Polytechnique de Paris

IMSIA

828 boulevard des Maréchaux

91120 Palaiseau, France

Abstract

Dielectric elastomers are soft active materials capable of large deformations when activated by a high voltage. They consist of a thin elastomer membrane (generally made of silicone or acrylic), sandwiched between compliant electrodes. The thickness of the assembly is about 100 microns. When a high voltage is applied between the electrodes, the membrane is squeezed between the electrodes, and increases in area by up to 100%.

This electromechanical conversion principle can be used to build loudspeakers. Prototypes have been developed and tested by several research groups, and models have been proposed to estimate their performance.

An intrinsic characteristic of dielectric elastomer loudspeakers is their multi-physic nature. Indeed, the actuation mechanism is itself a coupling between electrostatics and mechanics; the membrane is very thin and light, and couples therefore strongly with the surrounding air which is comparatively heavy; and finally the electrode electrical resistivity induces a coupling between electrodynamics and mechanics.

The models proposed so far did not consider all of these couplings together, which limited their use to qualitative estimations. In this thesis, a multi-physic model of dielectric elastomer loudspeakers is set-up, in order to optimize their acoustic performances, in terms of frequency response, radiated level, and directivity. The strong couplings between electrostatics, membrane dynamics, acoustics and electrodynamics are studied with a finite element model in FreeFEM. This model is validated by dynamical and acoustical measurements, and then used to improve the performances of the prototype, by working on several levels: optimization of the excitation, filtering, damping and control.

Résumé

Les élastomères diélectriques sont des matériaux actifs souples capables de grandes déformations sous chargement électrique. Ils sont constitués d'une fine membrane d'élastomère (en général en silicone ou en acrylique), recouverte de chaque côté par des électrodes souples et étirables. L'ensemble a une épaisseur de l'ordre de 100 microns. Lorsqu'une tension électrique est appliquée entre les électrodes, la membrane se comprime et sa surface peut augmenter de plus de 100%.

Ce principe de conversion électromécanique peut être utilisé pour réaliser des haut-parleurs. Des prototypes ont été développés par plusieurs groupes de recherche, et des modèles ont été proposés pour évaluer leurs performances.

Une caractéristique intrinsèque des haut-parleurs en élastomères diélectriques est leur nature multiphysique. En effet, le mécanisme d'actionnement est lui-même un couplage entre électrostatique et mécanique; la membrane est très fine et légère, et se couple ainsi fortement à l'acoustique car l'air est lourd par rapport à la membrane; et enfin la résistivité des électrodes engendre un couplage entre l'électro-dynamique et la mécanique.

Les modèles proposés jusqu'alors ne considéraient pas l'ensemble de ces couplages, limitant leur utilisation à des estimations qualitatives. Dans cette thèse, un modèle multiphysique de haut-parleurs en élastomères diélectriques est mis en place, afin de permettre l'optimisation de leurs performances acoustiques, en terme de réponse en fréquence, niveau rayonné, et directivité. Les couplages forts entre électrostatique, dynamique membranaire, acoustique, et électrodynamique sont étudiés à l'aide d'un modèle par éléments finis dans FreeFEM. Ce modèle est validé par des comparaisons avec des mesures dynamiques et acoustiques, et ensuite utilisé pour améliorer les performances du prototype, en travaillant sur plusieurs plans : optimisation de l'excitation, filtrage, amortissement, et contrôle.

List of publications

The work carried out during this PhD project resulted in several publications in peer-reviewed journals and conferences.

Articles in peer-reviewed journals

- Garnell, E., Rouby, C., & Doaré, O. (2019). Dynamics and sound radiation of a dielectric elastomer membrane. *Journal of Sound and Vibration*, 459, 114836.
- Garnell, E., Doaré, O., & Rouby, C. (2020). Coupled vibro-acoustic modeling of a dielectric elastomer loudspeaker. *The Journal of the Acoustical Society of America*, 147(3), 1812-1821.
- Garnell, E., Rouby, C., & Doaré, O. Resistivity-induced coupling between voltage distribution and vibrations in dielectric elastomers. Submitted in September 2020.
- Garnell, E., Doaré, O., & Rouby, C. Model based adaptive filtering of dielectric elastomer loudspeakers. Submitted in October 2020.
- Garnell, E., Aksoy, B., Rouby, C., Shea, H., & Doaré, O. Optimization of the electrode shape of dielectric elastomer actuators for dynamic applications. Submitted in November 2020.

Articles in conference proceedings

- Garnell, E., Doaré, O., & Rouby, C. (2019). Resonance modes for exterior vibro-acoustic problems, application to a dielectric elastomer loudspeaker. ICA 2019, Aachen.
- Garnell, E., Doaré, O., & Rouby, C. (2019). Modèle vibro-acoustique couplé d'un haut-parleur en élastomère diélectrique. CFM 2019, Brest.
- Garnell, E., Doaré, O., & Rouby, C. (2019). Dynamique et rayonnement acoustique d'une membrane d'élastomère diélectrique. CMSA 2019, Giens.

Other workshops and conferences

- Journées Jeunes Chercheurs en Acoustique et Bruit 2018, Le Mans. Industrial prize.
- Journées Jeunes Chercheurs en Acoustique et Bruit 2019, Femto-ST, Besançon.
- Journées thématiques de la fédération francilienne de mécanique 2019: « Ondes et vibrations en milieux complexes », Saclay.

Acknowledgement

My greatest gratitude goes to my two supervisors, Olivier Doaré and Corinne Rouby, who came up with the idea of this thesis, and accompanied me during these three years. I am thankful for their trust and support, and the serene work atmosphere it led to. This helped me a lot in moving forward efficiently, and enjoying going to work every day. I appreciated Corinne's great attention and rigor which helped clarifying many points in particular before submitting articles, and Olivier's physical sense, which always pointed out new possible directions for my work.

I would like to thank sincerely Morvan Ouisse and Jean-François Deü for their very careful reading of the manuscript, and the whole jury for the interesting and stimulating discussions during the defense, I wish I had some more time to investigate ideas which have been suggested !

I would like to thank all people I interacted with in the lab during these three years. I appreciated the technical support in manufacturing the prototypes, setting up the measurement tools, buying the needed materials and train tickets, and the useful advices of Nicolas Baudet, Lahcene Cherfa, Thierry Pichon, Nicolas Thurieau and Cécile Callo-Labbe.

The group of PhD students, post-docs and interns at the lab formed a great team to spend time with, both for working and socializing. Thanks to you all David, David, David, Romain, Aurore, Haiqin, Marine, Thomas, Till, Jeremy, Aurélien, Guillaume, Joar, Jonathan, Baptiste, Lisa !

A special thought for my office-mates Tommy, Nicolas, Robin and Elodie, who created both a good studios context, and great company for coffee breaks. Working remotely for several month made me realize how important this is. I will also miss the lunch breaks running with Robin and Ludo, or climbing with Mathilde.

The doors of the senior researchers offices were always opened, and made it natural to come and ask for an advice. I am grateful to Benjamin Cotté, Cyril Touzé, Jean Boisson, Jean-François Semblat, Romain Monchaux, Fabien Szmytka, Luc Pastur, for being available when I came knocking on the door. I would also like to thank Eliane Bécache, Claude Stolz, Marc Bonnet and Stéphane Job for helpful discussions.

After two years trying to manufacture reliable prototypes in the lab at IMSIA, I realized it could be efficient to collaborate with teams who are specialized in handling soft materials. I contacted Prof. Herbert Shea, from the Soft Transducer Laboratory at the EPFL, who kindly offered me to spend a month in his lab to benefit from the group's extensive manufacturing knowledge. I would therefore like to cheerfully thank the whole team who welcomed me warmly, Herbert, Bekir, Fabio, Sylvain, Vito, Edouard, Ronan, Djen and Giulio.

I ended up writing my thesis during the lock-down due to the Covid-19, and I would like to thank Gerard and Michelle Miquel for lending us their country house, where I could work efficiently in a calm natural environment.

Finally I'm grateful to my parents and family for their long term support in my studies, and to Faustine for stimulating my life during this whole period.

Contents

Main variables	1
1. Introduction	3
1.1. General context	3
1.2. A short history of dielectric elastomers	4
1.3. Dielectric elastomer loudspeakers	5
1.3.1. Founding work	5
1.3.2. First models and dynamic experiments	7
1.3.3. More recent work	8
1.4. Related work on dielectric elastomers	10
1.4.1. Non-linear dynamics	10
1.4.2. Viscosity	11
1.5. Goals of the thesis	12
1.6. Organization of the thesis	14
2. Model of a DE loudspeaker	17
2.1. Overview of the modelling procedure	17
2.2. Electromechanical coupling	18
2.2.1. Literature review	18
2.2.2. Theory	22
2.3. Hyper-elastic membrane mechanics	25
2.3.1. Literature review	25
2.3.2. Theory	25
2.4. Electrical model of the dielectric elastomer membrane	27
2.4.1. Literature review	27
2.4.2. Theory	28
2.5. Acoustic radiation	30
2.5.1. Literature review	30
2.5.2. Theory	32
2.6. Numerical procedure	36
2.6.1. Set of coupled equations	36
2.6.2. Static deformation	37
2.6.3. Linear dynamics	38
2.7. Conclusion	44
3. Experimental setup	45
3.1. Fabrication process	45
3.1.1. Fabrication of the membranes	45
3.1.2. Applying soft conductive electrodes	49
3.1.3. Design of the electrode connections	50
3.2. Prototype design	53

3.3. Identification of the material parameters	55
3.3.1. Hyper-elastic parameters	55
3.3.2. Membrane thickness	59
3.4. DE loudspeaker characterization procedure	62
3.4.1. Overview	62
3.4.2. Static deformation	62
3.4.3. Impedance measurements	62
3.4.4. Modal analysis and membrane dynamics measurements	63
3.4.5. Acoustic radiation	65
3.5. Conclusion	65
4. Comparison of experimental and numerical results	67
4.1. Parameters of the prototype	67
4.2. Static deformation	67
4.2.1. Without applied voltage	67
4.2.2. With applied voltage	69
4.3. Membrane dynamics	73
4.3.1. Free response	73
4.3.2. Forced response	76
4.4. Acoustic radiation	79
4.4.1. Pressure on axis	79
4.4.2. Directivity	82
4.4.3. Harmonic distortion	82
4.5. Demonstration of the multi-physics nature of the studied device	83
4.5.1. Influence of the cavity stiffness	84
4.5.2. Influence of the vibroacoustic coupling	84
4.6. Conclusion	85
5. Optimization	87
5.1. Static analysis	87
5.1.1. Limits of dielectric elastomer membranes	87
5.1.2. Optimal parameters for low frequency behavior	89
5.1.3. Acoustic radiation with the optimal parameters	91
5.1.4. Conclusion	93
5.2. Optimization of the electrode shape	93
5.2.1. Introduction	93
5.2.2. Definition of the optimization problem	94
5.2.3. Objective functions	95
5.2.4. Optimization procedure	97
5.2.5. Results	98
5.2.6. Experimental investigation	101
5.2.7. Conclusion	103
5.3. Acoustic damping	104
5.3.1. Theory	104
5.3.2. Results	106
5.3.3. Conclusion	108
5.4. Control and filtering solutions	108
5.4.1. Introduction	108

5.4.2. Description of the studied system	109
5.4.3. Theory of the control strategy	109
5.4.4. Results	111
5.4.5. Conclusion	117
5.5. Conclusion	118
6. Resistive effects	119
6.1. Literature review	119
6.1.1. Lumped models	119
6.1.2. Transmission line models	120
6.1.3. Goal of the present work	121
6.2. Theory	121
6.2.1. Description of the studied system	122
6.2.2. Transmission line model	122
6.2.3. Model based on Maxwell's equations	124
6.2.4. Comparison of transmission line and Maxwell models	131
6.2.5. Linearized coupled equations	131
6.3. Application	131
6.3.1. Coupled equations	132
6.3.2. Experimental setup	133
6.4. Results	135
6.4.1. Membrane dynamics	136
6.4.2. Impedance	136
6.4.3. Voltage on the membrane	138
6.5. Conclusion	140
7. Conclusion	143
7.1. Summary of the main results	143
7.2. Perspectives	144
7.2.1. Model improvement	144
7.2.2. Optimization	144
Bibliography	147
Appendix	155
A. Constitutive equations of dielectric elastomers	157
B. Linearized weak forms	161
B.1. Static deformation	161
B.1.1. Solving step one	161
B.1.2. Solving step two	163
B.2. Dynamics	164
C. Validation of the axisymmetric perfectly matched layers implementation	167
C.1. Description of the studied system	167
C.2. Theory	168
C.2.1. Weak form of the governing equation	168
C.2.2. PML definition	168

C.2.3. Pressure computation using the Rayleigh integral	169
C.3. Results	169
C.3.1. Frequency range of interest	170
C.3.2. Mesh	170
C.3.3. Convergence analysis	170
C.4. Conclusion	171
D. Validation of modal methods for exterior vibroacoustic problems	173
D.1. Description of the studied system	173
D.2. Governing equations	174
D.3. Numerical solving	175
D.3.1. Finite element discretization	175
D.3.2. Modal analysis	175
D.4. Results	177
D.4.1. Modal parameters	178
D.4.2. Convergence of the modal summation	180
D.5. Conclusion	182

Main variables

In the whole thesis, capital letters denote dimensional variables and small letters non-dimensional variables.

In the following list, the main dimensional variables are defined.

Variables with an overbar stand for variables defined in the **reference configuration** [see fig. 2.1].

Geometry

$\mathbf{C} = \mathbf{F}^T \mathbf{F}$	Cauchy deformation tensor	-
$\mathbf{F} = \partial \mathbf{X} / \partial \bar{\mathbf{X}}$	Displacement gradient	-
\mathbf{n}	Normal unit vector	-
$\mathbf{u}_1, \mathbf{u}_2$	In-plane unit vectors	-
\check{H}	Membrane thickness at center in reference configuration	m
$\lambda_1, \lambda_2, \lambda_n$	Radial, ortho-radial and normal stretches	-
Γ	Electrode repartition function	-
A	Membrane radius in deformed configuration	m
H	Membrane thickness	m
R	Radial coordinate	m
R_E	Electrode radius	m
V	Volume	m ³
X	Radial displacement	m
Y	Vertical displacement	m
Z	Vertical coordinate	m

General variables

ϵ	Permittivity	F m ⁻¹
μ	Shear modulus	Pa
Ω	Angular frequency	rad s ⁻¹
ρ_f	Density of air	kg m ⁻³
ρ_s	Density of the membrane	kg m ⁻³
ρ_{ratio}	Ratio of electrode over membrane mass per unit area	-
$c = C_f / C_s$	Non-dimensional speed of sound	-
C_f	Speed of sound in air	m s ⁻¹
C_s	Speed of shear waves in the membrane	m s ⁻¹
F	Frequency	Hz

G	Green function	m^{-1}
J_m	Material parameter of Gent's law	-
$m = \rho_f \bar{A} / \rho_s \check{H}$	Non-dimensional air density	-

Electrical

D	Electric displacement	C m^{-2}
E	Electric field	V m^{-1}
P	Polarization	C m^{-2}
ϱ_e	Electrode resistivity	Ω/\square
U	Voltage applied to the electrodes	V
W	Alternative excitation signal	V^2

Stresses

σ_1	Radial stress	Pa
σ_2	Orth-radial stress	Pa
P	Pressure	Pa
S_1	Radial nominal stress	Pa
S_2	Orth-radial nominal stress	Pa

Modal parameters

ψ_n	Modeshape n	-
k_n	Modal stiffness	-
m_n	Modal mass	-

Introduction

In this chapter the scientific context of the thesis is presented, starting from a general overview of dielectric elastomer applications to the challenges for modelling, designing and manufacturing efficient dielectric elastomer loudspeakers. The goals of the thesis are then stated, and its structure is outlined.

1.1 General context

We are today surrounded by loudspeakers, in our electronic devices, cars, buildings, etc. The vast majority are electro-dynamic loudspeakers, in which the sound-radiating membrane is moved by a coil oscillating inside a magnet. This principle has been developed by Rice and Kellogg in 1925 [92], and has been gradually improved since then.

For example, a high-frequency tweeter has been built in a larger woofer by Altec Lansing in 1943, yielding a coaxial loudspeaker (Altec Lansing Model 604 Duplex radiator) that outperformed most of other loudspeakers at that time.

However, the physical principle remained the same for almost 100 years, and most innovations concerning loudspeakers concerned the enclosure, such as horn loudspeakers as the Klipschorn [65], or bass reflex which has been developed by Jensen in the 1940s. The reader is referred to [5] for a short history of the development of hi-fi loudspeakers.

Even though electrodynamic loudspeakers have shown their ability to perform well in a wide range of applications, they still have a few drawbacks. The magnet which is required to put into motion the voice coil is heavy, and also bulky. Strong magnets are made out of neodymium, which is costly. To obtain the necessary power, the magnet and voice coil need to be relatively thick, so manufacturing flat loudspeakers remains a challenge. Also, their distortion is rather large: the total harmonic distortion lies around 3% at low frequencies.

The last limitation (distortion) has been addressed by electro-static loudspeakers (ESLs), which have been patented by Janszen in 1953 [55]. They consist of a very thin plastic sheet placed between rigid and perforated metal electrodes (see fig. 1.1).

The main advantages of this driving mechanism is that the moving part is very light, and driven on its whole surface. The coupling with acoustics is therefore very strong, and the diaphragm is heavily damped. A very flat frequency response can be obtained, and distortion is reduced by one order of magnitude compared to conventional electrodynamic drivers.

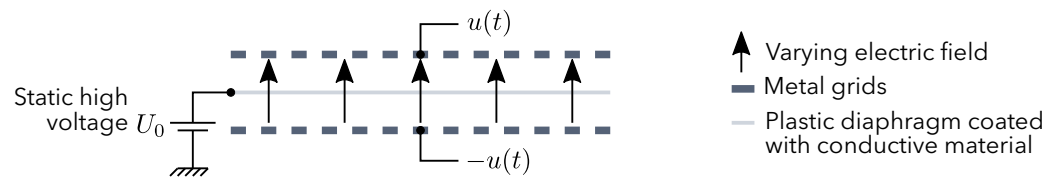


Fig. 1.1. Schematics of electrostatic loudspeakers. A thin plastic diaphragm is coated with conductive material, and placed between perforated metal plates. A high voltage static bias U_0 is applied to the diaphragm, and the electrodes are driven by the audio signal $u(t)$.

ESLs have been commercialized from the late 1950s to nowadays, mostly for high-end loudspeakers. They are most of the time combined with a conventional woofer, because ESLs behave as acoustic dipoles, and can therefore not radiate properly at low frequencies.

The last type of loudspeakers which have obtained a commercial success are piezoelectric drivers. A piezoelectric crystal bends when a voltage is applied across its electrodes, and this mechanism can be used to radiate sound. Most piezoelectric drivers are used in applications where a high level is desired for a small size, and where cost is a major constraint. They are limited to high frequencies as only small displacements can be obtained.

In this thesis, we will investigate another type of loudspeakers, based on a different physical principle. We will use an active material (dielectric elastomer) like piezoelectric crystals, but which is capable of much larger deformations (up to more than 100%), and should thus perform better at low frequencies.

Dielectric elastomer loudspeakers should also help address some limitations of electrodynamic loudspeakers, as it should be possible to obtain much lighter and flatter devices, by avoiding using a magnet.

The ultimate goal is to obtain small and flat loudspeakers, which can radiate at low frequencies, with limited distortion.

1.2 A short history of dielectric elastomers

Dielectric elastomer (DEs) are soft active materials, which have been studied for about 20 years now, after Pelrine *et al.* [87] showed that deformations of more than 100% in area can be achieved when a high voltage is applied.

The working principle is the following, and is described in fig. 1.2:

- A soft elastomer membrane is coated on both sides with conductive and stretchable electrodes.
- A high voltage is applied between the electrodes. This brings positive charges on one side of the membrane and negative charges on the other.
- The positive and negative charges are attracted to each other, and thus apply a normal pressure on the membrane surfaces.

- The membrane is therefore squeezed between the electrodes, and since the elastomer is usually incompressible, the decrease in thickness results in an increase in area.

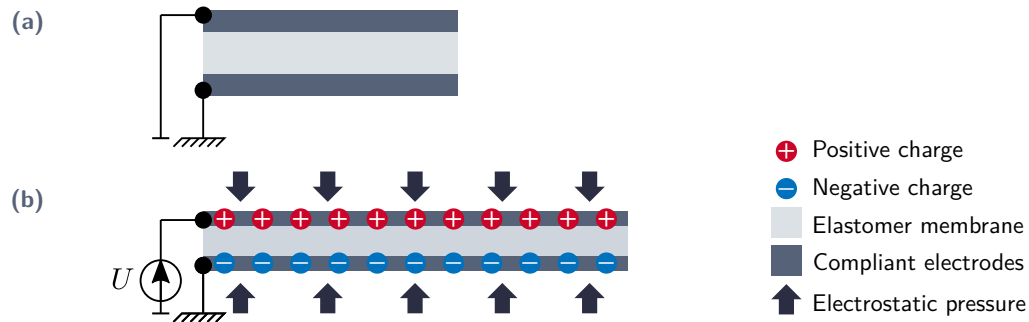


Fig. 1.2. Principle of dielectric elastomers. **(a)** Initial state, no voltage applied. **(b)** Deformed state, a voltage U is applied between the electrodes.

The research interest in DEs is high for several reasons.

First, DE actuators are soft, contrary to all motor-based solutions. This is of primary interest in robotics, where nature inspired robots become possible. Indeed, DEs reproduce the behavior of real muscles, as they have similar achievable stretch, energy density and stiffness.

Second, they offer combined actuation and position sensing. The deformation of the device is related to its capacitance, which is easily measured during actuation. The deformation can thus be monitored in real time. Self-sensing strategies can then be implemented to control the actuator in closed loop without any added sensor. Huge improvements of the actuator precision can be obtained.

DEs also work as energy harvesters, and can thus be used to build soft generators, that can be embedded in deformable structures, such as robots, cloths, gloves, etc.

It is beyond the scope of this introduction to provide a general review of the multiple possible applications of DEs, as it has been an active field of research for more than twenty years. For a broader view of the field, the reader is referred to the reviews by Anderson *et al.* [4], Rosset and Shea [99], and Gu *et al.* [40].

1.3 Dielectric elastomer loudspeakers

1.3.1 Founding work

The first published work on DE loudspeakers is the study by Heydt, Pelrine, Kornbluh and Mason from SRI International [43], in which inflated bubbles of silicone membrane coated with graphite powder are investigated. This configuration will be studied in the whole thesis, so the principle is described in fig. 1.3.

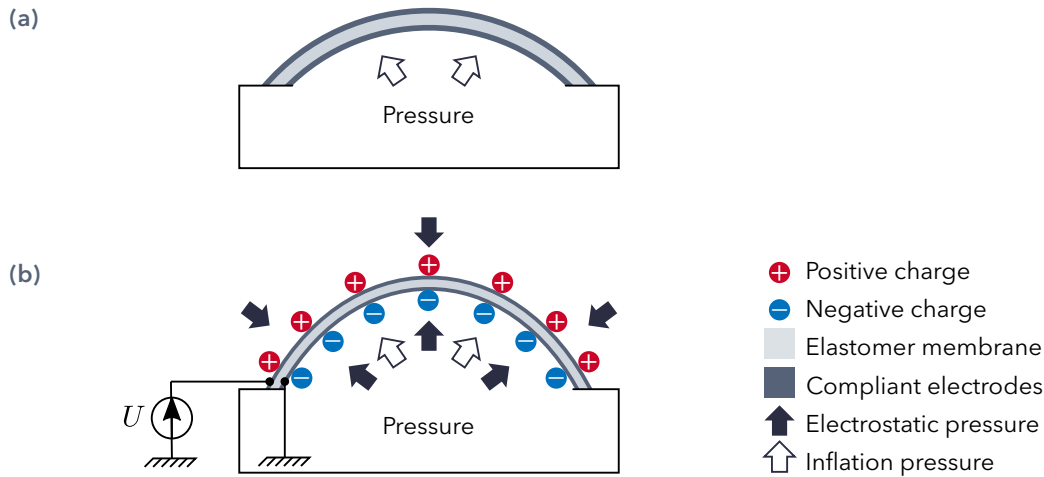


Fig. 1.3. Inflated DE membrane. **(a)** Initial configuration, the membrane is inflated over a closed cavity. **(b)** When a high voltage is applied, the membrane increases in area, and because of the the initial pressure, its moves outwards.

It was found in [43] that DEs have a high potential for making loudspeakers, because of their large achievable deformation, quick response and high energy density. A promising sensitivity of 100 dB SPL/1W/1m was obtained, exceeding the average sensitivity of standard electrodynamic loudspeakers (about 90 dB SPL/1W/1m). The main identified limitations are the high voltage required to actuate the speaker, as well as the large distortion. However, it is indicated that the results were obtained without optimizing the design to improve those characteristics.

A similar device was further investigated in [46], where an array of inflated bubbles was considered. A radiated sound pressure level of more than 70 dB was obtained in the frequency range 1-20 kHz. It was also shown that shaping the excitation signal by a square root helps reducing a lot the major non-linearity coming from the square dependence of the electrostatic pressure on the applied voltage, reducing the total harmonic distortion to less than 5 % over the whole frequency range.

A patent of SRI international on the device studied in [43, 46] was published in 2002 [86].

An experimental study by the same authors in 2006 [45] investigated this time a single large inflated DE membrane, and not an array of small bubbles. The sound radiation properties were analysed, and it was found experimentally that a prototype with a positive inflation pressure (membrane inflated towards the outside) had a more omnidirectional directivity than a membrane inflated with a negative pressure. General ideas of possible applications, where the directivity could be controlled by the inflation pressure, or by signal processing methods were mentioned but not studied.

The results of [45] have been patented in 2009 [44], where different biasing mechanisms were included in the patent, such as inflation pressure, foam backing, push-pull configuration, etc.

1.3.2 First models and dynamic experiments

The pioneering work of Pelrine *et al.* raised a large interest in the research community, and several teams started investigating in more details the dynamics and sound radiation of DE membranes.

A substantial work has been carried out by Fox, Mockensturm and Goulbourne on the dynamics of inflated DE membranes. The purpose of their work is not loudspeakers, as they focused on the low frequency range.

Their first numerical study [81] focused on the transition between multiple state of equilibrium. The equations for the dynamics of axisymmetric DE membranes are derived, and used to analyse the static behavior of a spherical membrane, as well as the transient response of the membrane to a step input voltage.

The dynamics of an inflated DE membrane were then analysed experimentally in [32, 31] in the low frequency range (up to 200 Hz). A resonance was observed, and the influence of the excitation frequency on the membrane displacement was measured.

Their most complete study is [30], where the influence of the major design parameters (cavity volume, inflation pressure, bias voltage) on the membrane resonance frequencies has been experimentally analysed. However, no model was proposed to compute the forced dynamics of the membrane, so only experimental conclusions could be drawn.

Among the early works it is worth mentioning the study by Dubois *et al.* [25], where a millimetric flat DE membrane was investigated. The electrostatic pressure created by the applied voltage decreases the tension in the membrane, which decreases its first resonance frequency. A decrease in frequency of 77 % is observed when the voltage is applied, and a simple model is derived to explain this decrease.

A similar study was performed by Hochradel *et al.* [47], but for an inflated membrane. The change in frequency due to the electric voltage was studied, as well as the dynamical and acoustical response of the membrane when actuated by an oscillating signal. A model has been developed, but only to analyse the influence of the static voltage on the first resonance frequency of the system.

Also, the work by Keplinger *et al.* published in Science is interesting, as it demonstrated the possibility to manufacture transparent loudspeakers using DEs. This is made possible by the use of ionic hydrogels as electrodes, instead of the electronic conductors which are generally used (carbon or metal based). Ionic conductors are found to have a higher conductivity than electronic conductors, which is important for the high frequency efficiency of DE loudspeakers.

Transparent DE loudspeakers have also been studied by Yu *et al.* [122], where transparency is achieved by using carbon nanotube electrodes. The loudspeaker frequency response is measured, but the sound generation mechanism is unclear as the loudspeaker consists only in a stretched DE film. Without any biasing mechanism the DE membrane should move in plane, and thus does not radiate sound efficiently.

Transparent DE loudspeakers have also been demonstrated by Xu *et al.* [120], where graphene based electrodes are used.

The first model of the dynamics of an inflated DE membrane, that does not make the assumption that the membrane behaves like a one-degree-of-freedom system is the study by Zhu *et al.* [126]. The eigenmodes of an inflated membrane around a non-linear static equilibrium are computed, and the influence of the inflation pressure and bias voltage are analysed. This paper is also the first to compute the frequency-response functions of an inflated DE membrane, using time integration. Interesting non-linear phenomena are observed, such as sub- and super-harmonic resonances. However, the results presented in this study are purely numerical, and are not validated by experiments.

1.3.3 More recent work

Directivity

The team of Maeda *et al.* carried out several studies on the use of inflated DE membranes as loudspeakers.

They investigated the directivity of a hemispherical membrane [51], showing that an almost omni-directional directivity could be achieved in a hemisphere. A suggested potential application of DE loudspeakers is room impulse response measurements, where an omnidirectional point source is required. However, the maximum sound pressure level radiated by DE loudspeakers may limit this application.

This study was extended to the case of a spherical loudspeaker in [52], where the directivity of an inflated VHB (commercial 3M acrylic tape) membrane is measured. The authors claim that they explained the observed directivity by membrane modes shapes measurements, but this part of the study suffers from methodological flaws.

Other biasing mechanisms

Other geometries based on different biasing mechanisms than the inflation have also been investigated.

Sugimoto *et al.* [107] used a rigid elastomer instead of the commonly used silicone or acrylic membranes. The rigidity of the elastomer allows the authors to avoid the use of a frame to hold the membrane. To convert the in-plane displacement to out-of-plane displacement, the DE is bent into a semi-cylindrical shape. The influence of the major design parameters is investigated experimentally, but no model capable of computing the radiated pressure is provided. The sensitivity is also analysed, and found to lie around 70 dB/W/m, that is to say about 20 dB lower than standard loudspeakers.

The same team investigated the push-pull configuration suggested by Heydt *et al.* [44], in which two membranes are placed one upon another, with a rigid connector between them. When one membrane increases in area, the other decreases. They proposed a model to compute the fundamental resonance [106]. It is found that the push-pull configuration reduces the second harmonic distortion by 10 dB, the non-linearity of one membrane being compensated by the other.

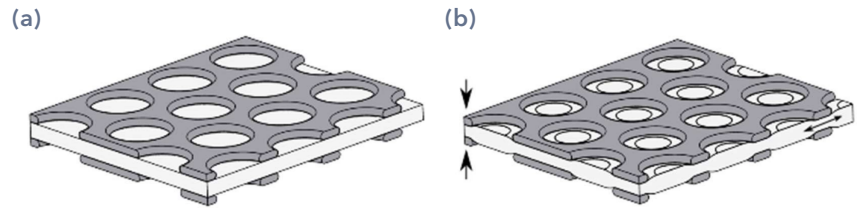


Fig. 1.4. From Rustighi *et al.* [102], ©. Working principle of DE with perforated rigid electrodes. **(a)** Un-deformed configuration. **(b)** Deformed configuration, when an actuation voltage is applied.

A team at Darmstadt, Germany, developed another interesting concept for using DEs as loudspeakers [113, 59]. Contrary to most other studies, rigid electrodes are used. They are made of perforated metal plates, as shown in fig. 1.4. A stack of alternating elastomer and electrode layers is built. When a voltage is applied between the electrodes, the elastomer is squeezed and the excess material can move in the electrode holes. The whole stack is then compressed, and a normal displacement is obtained, so sound can be radiated. One of the main advantages of this geometry is that metal electrodes are used, which are thus very conductive. The high frequency response will not be limited by the electrical behavior of the system.

This acoustic actuator is then used for active noise control with promising results in double glazed windows [42].

A more in-depth experimental analysis of the sound radiation of the sandwich structure proposed in [59] is performed in [102]. The sound radiation properties of the flat perforated plate loudspeaker are studied, including frequency response, directivity, and harmonic distortion. Sound radiation in the frequency range 1-15 kHz is demonstrated.

Coupling with acoustics

Few authors investigated the influence of the coupling between acoustics and mechanics on DE vibrations.

A first attempt is the work by Lassen, but the methodology and the results presented in [71] are doubtful and unreliable. The influence of acoustics is modelled by the plane wave impedance, which does not hold in the near field.

Another attempt is found in the paper by Chakravarty [16], but it is restricted to a flat membrane, and studies only the variation of the first resonance frequency when the various design parameters are varied. The coupling with acoustics is taken into account by analytical formulas valid only for flat circular membranes. This is thus of little use to study inflated DE membranes.

Abbad *et al.* [1] studied both experimentally and numerically a tunable Helmholtz resonator, in which one of the cavity walls is made of a stretched dielectric elastomer membrane. The membrane is flat, so a membrane model with uniform tension is used, and coupled to acoustics in a commercial finite element code.

In a different context, Rothmund *et al.* [100] from the Harvard group studied a transparent DE membrane for active noise control in ducts. The membrane is pre-stressed and placed in a duct, and a plane wave is sent on it to analyse the transmission loss. The membrane is also used as an actuator to implement active noise cancellation, leading to an improvement of 10 dB of the transmission loss. The interaction between acoustics and the membrane dynamics is taken into account, but in this case it is relatively simple since only plane waves propagate in the duct.

Improvement by signal processing

The team at Darmstadt recently investigated possible improvements of the frequency response and directivity of DE loudspeakers by means of digital signal processing [66].

A DE loudspeaker made of an array of inflated bubbles, such as described in [86] was studied. The audio signal is processed by a digital signal processor (DSP) before it is fed into the high voltage amplifier and the DE loudspeaker. This method is shown to enable great improvements of the frequency response, as well as of the total harmonic distortion.

Some of the main limitations of this method is that the response of the speaker needs to be precisely known to design correctly the filters. If the system response changes (aging, change of the inflation pressure), the filters become inappropriate.

1.4 Related work on dielectric elastomers

1.4.1 Non-linear dynamics

Due to their large deformations, DE are non-linear in nature. For accurate description of their properties, hyper-elastic material models are needed, and geometrical non-linearities must also be taken into account. What is more, the relation between the electrostatic pressure and the voltage is quadratic. Also, elastomer membranes often exhibit visco-elastic behavior, which may require non-linear visco-elastic models to be described. For all these reasons, there is a substantial literature on the non-linear dynamics of DE actuators.

As noticed above, the effect of non-linearities on the dynamics was observed in the first studies on the use of DEs as loudspeakers [46] in the form of harmonic distortion of the radiated acoustic pressure.

The first study on the non-linear dynamics of DEs may be the paper by Zhu *et al.*, who investigated the oscillations of a DE balloon using a 1-DOF model [125]. The frequency response is studied, and sub-harmonic, harmonic, as well as super-harmonic resonances are observed. Also, the oscillation amplitude may jump when the excitation frequency is varied.

This study was extended to multiple-DOF models in Zhu *et al.* [126], where an inflated dielectric membrane is analysed using time integration of non-linear membrane equations.

Apart from the study by Zhu *et al.*, most of the studies on non-linear dynamics of DEs focus on 1-DOF devices.

For example, Xu *et al.* showed that even for a simple DE slab undergoing uniform deformation [116], complex dynamics are observed, in particular pulsating (modulated) responses when the system is excited with a sine electrical signal.

Cao *et al.* tried to design DE systems to observe strongly non-linear behaviors. A planar DE actuator which oscillates out of plane when an oscillating voltage is applied is studied in [14]. A 1-DOF model is set-up, including viscosity, and used to analyse the non-linear dynamics. A prototype is also built, and shown to exhibit sub-harmonic, harmonic, and super-harmonic responses.

A similar study but for a 1-DOF oscillator with two stable equilibrium positions was carried out by the same team [13]. The non linear dynamics of a bi-stable DE oscillator are studied, and various oscillation regimes are identified depending on the amplitude and frequency of the excitation.

This prototype was designed to reach the largest possible displacement at resonance, so a membrane designed for use as a loudspeaker may not vibrate in this strongly non-linear regime, and exhibit the same complex dynamics.

Some authors also started investigating control strategies to handle the non-linear dynamics, such as Li *et al.* [72] who show that the non-linear dynamical response can be controlled using a PID and a feedback loop.

We listed above some interesting works on the non-linear dynamics of DE devices, which are more or less closely related to loudspeakers applications. It appears that most studies either focus on 1-DOF systems where a physical understanding of the observed non-linear phenomena is possible, or demonstrate rich dynamic behaviors on more complex systems. To study and reduce the distortion of DE loudspeakers, there is more a need of models capable of predicting the weakly non-linear dynamic response over a large frequency range, than a need of models focusing on 1-DOF systems exhibiting a strongly non-linear behavior.

We therefore believe that setting-up multiple-DOF models of DE loudspeakers is the primary step, first to study linear dynamics and then to compute the harmonic distortion. The non-linear dynamics could unfortunately not be studied for time reasons in this thesis.

1.4.2 Viscosity

Two types of materials are commonly used to manufacture DE actuators: silicone and acrylic elastomers.

Acrylic (and especially the very commonly used 3M VHB) exhibits the most impressive electromechanical coupling, with the largest obtained static deformations and energy density.

However, VHB has a large viscosity, and typically creeps during several minutes when actuated. The effects of visco-elasticity on the dynamics have thus been studied by several research groups, and shown to affect the non-linear dynamics of DE devices [124, 17, 103, 50, 123].

Silicone elastomers on the other hand have a lower viscosity, and react faster [96]. The dynamics will thus be less influenced by visco-elastic effects in silicone elastomers than in acrylics.

Silicone is used in this thesis, and loss phenomena are taken into account by simple damping models, and not visco-elastic models. This choice will be justified by experimental analyses.

1.5 Goals of the thesis

The study of the literature on DE loudspeakers reveals that the field is currently in a state where most ideas and options on how to produce sound with these materials have been tested.

There are many studies that show that sound radiation of interesting level can be obtained in a rather large frequency range [45, 88, 102], that distortion can be reduced to acceptable values by signal processing methods [45, 66], and that the device can be made transparent by using specific types of electrodes [122, 63, 120].

However, there is still no commercially available DE loudspeaker. We believe several reasons explain this:

- DEs need high voltage to be actuated. This may be dangerous, and requires bulky high voltage amplifiers. This limitation is addressed by research teams working on the manufacturing processes, who aim at producing reliable thinner membranes and electrodes. One may hope that stacked DE actuators with low operation voltages should be available in the coming years.
- DE loudspeaker designs are non-linear in nature, which is in contradiction with the desired behavior of loudspeakers. The non-linear dynamics of DE devices are studied by several research groups, and control strategies to limit the harmonic distortion start to appear.
- Most studies demonstrate the possibility to make loudspeakers out of DEs, but few try to optimise for real the system. We believe the reason why no real optimization is performed is that there are still modelling issues that are not addressed. The models used currently for DE loudspeakers allow to qualitatively explain the main characteristics, but are not predictive. To the author's knowledge there is no study where a model is shown to be able to predict quantitatively the sound radiation properties of a DE loudspeaker.

Therefore, the goal of this thesis is to develop an accurate model of DE loudspeakers, that is capable of computing the acoustic and dynamic response of sufficiently precisely, so that it can be used for design purposes, for example to run optimization routines to improve the behavior of the loudspeaker.

Several difficulties are raised by this goal, the main being the multi-physics nature of DE membranes. Indeed, the excitation mechanism itself is a coupling between electrostatics and mechanics. The DE membranes are usually so thin that the surrounding air must be considered as a heavy fluid, leading to strong vibroacoustic coupling. Also, due to the high electrode resistivity, the dispersion of electric charges on the electrodes takes time, and appears to be coupled to the membrane vibrations. This questions the validity of electrostatic models to describe the electrical part of the system.

Neglecting some of these couplings is perfectly acceptable for a phenomenological approach, if the goal is to provide an understanding of the global behavior of DE loudspeakers. However, as soon as a predictive model is needed, these couplings need to be taken into account.

Predictive models have been developed for other DE devices, but not yet for loudspeakers. Models for loudspeakers typically require features that may not be useful for other uses. A large frequency range is studied, from a few hundred hertz to more than 10 kHz. This implies that the model will need multiple degrees of freedom, as many modes will contribute to the dynamics and sound radiation. There is a substantial literature on 1-DOF models for DE, but fewer studies using multiple-DOF models.

Also, loudspeakers should behave as linear systems. Even though non-linear models are useful to predict and reduce the distortion for example, we believe that many limitations of DE loudspeakers can be addressed by linear analyses. Therefore we will work here with linear models, which allow solving in the frequency domain, which saves a lot of computational time. Being able to compute quickly frequency-responses opens the path for automatic optimization of the design, as the loudspeaker models can be fed into optimization routines.

To summarize, the main objectives of the thesis are:

- Develop a predictive model for DE loudspeakers.
- Use this model to optimize the parameters of the device, and investigate whether large improvements are achievable by properly choosing the appropriate values of the design parameters, or by setting up control strategies.
- Improve the modelling of DE devices in the high frequency range, where resistivity effects are important.

These objectives are in line with the conclusions of the recent review on DEs by Gu *et al.* [40], where the main challenges of the field are identified as:

- Accurate models to compute DE actuators dynamics are needed.
- Control strategies specifically designed for DE actuators should be developed.
- Driving electronics designed for DE actuators should be designed, to cope with the high voltage and low current context.

1.6 Organization of the thesis

In this thesis, a single geometry is investigated, namely inflated DE loudspeakers. This configuration was chosen because it is the most widely studied in the literature [45, 126, 51, 66, 30], and because it also appears to be simple, and can thus be implemented in real situations. The studied device is presented fig. 1.5, and the reader should keep this geometry in mind as it will be used throughout the thesis.

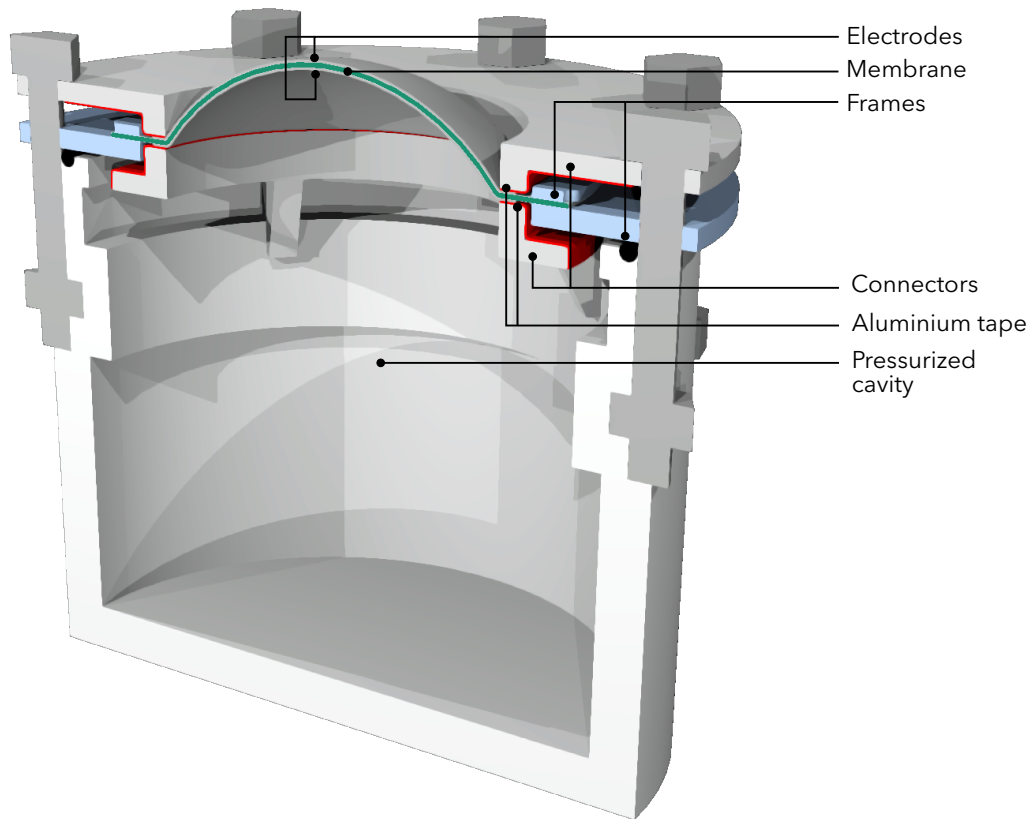


Fig. 1.5. Schematics of the studied device.

The second chapter presents the developed model of DE loudspeakers. The different physics that must be taken into account are analysed one by one, and coupled together. The numerical method based on finite elements which is used to solve the coupled equations is also presented.

In the third chapter, the experimental setup is introduced, including the manufacturing process of the membranes, the coating with soft electrodes, and the various measurement processes for static and dynamic analyses.

The fourth chapter presents the results of both the model and the experiments, in order to validate the model. Statics, dynamics and acoustics are validated successively.

In the fifth chapter, the model is used to examine whether the DE loudspeakers can be improved, by making the right choices of the design parameters. Static analysis are first

carried out to enhance the low-frequency behavior, the electrode shape is then optimized to improve the frequency response, and digital signal processing methods are finally investigated to control the frequency response and the directivity.

The electrode resistivity effects on the electrodynamical loading, and the resulting coupling between electrodynamics and mechanics is finally investigated in chapter 6. This effect has little consequences on the acoustical behavior, and is therefore omitted in chapter 2 for clarity reasons. However, it may enable possible new self-sensing strategies.

Model of a DE loudspeaker

In this chapter, the model that is developed to study inflated dielectric elastomer membranes is presented. First, an overview of the modelling procedure describing the main steps is given to identify the different physics that will be taken into account. The second section derives the constitutive equations of dielectric elastomer membranes. The three following sections study one by one the main physics involved: membrane mechanics, acoustics, and electrokinetics. Finally, the numerical procedure which is used to solve for all the steps is described.

2.1 Overview of the modelling procedure

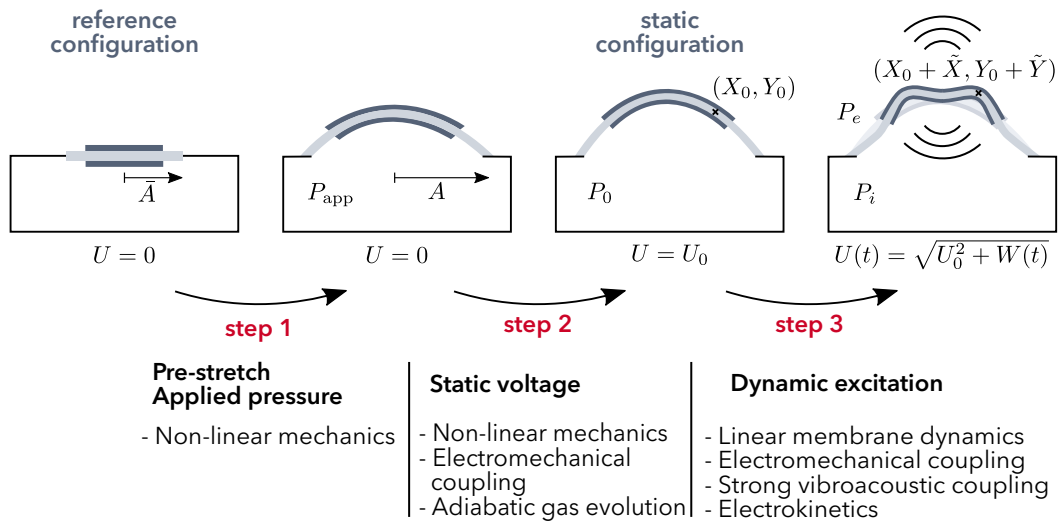


Fig. 2.1. Overview of the modelling procedure. In **step 1**, the membrane is pre-stretched from radius \bar{A} to radius A , and inflated with the applied pressure P_{app} . In **step 2**, the cavity is closed, and a static voltage U_0 is applied. The volume and the pressure in the cavity change. In **step 3** a dynamic excitation signal is superimposed to the static voltage. The membrane vibrates and couples to the surrounding air.

The modelling procedure is decomposed into the following steps [see fig. 2.1], which mimic the experimental procedure:

- **step 1.** The membrane is originally at rest in a reference state denoted hereafter as **reference configuration**. During **step 1**, the membrane is equi-biaxially pre-

stretched from the radius \bar{A} to the radius A , and inflated with the applied pressure P_{app} . In order to compute the resulting deformation, a hyper-elastic model is used for the membrane. The non-linear static equilibrium is computed using the Newton-Raphson algorithm.

- **step 2.** The cavity is closed and contains a fixed quantity of air, whose thermodynamic evolution is supposed to be adiabatic. This is valid as long as the timescale of the mechanical dynamics is smaller than the timescale for thermal conduction. A static voltage U_0 is applied between the electrodes.

To compute the resulting equilibrium, the same non-linear model as in **step 1** is used, but this time including electromechanical coupling. The obtained equilibrium is denoted the **static configuration**. In this configuration, the membrane coordinates are written (X_0, Y_0) , and the pressure in the cavity P_0 . All variables that refer to this configuration are written with the subscript zero.

- **step 3.** An alternating signal is superimposed to the static voltage U_0 . This signal vibrates the membrane which radiates sound in the surrounding air.

The strong couplings between the membrane vibrations and acoustics must be taken into account to yield accurate results. Also, due to resistivity effects, the effective voltage on the electrodes may differ from the applied voltage U . This will be taken into account by electrokinetics lumped models. During **step 3**, only linear vibrations are considered, and all quantities will be linearized around the **static configuration**.

2.2 Electromechanical coupling

In this section, a model to describe the electromechanical coupling is derived, first in a general 3D case, and later simplified to membrane mechanics.

2.2.1 Literature review

Uniform deformation of flat DE membranes

The first works on DEs, by Pelrine *et al.* [87, 88] used simple models to describe the electromechanical coupling.

They model the DE device as a parallel plate capacitor, whose energy is written as:

$$\mathcal{E} = \frac{Q^2}{2C} = \frac{Q^2 H}{\epsilon S}, \quad (2.1)$$

where C is the capacitance, Q the electrical charge on the top electrode, ϵ the dielectric permittivity of the membrane, H the thickness of the capacitor and S its area. The change in energy due to a change of thickness and area can be expressed as:

$$d\mathcal{E} = \frac{Q^2}{\epsilon S} dH - \frac{Q^2 H}{\epsilon S^2} dS. \quad (2.2)$$

Assuming that the elastomer is incompressible yields the following constraint between the thickness and the area:

$$\frac{dS}{S} = -\frac{dH}{H} . \quad (2.3)$$

Inserting this constraint in eq. (2.2) finally yields:

$$d\mathcal{E} = \frac{Q^2}{\epsilon S} dH . \quad (2.4)$$

The effective pressure that deforms the membrane is defined as:

$$\sigma = \frac{1}{S} \frac{d\mathcal{E}}{dH} = \frac{Q^2}{\epsilon S^2} . \quad (2.5)$$

The charge on the electrodes can be related to the applied voltage by Gauss's law, which gives:

$$\sigma = \frac{\epsilon U^2}{H^2} = \epsilon E^2 , \quad (2.6)$$

where U is the applied voltage, and E the electric field. Equation (2.6) defines the effective electrostatic pressure, which is found to be twice the Maxwell pressure which equals $\sigma_{\text{Max}} = 1/2\epsilon E^2$. This doubling of the effective pressure is directly related to the incompressibility constraint.

A more detailed look at the electric field and interaction between the electric charges gives a different interpretation of the electrostatic loading of the membrane. An investigation of the pressure created by a distribution of electric charges was performed by Wissler and Mazza [115], who found that there is both a normal pressure $\sigma_z = 1/2\epsilon E^2$ which is applied normal to the membrane surface, and a pressure in the membrane plane of value $\sigma_r = -1/2\epsilon E^2$. The pressure in the membrane plane can be interpreted as the repulsion between charges of similar sign.

The comparison between these two points of view is shown in fig. 2.2.

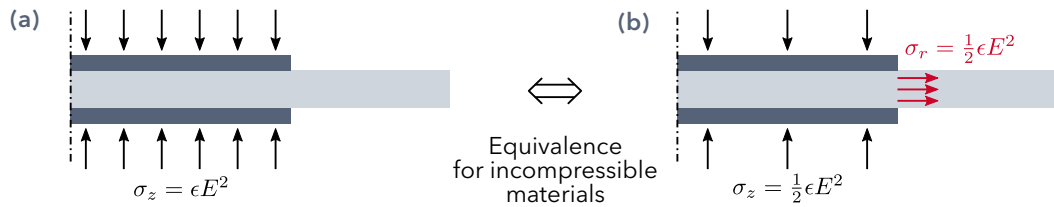


Fig. 2.2. Electrostatic loading of an axisymmetric DE membrane. **(a)** Point of view of Pelrine *et al.* [88]. **(b)** Force repartition obtained from the analysis of charge distributions [115]. The two points of view describe stress states which result in the same deformation for incompressible materials, as the distribution in **(b)** is obtained by superimposing the hydrostatic stress $\sigma = 1/2\epsilon E^2$ to the distribution of **(a)**. The equivalence is valid for flat membranes.

Deformation of DE curved membranes

When the membrane is curved, the analysis of the charge distribution becomes a little more complicated, and is schematized in fig. 2.3. The surface charge on the outer

electrode will be lower than the surface charge on the inner electrode. This results in a different electrostatic pressure applied on the two electrodes.

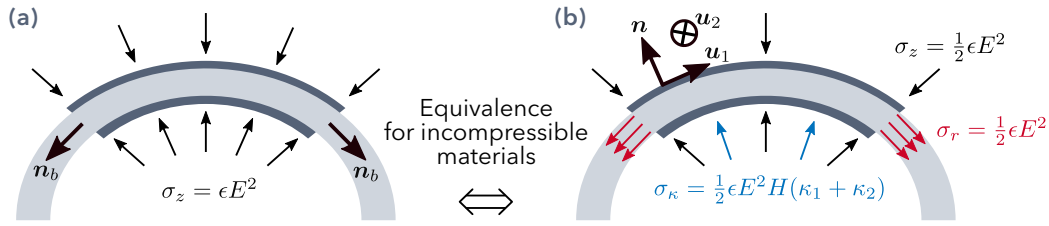


Fig. 2.3. Electrostatic stresses generated by charged electrodes on a curved DE membrane. κ_1 and κ_2 are the curvatures in the radial and orthoradial directions respectively. **(a)** Pelrine's point of view: double normal pressure. **(b)** Stress distribution found by analyzing the charge distribution.

Anticipating a little on the following, the equilibrium equations of an inflated axisymmetric hyper-elastic membrane read [2]:

$$\frac{\partial \sigma_1 H R}{\partial R} = \sigma_2 H, \quad \kappa_1 H \sigma_1 + \kappa_2 H \sigma_2 = P, \quad (2.7)$$

where σ_1 is the radial stress (along \mathbf{u}_1) and σ_2 the ortho-radial stress (along \mathbf{u}_2), H the membrane thickness, P the inflation pressure, R the radial coordinate. The jump condition at the membrane border reads:

$$[[H\sigma_1]] + H t_s = 0, \quad (2.8)$$

where t_s is the surface stress applied on the membrane border in the direction \mathbf{n}_b [see fig. 2.3], $[[H\sigma_1]] = (H\sigma_1)_{\text{in}} - (H\sigma_1)_{\text{out}}$ is the jump of $H\sigma_1$ across a discontinuity surface of normal \mathbf{n}_b .

The stress state can be described in two different manners.

First description of the electromechanical coupling The total stresses read:

$$\sigma_1 = \sigma_{1m} - 2\sigma_{\text{Max}}, \quad \sigma_2 = \sigma_{2m} - 2\sigma_{\text{Max}}, \quad (2.9)$$

where $\sigma_{\text{Max}} = 1/2\epsilon E^2$, and σ_{1m} and σ_{2m} are the mechanical parts of the principal stresses.

These expressions will be obtained rigorously in the following section, and are used here to explain fig. 2.3. The total set of equilibrium equations for the DE membrane comprises eqs. (2.7) to (2.9), and describes the stress state shown in fig. 2.3a.

Second description of the electromechanical coupling We define new stresses by:

$$\tilde{\sigma}_1 = \sigma_{1m} - \sigma_{\text{Max}} = \sigma_1 + \sigma_{\text{Max}}, \quad \tilde{\sigma}_2 = \sigma_{2m} - \sigma_{\text{Max}} = \sigma_2 + \sigma_{\text{Max}}, \quad (2.10)$$

Inserting these expressions in the equilibrium equations (2.7) and (2.8) yields:

$$\kappa_1 H \tilde{\sigma}_1 + \kappa_2 H \tilde{\sigma}_2 = P + \sigma_{\text{Max}}(\kappa_1 H + \kappa_2 H) , \quad (2.11a)$$

$$\frac{\partial \tilde{\sigma}_1 H R}{\partial R} + R \frac{\partial \sigma_{\text{Max}} H}{\partial R} = \tilde{\sigma}_2 H , \quad (2.11b)$$

$$[[H \tilde{\sigma}_1]] + [[H \sigma_{\text{Max}}]] + H t_s = 0 . \quad (2.11c)$$

If the thickness is uniform, the electrostatic pressure σ_{Max} is uniform too, and the second term in eq. (2.11b) vanishes. The set of equations (2.11) then corresponds exactly to the stresses described in fig. 2.3b. If the thickness is not uniform, the second equilibrium has one more term compared to eq. (2.7), that is related to the variation of the electrostatic stress along the radius.

This second description of the electrostatic coupling is easier to interpret in terms of electric charge distributions, but is way less practical to use for numerical calculations than the first description where only a normal electrostatic pressure is required.

Moreover, the first description of the electrostatic coupling comes out naturally from the analysis of DE membranes based on energy considerations, as it will be shown in section 2.2.2.

General models for non-uniform deformations

While the approach proposed by Pelrine *et al.* is valid to describe one-degree-of-freedom system, this method is harder to apply to deformable membranes undergoing non-uniform deformations.

A unifying theory of DEs has been proposed by Suo *et al.* [109, 108], where the coupled electromechanical equations are obtained starting from the definitions of work, electric charges, and force.

Another general approach to obtain coupled electromechanical equations derives from the work by Coleman and Noll [19], who proposed a framework based on thermodynamics to derive coupled multi-physics constitutive relations. This framework was used to derive the constitutive equations for electromagnetism, mechanics, and electromagnetism coupled to mechanics by Kovetz [69]. Edmiston and Steigmann [26], and Dorfmann and Ogden [24] applied it successfully to DEs.

A review of the different modelling approaches for non-linear electromechanics has been written by Bustamante *et al.* [12].

In this thesis, we will use the approach proposed by Kovetz [69], and its application to DEs by Edmiston and Steigmann [26] as it appears to be one of the most comprehensive and rigorous.

2.2.2 Theory

The method of Edmiston and Steigmann [26] to derive the constitutive relations of dielectric elastomers is summarized in appendix A. The constitutive equations are here simplified to membrane kinematics.

Constitutive relations in a general 3D case

We consider a dielectric body partially covered by electrodes on its surface.

In the absence of any electric charge or mechanical load, the body occupies a reference configuration, where each material particle is identified by its position $\bar{\mathbf{X}}$ ¹. Under electrical and mechanical loading, the body is transformed to a deformed configuration: the material point initially in $\bar{\mathbf{X}}$ moves to the position \mathbf{X} .

The deformation gradient tensor is defined by $\mathbf{F} = \partial \mathbf{X} / \partial \bar{\mathbf{X}}$, and the Cauchy-Green tensor by $\mathbf{C} = \mathbf{F}^T \cdot \mathbf{F}$.

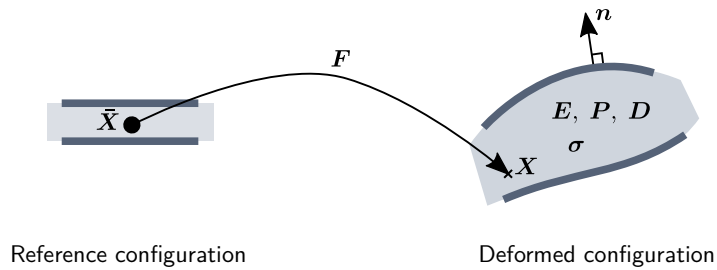


Fig. 2.4. Description of a material sample and definition of external loads

The problem is sketched in fig. 2.4. The mass density is denoted by ρ_s , the Cauchy stress tensor by $\boldsymbol{\sigma}$, and the electric displacement by $\mathbf{D} = \epsilon_0 \mathbf{E} + \mathbf{P}$, where ϵ_0 is the vacuum permittivity, \mathbf{E} the electric field and \mathbf{P} the electric polarization density, all in the deformed configuration.

The constitutive relations of a general DE system read [see appendix A]:

$$\boldsymbol{\sigma} = \boldsymbol{\sigma}_0 + \boldsymbol{\sigma}_{\text{Maxwell}} , \quad (2.12a)$$

$$\text{with } \boldsymbol{\sigma}_0 = 2\rho_s \mathbf{F} \cdot \frac{\partial \phi_0}{\partial \mathbf{C}} \cdot \mathbf{F}^T , \quad \text{and } \boldsymbol{\sigma}_{\text{Maxwell}} = \epsilon \left(\mathbf{E} \otimes \mathbf{E} - \frac{1}{2} \mathbf{E} \cdot \mathbf{E} \mathbf{I} \right) , \quad (2.12b)$$

where ϕ_0 is a purely mechanical free energy, \mathbf{I} the identity operator, and ϵ is the dielectric permittivity of the membrane.

Reduction of the constitutive equations to the case of a membrane

The constitutive laws of the DE have been given in the general 3D case. In the case of a membrane they can be significantly simplified.

¹ In the whole thesis, variables with an over-bar are defined in the reference configuration.

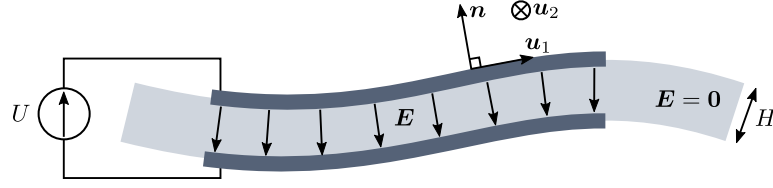


Fig. 2.5. Assumptions on the electric field in a thin DE membrane.

Concerning the electrostatics, the classical approximation for a thin dielectric between electrodes is made: the electric field is assumed to be normal to the membrane, and null outside of the dielectric portion covered with electrodes [see fig. 2.5]. Fringe effects are neglected. This leads to:

$$\mathbf{E} = -E \mathbf{n} , \quad \text{with } E = \frac{U}{H} , \quad (2.13)$$

where \mathbf{n} is the normal to the membrane, H the thickness, and U the electric potential difference between the electrodes. The electric field E does not vary in the thickness direction.

A specific form of the mechanical free energy now needs to be chosen. In the following the elastomer is assumed to behave according to the Gent material law [35] (this assumption will be validated in the experimental section 3.3.1). A Lagrange multiplier Π is used to impose the incompressibility constraint $J = \det(\mathbf{F}) = 1$:

$$\phi_0 = -\frac{\mu J_m}{2} \log \left(1 - \frac{I_1 - 3}{J_m} \right) + \frac{\Pi}{\rho_s} (J - 1) , \quad (2.14)$$

where $I_1 = \text{tr } \mathbf{C}$ is the first invariant of the Cauchy-Green tensor, μ is the shear modulus, and J_m is a parameter describing the stiffening of the material at large strains.

In the principal basis [see fig. 2.5], the deformation gradient and the right Cauchy-Green deformation tensor read:

$$\mathbf{F} = \lambda_1 \mathbf{u}_1 \otimes \mathbf{u}_1 + \lambda_2 \mathbf{u}_2 \otimes \mathbf{u}_2 + \lambda_n \mathbf{n} \otimes \mathbf{n} , \quad (2.15)$$

$$\mathbf{C} = \mathbf{F}^T \mathbf{F} = \lambda_1^2 \mathbf{u}_1 \otimes \mathbf{u}_1 + \lambda_2^2 \mathbf{u}_2 \otimes \mathbf{u}_2 + \lambda_n^2 \mathbf{n} \otimes \mathbf{n} , \quad (2.16)$$

where λ_1 and λ_2 are the two principal planar stretches and λ_n the normal stretch.

Inserting eqs. (2.13) to (2.16) into eq. (2.12) provides the expression of $\boldsymbol{\sigma}$ in the principal basis ($\boldsymbol{\sigma} = \sigma_1 \mathbf{u}_1 \otimes \mathbf{u}_1 + \sigma_2 \mathbf{u}_2 \otimes \mathbf{u}_2 + \sigma_n \mathbf{n} \otimes \mathbf{n}$):

$$\sigma_1 = \frac{\mu J_m}{J_m - I_1 + 3} \lambda_1^2 - \frac{\epsilon E^2}{2} + \Pi , \quad (2.17a)$$

$$\sigma_2 = \frac{\mu J_m}{J_m - I_1 + 3} \lambda_2^2 - \frac{\epsilon E^2}{2} + \Pi , \quad (2.17b)$$

$$\sigma_n = \frac{\mu J_m}{J_m - I_1 + 3} \lambda_n^2 + \frac{\epsilon E^2}{2} + \Pi . \quad (2.17c)$$

The mechanical equilibrium equations are exactly the same as classical purely mechanical equations. The coupling with electrostatics appears only in the constitutive relation

defining the stress. Therefore, classical membrane equations can be used, in which plane stress is assumed: $\boldsymbol{\sigma} \cdot \mathbf{n} = \sigma_n = 0$ [2]. This provides the expression of the Lagrange multiplier Π .

The constitutive equations for the principal planar strains of a DE membrane are thus obtained:

$$\sigma_1 = \frac{\mu J_m}{J_m - I_1 + 3} (\lambda_1^2 - \lambda_n^2) - \epsilon E^2, \quad (2.18a)$$

$$\sigma_2 = \frac{\mu J_m}{J_m - I_1 + 3} (\lambda_2^2 - \lambda_n^2) - \epsilon E^2, \quad (2.18b)$$

where $I_1 = \lambda_1^2 + \lambda_2^2 + \lambda_n^2$. The stretches are linked by the incompressibility relation $\lambda_1 \lambda_2 \lambda_n = 1$. Here one may notice that due to incompressibility the electromechanical coupling results in an increased stress in the planar directions that is twice the commonly called Maxwell pressure $\sigma_{\max} = \epsilon E^2/2$. This is due to the coupling between the normal and planar deformations of the membrane.

Finally, the non-dimensional nominal stresses $s_1 = \sigma_1/\mu\lambda_1$ and $s_2 = \sigma_2/\mu\lambda_2$ are defined, and read:

$$s_1 = \frac{J_m}{J_m - I_1 + 3} (\lambda_1 - \lambda_1^{-3}\lambda_2^{-2}) - \frac{U^2}{\mu\bar{H}^2} \lambda_1 \lambda_2^2, \quad (2.19a)$$

$$s_2 = \frac{J_m}{J_m - I_1 + 3} (\lambda_2 - \lambda_1^{-2}\lambda_2^{-3}) - \frac{U^2}{\mu\bar{H}^2} \lambda_1^2 \lambda_2. \quad (2.19b)$$

where \bar{H} is the thickness of the membrane in the reference configuration [see fig. 2.6].

Note on damping

In all the foregoing, we did not mention the losses inherent to the membrane material, which has been modelled so far as a loss-free hyper-elastic material.

In practice, the silicone used to manufacture the membrane exhibits a visco-elastic behavior. However, in this thesis the structural losses will be taken into account by a constant loss factor η , by considering a complex shear modulus:

$$\mu^* = \mu(1 + i\eta), \quad (2.20)$$

where μ is the real loss-free shear modulus. This expression is substituted in the equation defining the stresses eq. (2.19), which yields:

$$s_1 = \frac{J_m(1 + i\eta)}{J_m - I_1 + 3} (\lambda_1 - \lambda_1^{-3}\lambda_2^{-2}) - \frac{U^2}{\mu\bar{H}^2} \lambda_1 \lambda_2^2, \quad (2.21a)$$

$$s_2 = \frac{J_m(1 + i\eta)}{J_m - I_1 + 3} (\lambda_2 - \lambda_1^{-2}\lambda_2^{-3}) - \frac{U^2}{\mu\bar{H}^2} \lambda_1^2 \lambda_2. \quad (2.21b)$$

The loss factor will be tuned on experimental data, and this simple damping model will be validated in chapter 4, by comparisons with experiments.

More realistic damping models for DEs have been developed by other authors, and can be implemented if the simple constant structural damping does not capture the experimental behavior.

2.3 Hyper-elastic membrane mechanics

We now return to the problem of the dynamics of a DE membrane in an inflated configuration, as sketched in fig. 2.6. The equilibrium equations of axisymmetric hyperelastic membranes are derived, and a weak form of these equations is obtained, for later implementation in finite elements.

2.3.1 Literature review

Hyperelastic membranes have been studied for a long time, and the static equilibrium equations have been written by Adkins and Rivlin in 1952 [2].

The equilibrium equations for dynamics are for example available in [73].

2.3.2 Theory

Definition of the useful variables

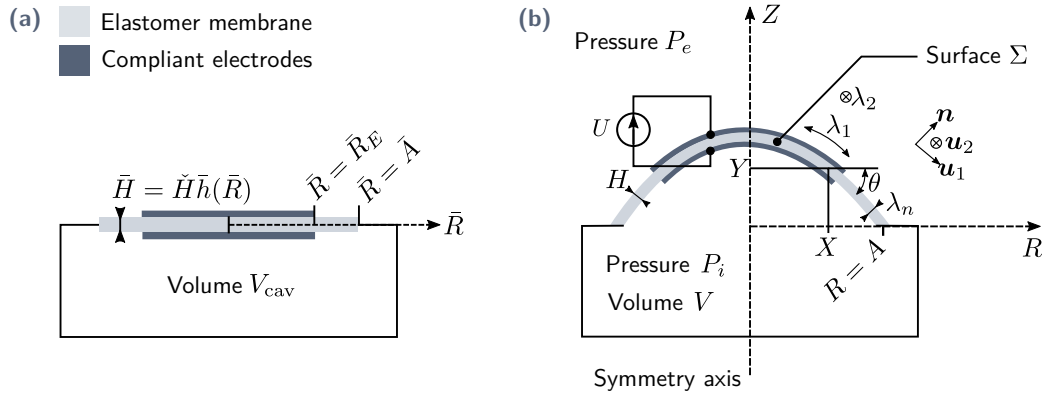


Fig. 2.6. Schematics of the studied system. **(a)** Reference configuration, where the membrane is flat. In the example shown, $\Gamma(\bar{R}) = 1$ for $\bar{R} < \bar{R}_E$ and $\Gamma(\bar{R}) = 0$ for $\bar{R} > \bar{R}_E$. **(b)** Deformed configuration, where the membrane is stretched and inflated.

Only axisymmetric deformations are studied in the present work. The thickness of the membrane as well as the electrodes can be of any axisymmetrical shape. The function $\Gamma(\bar{R})$ describes the electrode location: it equals unity when electrodes are present at radius \bar{R} in the reference configuration [see fig. 2.6a], and zero otherwise. The membrane is pre-stretched from the radius \bar{A} to a radius A and inflated with the pressure P_{app} . A voltage

U is then applied between the electrodes. The pressure inside the cavity is denoted P_i , and the exterior pressure P_e .

The material points of the membrane identified by the radius \bar{R} in the reference configuration move to the radius $X(\bar{R}, T)$ and to the altitude $Y(\bar{R}, T)$ in the deformed configuration at time T [see fig. 2.6b]. The corresponding stretches are denoted by λ_1 and λ_2 respectively. The principal stretches as well as the angle of incline θ , defined in fig. 2.6b, can be expressed in terms of the variables X and Y :

$$\begin{aligned} \lambda_1 &= \sqrt{\left(\frac{\partial X}{\partial \bar{R}}\right)^2 + \left(\frac{\partial Y}{\partial \bar{R}}\right)^2}, & \lambda_2 &= \frac{X}{\bar{R}}, & \lambda_n &= \frac{1}{\lambda_1 \lambda_2} = \frac{H}{\bar{H}}, \\ \cos \theta &= \frac{1}{\lambda_1} \frac{\partial X}{\partial \bar{R}}, & \sin \theta &= \frac{1}{\lambda_1} \frac{\partial Y}{\partial \bar{R}}, \end{aligned} \quad (2.22)$$

where $\bar{H}(\bar{R})$ and $H(\bar{R})$ are the non-uniform thickness of the membrane in reference and deformed configuration respectively. The thickness in the reference configuration is written $\bar{H}(\bar{R}) = \bar{H} \bar{h}(\bar{R})$, where \bar{H} is the thickness at the center, and $\bar{h}(\bar{R})$ a non-dimensional function which equals one at the center.

Equilibrium equations of the membrane

The dynamic equilibrium equations are derived from the classical membrane equations, commonly written along the normal and the tangential directions [73]. Given the axisymmetry of the problem, they are here projected along the radial and the vertical directions:

$$\rho_s(1 + \Gamma \rho_{\text{ratio}}) \frac{XH}{\cos \theta} \frac{\partial^2 X}{\partial T^2} = -\frac{\sigma_2 H}{\cos \theta} - (P_i - P_e)X \frac{\sin \theta}{\cos \theta} + \frac{\partial}{\partial X}(\sigma_1 X H \cos \theta), \quad (2.23a)$$

$$\rho_s(1 + \Gamma \rho_{\text{ratio}}) \frac{XH}{\cos \theta} \frac{\partial^2 Y}{\partial T^2} = (P_i - P_e)X + \frac{\partial}{\partial X}(\sigma_1 X H \sin \theta), \quad (2.23b)$$

where ρ_{ratio} is the ratio of the electrode over the membrane mass per unit area. The dependence in radius R and time T of X, Y, θ, H has been omitted for clarity.

These equations are the same as those derived by Zhu et al. [126], and are similar to those used by Mockensturm and Goulbourne [81], except that they neglect tangential inertia. If all inertia is neglected eq. (2.23) is equivalent to the well-known hyperelastic membrane equations derived by Atkins [2]. Note that the electrostatic coupling appears only in constitutive equations (2.21), and not in equilibrium equations (2.23).

All the equations of the problem are now transformed into a non-dimensional form, by introducing non-dimensional variables, written with small letters:

$$\begin{aligned} r &= \frac{R}{\bar{A}}, & z &= \frac{Z}{\bar{A}}, & \bar{r} &= \frac{\bar{R}}{\bar{A}}, & a &= \frac{A}{\bar{A}}, & x &= \frac{X}{\bar{A}}, \\ y &= \frac{Y}{\bar{A}}, & \bar{h} &= \frac{\bar{H}}{\bar{H}}, & t &= \frac{C_s}{\bar{A}} T, & p_i &= \frac{\bar{A} P_i}{\mu \bar{H}}, & p_e &= \frac{\bar{A} P_e}{\mu \bar{H}}, \end{aligned} \quad (2.24)$$

where $C_s = \sqrt{\mu/\rho_s}$ is the speed of shear waves in the elastomer.

Using the geometrical relations eq. (2.22) and the definition of the non-dimensional parameters eq. (2.24) we obtain from eq. (2.23) the non-dimensional equilibrium equations:

$$\left(\frac{\bar{h}\bar{r}s_1x'}{\lambda_1} \right)' - (p_i - p_e)xy' - s_2\bar{h} = \bar{r}(\bar{h} + \Gamma\rho_{\text{ratio}})\ddot{x}, \quad (2.25a)$$

$$\left(\frac{\bar{h}\bar{r}s_1y'}{\lambda_1} \right)' + (p_i - p_e)xx' = \bar{r}(\bar{h} + \Gamma\rho_{\text{ratio}})\ddot{y}, \quad (2.25b)$$

where the prime (') stands for the space derivative $\partial/\partial\bar{r}$, and the dot (·) is the time derivative $\partial/\partial t$.

The boundary conditions for the membrane displacement are the following. Because of axisymmetry, and as the displacement and the curvature of the membrane are continuous, the radial displacement and the membrane slope are null at the center. The membrane is clamped at the outer edge at $R = A$. This reads:

$$x(\bar{r} = 0) = 0, \quad x(\bar{r} = 1) = a, \quad y'(\bar{r} = 0) = 0, \quad y(\bar{r} = 1) = 0. \quad (2.26)$$

Weak form of the membrane equilibrium equations

Multiplying eq. (2.25) by test functions \mathcal{X} and \mathcal{Y} , and integrating by part on the membrane Σ yields the following weak form of the membrane equilibrium equations:

$$\begin{aligned} & \int_{\Sigma} \mathcal{Y}' \frac{\bar{h}\bar{r}s_1y'}{\lambda_1^2} dl + \int_{\Sigma} \mathcal{X}' \frac{\bar{h}\bar{r}s_1x'}{\lambda_1^2} dl + \int_{\Sigma} \frac{1}{\lambda_1} s_2\bar{h}\mathcal{X} dl - \int_{\Sigma} \frac{1}{\lambda_1} (p_i - p_e) (-y'\mathcal{X} + x'\mathcal{Y}) x dl \\ & = - \int_{\Sigma} \frac{1}{\lambda_1} (\bar{h} + \Gamma\rho_{\text{ratio}}) (\mathcal{Y}\ddot{y} + \mathcal{X}\ddot{x}) \bar{r} dl \quad \forall \mathcal{X}, \mathcal{Y} \quad |\mathcal{X}(\bar{r} = 1) = \mathcal{Y}(\bar{r} = 1) = 0, \end{aligned} \quad (2.27)$$

where $dl = \lambda_1 d\bar{R}$ is the element length of the membrane.

2.4 Electrical model of the dielectric elastomer membrane

In section 2.2, we derived the constitutive equations of dielectric elastomers, and modelled the influence of the applied voltage on the stress state. In the present section, we want to estimate the effective voltage on the electrodes, which may differ, as we will see, from the voltage applied to the electrical connections of the membrane.

2.4.1 Literature review

When DEs are used in high frequency applications (several kHz) such as loudspeakers [45, 51, 31], the resistivity of the electrodes starts to play a significant role. Combined with the capacitive nature of the DE membrane, it creates an equivalent resistor-capacitor circuit, that is characterized by its time constant τ_{RC} or its characteristic frequency ω_{RC} .

For frequencies $\omega > \omega_{RC}$, the effective voltage which actuates the transducer is smaller than the supplied voltage, leading to a decrease in performance at high frequencies.

What is more, it has then been noticed that at higher frequencies, lumped RC models do not describe correctly the electrical behavior of DEs, and transmission line models which account for the spacial variation of the voltage on the electrodes have been proposed as a refinement [117, 58, 39], either to study the voltage distribution on DE membranes for actuator applications, or to investigate self-sensing of stacked DE transducers where the resistivity of the electrodes connections is large [49, 48].

The effects of electrode resistivity will be studied in details in chapter 6, and in the present chapter we settle for the lumped model to compute the electrical behavior of the DE membrane, as the electrode resistivity is sufficiently low.

2.4.2 Theory

Lumped electrical model

The most simple way to account for electrode resistivity is to build a lumped model of the membrane and its electrodes, which forms an RC circuit [see fig. 2.7].

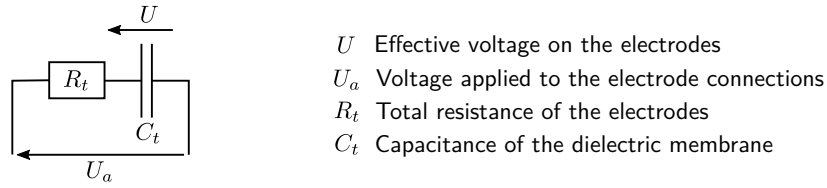


Fig. 2.7. Lumped electrical model of the DE membrane. The voltage supplied by the generator is U_a , and the voltage that effectively deforms the membrane is U .

The circuit is a low-pass filter, whose transfer function in the frequency domain reads:

$$\frac{\hat{U}}{\hat{U}_a} = \frac{1}{1 + i\frac{\omega}{\omega_{RC}}}, \quad (2.28)$$

where $\omega_{RC} = 1/R_t C_t$. In this section hats denote Fourier transforms ($\hat{U} = \mathcal{F}(U)$).

Effect on the chosen electrical signal

The Maxwell stress, which is responsible for the electromechanical activation, is proportional to the squared voltage [see eqs. (2.12) and (2.13)]. This will be the major source of non-linearity. However, shaping the input signal can help reducing distortion, as shown by Heydt et al. [46], and Kaal and Herold [57]. The following voltage is therefore applied to the electrode connections:

$$U_a(t) = \sqrt{U_0^2 + W_a(t)}, \quad \text{with } U_0^2 > |W_a|, \quad (2.29)$$

where U_0 is a DC voltage, and $W_a(t)$ an alternating component (in V^2) which corresponds to the audio signal that is played on the loudspeakers.

The first order effect of the RC filter on the voltage U_a applied to the electrodes is now estimated. For small amplitudes of W_a compared to U_0^2 , the applied voltage can be linearized as:

$$U_a(t) = \sqrt{U_0^2 + W_a(t)} \approx U_0 + \frac{W_a(t)}{2U_0} . \quad (2.30)$$

Filtering U_a by the RC circuit eq. (2.28) yields:

$$U(t) \approx U_0 + \frac{1}{2U_0} W(t) , \quad \text{with } W(t) = \mathcal{F}^{-1} \left(\frac{\hat{W}_a(\omega)}{1 + i\frac{\omega}{\omega_{RC}}} \right) , \quad (2.31)$$

where \mathcal{F}^{-1} is the inverse Fourier transform. Finally, by squaring and keeping the first order term:

$$U^2(t) \approx U_0^2 + W(t) . \quad (2.32)$$

At low frequencies, $1 + i\omega/\omega_{RC} \approx 1$, meaning that the electrical circuit has no effect, so $U(t) = U_a(t)$. The expression eq. (2.32) is therefore exact at low frequencies, even for large values of W_a .

Above the cutting frequency ω_{RC} , the voltage is no longer uniform on the electrodes, while the model still assumes a uniform distribution. The correction of W by the RC circuit should therefore only be seen as a qualitative way to account for the decrease of the excitation amplitude above ω_{RC} .

Finally, using eq. (2.32) in the constitutive relations eq. (2.21) yields:

$$s_1 = \frac{J_m(1+i\eta)}{J_m - I_1 + 3} (\lambda_1 - \lambda_1^{-3}\lambda_2^{-2}) - u_0^2 \frac{\Gamma}{\bar{h}^2} \lambda_1 \lambda_2^2 - w \frac{\Gamma}{\bar{h}^2} \lambda_1 \lambda_2^2 , \quad (2.33a)$$

$$s_2 = \frac{J_m(1+i\eta)}{J_m - I_1 + 3} (\lambda_2 - \lambda_1^{-2}\lambda_2^{-3}) - u_0^2 \frac{\Gamma}{\bar{h}^2} \lambda_1^2 \lambda_2 - w \frac{\Gamma}{\bar{h}^2} \lambda_1^2 \lambda_2 , \quad (2.33b)$$

where $u_0 = \sqrt{\epsilon/\mu} U_0 / \check{H}$ is the non-dimensional static voltage, and $w = \epsilon W / \mu \check{H}^2$ the non-dimensional excitation. In both equations, the first term is the mechanical stress, the second is the stress created by the static voltage, and the third is the dynamical stress due to the alternating component of the excitation voltage. This last term is proportional to W , meaning the excitation force depends linearly on the audio signal. The electric field is non-zero only where the electrodes are located, as indicated by the factor Γ in eq. (2.33).

2.5 Acoustic radiation

2.5.1 Literature review

Strong vibroacoustic coupling

The DE membrane thickness is typically around $50\text{ }\mu\text{m}$ in the **reference configuration**, and around $25\text{ }\mu\text{m}$ in the **static configuration**. A non-dimensional parameter describing the relation between the membrane mass and the mass of the air put into motion by the membrane can be built:

$$m = \frac{\rho_f \bar{A}}{\rho_s \bar{H}}, \quad (2.34)$$

where ρ_f is the fluid density, ρ_s the membrane density, \bar{A} the initial membrane radius and \bar{H} the initial thickness at the center. For typical values of the thickness and radius, this parameter is of the order of one:

$$m \approx \frac{1.2 \times 0.02}{1000 \times 50 \times 10^{-6}} \approx 0.5, \quad (2.35)$$

meaning that the air surrounding the membrane is comparatively heavy. Strong vibroacoustic coupling therefore needs to be accounted for to yield an accurate prediction of the membrane vibrations and acoustic radiation. The parameter m will appear as an added mass in the boundary conditions between the membrane and the air [see eq. (2.51)].

Strong vibroacoustic coupling has been investigated in depth for the past fifty years or more, and several formulations of the vibroacoustic problem have been proposed, either with symmetric matrices or not, using different state variables to describe the fluid and solid domains (displacement, velocity, pressure, displacement potential...). These different formulations can be found in Morand & Ohayon [82] or in Sigrist [104] for example. A shorter summary is available in the article by Ohayon & Schotté [84], where the standard formulation using the pressure and the structure displacement is given.

Model order reduction methods have been developed for fluid-structure interaction problem, including for strong vibroacoustic coupling. These methods are generally based on substructuring: modes of substructures (the fluid only, the structure only) are computed, and the coupled system is then reduced using these uncoupled modal bases. Symmetric matrices can be obtained at the end [84, 82]. The dynamic substructuring methods can be extended to exterior vibroacoustic problems by modelling the exterior fluid by the Boundary Element Method (BEM) [85, 82].

The methods proposed in Morand & Ohayon [82] for modal order reduction of exterior fluid structure problems imply coupling FEM and BEM softwares, which may rise practical issues to obtain reliable results. Moreover, a new type of non-reflective boundary condition has been developed after Morand & Ohayon [82], namely the Perfectly Matched Layers (PMLs). These boundary conditions are very well suited for finite element calculations in open domains, and thus new methods have been developed based on PMLs to reduce exterior vibroacoustic problems. This is investigated in next section.

Perfectly matched layers

Perfectly Matched Layers are an efficient way to ensure reflection-free boundary conditions in a finite element calculation. They consist of an added absorbing layer placed around the outer boundary. PMLs have first been suggested by Berenger [7] for calculations in the time domain, but they are well suited to frequency domain computations as well. They are nowadays implemented in most commercial finite element softwares for acoustics. Here axisymmetric PMLs are used, with the complex change of variables introduced by Collino and Monk [20].

Modal methods for exterior acoustics

In order to compute the pressure radiated by the DE loudspeaker fast enough to later perform optimization, the dynamics and radiation will be solved using modal methods.

The most common modal approach for exterior acoustics is based on the so-called *radiation modes* [9, 22, 89]. Radiation modes are obtained by diagonalizing the radiation operator, which defines the power radiated by a structure. The radiation modes can then be used to efficiently compute the power radiated by the structure, but not the radiated acoustic pressure. What is more, they are frequency-dependent, and therefore need to be computed for all frequencies of interest.

Modal methods have also been investigated to compute the radiated pressure, but this field has less been investigated. For damped and open (exterior radiation) systems, complex resonance modes will be obtained (in opposition to classical real un-damped modes [29]). At this point, a clarification of the distinction between resonance modes and eigenmodes is necessary.

The general fluid-structure problem can be written in the general matrix form:

$$[-\Omega^2 \mathbf{M}_{\text{tot}} + \mathbf{K}_{\text{tot}}(\Omega)] \mathbf{X}_{\text{tot}} = \mathbf{F}_{\text{tot}} , \quad (2.36)$$

where \mathbf{M}_{tot} and \mathbf{K}_{tot} are the total fluid-structure mass and stiffness matrices, \mathbf{X}_{tot} the vector of unknowns (containing both the acoustic and structural unknowns), and \mathbf{F}_{tot} the excitation, which may contain both excitations of the structure and of the fluid. The stiffness matrix generally depends on frequency because of the Sommerfeld radiation condition. The eigenfrequencies Ω_n and eigenmodes Ψ_n of eq. (2.36) are defined by the following linear eigenvalue problem:

$$[-\Omega_n^2 \mathbf{M}_{\text{tot}} + \mathbf{K}_{\text{tot}}(\Omega)] \Psi_n = 0 \quad (2.37)$$

so the eigenfrequencies and eigenmodes depend on the frequency Ω , and need to be computed for all frequencies. They are therefore of little use for reducing the system eq. (2.36). On the other hand, the resonance frequencies Λ_n and the resonance modes Φ_n are defined by the non-linear eigenvalue problem:

$$[-\Lambda_n^2 \mathbf{M}_{\text{tot}} + \mathbf{K}_{\text{tot}}(\Lambda_n)] \Phi_n = 0 , \quad (2.38)$$

which is non-trivial to solve. However, the obtained resonance modes do not depend this time on frequency. Filippi and Habault [29] derived an analytical modal expansion

formula on the resonance mode basis, but it requires the knowledge of the derivatives of the eigenvalues with respect to frequency, which are impractical to obtain.

This type of non-linear eigenvalue problem, where the stiffness matrix depends on frequency is frequently obtained in structural mechanics, when part of the system has a viscous behavior for example. Several modal methods have been investigated to reduce such problems [101].

The general idea for using modal methods for exterior problem is to discretize the continuous spectrum that exists in open domains. Indeed, in bounded domains, free vibrations can only occur at a set of discrete frequencies, the eigenfrequencies of the system. In open domain, free oscillations may occur for all frequencies, which can be interpreted as a continuous spectrum of eigenfrequencies [77].

Marburg [77, 79, 78] studied the use of resonance modes as a basis to compute the pressure radiated by open systems in acoustics. He investigates a simple open acoustic resonator [79], using finite elements to describe the acoustics around the object, and infinite elements to model the Sommerfeld radiation condition. This model coupling finite elements and infinite elements leads to a quadratic eigenvalue problem, with a damping matrix that represents the loss of energy through radiation.

Compared to interior problems, it is found that a large number of modes is needed in the reduced basis in order to obtain a good convergence of the modal summation solution. This is directly related to the fact that many modes are needed to approximate the continuous spectrum that characterizes open systems. Marburg concludes that modal approaches for exterior problems are particularly interesting to perform structural optimization in view of improving the acoustic behavior of the structure.

There is also a substantial literature in the field of optics and photonics [70, 121], where nano-scale open light resonators have been investigated using resonance modes (also called Quasi Normal Modes). The coupling of finite element methods and PMLs appears to be one of the most efficient method to compute resonance modes, and modal superposition is shown to work on such a reduced modal basis. The advantage of the PMLs to model the Sommerfeld radiation condition is that frequency independent matrices can be obtained, leading to a linear eigenvalue problem (contrary to the quadratic eigenvalue problem which is obtained when infinite elements are used [79]). The modal method is claimed to provide a better physical understanding of the radiation properties of the studied system compared to direct approaches where the governing equations are solved for all frequencies of interest.

Thus, we will use modal approaches using PMLs to solve for the fluid loaded dynamics and acoustical radiation of the DE membrane.

2.5.2 Theory

Acoustic equilibrium equations

The pressure difference between the inside and the outside of the cavity is small compared to the atmospheric pressure, so the fluid density ρ_f and the speed of sound C_f are assumed to be the same inside and outside.

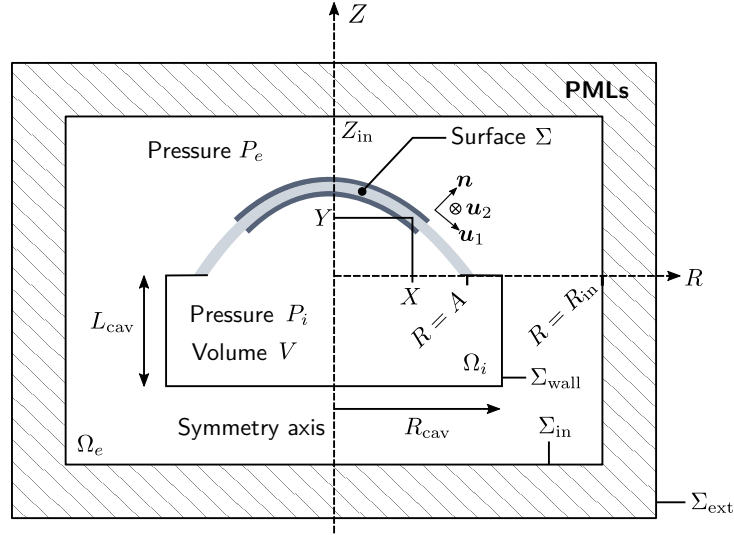


Fig. 2.8. Definition of the variables for acoustic calculations.

The pressure field inside the cavity is split into a static part P_0 , a uniform oscillating part P_u , and an acoustic part P_a :

$$P_i = P_0 + (P_u + P_a)e^{i\Omega T} . \quad (2.39)$$

The total dynamic pressure satisfies the Helmholtz equation, and the uniform pressure is proportional to the volume variation of the cavity. This yields the following system of governing equations [82]:

$$\Omega^2 P_a + \Omega^2 P_u + C_f^2 \Delta P_a = 0 , \quad (2.40a)$$

$$\int_{\Omega_i} P_a R dS = 0 , \quad (2.40b)$$

$$P_u + C_f^2 \frac{\rho_f}{V_0} 2\pi \int_{\Sigma} \frac{1}{\lambda_{10}} (-Y'_0 \tilde{X} + X'_0 \tilde{Y}) X_0 dL = 0 , \quad (2.40c)$$

where $dL = \lambda_{10} d\bar{R}$ is the element length of the membrane, and $dS = dR dZ$ the element surface of Ω_i and Ω_e . The integrations domains are defined in fig. 2.8.

The interior pressure satisfies Neumann boundary conditions: the normal velocity on the walls of the cavity Σ_{wall} is null, and the normal velocity equals the membrane normal velocity on the membrane Σ :

$$\nabla P_a \cdot \mathbf{n} = 0 \quad \text{on } \Sigma_{\text{wall}} , \quad (2.41a)$$

$$\nabla P_a \cdot \mathbf{n} = \rho_f \Omega^2 \frac{1}{\lambda_{10}} (-Y'_0 \tilde{X} + X'_0 \tilde{Y}) \quad \text{on } \Sigma . \quad (2.41b)$$

The exterior pressure also obeys the Helmholtz equation:

$$\Omega^2 P_e + C_f^2 \Delta P_e = 0 , \quad (2.42)$$

and satisfies Neumann boundary conditions on the cavity walls and on the membrane:

$$\nabla P_e \cdot \mathbf{n} = 0 \quad \text{on } \Sigma_{\text{wall}} , \quad (2.43a)$$

$$\nabla P_e \cdot \mathbf{n} = -\rho_f \Omega^2 \frac{1}{\lambda_{10}} (-Y'_0 \tilde{X} + X'_0 \tilde{Y}) \quad \text{on } \Sigma , \quad (2.43b)$$

as well as a Sommerfeld radiation condition on the outer boundary Σ_{in} . This boundary condition will be implemented by PMLs, using the complex change of coordinates defined in the following section.

Axisymmetric perfectly matched layers

In order to define perfectly matched layers in the regions shown in fig. 2.8, a complex change of coordinates is defined. The coordinates will become complex in the PML region, creating numerical absorption properties.

The same procedure as in Collino and Monk's work [20] is followed, with a single change: the frequency dependence of the change of coordinates is removed so that frequency independent mass and stiffness matrices can be obtained. Thus, we define:

$$\hat{r} = \begin{cases} r - i \int_{r_{\text{in}}}^r \Theta_r(r) ds & \text{for } r > r_{\text{in}} \\ r & \text{otherwise} \end{cases}, \quad \hat{z} = \begin{cases} z - i \int_{z_{\text{in}}}^z \Theta_z(z) ds & \text{for } |z| > |z_{\text{in}}| \\ z & \text{otherwise} \end{cases}, \quad (2.44)$$

where classical quadratic attenuation functions are chosen:

$$\Theta_r(r) = \Theta_0 (r - r_{\text{in}})^2, \quad \Theta_z(z) = \Theta_0 (z - z_{\text{in}})^2, \quad (2.45)$$

Θ_0 being an attenuation parameter that should be adjusted.

These changes of variables imply the following changes of the partials derivatives:

$$\frac{\partial}{\partial \hat{r}} = \frac{1}{\gamma_r(r)} \frac{\partial}{\partial r}, \quad \frac{\partial}{\partial \hat{z}} = \frac{1}{\gamma_z(z)} \frac{\partial}{\partial z}, \quad (2.46)$$

where the γ_i functions are defined as follows:

$$\gamma_r(r) = \begin{cases} 1 - i\Theta_r(r) & \text{for } r > r_{\text{in}} \\ 1 & \text{otherwise} \end{cases}, \quad \gamma_z(z) = \begin{cases} 1 - i\Theta_z(z) & \text{for } |z| > |z_{\text{in}}| \\ 1 & \text{otherwise} \end{cases}. \quad (2.47)$$

The changes of variables eq. (2.44) will then be inserted in the equations governing exterior acoustics. If the parameter Θ_0 of the PMLs is correctly chosen, the reflections of outgoing waves on the PMLs should be negligible in the frequency range of interest.

Weak form of the acoustic equilibrium equations

Non-dimensional pressures are defined as:

$$p_a = \frac{\bar{A}P_a}{\mu\bar{H}}, \quad p_e = \frac{\bar{A}P_e}{\mu\bar{H}}, \quad p_0 = \frac{\bar{A}P_0}{\mu\bar{H}}, \quad p_u = \frac{\bar{A}P_u}{\mu\bar{H}}. \quad (2.48)$$

In the following non-dimensional equations, the prime stands for space derivative $\partial/\partial\bar{r}$.

The use of the displacement potential instead of the acoustic pressure as state variable for the fluid will largely improve the convergence of the modal summation to compute the radiated pressure in section 2.6. The displacement potentials are defined for interior and exterior acoustics as:

$$p_a = \omega^2 q_a, \quad p_e = \omega^2 q_e. \quad (2.49)$$

The complete set of non-dimensional equations for acoustics reads:

$$\omega^2 q_a + p_u + c^2 \Delta q_a = 0, \quad (2.50a)$$

$$\int_{\Omega_i} q_a r ds = 0, \quad (2.50b)$$

$$p_u + \frac{mc^2}{v_0} 2\pi \int_{\Sigma} \frac{1}{\lambda_{10}} (-y'_0 \tilde{x} + x'_0 \tilde{y}) x_0 dl = 0, \quad (2.50c)$$

$$\omega^2 p_e + c^2 \Delta p_e = 0, \quad (2.50d)$$

where $c^2 = C_f^2/C_s^2$ is a non-dimensional parameter describing the relation between the speed of sound in the membrane and in the air, and $v_0 = V_0/\bar{A}^3$ is the non-dimensional volume of the cavity in the **static configuration** [see fig. 2.1]. The boundary conditions read:

$$\nabla q_a \cdot \mathbf{n} = 0 \quad \text{on } \Sigma_{\text{wall}}, \quad (2.51a)$$

$$\nabla q_a \cdot \mathbf{n} = m \frac{1}{\lambda_{10}} (-y'_0 \tilde{x} + x'_0 \tilde{y}) \quad \text{on } \Sigma, \quad (2.51b)$$

$$\nabla p_e \cdot \mathbf{n} = 0 \quad \text{on } \Sigma_{\text{wall}}, \quad (2.51c)$$

$$\nabla p_e \cdot \mathbf{n} = -m\omega^2 \frac{1}{\lambda_{10}} (-y'_0 \tilde{x} + x'_0 \tilde{y}) \quad \text{on } \Sigma. \quad (2.51d)$$

Multiplying eq. (2.50c) by a test scalar \mathcal{P}_u yields the weak form of the equation governing the uniform pressure in the cavity:

$$\mathcal{P}_u p_u + \mathcal{P}_u \frac{mc^2}{v_0} 2\pi \int_{\Sigma} \frac{1}{\lambda_{10}} (-y'_0 \tilde{x} + x'_0 \tilde{y}) x_0 dl = 0, \quad \forall \mathcal{P}_u. \quad (2.52)$$

Multiplying eq. (2.50a) by a test function \mathcal{Q}_a , integrating by parts, taking into account the boundary conditions eq. (2.51), and using a Lagrange multiplier κ_i to ensure the mean pressure constraint eq. (2.50b) yields the weak form of the Helmholtz equation governing the interior pressure:

$$\begin{aligned}
& -\omega^2 \int_{\Omega_i} q_a \mathcal{Q}_a r ds + c^2 \int_{\Omega_i} \nabla q_a \cdot \nabla \mathcal{Q}_a r ds \\
& - \int_{\Omega_i} p_u \mathcal{Q}_a r ds - mc^2 \int_{\Sigma} \frac{1}{\lambda_{10}} (-y'_0 \tilde{x} + x'_0 \tilde{y}) \mathcal{Q}_a x_0 dl \\
& + \kappa_i \int_{\Omega_i} \mathcal{Q}_a r ds + \mathcal{K}_i \int_{\Omega_i} q_a r ds = 0, \quad \forall \mathcal{Q}_a, \forall \mathcal{K}_i. \quad (2.53)
\end{aligned}$$

The weak form of the Helmholtz equation governing exterior acoustics is obtained in a similar manner, but the PML change of coordinates defined in previous section is now inserted, in order to implement the Sommerfeld radiation boundary condition.

$$\begin{aligned}
& -\omega^2 \int_{\Omega_e} q_e \mathcal{Q}_e \hat{r} ds + c^2 \int_{\Omega_e} \left(\frac{\gamma_z}{\gamma_r} \frac{\partial q_e}{\partial r} \frac{\partial \mathcal{Q}_e}{\partial r} + \frac{\gamma_r}{\gamma_z} \frac{\partial q_e}{\partial z} \frac{\partial \mathcal{Q}_e}{\partial z} \right) \hat{r} ds \\
& + mc^2 \int_{\Sigma} \frac{1}{\lambda_{10}} (-y'_0 \tilde{x} + x'_0 \tilde{y}) \mathcal{Q}_e x_0 dl = 0, \quad \forall \mathcal{Q}_e. \quad (2.54)
\end{aligned}$$

2.6 Numerical procedure

In this section, the numerical procedure used to solve the problem introduced in section 2.1 is described. First, the set of coupled equations to be solved is summarized, and the methods to calculate the static deformation and the linear vibrations are then presented.

2.6.1 Set of coupled equations

As the coupled problem will be solved using finite elements, the weak forms of all the coupled equations are necessary. They have been derived in the previous sections, and are listed here altogether, in non-dimensional form.

- Material behavior eq. (2.33):

$$s_1 = \frac{J_m(1+i\eta)}{J_m - I_1 + 3} (\lambda_1 - \lambda_1^{-3} \lambda_2^{-2}) - u_0^2 \frac{\Gamma}{h^2} \lambda_1 \lambda_2^2 - w \frac{\Gamma}{h^2} \lambda_1 \lambda_2^2, \quad (2.55a)$$

$$s_2 = \frac{J_m(1+i\eta)}{J_m - I_1 + 3} (\lambda_2 - \lambda_1^{-2} \lambda_2^{-3}) - u_0^2 \frac{\Gamma}{h^2} \lambda_1^2 \lambda_2 - w \frac{\Gamma}{h^2} \lambda_1^2 \lambda_2, \quad (2.55b)$$

- Membrane equilibrium eq. (2.27):

$$\begin{aligned}
& \int_{\Sigma} \mathcal{Y}' \frac{\bar{r} \bar{h} s_1 y'}{\lambda_1^2} dl + \int_{\Sigma} \mathcal{X}' \frac{\bar{r} \bar{h} s_1 x'}{\lambda_1^2} dl + \int_{\Sigma} \frac{1}{\lambda_1} s_2 \bar{h} \mathcal{X} dl - \int_{\Sigma} \frac{1}{\lambda_1} (p_0 + p_u) (-y' \mathcal{X} + x' \mathcal{Y}) x dl \\
& = - \int_{\Sigma} \frac{1}{\lambda_1} (\bar{h} + \Gamma \rho_{\text{ratio}}) (\mathcal{Y} \ddot{y} + \mathcal{X} \ddot{x}) \bar{r} dl - \int_{\Sigma} \frac{1}{\lambda_1} (\ddot{q}_a - \ddot{q}_e) (-y' \mathcal{X} + x' \mathcal{Y}) x dl, \\
& \quad \forall \mathcal{X}, \mathcal{Y}, |\mathcal{X}(\bar{r}=1) = \mathcal{Y}(\bar{r}=1) = 0|. \quad (2.56)
\end{aligned}$$

Here the changes of state variable for the interior and exterior fluids, which were introduced in section 2.5.2, have been inserted in eq. (2.27).

- Uniform pressure in the cavity eq. (2.52):

$$\mathcal{P}_u p_u + \mathcal{P}_u \frac{mc^2}{v_0} 2\pi \int_{\Sigma} \frac{1}{\lambda_{10}} (-y'_0 \tilde{x} + x'_0 \tilde{y}) x_0 dl = 0, \quad \forall \mathcal{P}_u. \quad (2.57)$$

- Interior acoustics eq. (2.53):

$$\begin{aligned} & -\omega^2 \int_{\Omega_i} q_a \mathcal{Q}_a r ds + c^2 \int_{\Omega_i} \nabla q_a \cdot \nabla \mathcal{Q}_a r ds \\ & - \int_{\Omega_i} p_u \mathcal{Q}_a r ds - mc^2 \int_{\Sigma} \frac{1}{\lambda_{10}} (-y'_0 \tilde{x} + x'_0 \tilde{y}) \mathcal{Q}_a x_0 dl \\ & + \kappa_i \int_{\Omega_i} \mathcal{Q}_a r ds + \mathcal{K}_i \int_{\Omega_i} q_a r ds = 0, \quad \forall \mathcal{Q}_a, \forall \mathcal{K}_i. \end{aligned} \quad (2.58)$$

- Exterior acoustics section 2.5.2:

$$\begin{aligned} & -\omega^2 \int_{\Omega_e} q_e \mathcal{Q}_e \hat{r} ds + c^2 \int_{\Omega_e} \left(\frac{\gamma_z}{\gamma_r} \frac{\partial q_e}{\partial r} \frac{\partial \mathcal{Q}_e}{\partial r} + \frac{\gamma_r}{\gamma_z} \frac{\partial q_e}{\partial z} \frac{\partial \mathcal{Q}_e}{\partial z} \right) \hat{r} ds \\ & + mc^2 \int_{\Sigma} \frac{1}{\lambda_{10}} (-y'_0 \tilde{x} + x'_0 \tilde{y}) \mathcal{Q}_e x_0 dl = 0, \quad \forall \mathcal{Q}_e. \end{aligned} \quad (2.59)$$

2.6.2 Static deformation: **step 1** and **step 2**

The first stage of the numerical procedure consists of solving for the static deformation of the membrane when it is pre-stretched, inflated, and when a static voltage is applied to the electrode connections. This stage contains **step 1** and **step 2**, which have been defined in fig. 2.1.

Solving **step 1**

In this first step, the interior pressure is fixed $P_i = P_{\text{app}}$, and is therefore not a variable that needs to be solved for. The weak form which is solved therefore reads:

$$\begin{aligned} & \int_{\Sigma} \mathcal{Y}' \frac{\bar{r} \bar{h} s_1 y'}{\lambda_1^2} dl + \int_{\Sigma} \mathcal{X}' \frac{\bar{r} \bar{h} s_1 x'}{\lambda_1^2} dl + \int_{\Sigma} \frac{1}{\lambda_1} s_2 \bar{h} \mathcal{X} dl - \int_{\Sigma} \frac{1}{\lambda_1} p_{\text{app}} (-y' \mathcal{X} + x' \mathcal{Y}) x dl = 0, \\ & \forall \mathcal{X}, \mathcal{Y} | \mathcal{X}(\bar{r} = 1) = \mathcal{Y}(\bar{r} = 1) = 0. \end{aligned} \quad (2.60)$$

Equation (2.60) is of the form :

$$\Re([x, y], [\mathcal{X}, \mathcal{Y}]) = 0, \quad \forall \mathcal{X}, \mathcal{Y}. \quad (2.61)$$

It is solved using the Newton Raphson algorithm. First an initial guess of the solution is made in the form of a spherical cap, and denoted $\mathbf{x}_i = [x_i, y_i]$. Then the residual

$\Re([x, y], [\mathcal{X}, \mathcal{Y}])$ is linearized to provide the gradient for Newton-Raphson's method. Introducing the perturbation $\tilde{x} = [\tilde{x}, \tilde{y}]$ by $x = [x, y] = x_i + \tilde{x}$, the linearized weak form reads:

$$\Re([x_i, y_i], [\mathcal{X}, \mathcal{Y}]) + \langle \Re'([x_i, y_i], [\mathcal{X}, \mathcal{Y}]), [\tilde{x}, \tilde{y}] \rangle = 0 . \quad (2.62)$$

The explicit linearized form of eq. (2.62) is provided in appendix B. The linear equation (2.62) is solved at each step of Newton-Raphson's method to find the increment \tilde{x} to update the initial guess x_i : $x_i = x_i + \tilde{x}$. This is repeated until \tilde{x} is sufficiently small ($\|\tilde{x}\|_2 < 1e^{-8}$).

FreeFEM [41] is used to assemble the stiffness matrix and the force vector, and to solve the non-linear inflation problem. The membrane is meshed in the **reference configuration**, and 100 Lagrange P2 elements along the radius are used.

Solving step 2

In **step 2**, the cavity is closed, and a static voltage is applied between the electrodes. The membrane deforms and the pressure in the cavity thus changes. The solving method is similar to **step 1**, but this time the interior pressure is a variable, and eq. (2.57) must be solved too. The new weak form reads:

$$\Re([x, y, p_u], [\mathcal{X}, \mathcal{Y}, \mathcal{P}_u]) = 0, \quad \forall \mathcal{X}, \mathcal{Y}, \mathcal{P}_u , \quad (2.63)$$

and the explicit form is given in appendix B. Here again, FreeFEM is used to assemble the stiffness matrix and force vector of the problem. The coupling between the membrane and the uniform pressure is taken into account by adding a line and column to the stiffness matrix obtained in **step 1**. The tangent stiffness matrix for **step 2** is of the form:

$$\mathbf{K}_{\text{tot}} = \begin{bmatrix} K_u & K_u^s \\ K_s^u & K_s \end{bmatrix} . \quad (2.64)$$

where K_u is the stiffness added by the cavity, coming from eq. (2.57); K_s is the membrane stiffness matrix, coming from eq. (2.56); and K_u^s, K_s^u describe the coupling between the membrane and the uniform pressure in the cavity.

At the end of this step, the **static configuration** is known, which means that $x_0(\bar{r})$, $y_0(\bar{r})$ and their derivatives, as well as p_0 and v_0 are known.

2.6.3 Linear dynamics: step 3

PML validation

The PML parameters (thickness, attenuation Θ_0 , and distance from the membrane) have been adjusted on a numerical test case, consisting of a flat piston embedded in an infi-

nite baffle. For this setup, the Rayleigh integral provides an exact solution for the radiated pressure. Further details on this test case are given in appendix C.

Discretization using finite elements

The membrane and the interior and exterior domains are meshed this time in the **static configuration**. Lagrange P2 elements are used in all domains. The meshed geometry is shown in fig. 2.9.

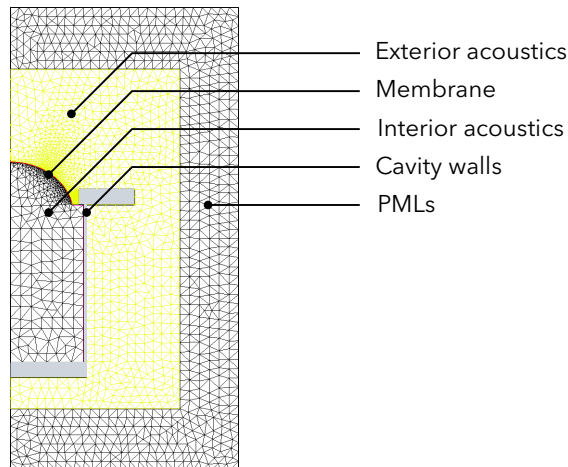


Fig. 2.9. Mesh of the fully coupled model. The yellow area is the acoustical domain, the exterior black area is the PML, the interior black area is the interior fluid, and the membrane mesh is too thin to be visible on this picture. The grey area corresponds to the walls of the cavity.

The number of elements along the radius of the membrane is chosen so that there are 12 elements per flexural wavelength at 5 kHz, and similarly the number of acoustic elements is chosen so that there are 12 elements per acoustic wavelength at 5 kHz. The pressure fluctuations close to the membrane are governed by the wavelength of the flexural waves in the membrane and not by the acoustic wavelength. Therefore, at the interface the size of the acoustic elements is the same as the size of the membrane elements, and a conforming mesh is used.

Assembly of the coupled mass and stiffness matrices

The linearized weak form of the coupled vibroacoustic problem is given in appendix B, and is discretized using finite elements in order to obtain the total stiffness and mass finite element matrices:

$$\left(-\omega^2 \begin{bmatrix} M_a & 0 & 0 & 0 & 0 \\ 0 & 0 & 0 & 0 & 0 \\ 0 & 0 & 0 & 0 & 0 \\ 0 & 0 & 0 & M_e & 0 \\ M_s^a & 0 & 0 & M_s^e & M_s \end{bmatrix} + \begin{bmatrix} K_a & K_a^\kappa & K_a^u & 0 & K_a^s \\ K_\kappa^a & 0 & 0 & 0 & 0 \\ 0 & 0 & K_u & 0 & K_u^s \\ 0 & 0 & 0 & K_e & K_e^s \\ 0 & 0 & K_s^u & 0 & K_s \end{bmatrix} \right) \begin{bmatrix} q_a \\ \kappa \\ p_u \\ q_e \\ \tilde{\mathbf{x}}^T \end{bmatrix} = \begin{bmatrix} 0 \\ 0 \\ 0 \\ 0 \\ \mathcal{F} \end{bmatrix}, \quad (2.65)$$

which is written in condensed form as:

$$(-\omega^2 \mathbf{M}_{\text{tot}} + \mathbf{K}_{\text{tot}}) \mathbf{X}_{\text{tot}} = \mathbf{F}_{\text{tot}}. \quad (2.66)$$

The different sub-matrices are defined by the weak forms derived in the previous sections, and explicitly given in appendix B. The force \mathcal{F} is the electrostatic force applied on the membrane, due to the terms in w in eq. (2.33).

The matrices \mathbf{M}_{tot} and \mathbf{K}_{tot} are both frequency independent, as the PMLs have been modified to become frequency independent, and because losses in the membrane have been modelled by a constant loss factor.

Forced response

A first method to solve the system eq. (2.66) is to use a direct approach: the system is inverted for all frequencies of interest.

$$\mathbf{X}_{\text{tot}} = (-\omega^2 \mathbf{M}_{\text{tot}} + \mathbf{K}_{\text{tot}})^{-1} \mathbf{F}_{\text{tot}}. \quad (2.67)$$

This method, later referred to as the **FEM method**, may be time consuming if many frequency bins are required, and provides little insight for understanding the dynamics of the system.

A second option is to use a modal approach, which provides a clearer physical interpretation of the results, and is much more efficient to compute several frequency response functions of the same system but with various excitation forces. As the matrices are frequency-independent, a linear eigenvalue problem is obtained. Standard eigenvalue solvers are therefore used to compute the modes of the homogeneous system eq. (2.66) with $\mathbf{F}_{\text{tot}} = 0$.

In the present case, the mass and stiffness matrices are not symmetric so left and right eigenvectors (Ψ_n^L and Ψ_n^R) need to be computed:

$$\Psi_n^L (-\omega_n^2 \mathbf{M}_{\text{tot}} + \mathbf{K}_{\text{tot}}) = 0, \quad (-\omega_n^2 \mathbf{M}_{\text{tot}} + \mathbf{K}_{\text{tot}}) \Psi_n^R = 0. \quad (2.68)$$

We recall that the resonance frequencies ω_n are complex due to the losses in the PMLs and to the structural damping η .

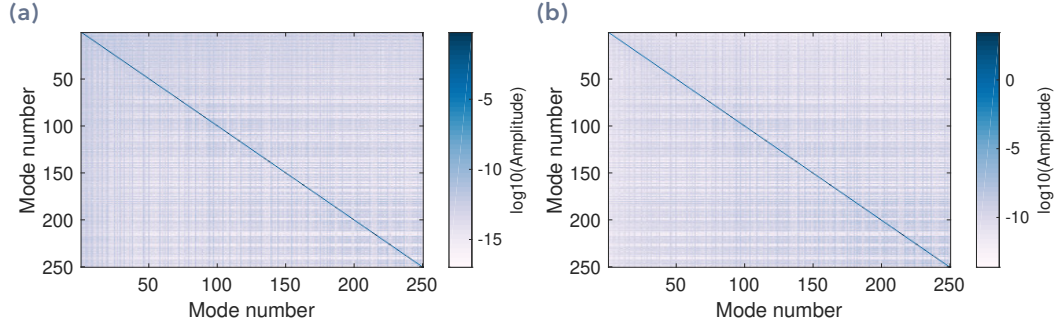


Fig. 2.10. (a) Computed modal mass matrix, and (b) computed modal stiffness matrix, for mode orthogonality check. A quantitative indicator I_{qual} of how close the matrices are to diagonal matrices can be defined, by computing the ratio between the smallest diagonal element over the largest non-diagonal element. It yields $I_{\text{qual}} = 7.5 \times 10^5$ for the modal mass, and $I_{\text{qual}} = 1.4 \times 10^4$ for the modal stiffness. These values can be considered very large, close to the numeric precision of the export of data from FreeFEM.

If all eigenvalues are of order one, the following bi-orthogonality relations hold:

$$\Psi^L \mathbf{M}_{\text{tot}} \Psi^R = \text{diag}(m_n), \quad \Psi^L \mathbf{K}_{\text{tot}} \Psi^R = \text{diag}(k_n), \quad (2.69)$$

where m_n and k_n are the modal mass and stiffness of mode n , and Ψ^L and Ψ^R the matrices containing the left and right modeshapes. The bi-orthogonality relations are checked in fig. 2.10 where the modal mass and stiffness matrices of a typical inflated membrane coupled to acoustics are plotted.

The total displacement is projected onto the right modeshapes basis $\mathbf{X}_{\text{tot}} = \Psi^R \alpha$. By inserting this into eq. (2.66), left-multiplying by Ψ^L , and using the bi-orthogonality relations, the modal amplitudes can be expressed as:

$$\alpha_n(\omega) = \frac{F_n}{m_n(\omega_n^2 - \omega^2)}, \quad (2.70)$$

where the modal force is defined as:

$$F_n = \Psi_n^L \mathbf{F}_{\text{tot}}. \quad (2.71)$$

The displacement and the acoustic pressure are then known everywhere:

$$p_e = \sum_n \omega^2 \alpha_n(\omega) \Psi_{n,e}^R, \quad p_a = \sum_n \omega^2 \alpha_n(\omega) \Psi_{n,a}^R, \quad (2.72a)$$

$$\tilde{x} = \sum_n \alpha_n(\omega) \Psi_{n,x}^R, \quad \tilde{y} = \sum_n \alpha_n(\omega) \Psi_{n,y}^R, \quad (2.72b)$$

where Ψ_n^R has been split into parts containing the different types of degrees of freedom, $\Psi_{n,e}^R$ containing for example the exterior acoustics degrees of freedom. This method will

be referred to as the **modal method**. Due to the use of the displacement potential as the state variable for the fluid, the obtained pressure is proportional to the membrane acceleration, which is expected for acoustic radiation. If the pressure had been used instead as the state variable, the radiated pressure would have been proportional to the displacement, which would have led to poor convergence of the modal summation for the radiated pressure [see appendix D].

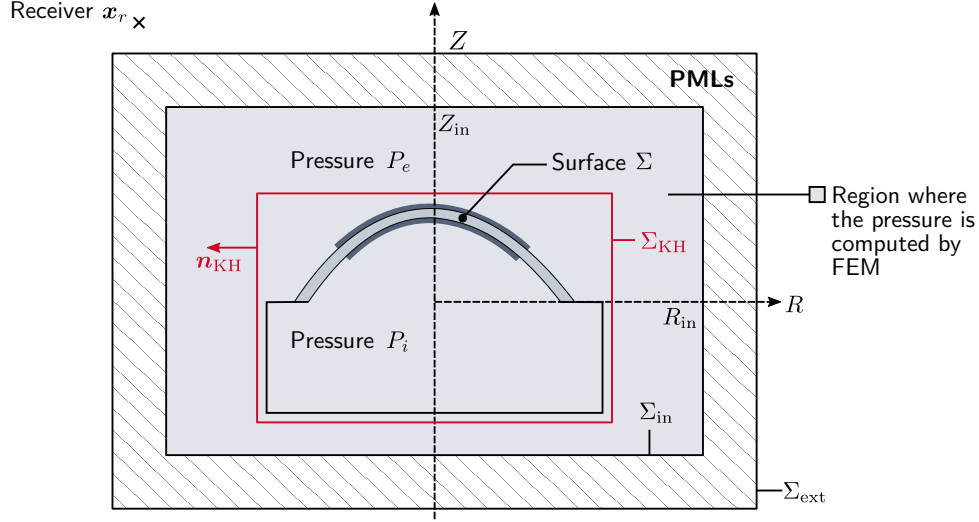


Fig. 2.11. Definition of the variables for the propagation of the near field solution to the far field using the Kirshoff-Helmholtz integral.

The **modal method** works to compute the pressure in the near field, in the part of the acoustical domain that is meshed [see fig. 2.11]. If the far field pressure is needed, this near field solution is propagated using the Kirshoff-Helmholtz integral:

$$p_e(\mathbf{x}_r) = - \int_{\Sigma_{KH}} [p_e(\mathbf{x}) \nabla g(\mathbf{x}, \mathbf{x}_r) \cdot \mathbf{n}_{KH}(\mathbf{x}) - \nabla p_e(\mathbf{x}) \cdot \mathbf{n}_{KH}(\mathbf{x}) g(\mathbf{x}, \mathbf{x}_r)] ds(\mathbf{x}) , \quad (2.73)$$

where Σ_{KH} is a surface enclosing the loudspeaker [see fig. 2.11], \mathbf{x}_r the location of the receiver, $\mathbf{n}_{KH}(\mathbf{x})$ the outer normal to Σ_{KH} , and g the free-field Green's function:

$$g(\mathbf{x}, \mathbf{x}_r, \omega) = \frac{e^{-i\|\mathbf{x}-\mathbf{x}_r\|\omega/c}}{4\pi\|\mathbf{x}-\mathbf{x}_r\|} . \quad (2.74)$$

The modal expansion of p_e eq. (2.72a) can be used in eq. (2.73), and this method will be referred to as the **modal KH method**.

Truncation of the modal basis

When the modes of a resonant system coupled to an exterior fluid are computed using PMLs, two types of modes will be obtained [70]: the resonant modes of the fluid loaded structure referred to hereafter as *membrane modes* [see fig. 2.12a], and a series of so called *PML modes* [see fig. 2.12b]. The *PML modes* arise from reflections inside the

PMLs, so they will change both in frequency and in shape if the PML parameters (size, attenuation, number of elements) are changed.

Both the structural and the acoustic response are dominated by *membrane modes* and it is interesting to study only these modes for the physical interpretation they provide.

The pressure in the *PML modes* is very large inside the PMLs and smaller in the physical part of the model [see fig. 2.12b]. As the PML is largely damped, *PML modes* have a high modal loss factor. A damping criterion is thus used to distinguish *membrane modes* from *PML modes*. Figure 2.13 shows that there is a clear distinction in damping between the two types of modes, and that the chosen criterion is efficient in sorting them out. As emphasized in fig. 2.13, the damping value of 5% will be used in the following to distinguish between the two types of modes.

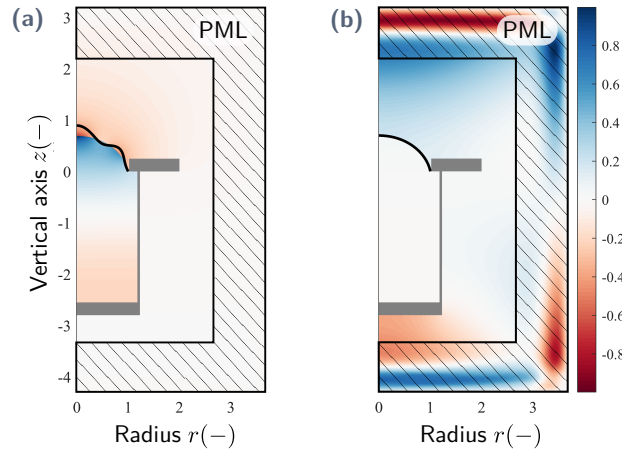


Fig. 2.12. (a) Example of a *membrane mode*. (b) Example of a *PML mode*. PML modes are characterized by large pressure values in the PML layer. The black line shows the membrane part of the modeshape. The color scale for the acoustic pressure is the same on both plots.

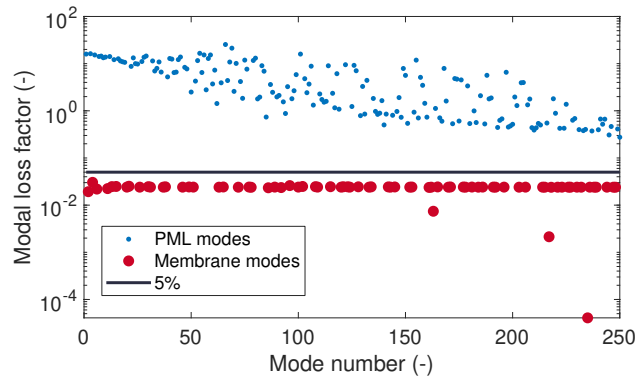


Fig. 2.13. Computed modal loss factor of the first 250 modes. The structural loss factor η is set to 4%, so all modes with a damping higher than 5% are considered to be *PML modes*.

The two types of modes (*membrane* and *PML modes*) must be included in the modal summation to provide accurate reconstructions of the acoustic and structural responses.

In the present study the modal basis is truncated by selecting all the modes that have an absolute value of their eigenfrequency below a given threshold. The threshold is chosen so that the modal solution is close enough to the direct calculation (*FEM*).

Different modal basis truncations have been suggested by Marburg [77] for example. However, in the present context, selecting the relevant modes according to the absolute value of their eigenfrequencies performs well. This requires to run the costly direct calculation *FEM* one time. Yet, once the modes are computed and the modal truncation criterion is defined, calculating various frequency responses for various excitations can be performed quickly using the modal approach.

The modal method for exterior fluid-structure problems is studied in more details in appendix D on a simpler system consisting of a flat piston embedded in an infinite baffle. The convergence of the modal summation to the direct calculation is studied for different modal truncations, both for the radiated pressure and for the membrane dynamics.

The convergence will also be checked in chapter 4 when the results of the model for the exterior radiation are shown, in section 4.4.

2.7 Conclusion

In this chapter, a complete model of a inflated DE loudspeaker has been set up. Three different physics are strongly coupled together: mechanics, electrostatics and acoustics. The obtained coupled problem is solved by finite elements, in the open-source software FreeFEM.

In order to compute quickly frequency response functions for both acoustics and dynamics, the system of equations is projected on a basis of coupled fluid/structure modes, which are computed by implementing frequency-independent perfectly matched layers.

In the following chapter, a prototype is built to validate this model, and the results of the model are compared to experimental data in chapter 4.

Experimental setup

In this chapter the fabrication process of DE loudspeakers is described, from manufacturing the silicone membrane to applying the compliant electrodes. The prototype design is then presented and explained.

The different measurements needed to identify the model parameters are also described, and finally the setups for static, dynamic, and acoustic measurements are presented.

3.1 Fabrication process

3.1.1 Fabrication of the membranes

Elastomer membranes for use as DE actuators need to satisfy the following requirements:

- There should not be any defect in the membrane, meaning any small bubble in the silicone, or dust on the surface is not acceptable. Indeed, any defect would locally increase the electric field when a voltage is applied, up to a value higher than the breakdown field. The maximum voltage before breakdown is therefore determined by these defects [see fig. 3.1].
- The thickness should be as uniform as possible. The electric field is maximal where the thickness is minimal, so breakdown occurs at the thinnest point of the membrane. A uniform thickness guaranties that the breakdown is reached approximately for the same voltage on the whole membrane.

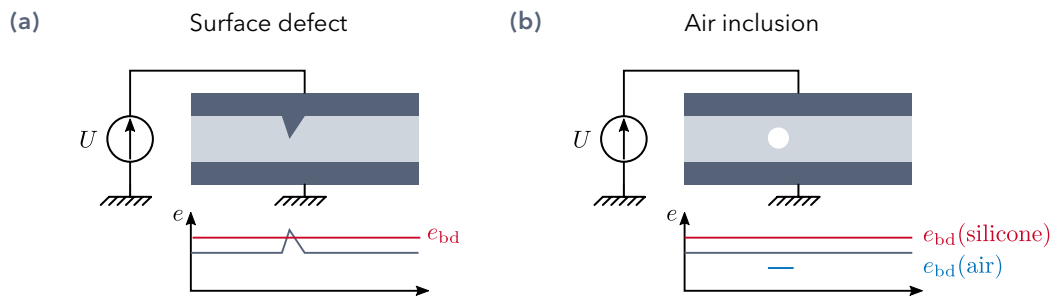


Fig. 3.1. Defects on DE membranes, and consequences on the breakdown voltage. $e_{bd}(\text{silicone})$ and $e_{bd}(\text{air})$ are the breakdown electric fields of silicone and air, and e is the actual local electric field. **(a)** When there is a surface defect, the electric field is locally higher, so dielectric breakdown occurs for lower applied voltages. **(b)** Air has a lower dielectric strength than silicone, so an air bubble locally reduces the total dielectric strength.

Spin-coating at IMSIA

The first prototypes were manufactured at IMSIA, using the tools I could find in the lab. Spin-coating appeared to be the easiest solution to manufacture acceptable membranes, in terms of thickness uniformity and amount of defects (dust, air inclusions, etc.). No proper spin-coater was available, so I used a polishing machine, which could only rotate at a given speed, around 500 rpm. The manufacturing process is summarized as follows:

1. Mix 10 g of silicone Part A, 10 g of silicone part B, and 12 g of isooctane. The solvent isooctane helps reducing the viscosity of the Nusil CF19-2186 silicone which is very viscous and impossible to spin-coat without added solvent. The mixing is performed by hand during 2 min.
2. Put the obtained mix under vacuum during 2 min to remove air bubbles.
3. Pour a small amount on a polystyrene culture dish, which is fixed on the polishing machine.
4. Spin the dish for 2 min.
5. Cure the membrane during 30 min at 80°.

The spin-coating process is schematized in fig. 3.2.

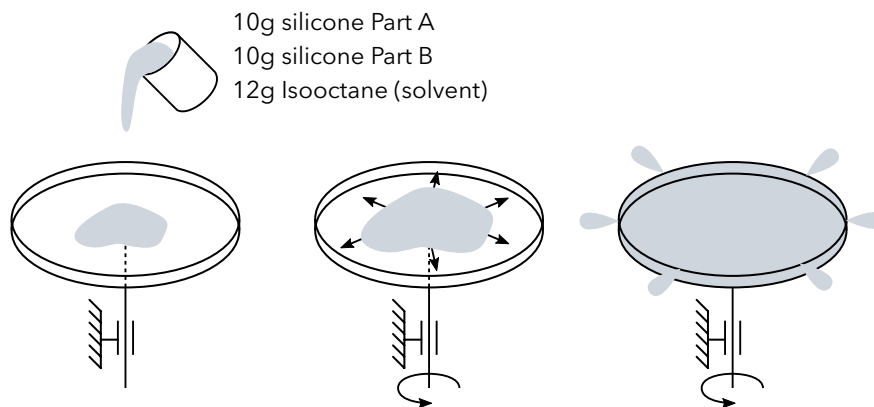


Fig. 3.2. Schematics of the spin-coating process, to manufacture thin DE membrane from Nusil CF19-2186 silicone.

In theory, the thickness of a spin-coated membrane is uniform, as a result of the balance between centrifugal and viscous forces [114]. The uniformity of the thickness will be checked in section 3.3.2.

Also, the spin-coating process should be carried out in a clean room, as dust particles falling on the membrane before it has cured must be avoided. No clean room is available at IMSIA, therefore limiting strongly the quality of the obtained membranes. To limit the amount of dust on the membrane, the culture dish lock is put on the dish at all times, and removed only to pour the silicone.

Once the membrane is cured in the culture dish, it is released by hand, and deposited on a paper sheet. Thanks to the low adhesion forces between the paper and the silicone

membrane, the membrane can be deposited on the sheet with very little stretch, so the membrane is considered to be at rest on the sheet. A PMMA frame is then pressed against the membrane, and thanks to electrostatic forces the membrane is then fixed on the frame. This process is described in fig. 3.3.

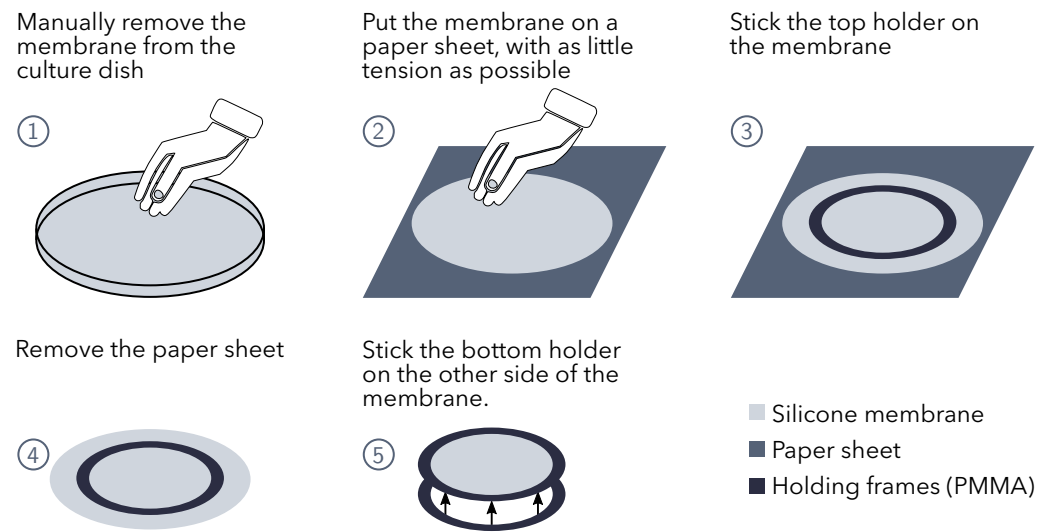


Fig. 3.3. Release of the membrane from the culture dish after spin-coating, and mounting on the holders.

The limitations of the process described in fig. 3.3 are related to the manual intervention, when the membrane is released from the culture dish and deposited on the paper sheet. Placing the membrane with no constraints and no wrinkles on the paper sheet is not easy, and is in particular hard for very thin membranes.

What is more, it is not possible to pre-stretch the membrane using this method. This may be a problem because of the Muhlins effect. Indeed once the membrane is stretched and released a few times, a residual deformation is obtained. For a membrane fixed on a frame with no initial tension, wrinkles appear in the rest state.

Manufacturing at LMTS: pre-stretching commercial membranes

Given the above-listed limitations of the fabrication process that could be implemented at IMSIA, I searched for collaborations with teams who are more specialized in the manufacturing and characterization of soft transducers. Prof. Herbert Shea responded positively to my request, so I spent a month at the LMTS, the soft transducers lab at the EPFL, in order to manufacture more accurate and efficient prototypes.

The manufacturing process that I used at the LMTS differs from what I implemented at IMSIA, as I could benefit from the experience in handling soft materials that has been gathered at the LMTS. I used silicone membrane that are sold by Wacker, under the name Elastosil. The main advantage of these membranes is that they are free from defects, there are no air inclusions nor dust particles on the surface. The membrane are delivered on a PET substrate, which should be removed before the membrane can be

used. The release process, as well as the pre-stretching process are described step-by-step in fig. 3.4. This process is inspired by the publication by Rosset *et al.* [95].

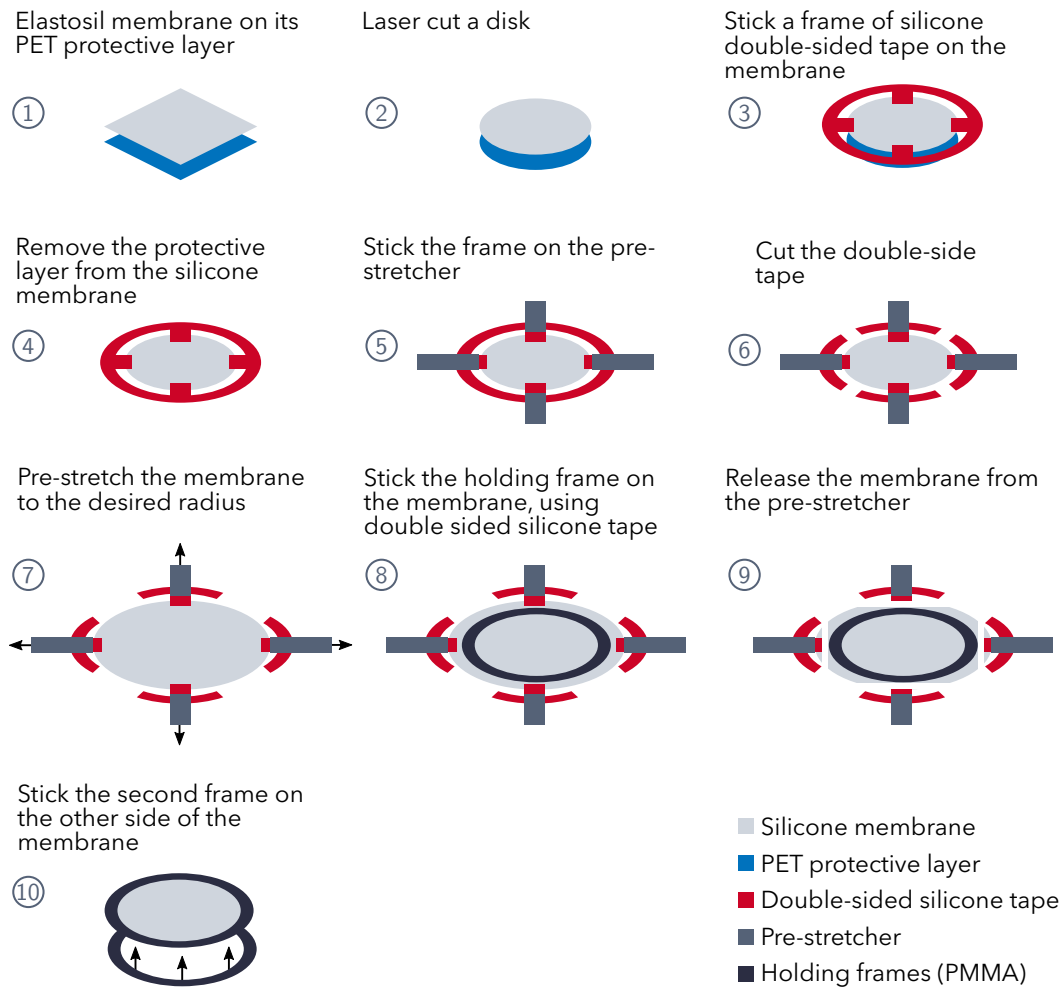


Fig. 3.4. Pre-stretching process, starting from a commercially available Wacker Elastosil membrane. In practice, the pre-stretcher has eight 'arms', and not four as shown here for clarity reasons.

The process described in fig. 3.4 is designed to precisely control the pre-stretch of the membrane. Indeed the membrane is fixed on a rigid component during the whole process, inhibiting any undesired stretch.

At the end of the process of fig. 3.4, a stretched membrane fixed at the outer radius on a rigid PMMA frame is obtained. It can then easily be handled to apply the soft conductive electrodes.

3.1.2 Applying soft conductive electrodes

Literature review

When manufacturing DEs, the main difficulty is to apply soft conductive electrodes. Indeed, the goal is to obtain electrodes with the highest possible conductivity, and at the same time limiting the added mass and stiffness. The electrodes should also remain conductive when they are stretched, typically up to 100% or more for common applications of DE transducers. Several technologies have been considered, with different properties, and application complexity. They are listed in table 3.1.

Tab. 3.1. Characteristics of the different electrode materials for DE actuators.

Material	Conductivity	Stretchability	Manufacturing
Carbon black	low	high	difficult to pattern
Carbon grease	high	high	difficult to pattern precisely
Carbon black loaded silicone	high	high	patterning possible
Carbon nano-tubes	very high	very compliant because very thin	difficult, slow

Conductive grease

At IMSIA, I used carbon conductive grease for the electrodes. It was deposited by hand, using a small pencil. Therefore, the accuracy of the shape of the deposited electrode was low (≈ 1 mm), and the electrode thickness was uneven, as I had no control on the local thickness. The average thickness of the electrodes could be estimated by measuring the mass of added carbon grease on the membrane.

This method was easy to implement and allowed me to quickly manufacture prototypes. However, the possible electrode shapes were limited to a disk, as the accuracy was not sufficient to paint several rings.

Conductive ink, made out of silicone and carbon black

In order to manufacture electrodes with more complex shapes, typically several concentric rings, and also to control the electrode thickness, I went to the LMTS where they have been developing manufacturing processes for DEs for more than ten years.

I used pad-printing to precisely deposit electrodes of a desired shape on the membranes which had been pre-stretched beforehand following the process explained in fig. 3.4. The pad printing process is described in fig. 3.5, and is inspired from [95].

The idea of pad printing is to use a soft silicone pad, to pick up ink from a reservoir called the cliché, and to stamp it on the membrane. This process is used in the industry to print on curved surfaces. At LMTS, I used a Teca-Print TPM101 machine to perform all the steps described in fig. 3.5.

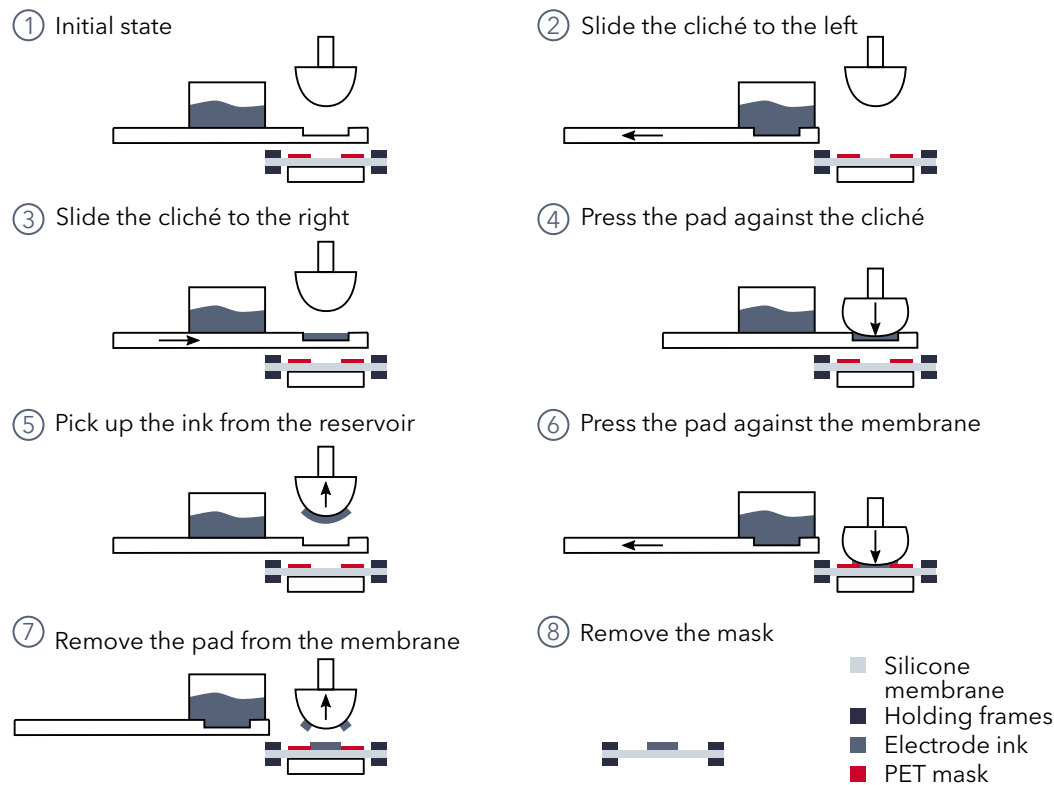


Fig. 3.5. Pad-printing process to apply soft electrodes made of silicone and carbon black. The steps 1-7 can be repeated several times in order to increase the thickness and thus the conductivity of the deposited electrodes. The mask can be patterned with any desired shape with a laser cutter. Once the electrode is deposited on one side, it is cured 30 min at 80°, and the process is repeated on the second side.

3.1.3 Design of the electrode connections

Two types of electrodes have been used in this thesis: full electrodes, which cover the whole surface, and patterned electrodes, which cover only a limited region of the DE membrane. The full electrodes have been used for general testing and for studying resistivity effects [see chapter 6], whereas the patterned electrodes have been used to optimize the electrode shape for improving the frequency response of the loudspeaker [see chapter 5].

Full electrodes

As full electrodes are used to study resistivity effects on an axisymmetric device, with an axisymmetric model, the electrodes connections should be axisymmetric as well, meaning that both the top and bottom electrodes should be connected to the high voltage supply on the whole outer perimeter of the membrane. The final prototype design is shown in fig. 3.6.

The main difficulty in designing full connections is that in order to ensure the electrical contact between the electrodes and the connections made of aluminum tape, a pres-

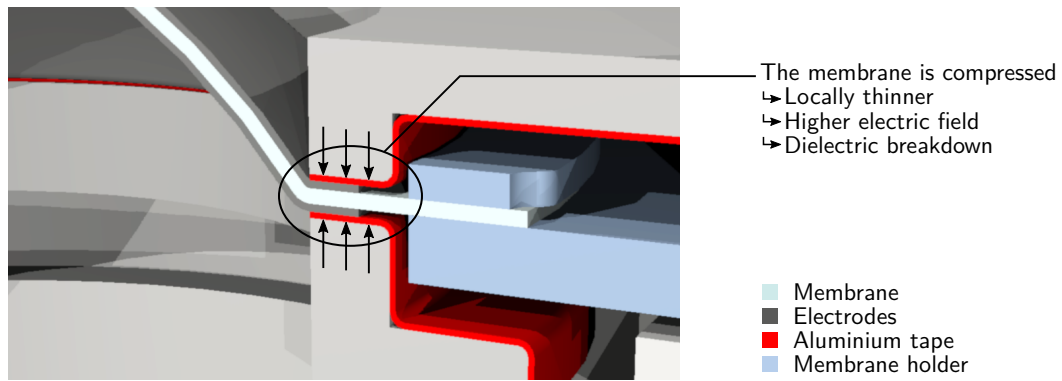


Fig. 3.6. Design of the electrode connections for full electrodes.

sure has to be applied between the connectors. This results in a local thinning of the membrane, and therefore to a locally higher electric field. As a consequence dielectric breakdown always occur between the connectors. In order to mitigate this effect, the connectors should be as flat as possible, so that the the pressure is uniform between the connectors, and the prototype should be designed in such way that the pressure between the connectors can be adjusted precisely. Also the sealing of the cavity, which is necessary to inflate the membrane is taken care of when the membrane is assembled to the holder, so the connection between the aluminum tape and the electrodes need not be airtight.

Patterned electrodes

In chapter 5, the shape of the electrodes will be optimized to improve acoustic criteria of the loudspeaker, like for the example the spectral balance. The electrode will be shaped as several concentric rings, whose radii are the optimized parameters.

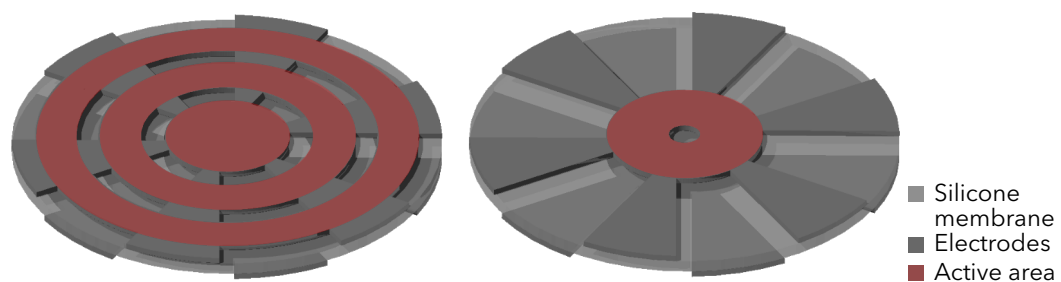


Fig. 3.7. Design of the connections patterned electrodes, for two different designs. The active area denotes zones where there are electrodes on both sides of the membrane.

Figure 3.7 shows the principle that has been chosen to design the electrode connections for ring-shaped electrodes. If there is an electrode on one side only of the membrane, the potential on the other side is not fixed. The electric field on areas covered on one side is therefore much lower than on areas covered on both sides. The electrostatic Maxwell pressure is thus applied only where there is an electrode on both sides of the membrane, and denoted the active area [see fig. 3.7]. In order to bring the electric charges to the

different active areas, there must be connections made of electrode material. These connections must have the lowest possible resistance, and thus the largest possible area. Therefore, radial connections are used, located alternatively on the top and bottom, and separated by a distance of 1 mm, see fig. 3.9.

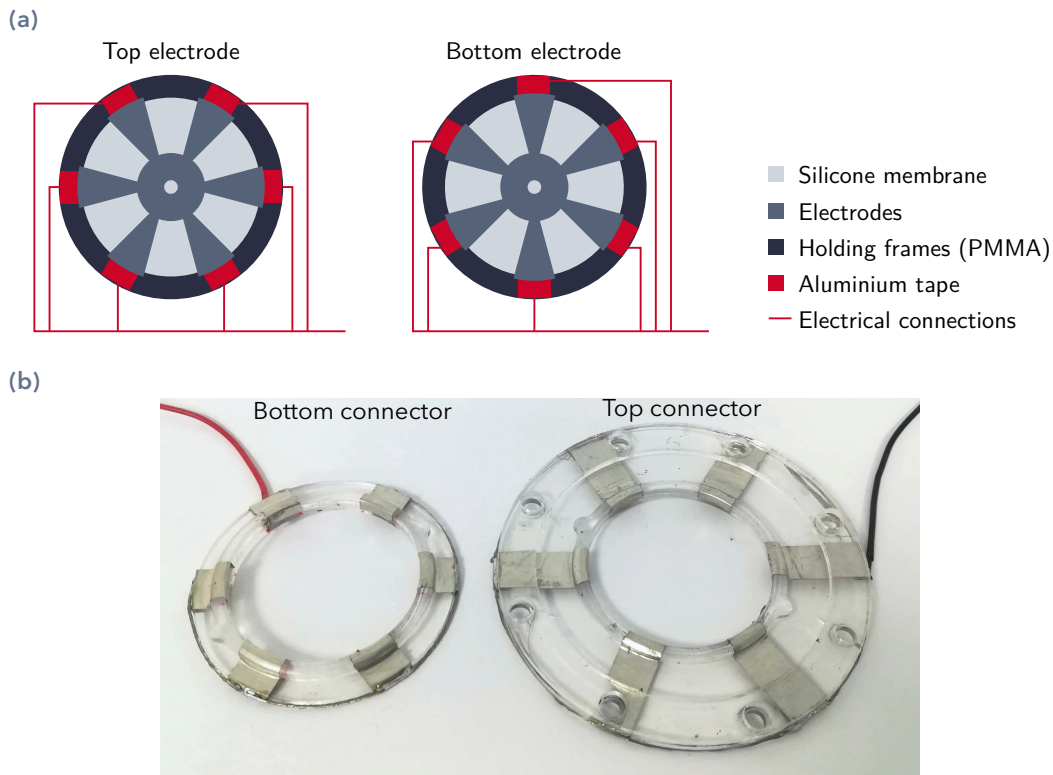


Fig. 3.8. Connections of the patterned electrodes. The top and bottom electrodes are connected on different zones at the border, so that the membrane is never squeezed between two connections. Thus, no dielectric breakdown should occur at the border. **(a)** Schematics, **(b)** picture of the connectors.

At the membrane border, the radial electrodes connections are connected to aluminum tape, as shown in fig. 3.8. The 3D shape of all pieces is the same as for the full electrodes [see fig. 3.6], except that the aluminum tape does not cover the whole perimeter of the connectors.



Fig. 3.9. Samples of dielectric elastomer membrane coated with patterned electrodes, with different electrode shapes.

3.2 Prototype design

The design of the prototype is explained in figs. 3.10 and 3.11, and pictures are shown in fig. 3.12.

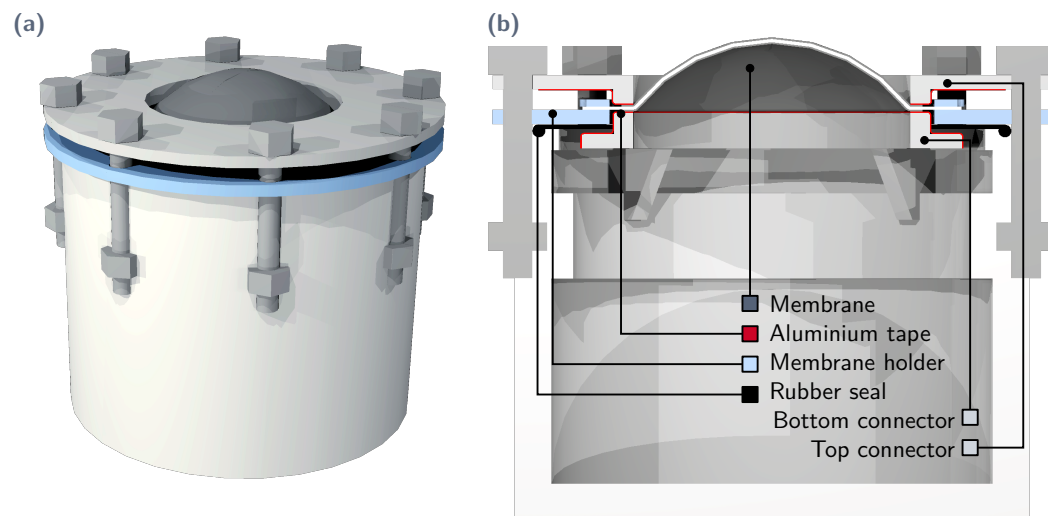


Fig. 3.10. Schematics of the prototype. (a) Whole prototype. (b) Slice view.

The membrane is initially sandwiched between two PMMA frames, as obtained at the end of the pre-stretching process. The electrodes are printed on the membrane while it is fixed on the frames. The membrane is then inserted in the prototype, in which the connection of the electrodes to the supply is made with aluminum tape, stuck on con-

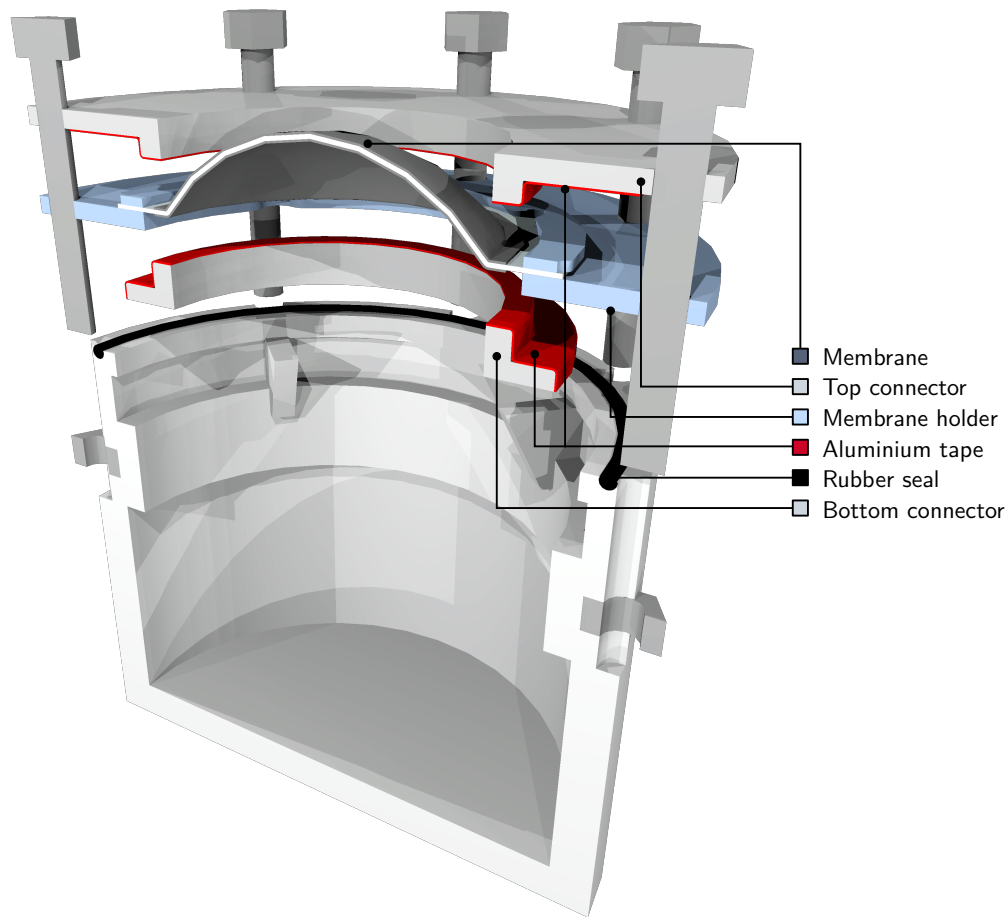


Fig. 3.11. Exploded view of the prototype.

nections 3D-printed pieces. The sealing of the cavity is ensured by a rubber seal, which is pressed against the bottom part of the membrane PMMA frame.

When the screws are tightened, the membrane is compressed between the two connection pieces, which ensures the electrical contact between the electrode and the aluminium on the whole perimeter.

This design is practical in the sense that the membrane can be changed quickly, by removing the eight screws.

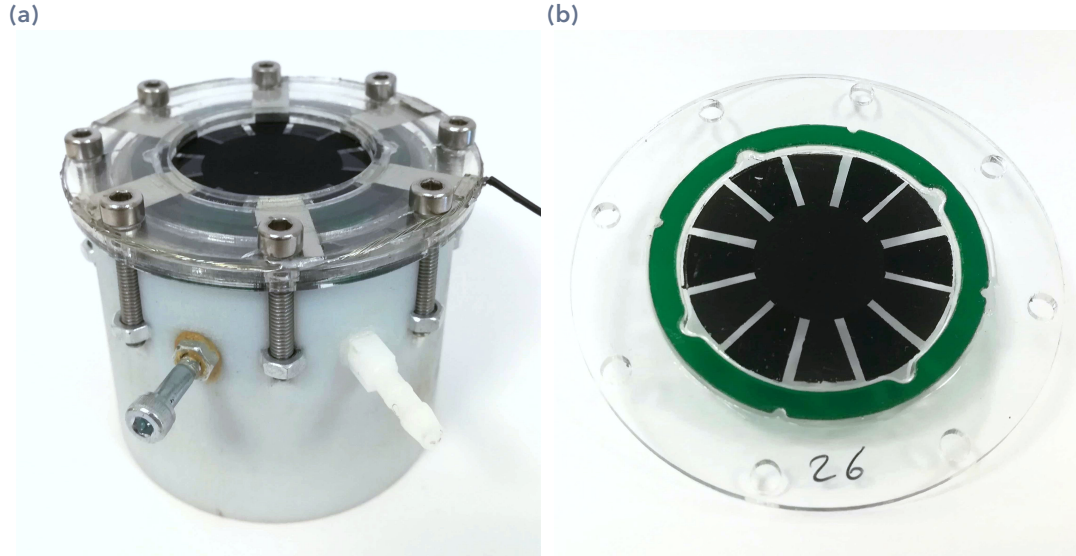


Fig. 3.12. (a) Picture of the prototype. (b) Picture of a membrane on its frame, with a printed patterned electrode.

3.3 Identification of the material parameters

3.3.1 Hyper-elastic parameters

Large deformations of the elastomer membrane are studied, so a hyper-elastic material law is necessary to model the non-linear mechanical behavior.

The hyper-elastic parameters are generally identified on uni-axial tensile tests, but due to the particular geometry of the membrane (very thin samples with a high aspect-ratio), these tests may not be best suited to identify the parameters of DE membranes. What is more, dielectric membranes are most of the time used in bi-axial stretch configurations, so identification of the hyper-elastic parameters on bi-axial tests usually delivers more accurate results [15, 97, 10].

In the present research, three methods have been used to identify the hyper-elastic material parameters: classical uni-axial tests, a method based on the work of Rosset *et al.* [97] where the stretch at the center of an inflated membrane is monitored, and a method where the deformation of an inflated membrane is compared to the results of a finite element calculation, using the model presented in section 2.6.2.

As mentioned in section 2.2, the Gent hyper-elastic constitutive strain energy is used [35]. This relation has only two parameters, and is well suited for elastomers. The strain energy reads:

$$\phi_0 = -\frac{\mu J_m}{2} \log \left(1 - \frac{I_1 - 3}{J_m} \right), \quad (3.1)$$

where the different variables have been defined in section 2.2.2.

In the rest of this section, the results are presented for a Wacker Elastosil 200 μm silicone membrane. Other materials and other thicknesses are used throughout this thesis, but the methods and the general conclusions are similar.

Uni-axial test

A sample of the membrane is tested in a traction machine. The sample is $\bar{L} = 86$ mm long, $\bar{l} = 10$ mm wide and $\bar{H} = 200$ μm thick. The deformation is assumed to be uniaxial, and the axial stress is estimated by:

$$\sigma = \frac{F\lambda_1}{\bar{H}\bar{l}}, \quad (3.2)$$

where F is the measured force, and $\lambda_1 = L/\bar{L}$ the axial strain, L being the current length of the sample.

For uni-axial traction, the Gent stress reads:

$$\sigma = \frac{\mu J_m}{J_m - I_1 + 3} \left(\lambda_1^2 - \frac{1}{\lambda_1} \right), \quad (3.3)$$

with $I_1 = \lambda_1^2 + 2/\lambda_1$.

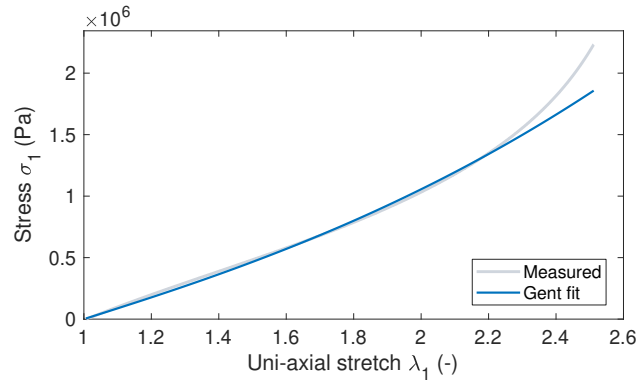


Fig. 3.13. Uni-axial testing to identify the hyper-elastic Gent parameters of a Wacker Elastosil 200 μm silicone membrane. The obtained parameters are $\mu = 2.9 \times 10^5$ Pa and $J_m = 54$. The test lasts 6 min.

The results are presented in fig. 3.13, where the measured stress is plotted with the fit of eq. (3.3). The obtained parameters are $\mu = 2.9 \times 10^5$ Pa and $J_m = 54$. However, their values depend a lot on the strain interval on which the gent model is fitted, indicating that the Gent model may not describe perfectly the hyper-elastic behavior of the Elastosil membrane.

Bi-axial test

The method described by Rosset *et al.* [97] is based on the inflation of an axisymmetric membrane of known thickness. At the center, the membrane is in an equi-biaxial stress state, so the membrane equilibrium equation reads:

$$\frac{2\sigma H}{R_c} = P, \quad (3.4)$$

where R_c is the radius of curvature of the membrane at the center, and P the inflation pressure. The thickness is related to the stretch by the relation $H = \bar{H}/\lambda^2$, where \bar{H} is the initial thickness and λ the stretch at the center (equal in all directions). This implies:

$$\sigma = \frac{PR_c\lambda^2}{2\bar{H}}. \quad (3.5)$$

Thus, if the initial thickness is known, and if the curvature radius R_c , the stretch at the apex λ , and the pressure P are measured simultaneously, the stress can be determined.

For equi-biaxial traction, the Gent stress reads:

$$\sigma = \frac{\mu J_m}{J_m - I_1 + 3} \left(\lambda^2 - \frac{1}{\lambda^4} \right), \quad (3.6)$$

with $I_1 = 2\lambda^2 + 1/\lambda^4$.

A test device similar to the one described by Rosset *et al.* [97] is set-up. A silicone membrane of known thickness is put on a frame without pre-stress, and placed over a closed cavity. Two parallel lines are drawn on the membrane using carbon conductive grease (which does not add any stiffness to the membrane). A piston actuated by a linear motor can inject air in the cavity to inflate the membrane. The pressure is measured using a Valyline pressure sensor, and the Z displacement of the apex of the membrane is recorded using a Keyence LK G-407 laser displacement sensor. In parallel, a video of the membrane is taken in side view, see fig. 3.14.

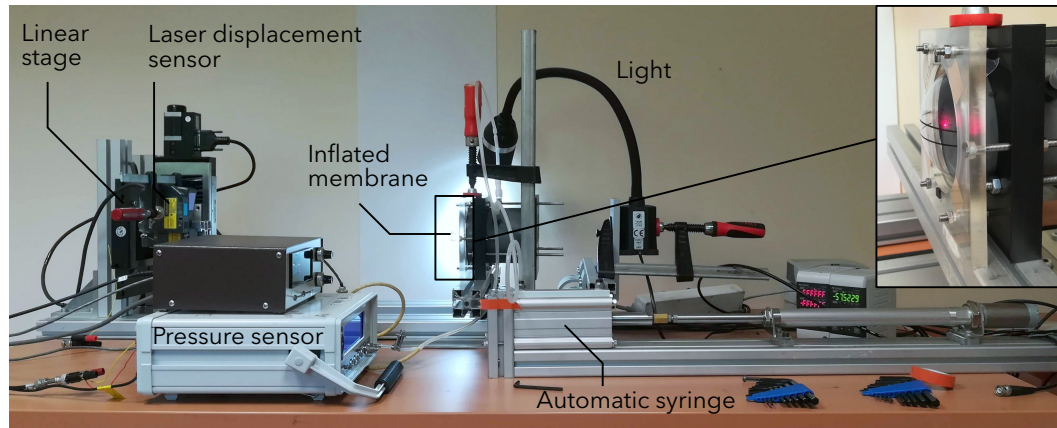


Fig. 3.14. Setup for the bi-axial inflation test, to identify the material parameters.

The video is used to measure the curvature radius at the center, by detecting the membrane contour and fitting a circle to the region between $R \in 0-5$ mm. The lines are used

to measure the stretch at the apex, by following their position using a point tracking algorithm (Matlab pointTracker). Two examples of recorded frames are shown in fig. 3.15, with the fitted circle and the tracked positions of the lines.

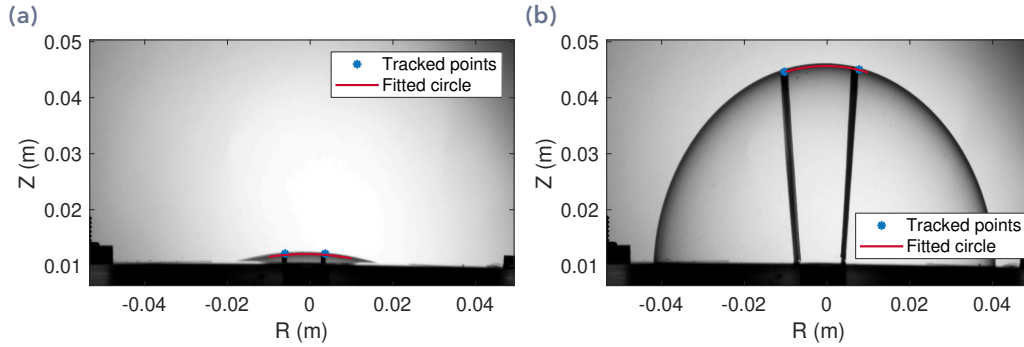


Fig. 3.15. Tracking of the points of interest during the inflation, and fitting of a circle at the apex to obtain the curvature radius. **(a)** Time 1, at the start of the inflation ($T = 0$). **(b)** Time 2, at the end of the inflation ($T = 4$ min).

Figure 3.15 shows that the membrane contour as well as the position of the lines are correctly detected, even when the membrane deforms a lot, here the maximum stretch at the apex is close to 2. Equation (3.6) is fitted on the measured stress, and plotted in fig. 3.16, for two different inflation rates.

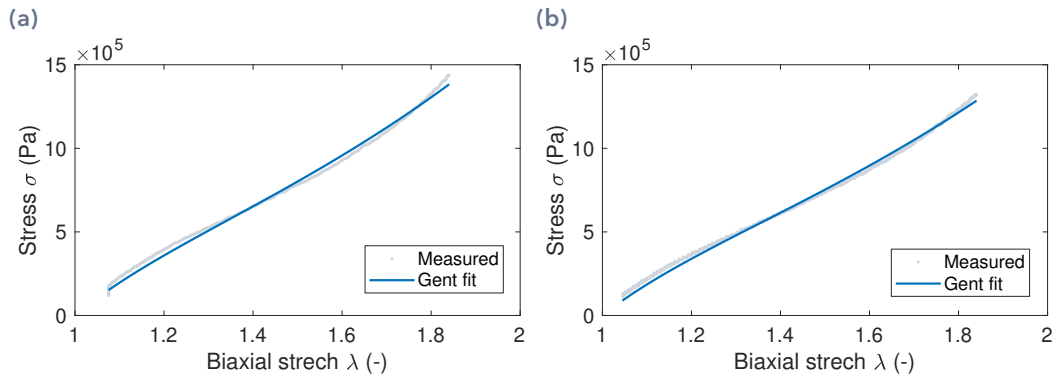


Fig. 3.16. Biaxial inflation test to identify the hyper-elastic Gent parameters of a Wacker Elastosil 200 μm silicone membrane. **(a)** Inflation duration 5 s. **(b)** Inflation duration 4 min. The obtained parameters are $\mu = 3.7 \times 10^5$ Pa and $J_m = 33$ for **(a)**, $\mu = 3.6 \times 10^5$ Pa and $J_m = \infty$ for **(b)**.

The obtained parameters depend on the inflation rate, especially the stiffening parameter J_m , which is very sensitive to the measurement precision. The large observed variation indicates that the performed inflation experiment does not provide an reliable value for J_m . Moreover, the obtained parameters are very different from those obtained by the uni-axial test. Here again, this indicates that the Gent free energy does not describe perfectly the material behavior. However, the membrane will later be used in a configuration

which is very close to bi-axial traction, so it is likely that the parameters obtained by the bi-axial test will provide a correct description of the material behavior during inflation.

Finite element based method

In this method, the non-linear finite element model presented in section 2.1 is used to compute the deformation of the membrane when it is inflated. The deformation of the inflated membrane is measured using a Keyence LK-G407 laser displacement sensor, which is moved over the membrane using a bi-directional linear stage. The material parameters μ and J_m are then adjusted in the code so that the computed deformations fit the measured deformation.

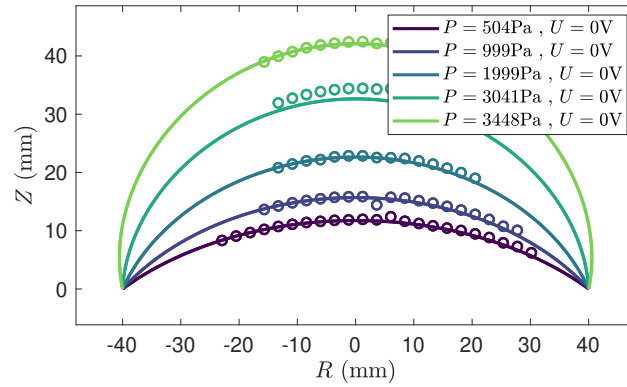


Fig. 3.17. Measured and computed deformation of an Elastosil 200 μm silicone membrane. — FEM calculations, \circ measurements. The obtained parameters are $\mu = 3.6 \times 10^5 \text{ Pa}$ and $J_m = 100$.

Figure 3.17 shows that once the material parameters are adjusted, the computed deformation agrees well with the measured one. What is more, the obtained shear modulus μ is close to the one obtained by the bi-axial test. This validates the use of the Gent free-energy to describe the material behavior, for deformations close to equi-biaxial strain.

The value of J_m differs a lot from the one found using the bi-axial test, but it has been noted that the bi-axial test is not reliable to estimate this parameter. The value found by the FEM method will thus be used in the following.

3.3.2 Membrane thickness

The membrane thickness is a parameter of primary importance for DEs. Indeed the Maxwell pressure, which is responsible for the actuation depends on the squared electric field: $\sigma_{\text{Max}} = \epsilon(U/H)^2$, so small errors in the thickness may lead to large errors in the calculation of the actuation of the device.

Two methods have been used to measure the thickness, the first one is based on a laser displacement sensor, and the second one used a microscope.

Laser displacement sensor method

The membrane which is used for the results in this section has been spin-coated using the home-made spin-coater [see section 3.1.1]. The measurement procedure is described in fig. 3.18, and the results are shown in fig. 3.19.

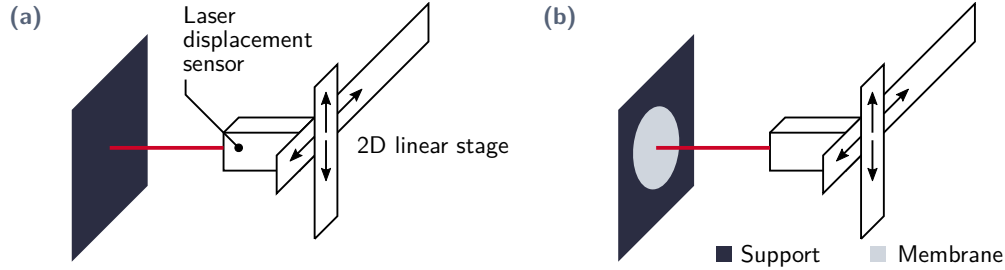


Fig. 3.18. Procedure to measure the membrane thickness using a Keyence LK-G37 laser displacement sensor. **(a)** The distance between the laser and the support is measured, and **(b)** the procedure is repeated with the membrane stuck on the support.

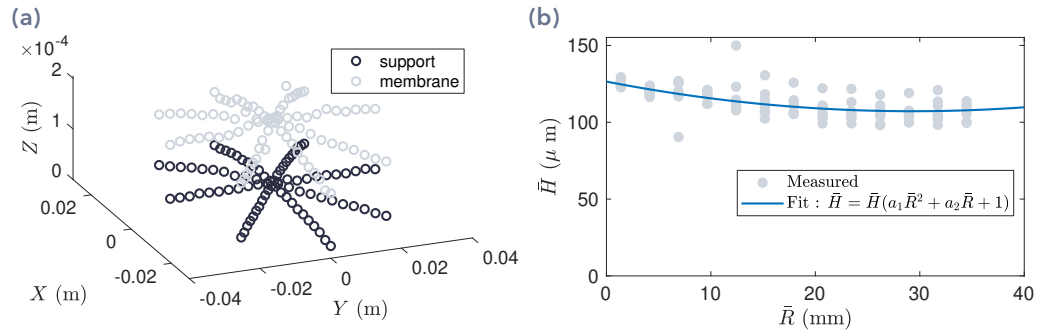


Fig. 3.19. Measurement of the thickness using a laser displacement sensor. **(a)** Measured position of the support, and of the membrane. The membrane thickness is the difference between the membrane and the support. **(b)** Thickness plotted as a function of the radius, and quadratic fit.

Figure 3.19 shows that the thickness of the spin-coated membrane is un-even: the membrane is thicker at the center. This feature has been observed on all the membranes I spin-coated. The low rotation speed may be the main reason.

To allow the use of the measured thickness in the finite element simulation, the thickness should be defined as an analytical function of the radius. A simple 3-parameter function $\bar{H}(\bar{R}) = \bar{H}(a_1 \bar{R}^2 + a_2 \bar{R} + 1)$ is thus fitted on the measurements, and plotted in fig. 3.19.

Microscope method

In order to validate the laser sensor measurements of the thickness, a membrane was cut in the middle, and the edge was measured using a microscope. An example of obtained picture is shown in fig. 3.20a, and the results in fig. 3.20b. The microscope method

yields the same results as the laser sensor method, so both methods can be considered validated. The laser method is more practical, because it is non-destructive.

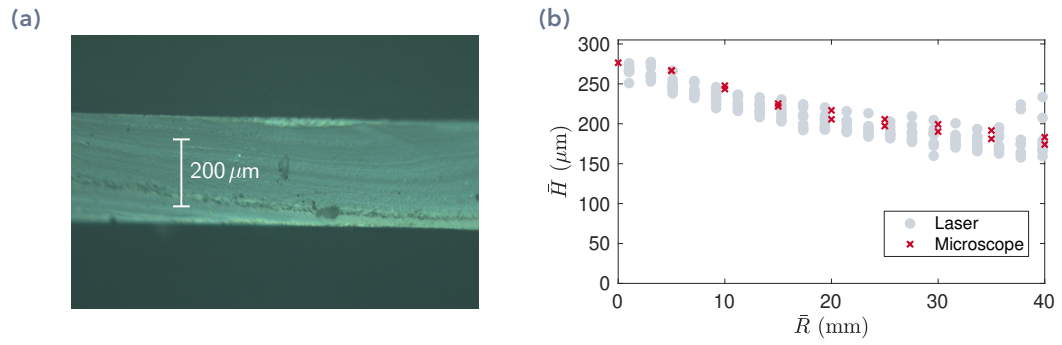


Fig. 3.20. Thickness measured by a calibrated microscope, by cutting the membrane and looking at the edge. **(a)** Picture obtained by the microscope. **(b)** Results, and comparison with the laser method.

3.4 DE loudspeaker characterization procedure

3.4.1 Overview

An overview of the measurement procedure is shown in fig. 3.21. The different steps of fig. 3.21 have been defined in section 2.1.

First the static deformation of the membrane when it is inflated and when a static voltage is applied is measured. The dynamics around this non-linear equilibrium are then studied, by measuring the membrane velocity and the acoustic radiation.

The setups for these different measurements are presented in the following sections.

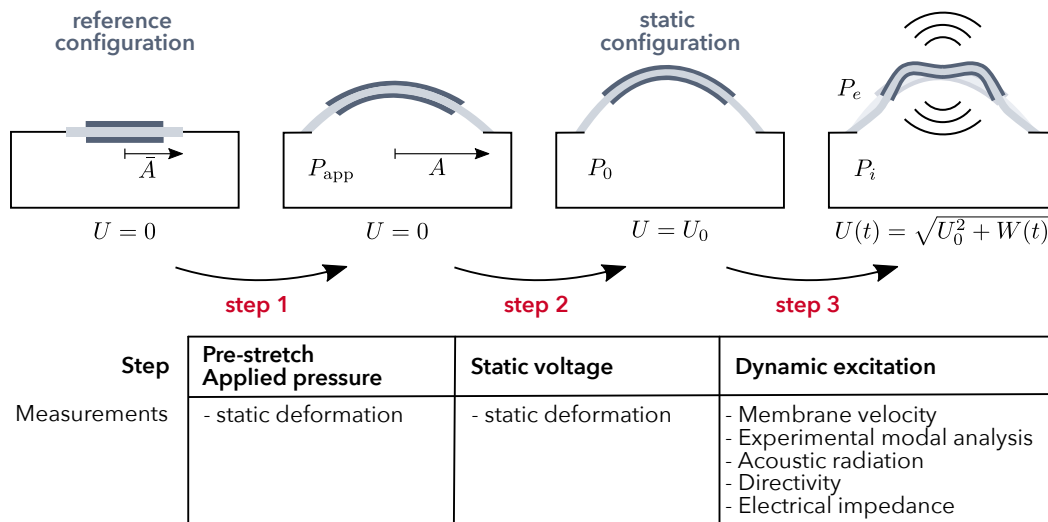


Fig. 3.21. Overview of the experimental procedure, indicating which measurements are performed at the different steps.

3.4.2 Static deformation

The static deformation of the membrane (when it is inflated and when a static voltage is applied [see fig. 3.21]) is measured using a Keyence LK-G407 laser displacement sensor, using the setup shown in fig. 3.22. The laser is moved over the membrane using a Newport 2-directional linear stage, and the position of the membrane is measured on one or more diameters. Meanwhile, the pressure is recorded by a Furness Control manometer.

3.4.3 Impedance measurements

The setup for impedance measurements is shown in fig. 3.23.

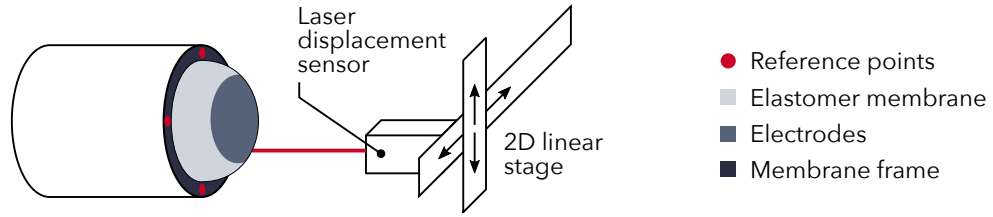


Fig. 3.22. Setup to measure the static deformation of the membrane. The reference points are used to estimate the position of the membrane holder, to provide a reference.

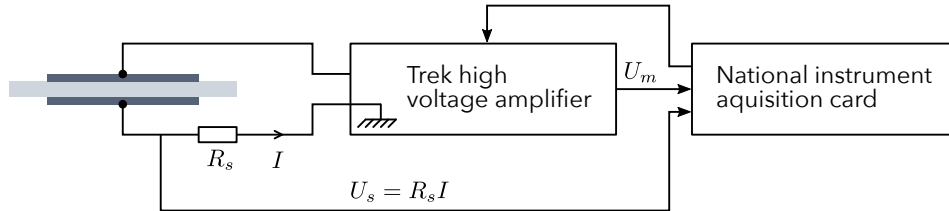


Fig. 3.23. Setup to measure the impedance of the DE membrane. U_m is the voltage monitor output of the high voltage amplifier, and U_s the voltage across the shunt resistor used to measure the current.

Matlab is used to generate a white noise or a frequency sweep, and a National Instruments card then sends the signal to the high voltage amplifier and finally to the membrane.

The current monitor of the TREK amplifier cannot be used, as it provides erroneous results at high frequencies. Therefore, a shunt resistor of $R_s = 500 \Omega$ is added in series with the membrane. The amplifier can deliver at most 20 mA, so the maximum voltage across the shunt resistor will be 10 V, which is the maximum input voltage of the NI card. Also, the shunt resistor is much lower than the resistance of the electrodes which is of the order of 10 k Ω , so it will not affect the electrical behavior of the membrane.

The voltage monitor of the Trek amplifier is used to measure the voltage, but it has a low-pass behavior, because of the combined effect of the internal resistance of this monitor output, and of the internal capacitance of the NI card, which is about 100 pF. As a result, measurements above 5 kHz should be interpreted with care, as the measured voltage can be lower than the effective voltage. This effect can be compensated for by inverse filtering, but the accuracy of this tweak could not be assessed.

3.4.4 Modal analysis and membrane dynamics measurements

Measurement of transfer functions

In order to measure the membrane dynamics, a Polytec PSV-500 laser scanning vibrometer is used [see setup in fig. 3.24]. The DE membrane is excited with the signal given in section 2.4, so the excitation force is proportional to W_a . Therefore, the transfer function between W_a and the membrane normal velocity is computed, on a mesh of approximately

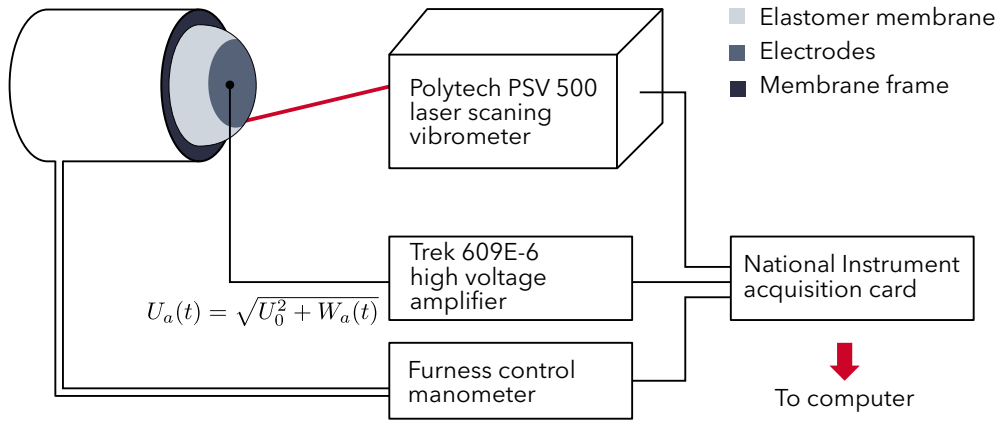


Fig. 3.24. Measurement setup for modal analysis.

300 points [see fig. 3.25a]. For each point, the transfer function is estimated using the H_1 estimator:

$$H_1 = \frac{G_{W,\dot{Z}}}{G_{W,W}}, \quad (3.7)$$

where $G_{W,\dot{Z}}$ is the cross power spectral density between the excitation signal W_a and the membrane velocity \dot{Z} , and $G_{W,W}$ the power spectral density of W_a . This estimate of the transfer function suppresses uncorrelated noise on the output \dot{Z} [27]. The Welch method is used to estimate the power spectral densities, by averaging over six Hanning windows for each measured point. The coherence between the velocity and the excitation signal is also computed, to provide an indicator of the measurement quality: the coherence should be equal to unity if the velocity is perfectly correlated to the excitation, and smaller than unity otherwise [see fig. 3.25].

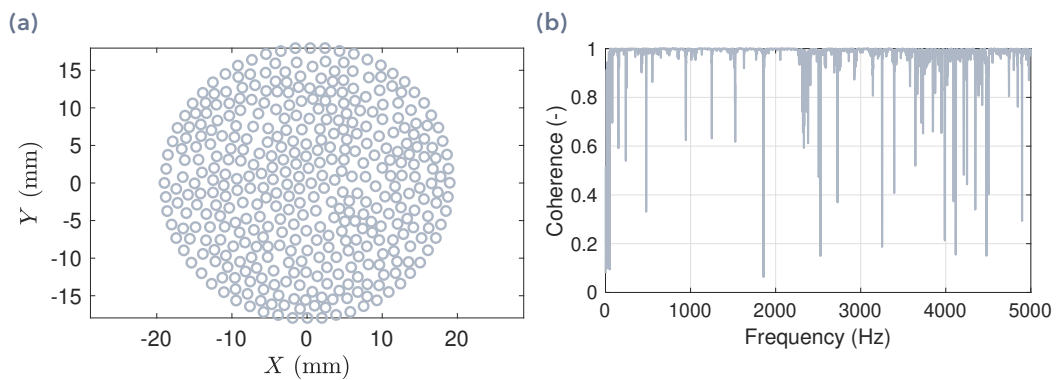


Fig. 3.25. (a) Mesh for modal analysis: each circle is a measured point. Here the membrane radius is $A = 19$ mm. (b) Example of the coherence between \dot{Z} and W_a for an arbitrary chosen point.

Figure 3.25b shows that the coherence is close to unity over the whole frequency range of interest 50-5000 Hz. The sharp drops most likely come from optics, as the membrane surface is black which is not optimal for reflecting the laser.

Extraction of the modal parameters

Once the transfer function between the excitation W_a and the membrane velocity \dot{Z} is measured for all points of the mesh, this data can be used to extract the modal parameters, namely the eigenfrequencies, the modal loss factor, and the modeshapes. This procedure is called experimental modal analysis, and many different algorithms have been developed to perform this extraction.

The most simple option is to identify the peaks in the amplitude plot of the frequency response, and measure their amplitude and phase. This works if all modes are well separated in frequency, which may not be the case for the considered membrane. What is more, a different set of eigenfrequencies would be found for each point of the mesh, making the global interpretation of the obtained modes very cumbersome. This method can be classified in the SDOF class (Single Degree Of Freedom): all points are treated one by one, without using the knowledge of the other points.

More advanced techniques have been developed, making use of the knowledge of all points to identify the modal parameters. These methods are called Multiple Degrees Of Freedom methods. The most used is the Least Square Complex Exponential method [27], which builds an auto-regressive model of the system in the time domain. In the present thesis I used the open-source Abravibe toolbox [11], which provides routines that perform the Least Square Complex Exponential modal extraction.

3.4.5 Acoustic radiation

Acoustic measurements are performed in the anechoic chamber at IMSIA, whose dimensions are $3 \times 3 \times 3 \text{ m}^3$, in which is specified down to 120 Hz. The loudspeaker is placed 1 m above a rotating platform, which can be controlled with a precision of 1° . Two Bruel and Kjaer half inch free-field microphones are placed on axis of the loudspeaker, one in the near-field and the other in the far-field [see fig. 3.26]. The acoustic pressure, and the excitation signal W_a are recorded simultaneously using a National Instrument acquisition card. The transfer function between the pressure and W_a is computed using the H_1 transfer function estimate, like for the modal analysis [see section 3.4.4].

The loudspeaker can be rotated while keeping the microphone fixed, in order to obtain directivity plots [see fig. 3.26].

3.5 Conclusion

In this chapter, the different measurement setups that are used throughout the thesis have been presented.

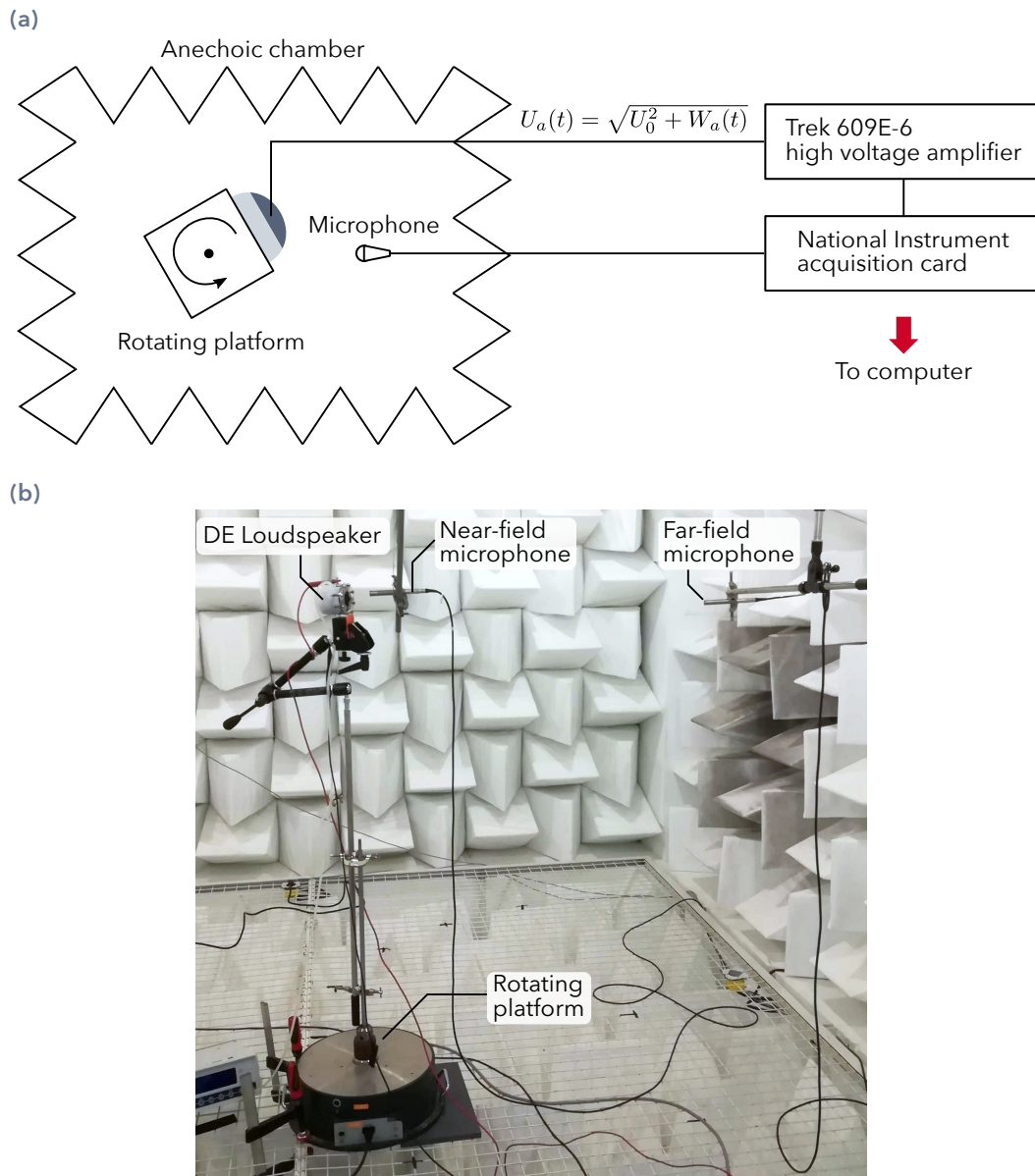


Fig. 3.26. Measurement setup for acoustic measurements: pressure radiated on-axis and directivity. (a) Schematics of the setup. (b) Picture of the setup in the anechoic chamber.

The static, dynamic and acoustic results will be analysed together with the numerical calculations in the following chapter.

Comparison of experimental and numerical results

In this chapter, the results of the model derived in chapter 2 are compared to experimental results, obtained following the procedure of chapter 3. First the static deformation of the membrane is investigated, and then dynamic results are presented, including membrane free and forced vibrations, as well as acoustic radiation.

Finally, the multiphysics nature of the device is demonstrated, by showing the influence of the coupling with the cavity stiffness, and of strong vibroacoustic coupling.

4.1 Parameters of the prototype

All the results and calculations presented in the thesis are obtained with the parameters given in table 4.1. These parameters correspond to a membrane of Wacker Elastosil silicone, of initial thickness $50\mu\text{m}$, equi-biaxially pre-stretched by 1.1. The electrodes are applied by pad-printing, using a mix of silicone, carbon black and iso-octane. During the pad-printing process, the conductive ink penetrates in the silicone membrane, and this relaxes the tension. This is why the pre-stretch in table 4.1 is smaller than the applied pre-stretch.

4.2 Static deformation

4.2.1 Without applied voltage

Position of the center

The membrane is inflated, and the position of the center point is monitored together with the inflation pressure. The result is plotted in fig. 4.1 for two membranes with different electrodes.

Figure 4.1 shows that the two membranes have a similar mechanical behavior, and that the inflation is correctly captured by the finite element model. The material hyper-elastic

Tab. 4.1. List of all experimental dimensional and non-dimensional parameters. These parameters are used in all experiments and numerical results presented in the thesis.

Parameter	Dimensional	Value	Non-dimensional	Value
Thickness at the center	\tilde{H}	46 μm	-	-
Cavity volume	V_{cav}	37 mL	$v_{\text{cav}} = V_{\text{cav}}/A^3$	6.3
Electrode radius	\bar{R}_E	1.8 cm	\bar{r}_E	1
Shear modulus	μ	$4.8 \times 10^5 \text{ Pa}$	-	-
Inflation pressure	P_{app}	1000 Pa	p_{app}	1.27
Membrane density	ρ_s	1042 kg m^{-3}	-	-
Gent parameter	J_m	100	J_m	100
Static voltage	U_0	1000 V	u_0^2	0.011
Electrode surface density	ρ_{elec}	0.09 kg m^{-2}	ρ_{ratio}	0.5
Membrane radius	\bar{A}	1.8 cm	-	-
Stretched membrane radius	A	1.9 cm	a	1.056
Excitation signal	W	$2 \times 10^5 \text{ V}^2$	-	-
Relative permittivity	ϵ_r	2.8	-	-
Loss factor	η	2%	η	2%
Speed of sound	C_f	343 ms^{-2}	c^2	255
Air density	ρ_f	1.2 Kg m^{-3}	m	0.45
Cavity depth	L_{cav}	1.5 cm	$l_{\text{cav}} = L_{\text{cav}}/A$	0.86
Cavity radius	R_{cav}	3 cm	$r_{\text{cav}} = R_{\text{cav}}/A$	1.18

parameters have been adjusted on this measurement [see section 3.3], which explains the perfect match between the measurements and the finite element simulation.

The slight difference between the two measurements may be due to the electrode material. When the electrodes are printed using the pad-printing method [see section 3.1.2], the ink relaxes the pre-stressed membrane, and the tension decreases. So the larger the electrode, the stronger this effect.

This may be the reason that slightly increases the slope at the origin for the membrane with full electrodes.

Deformation of the membrane

In order to further validate the finite element model, the full deformed shape of the membrane is measured, and plotted together with the simulation in fig. 4.2. The model perfectly captures the deformed shape of the membrane with partial electrodes ($\bar{r}_E = 0.52$), which is in-line with the conclusions drawn from fig. 4.1.

The fit between the model and the measurement is slightly worse for the membrane with full electrodes, which again indicates that the electrodes change the behavior of the silicone membrane.

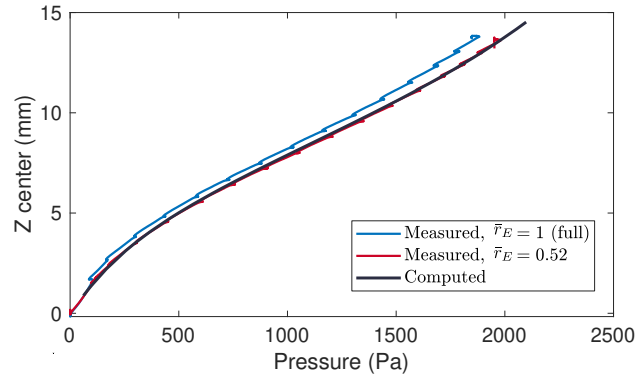


Fig. 4.1. Position of the membrane apex, when the membrane is inflated. Two membranes are measured, one with electrodes covering the whole surface ($\bar{r}_E = 1$), and a second with electrodes only on a disk of radius $\bar{r}_E = 0.52$.

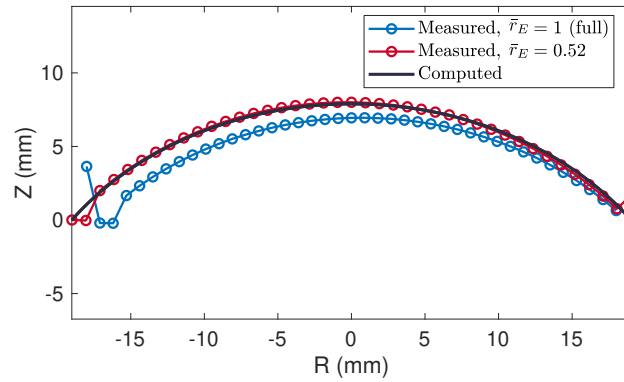


Fig. 4.2. Deformation of a membrane inflated to $P_{app} = 1000$ Pa, measured and computed. The membrane with full electrodes used in this measurement is not the same as in fig. 4.1, which explains the difference between fig. 4.1 and fig. 4.2. This difference provides an estimation of the measurement dispersion. The points which are not aligned with the others are measurement errors, which occur when the laser is not properly reflected by the membrane.

4.2.2 With applied voltage

Comparison with Zhu *et al.*

Zhu *et al.* studied the static deformation and the dynamics of an inflated DE membrane [126]. They computed the static deformation resulting from a pre-stretch of the membrane, inflation, and applied static voltage. These conditions correspond to particular parameters of the studied situation where we also account for non-uniform thickness, change in the inflation pressure due to adiabatic evolution of the gas in the cavity, and Gent material behavior instead of Neo-Hookean in [126].

For the non-dimensional parameters in table 4.2, the static deformation computed using the finite element method developed in the present thesis is compared to the results obtained by Zhu *et al.* by the shooting method in fig. 4.3.

Tab. 4.2. Non-dimensional parameters used to compare with the static deformation results of Zhu *et al.* [126].

V_{cav}	J_m	a	\bar{h}
∞	∞	3	1

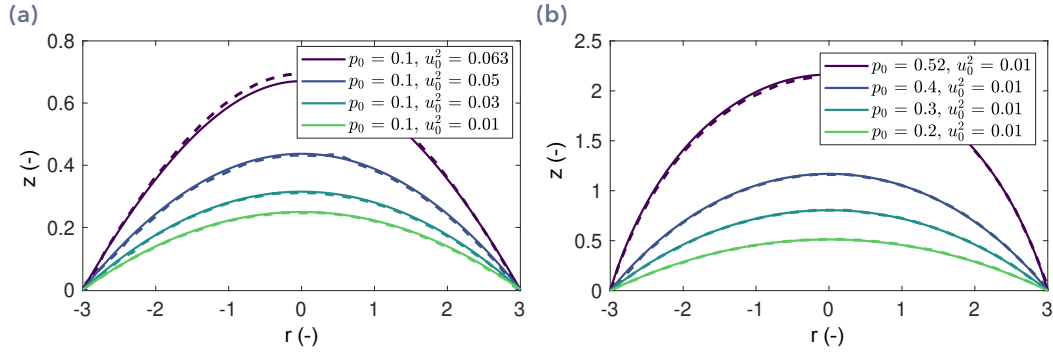


Fig. 4.3. Static deformation of the membrane when it is inflated and when a static voltage is applied, comparison with the article from Zhu *et al.* [126]. — code used in this thesis, - - - Zhu *et al.* (a) Deformed shape for a fixed pressure and various applied voltages. (b) Deformed shape for a fixed voltage and various inflation pressures.

Figure 4.3 shows that the developed finite element method yields the same results as Zhu *et al.*. Yet, the change of internal pressure which occurs when a voltage is applied is not accounted for by Zhu *et al.*, so the presented method will now be validated by comparisons with experiments.

Comparison with experiments

Once the membrane is inflated, a static voltage is applied to the electrodes. The membrane further deforms, which increases the volume of the cavity. As a consequence, the pressure inside the cavity decreases. This corresponds to **step 2** in the figure describing the experimental procedure fig. 3.21. During this step, the relative displacement of the membrane ΔZ is measured and computed, and the pressure change ΔP is monitored [see fig. 4.4].

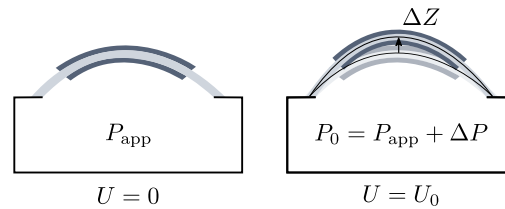


Fig. 4.4. Displacement of the membrane when a static voltage is applied. P_{app} is the applied pressure, P_0 the equilibrium pressure which is reached when the voltage U_0 is applied, and ΔP the pressure variation caused by the applied voltage [see fig. 2.1].

The membrane displacement ΔZ when a static voltage is applied can be measured by two methods.

In **method 1** a given voltage is applied, and the deformation of the whole membrane is measured by moving the laser displacement sensor using the setup of fig. 3.22).

In **method 2** the laser displacement sensor is fixed at a given radius, and the voltage is increased step by step, and the process is repeated for all the radii of interest.

The advantage of the second method is that it avoids errors related to the calibration of the distance between the membrane and the laser, as this distance remains fixed during the whole measurement. In **method 1**, the laser is moved by several centimeters between two measurements of the same point for a given voltage, so the distance between the laser and the membrane may vary due to positioning errors. In the following, the results of the two measurement methods are given, but method two is considered to be more reliable.

The results are plotted for two different membranes with different electrodes (full electrodes with $\bar{r}_E = 1$, and partial electrodes with $\bar{r}_E = 0.52$.) in figs. 4.5 and 4.6.

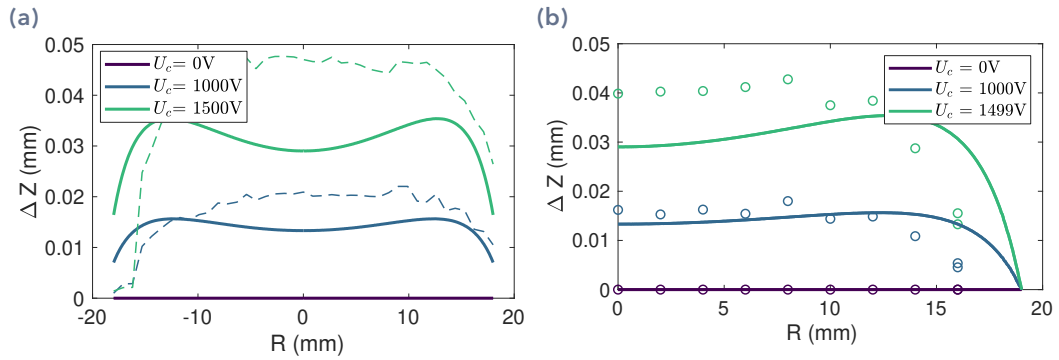


Fig. 4.5. Deformation of the membrane caused by the actuation voltage. The initial inflation pressure is $P_{app} = 1000$ Pa, the electrodes cover the whole membrane. — calculations, ○ and - - - measurements. (a) method 1, (b) method 2.

Figures 4.5 and 4.6 shows that the model predicts overall correctly the deformation of the membrane cause by the static voltage. For the full electrode [fig. 4.5], the membrane moves towards positive Z at all radii, versus with the partial electrode [fig. 4.6] the membrane move towards negative Z close to the border. This difference between the two electrodes is captured both by the measurements by and the model.

The measurements are very delicate, because the relative displacement caused by the voltage is small compared to the size of the membrane, and measuring such a small displacement of a soft elastomeric structure is difficult, especially because of viscoelastic relaxation. Therefore, the differences between the model and the measurements most likely come from measurement errors. The measurement error could be reduced by increasing the voltage, in order to increase the relative displacement, however, this increases the risk for electrical breakdown.

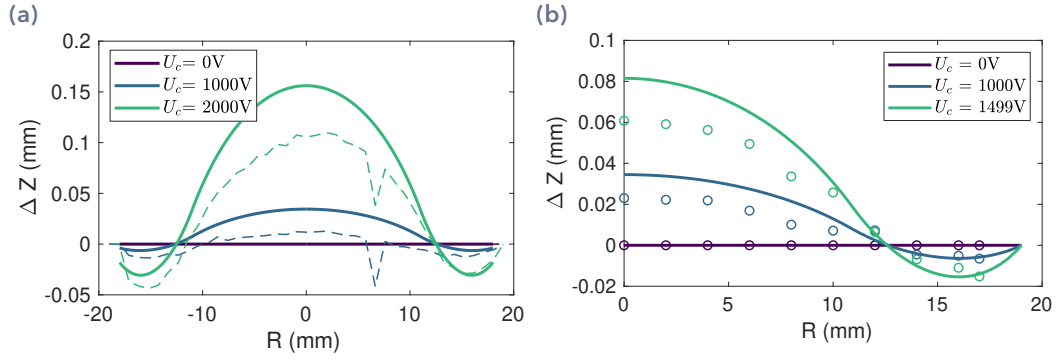


Fig. 4.6. Deformation of the membrane caused by the actuation voltage. The initial inflation pressure is $P_{app} = 1000$ Pa, the electrode radius is $\bar{r}_e = 0.52$. — calculations, \circ and - - - measurements. (a) method 1, (b) method 2.

For some radii $R > R_E$, the membrane seems to move inwards. To better understand what is happening there, the initial membrane position (for no voltage), the deformed position (magnified by 50), and the relative displacement between the two positions are plotted in fig. 4.7.

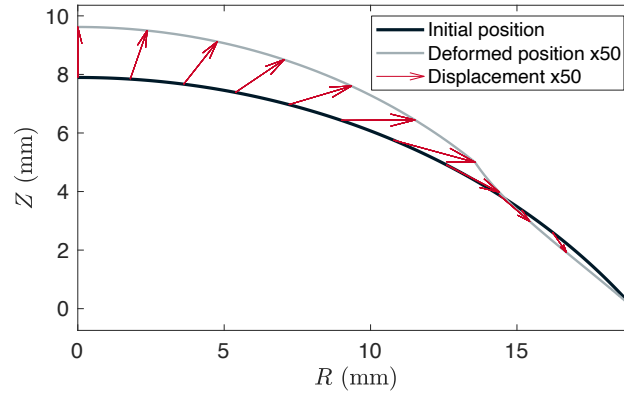


Fig. 4.7. Relative displacement of the membrane, caused by the static voltage. The membrane is initially inflated to $P_{app} = 1000$ Pa (Initial position), and a voltage of 1000 V is applied. In order to make the membrane displacement visible, the relative displacement is magnified by 50. The electrodes radius is $\bar{r}_E = 0.52$.

Figure 4.7 shows that in the membrane area that is not covered by an electrode, the displacement is indeed directed towards the inside of the membrane. This can be explained as follows: the voltage decreases the membrane tension in the area with an electrode, which therefore deforms more. The electrode area becomes comparatively stiffer than the rest of the membrane and shrinks, as seen in fig. 4.7.

4.3 Membrane dynamics

4.3.1 Free response

Comparison with Zhu *et al.*

As for the static validation [see section 4.2.2], the finite element method used to solve the equations can be partially validated by comparing the first eigenfrequencies to the results of Zhu *et al.* [126]. In their study, the cavity stiffness is not taken into account, meaning that the pressure is fixed inside the cavity, and does not vary as the membrane moves. What is more, the coupling with acoustics is not accounted for, and the electrodes cover the whole surface of the membrane.

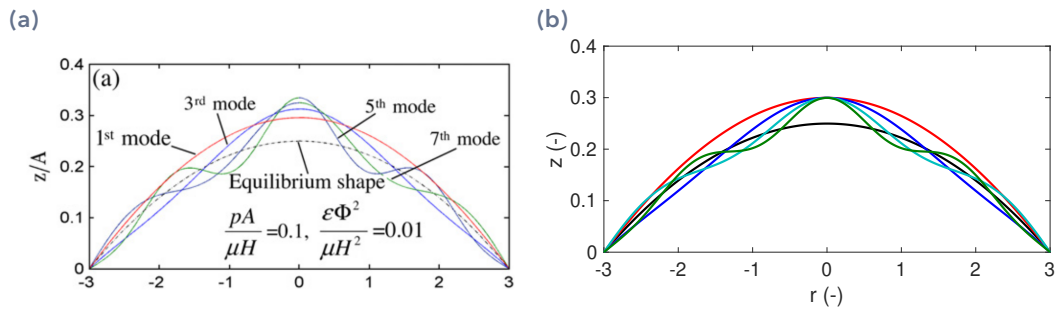


Fig. 4.8. (a) First modeshapes found by Zhu *et al.* from [126], (b) first modeshapes found using the code developed in this thesis. The scaling of the modes used in [126] is not given, so it has been chosen here to scale the modes to a maximal displacement of 0.05. This explains the differences between (a) and (b).

The non-dimensional frequencies are compared in table 4.3.

Tab. 4.3. Comparison of the first computed eigenfrequencies of the in-vacuo membrane to Zhu *et al.*

Mode number	1	2	3	4	5	6	7
ω present study	2.27	3.65	5.25	6.70	8.24	9.72	11.23
ω Zhu <i>et al.</i> [126]	2.3	3.7	5.2	6.7	8.2	9.7	11.2

The results of fig. 4.8 and table 4.3 compare well with the code used in the present study for the parameters used by Zhu *et al.* I find the same modeshapes and the same eigenfrequencies. However, many physics that we account for are neglected in [126], and experiments will next be presented to validate the calculation of the dynamics of the inflated DE membrane.

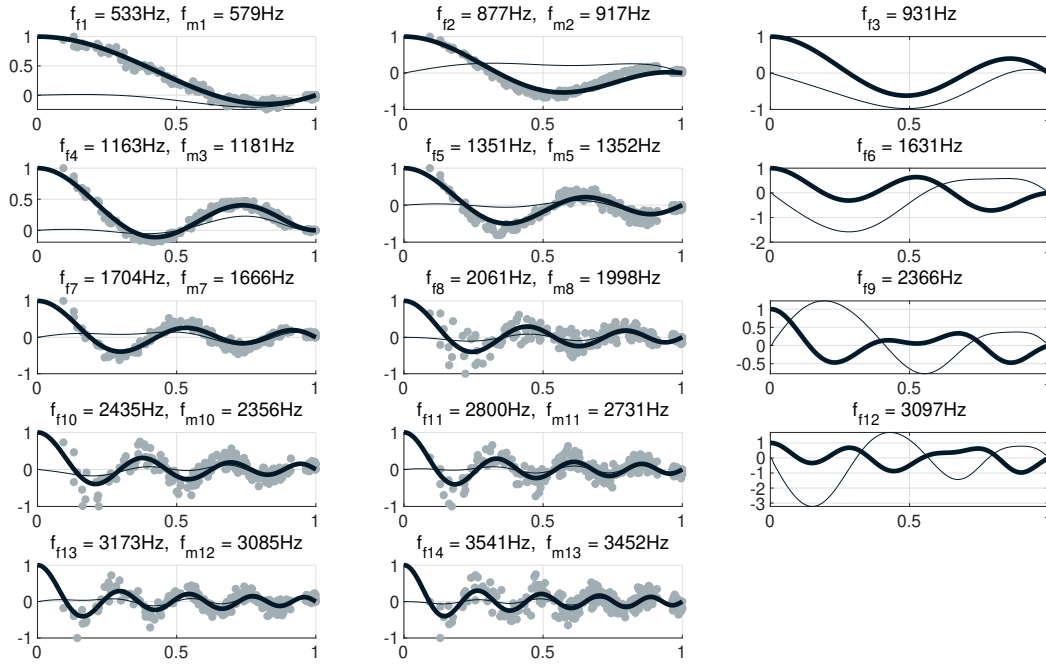


Fig. 4.9. Modes of a membrane with full electrodes, inflated to $P_{\text{app}} = 1000 \text{ Pa}$. — Z -component of the mode, — R -component of the mode, ● measurements. The x -axis is the non-dimensional radius r , and the modes are scaled so that the maximum amplitude of the Z -component of the mode is 1. The computed eigenfrequency of mode n is denoted f_{fn} , and the measured one f_{mn} .

Comparison with experiments

The modes of a DE membrane are measured following the procedure described in section 3.4.4, using a laser scanning vibrometer. The modes are plotted as a function of the membrane radius in fig. 4.9, even if they are measured on a mesh covering the whole membrane [see fig. 3.25]. Therefore, several points appear at the same radius in fig. 4.9, but are located at different positions on the membrane. By using this visualization of the modeshapes, their axisymmetry can be checked: if all points align on a single line, the mode is perfectly axisymmetric, and if there is a large vertical dispersion it means that points at the same radius but different positions have a different movement.

As the laser vibrometer measures only the vertical component of the velocity, only this component can be compared to the calculation. However, in order to get more information on the modeshape, the computed radial component is also shown in fig. 4.9. Thus, modes in which the membrane moves mainly along Z , and modes where it moves mainly in the radial direction can be distinguished.

Figure 4.9 shows that the model correctly captures the 14 first membrane modes. The first measured membrane modes are almost perfectly axisymmetric as there is no vertical dispersion of the measured points. The higher order modes deviate more from the axisymmetry, certainly due to the electrode connections which are not symmetric [see fig. 3.8] and add a non-symmetric mass distribution.

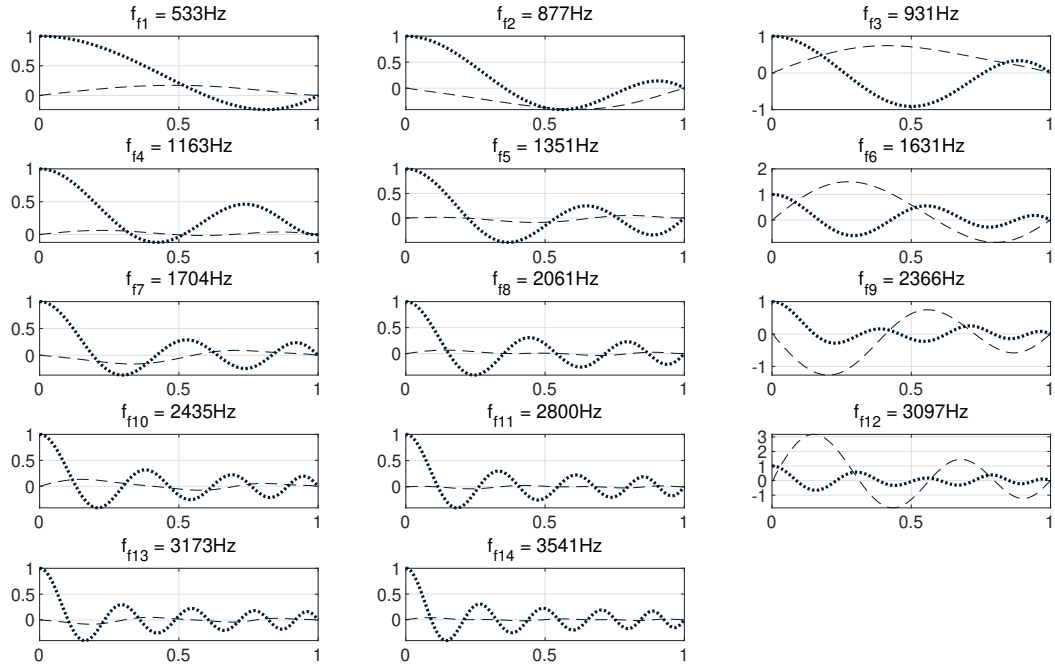


Fig. 4.10. Modes of the inflated membrane projected in the normal (.....) and tangential (---) directions.

It should also be noted that some computed modes could not be measured (modes 4, 6, 9 and 12). In these modes, the radial component is large compared to the vertical component. Thus, measuring the vertical component may not be sufficient to capture them. To better understand why these modes are not measured, another representation of the modeshapes is shown in fig. 4.10, where the modes are projected on the normal and tangential directions to the membrane.

Figure 4.10 shows that the modes that have a large radial component are the modes that have a large tangential component, and could not be measured experimentally. As only the normal component can be measured, it seems reasonable that the tangential modes could not be measured.

The membrane eigenfrequencies are plotted in fig. 4.11, where it can be seen that for most modes, the error between the measured and computed frequencies is below 5%. The relative error is larger for the first modes, but this absolute error is close to constant for the 14 first modes. The small discrepancy between measurements and numerical results may come from errors in the estimation of the model parameters, such as for example the shear modulus μ , the membrane thickness H , the electrode mass per unit area, etc.

Finally, the modal loss factor is also computed. It is recalled that a constant structural loss factor is used in the model to account for the losses in the membrane. So if only the membrane is modelled, all modes would have a loss factor equal to the structural loss factor. However, here strong coupling with acoustics is accounted for, and losses due to acoustic radiation may affect the modal damping. This is visible in fig. 4.12, where all computed modes have a loss factor close to 2 %, which is the used structural loss

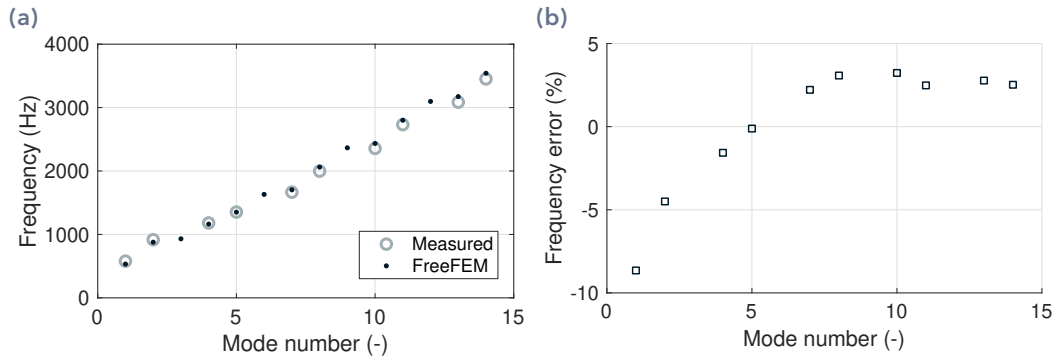


Fig. 4.11. Measured and computed eigenfrequencies of a membrane with full electrodes, inflated to $P_{app} = 1000$ Pa. **(a)** Frequencies. **(b)** Relative error between FEM and measurements.

factor, but the modes 4 and 5 have a slightly higher loss factor. As these modes radiate the most, they are more affected by the coupling with acoustics, and lose more energy through radiation.

Overall, the structural damping assumption is not really satisfied, as the computed modal loss factors differ significantly from the measured ones. However, since a modal description of the system is obtained using the numerical model, the measured loss factors can very easily be implemented in the model.

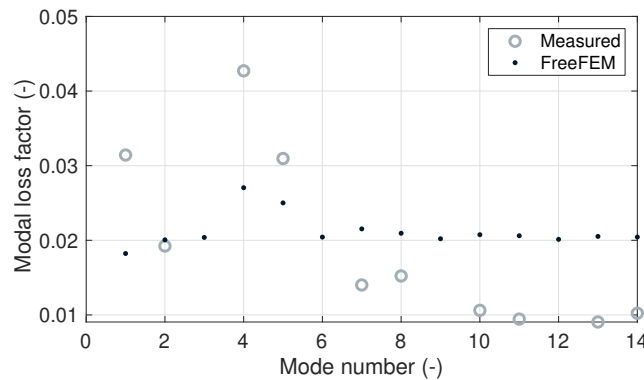


Fig. 4.12. Measured and computed modal loss factor of a membrane with full electrodes, inflated to $P_{app} = 1000$ Pa.

4.3.2 Forced response

Convergence of the modal summation

As explained in the theory section section 2.1, two methods are used to compute the frequency response of the dielectric membrane.

In the **FEM method** the system of governing equations is solved for all frequencies of interest, and in the **modal method** the solution is expanded on a basis of fluid/structure

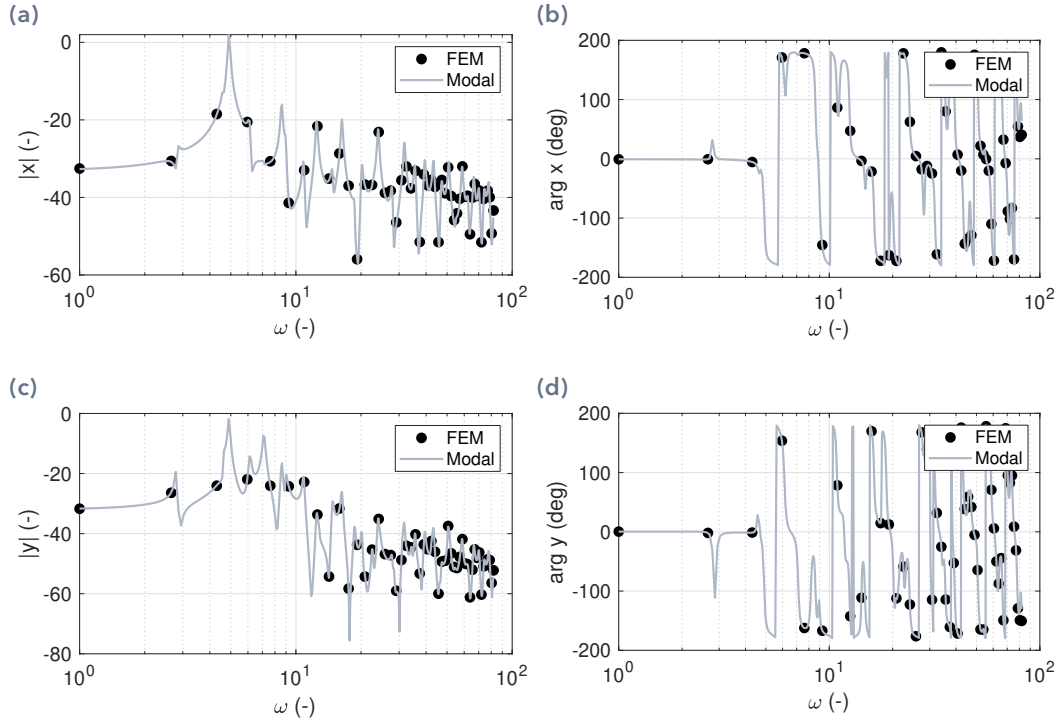


Fig. 4.13. Comparison of the **FEM method** and **modal method** for the membrane displacement, at radius $r = 0.5$. 300 modes, including PML modes are included in the modal summation. **(a)** Amplitude of the radial displacement x . **(b)** Phase of the radial displacement x . **(c)** Amplitude of the vertical displacement y . **(d)** Phase of the vertical displacement y .

coupled modes. The modal method is much faster to compute the system frequency responses, so it will be used in all the following. Here the convergence of the **modal method** to the **FEM method** is validated in fig. 4.13, for the structural part (the membrane dynamics).

The **modal method** yields exactly the same results as the **FEM method**, as seen in fig. 4.13, both for the phase and the amplitude. This validates the use of the fluid/structure coupled modes to compute the membrane dynamics. The results presented here are obtained with a modal basis comprising the 300 first modes, including both membrane modes and PML modes. It is interesting to point out that the same results are obtained if only the membrane modes are included in the modal basis, even if the results are not shown here for conciseness reasons.

The convergence of the **modal method** to the **FEM method** is also validated for a much simpler system in appendix D, where the convergence of the modal method is studied in greater details.

Comparison with experiments

The **modal method** has now been validated, and will be used for all the comparisons between numerical results and experiments.

The forced membrane dynamics, when the membrane is excited by the electrostatic excitation, are computed and compared to the frequency response function measured using the laser scanning vibrometer, as described in section 3.4.4.

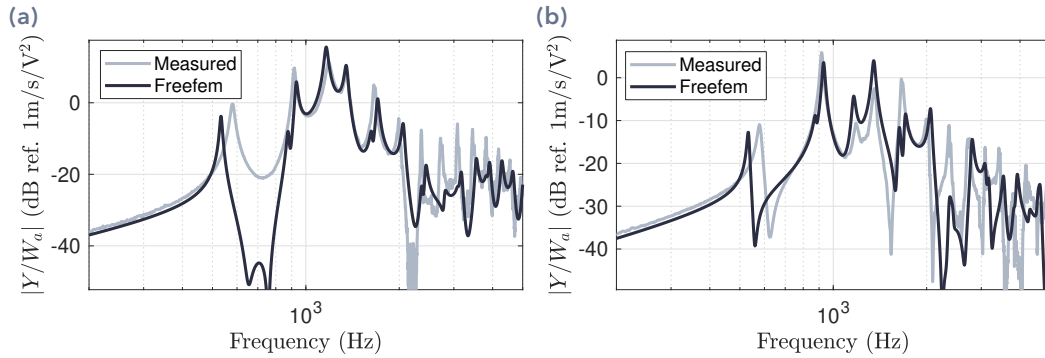


Fig. 4.14. Transfer function between the membrane velocity along Z and the excitation signal W_a , measured and computed for a membrane with full electrodes inflated to $P_{\text{app}} = 1000$ Pa, and with static voltage $U_0 = 1000$ V. **(a)** Average on 8 points around the radius $r = 0$. **(b)** Average on 20 points around the radius $r = 0.5$.

The transfer function between the membrane velocity and the excitation signal W_a is plotted in fig. 4.14 at two different radii. The computed frequency response is close to the measured one, for both chosen radii. There is an error in the frequency of the first mode, which has already been observed in fig. 4.11. The amplitude of most peaks is correctly estimated, and the errors for some of the modes may come from the damping: as analyzed in fig. 4.12, the damping model overestimates the damping at high frequencies, for modes 6 and above. The global behavior of the amplitude is correctly predicted, including the decrease of the response at high frequencies due to the resistivity of the electrodes, which is accounted for by the electrical model [see section 2.4.2].

The electrical impedance is plotted in fig. 4.15, and compared with the simple electrical model presented in fig. 2.7, which is fitted to the measurements. The obtained capacitance is $C_{\text{memb}} = 23$ nF, and resistance $R_{\text{memb}} = 1.1$ k Ω , which gives an electrical cutting frequency of 6 kHz.

The simple lumped RC electrical model seems sufficient to describe the electrical behavior of the DE membrane, as the impedance behaves at low frequencies as a pure capacitance, with the slope of -20 dB/dec, and like a resistance at high frequencies above 6 kHz. The deviation of the measured impedance from the model at high frequencies is most likely due to measurement errors, and especially to the voltage measurements. Indeed the voltage is measured using the voltage monitor output of the Trek high voltage amplifier, which itself has a low-pass behavior.

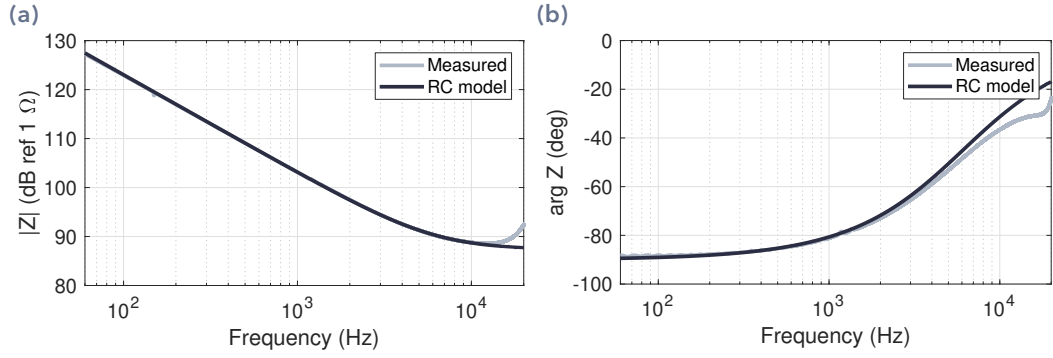


Fig. 4.15. Measured impedance, and fitted RC-model, for a membrane with full electrodes inflated to $P_{app} = 1000$ Pa, and with static voltage $U_0 = 1000$ V. (a) Amplitude. (b) Phase.

4.4 Acoustic radiation

4.4.1 Pressure on axis

Convergence of the modal summation

The convergence of the modal expansion of the radiated pressure is checked in fig. 4.16.

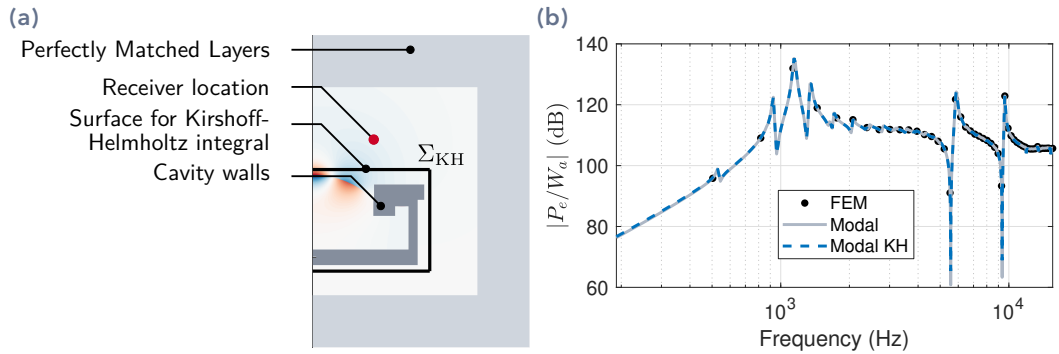


Fig. 4.16. (a) Definition of the integration surface for the Kirshoff-Helmholtz integral, and receiver location for pressure calculation. (b) Radiated pressure at the receiver location defined in figure (a), computed using the **FEM method**, the **modal method**, and the **modal KH method**.

Figure 4.16 shows first that the **modal method** yields the same results as the **FEM method**. This validates the modal summation procedure as well as the truncation of the modal basis. This convergence is no surprise, as it has been studied in details on a simpler system in appendix D.3.

Secondly, the **modal KH method** yields the same results as the **modal method** for a point located in the near field. This gives two indications: the Kirshoff-Helmholtz integral is

correctly calculated, and the Sommerfeld radiation condition is correctly implemented. Indeed, the free-field radiation condition is embedded in the free-field Green's function which is used in the Kirshoff-Helmholtz integral, so the KH-integral propagates the solution from the surface Σ_{KH} to the receiver assuming they are no reflections on the outer boundary of the domain. As it yields the same results as the **modal method** where the propagation is performed by finite elements and PMLs, it means that the finite elements and the PMLs correctly implement the Sommerfeld radiation condition.

Comparison with experiments

The pressure radiated by the membrane is measured in the anechoic chamber at IMSIA following the procedure of section 3.4.5, at two different distances: 6 cm and 1 m. Considering the size of the membrane (≈ 4 cm diameter), one measurement is performed in the acoustic near field, and the other in the far field. The near field results are shown in fig. 4.17, and the far field measurements in fig. 4.18.

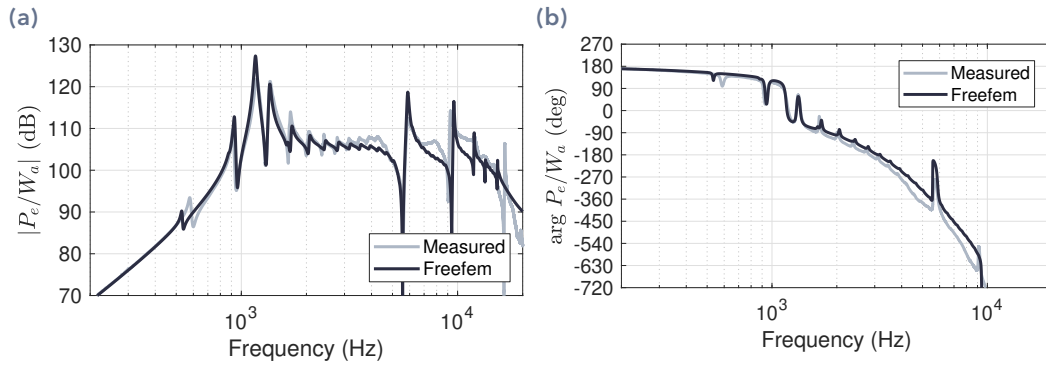


Fig. 4.17. Pressure radiated by membrane with full electrodes inflated to $P_{app} = 1000$ Pa, and with static voltage $U_0 = 1000$ V. The measurement is performed on axis at a distance from the membrane of 6 cm. **(a)** Amplitude, the decibels are dB ref. 2×10^{-5} Pa/1 V². **(b)** Phase.

Figures 4.17 and 4.18 show that the model computes accurately the pressure radiated by the membrane. Except for the first mode, the eigenfrequencies are correctly estimated, as already analysed in figs. 4.11 and 6.8.

Additionally, in the acoustical response, the modal behavior of the acoustic cavity on which the membrane is inflated is more visible in acoustical results than in velocity measurements. The large peaks at 5885 Hz, 9613 Hz and 11 940 Hz corresponds to acoustic modes of the cavity. As the membrane vibrations are strongly coupled to acoustics, the acoustic behavior of the cavity influences the membrane vibrations, which radiates sound in the free field. Therefore, the peaks at high frequencies in the radiated response highlight strong vibroacoustic coupling effects, as they would not occur if the membrane vibrations were not influenced by acoustics.

The radiation is not dominated by the first membrane modes, as it is the case for all standard loudspeakers. The cavity stiffens a lot the first modes, because these modes

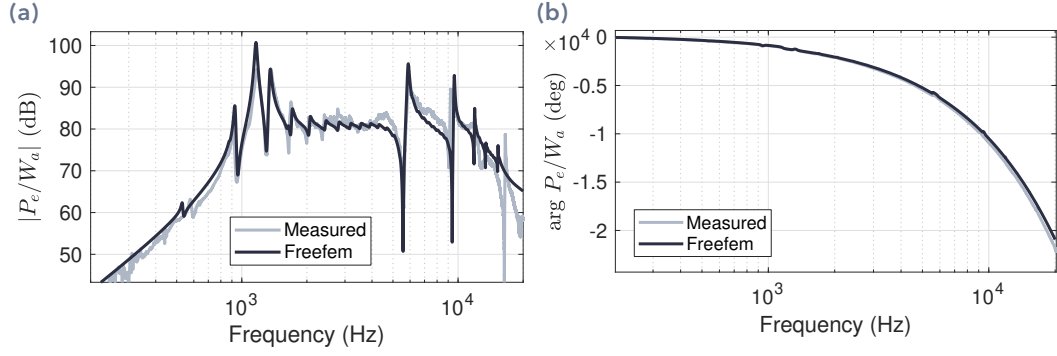


Fig. 4.18. Pressure radiated by membrane with full electrodes inflated to $P_{\text{app}} = 1000 \text{ Pa}$, and with static voltage $U_0 = 1000 \text{ V}$. The measurement is performed on axis at a distance from the membrane of 1 m. **(a)** Amplitude, the decibels are dB ref. $2 \times 10^{-5} \text{ Pa/1 V}^2$. **(b)** Phase.

generate a large change of the volume of the cavity. Thus, these modes radiate less than higher order modes.

There is a clear maximum of the radiation around 1200 Hz, where a couple of modes radiate a lot. This maximum is directly related to the ratio between the membrane mass and the cavity stiffness. The membrane mass can be estimated roughly by:

$$M_{\text{memb}} \approx \pi A^2 \rho_s H, \quad (4.1)$$

and the stiffness created by the compression of air in the cavity by:

$$K_{\text{cav}} \approx \pi A^2 c_f^2 \frac{\rho_f}{L}, \quad (4.2)$$

where L is the cavity depth. This yields the following resonance frequency:

$$f_{\text{res}} = \frac{1}{2\pi} \sqrt{\frac{K_{\text{cav}}}{M_{\text{memb}}}} = \frac{1}{2\pi} \sqrt{\frac{c_f^2 \rho_f}{LH \rho_s}} \approx 2000 \text{ Hz}, \quad (4.3)$$

for the membrane measured in figs. 4.17 and 4.18.

This is a very rough estimation of the resonance frequency, but the order of magnitude is coherent with the observations. The global frequency behavior of the membrane is dominated by the resonance of the membrane mass over the cavity stiffness, and this response is modulated by the modal behavior of the membrane. Of course, this interpretation is a simplification of the real phenomena, but provides a physical interpretation of the membrane dynamics and sound radiation. A related consequence is that increasing the cavity volume would reduce the frequency of the maximum in the response.

The influence of the major design parameters will be further analysed in chapter 5.

4.4.2 Directivity

Using the setup described in fig. 3.26, the directivity of the inflated DE loudspeaker is measured in the anechoic chamber. The same frequency response measurements as shown in section 4.4.1 are carried out for different angles between the loudspeaker axis and the microphone.

The results are presented in fig. 4.19 for arbitrary chosen frequencies which cover the frequency range of interest.

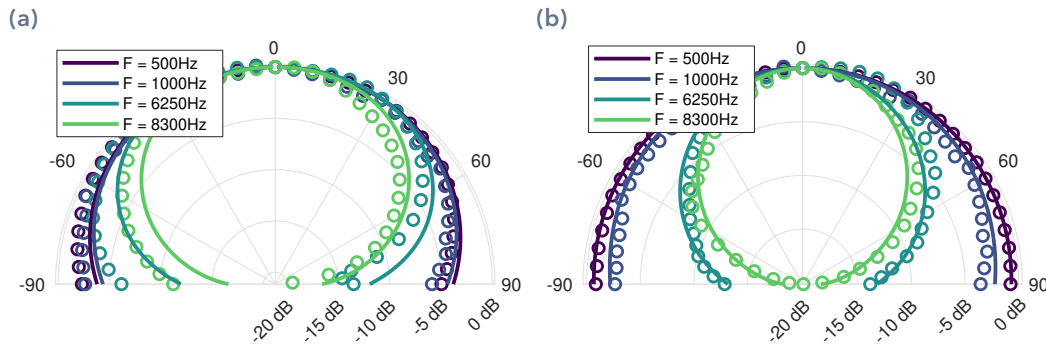


Fig. 4.19. Directivity of a membrane with the parameters given in table 4.1. **(a)** Near field: the microphone is placed at 6 cm from the center of the membrane. **(b)** Far field: the microphone is placed at 1 m from the loudspeaker. ○ Measurements, — FreeFEM.

The model captures well the directivity of the prototype up to more than 8 kHz. In the far field the computed directivity matches perfectly the measurements, but there is a larger error for the near field directivity. The error comes very likely from microphone positioning inaccuracies, as the measured directivity is not axisymmetric. The loudspeaker was maybe not placed perfectly on the rotation axis of the rotating platform [see fig. 3.26].

The radiation is omnidirectional up to more than 1 kHz, when the loudspeaker is acoustically compact. Above that frequency, it becomes more directional and radiates mostly on axis as the wavelength becomes smaller than the size of the loudspeaker enclosure.

4.4.3 Harmonic distortion

One of the most important quality criteria for loudspeakers is the Total Harmonic Distortion (THD), which is a measure of the non-linearity of the system.

If a sine wave is sent to the loudspeaker, the THD quantifies the amplitude of the higher order harmonics in the response compared to the fundamental. More precisely,

$$\text{THD} = \frac{\sqrt{P_2^2 + P_3^2 + P_4^2 + \dots}}{P_1}, \quad (4.4)$$

where P_i is the RMS amplitude of the i -th harmonic in the radiated pressure, $i = 1$ being the fundamental frequency.

The model which has been developed in this thesis is linear, so no predictions of the total harmonic distribution will be presented here.

However, the THD is relatively easily measured, using the exponential swept-sine method which has been developed by Farina in 2000 [28]. An exponential sweep is sent to the system and the response is measured, and then deconvolved by the inverse of the exponential sweep. The linear impulse response as well as higher order impulse responses are obtained simultaneously, enabling the calculation of the THD as a function of frequency.

The THD is plotted for three excitation amplitudes in fig. 4.20.

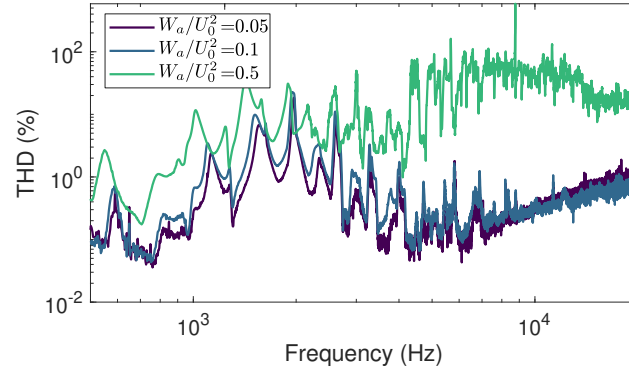


Fig. 4.20. THD of the DE loudspeaker, inflated to 1000 Pa, with static voltage $U_0 = 2000$ V, for different excitation levels $|W_a|/U_0^2$ (the applied voltage is $U = \sqrt{U_0^2 + W_a}$).

Figure 4.20 shows that the THD increases with the excitation level $|W_a|/U_0^2$, and reaches a maximum at each membrane eigenfrequency, because the membrane has larger displacements at these frequencies.

At high frequencies, above 4 kHz, the measurement with the highest excitation $|W_a|/U_0^2 = 0.5$ has a much higher distortion. This is related to the current limit of the TREK amplifier (20 mA) which saturates. Indeed, due to the capacitive behavior of the membrane, more current is required to excite the membrane at high frequencies. Using more a more powerful amplifier would reduce the THD at high frequencies of the measurement at $|W_a|/U_0^2 = 0.5$ to the values obtained for smaller values of $|W_a|/U_0^2$.

To conclude this section, the distortion measured on DE loudspeakers in standard conditions is rather high, in the order of 10% at medium frequencies. Further work is therefore needed to reduce this distortion to acceptable levels. As a comparison, the THD of standard electrodynamic loudspeakers lies around 1%.

4.5 Demonstration of the multi-physics nature of the studied device

In the previous sections, the results of the numerical model were compared to experiments. The numerical results were obtained using the fully coupled model, where the

strong vibroacoustic coupling and the coupling with the cavity stiffness were taken into account. In the present section, the influence of these couplings is studied, and it is shown that they are of primary importance to model the dynamics and sound radiation of a DE loudspeaker.

4.5.1 Influence of the cavity stiffness

First, the influence of the cavity stiffness is studied. Two calculations are performed. In the first one, only the membrane dynamics are considered, and the coupling with the cavity stiffness as well as the coupling with acoustics are neglected. In the second one, the coupling with the cavity stiffness is added, but still not the coupling with acoustics. The differences between the two calculations are therefore only due to the cavity stiffness. The results are plotted together with the measurements in fig. 4.21.

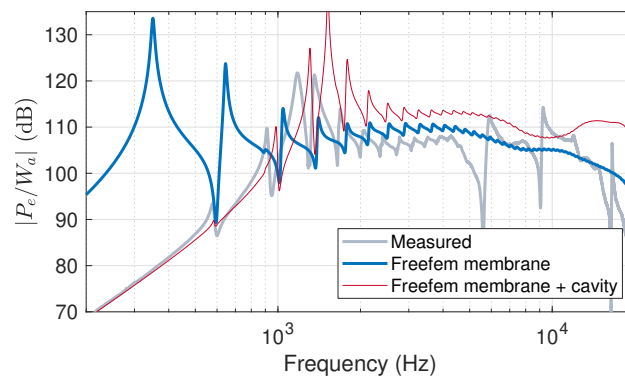


Fig. 4.21. Influence of the cavity stiffness on acoustic radiation. *FreeFem membrane* is computed by only considering the membrane. *FreeFem membrane + cavity* is obtained by computing the dynamics of the membrane coupled to the cavity stiffness.

Figure 4.21 shows that the stiffening effect of the cavity is of primary importance. The maximum of radiation is shifted from the first mode to the third and fourth modes, at a much higher frequency. Also, the eigenfrequencies increase when the cavity is taken into account. With the cavity in the model, the low frequency behavior is correctly captured, because low frequencies are stiffness dominated. This means all the relevant stiffness of the the system have correctly been accounted for. At high frequencies, there is still a large error between the measurement and the model, and in next section this will be related to strong vibroacoustic coupling effects.

4.5.2 Influence of the vibroacoustic coupling

The effect of strong vibroacoustic coupling is now studied, by comparing calculations with and without taking the coupling into account. The radiated pressure is plotted in fig. 4.22.

Figure 4.22 demonstrates that the coupling with acoustics has a large influence on the membrane vibrations, and therefore on the acoustical radiation.

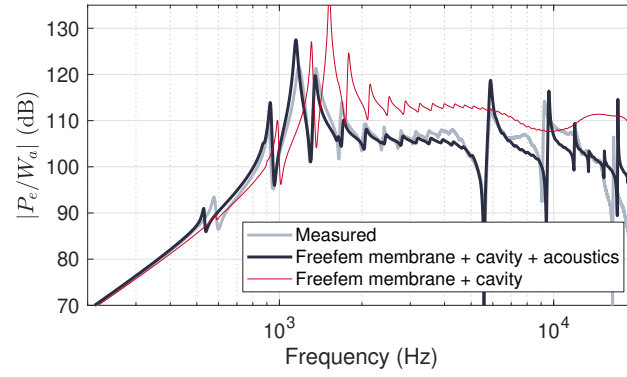


Fig. 4.22. Influence of vibro-acoustic coupling on acoustic radiation. *FreeFem membrane + cavity* is computed without taking the strong vibroacoustic coupling into account, and *FreeFem membrane + cavity + acoustics* is the result of the fully coupled model.

The main effect of the fluid is an added mass, as it decreases the frequencies of most eigenmodes of the membrane, as seen in fig. 4.23. The first modes, which create the largest fluid displacement, are the most heavily affected by the fluid loading, and their frequencies decrease by up to 13%. The higher order modes are less impacted by the fluid coupling.

Also, the coupling with exterior radiation increases the damping of the modes, as energy is lost through radiation. This effect is mostly visible for the modes 3-6, which are the ones that radiate the most, as seen in fig. 4.22.

The membrane modeshapes computed in vacuo and with fluid coupling are plotted in fig. 4.24, to analyse the fluid influence on the modeshapes. It appears that the modes which are the most influenced by the fluid coupling are the modes 3-6, that is to say the same which see their modal loss factor change a lot [see fig. 4.23c]. The location of the nodal lines change with the fluid loading, like for example for mode 5.

4.6 Conclusion

In this section the multi-physics model of an inflated DE loudspeaker that has been developed in chapter 2 is validated experimentally, in terms of static deformation, membrane dynamics and acoustical radiation. It is demonstrated that the model accurately captures the observed behavior of a DE loudspeaker prototype, and that all the different physics that were coupled together in chapter 2 are necessary to compute the dynamics.

This is to the author's knowledge the first fully coupled vibroacoustic model of DE loudspeakers, and thus the first time the acoustical behavior of a such structure is studied in fine details. This opens the path to optimization of the behavior of the DE loudspeaker, in terms of frequency response, radiation efficiency, directivity, etc. Several optimization ideas are presented in the next chapter, which builds upon the results of the coupled model.

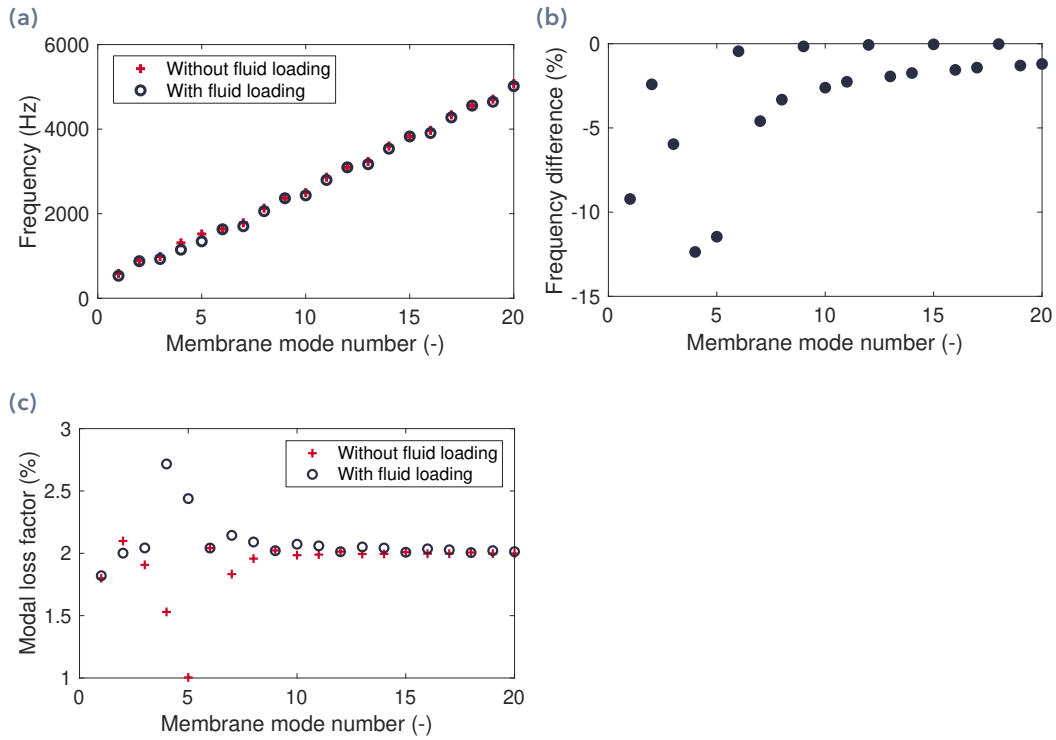


Fig. 4.23. Influence of the fluid loading on the membrane modes. (a) Eigenfrequencies in vacuo (*Without fluid*), and loaded with the surrounding fluid. (b) Relative difference between the in-vacuo and the fluid-loaded eigenfrequencies. (c) Computed loss factor of the membrane modes with and without taking into account the fluid loading.

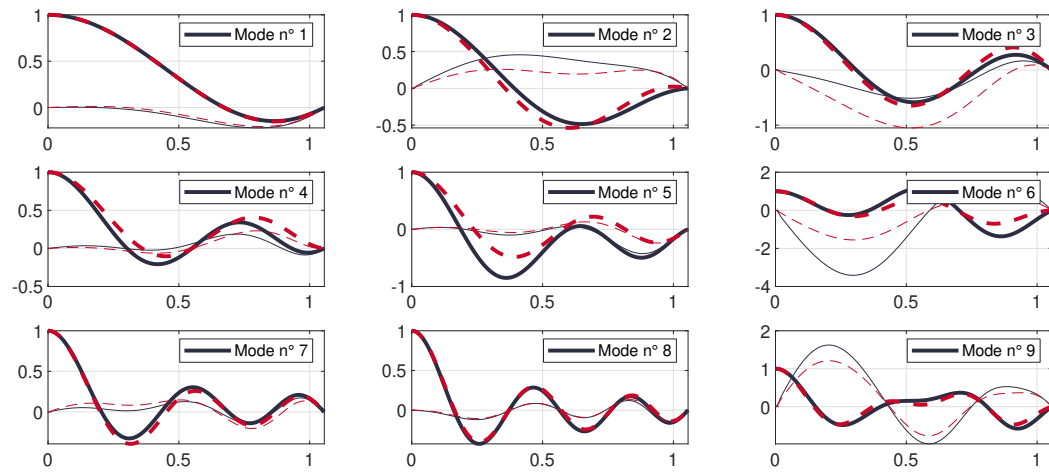


Fig. 4.24. Influence of the fluid loading on the membrane modeshapes. — z -component, with fluid loading. — r -component, with fluid loading. - - - z -component, no fluid loading. - - - r -component, no fluid loading. The x -axis is the non-dimensional radius r , and the y -axis is the amplitude, scaled so that the z -component of the mode has a maximum amplitude of 1.

Optimization

In this chapter, solutions to improve the acoustic behavior of the DE loudspeaker are investigated, using the numerical model that has been developed in chapter 2.

First, static analyses are performed in order to improve the low-frequency behavior. Second, the electrode shape is optimized in order to improve the spectral balance. Third, the cavity is filled with foam to damp out the acoustic modes. Finally, signal processing tools are used to compensate for defects in the frequency response.

5.1 Static analysis

5.1.1 Limits of dielectric elastomer membranes

Dielectric breakdown

When an electric field is applied across a dielectric material, the material will remain insulating up to a certain value of the electric field. Then, suddenly, a conductive path is created through the material and the current flowing through the membrane increases sharply [15]. This phenomenon is called dielectric breakdown, and is characterized by the electric field at which it occurs, called the dielectric strength of the material and written E_{bd} in the following. This is a non-reversible phenomena, the material gets damaged, and is no longer insulating after breakdown.

As dielectric breakdown is the main operating limit of DE transducers, a lot of research effort has been engaged to characterize precisely when it occurs, by which parameters it is influenced, and what can be done to increase the dielectric strength. The breakdown strength is typically related to the Young's modulus of the material [68], the pre-stretch [67, 54], the thickness [54], and humidity [6].

In the present thesis, silicone based DE membranes are used, made either of spin-coated Nusil CF19-2186, or commercially available film Wacker Elastosil 50 μm . For these two silicones, the dielectric strength is about $E_{bd} \approx 80 \text{ V}/\mu\text{m}$ [76]. In the following analysis, the stretch dependence will be neglected as the following study focuses on the method, and not on the exact results. Taking into account this dependence would only change slightly the numerical results, but not the general trends.

Solutions for controlling dielectric breakdown

The static inflation of DE membranes has been studied in details by several authors, which try to maximize the increase of the volume of the inflated membrane when a high voltage is applied between the electrodes. Impressive deformations by up to 1600% have been reported by Keplinger *et al.*[62]. They used the electrostatic stress to trigger the instability that occurs when inflating elastomer membranes, called the snap-through instability. This requires the precise selection of the system parameters in order to achieve the snap-through without reaching the dielectric breakdown, which definitively damages the membrane.

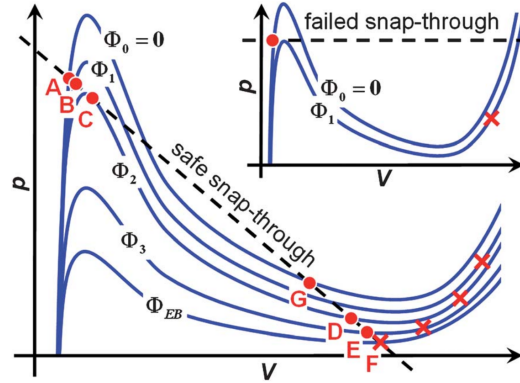


Fig. 5.1. From Keplinger *et al.* [62]. “Solid curves are the pressure-volume relations of a membrane subject to constant values of voltage, with conditions of electrical breakdown marked by crosses. When a large chamber is used, the pressure remains constant when the voltage triggers the snap-through instability, leading to electrical breakdown (inset). When a medium-sized chamber is used, the pressure drops as the voltage triggers the snap-through instability, averting electrical breakdown.” The red crosses indicate for each voltage the dielectric breakdown, which occurs when the membrane becomes too thin (when the volume is too large) for the given voltage. In the top right figure, breakdown occurs when the volume becomes larger than the point marked by the red cross.

Figure 5.1 is extracted from [62], and provides guidelines to achieve large deformations of inflated DE membranes. Two cases are studied: one case where the cavity is small, and where the pressure decreases a lot when the voltage is applied, and a second case where the cavity is large and where the pressure stays constant during the membrane deformation. The maximum voltage than can be applied is controlled by the dielectric breakdown field. The goal is therefore to obtain the snap-through instability without crossing the red cross which represents the dielectric breakdown conditions. By adjusting the cavity volume the evolution path in the $p - v$ plane can be tilted, in order to achieve a safe snap-through.

The goal of Keplinger *et al.* is different from ours. Our goal here is to choose the best parameters to enhance the low-frequency behavior of the DE loudspeaker. This can be studied by looking at the static behavior, by maximizing the achievable volume change of the membrane before breakdown. However, all instabilities should be avoided, as a linear behavior is desired. Therefore, the analysis of Keplinger *et al.* will be carried out on our system with the parameters given in table 4.1, in order to find the optimal inflation pressure.

5.1.2 Optimal parameters for low frequency behavior

The goal here is to maximize the achievable volume change of the inflated membrane under electrostatic actuation, without instability. For this purpose, the figure of Keplinger *et al.* is replicated with the parameters of table 4.1 in fig. 5.2.

This plot is obtained by solving for the static deformation for several pressures and applied voltages [step 1 and step 2, see section 2.1]. In the calculation the cavity volume is set to $v_{\text{cav}} = 100$, which is a sufficiently low value to avoid any snap-through instability.

The dielectric breakdown conditions are also estimated, by detecting when the maximum electric field on the membrane exceeds the dielectric breakdown field, which is assumed to be constant and equal to $E_{\text{bd}} = 80 \text{ V}/\mu\text{m}$.

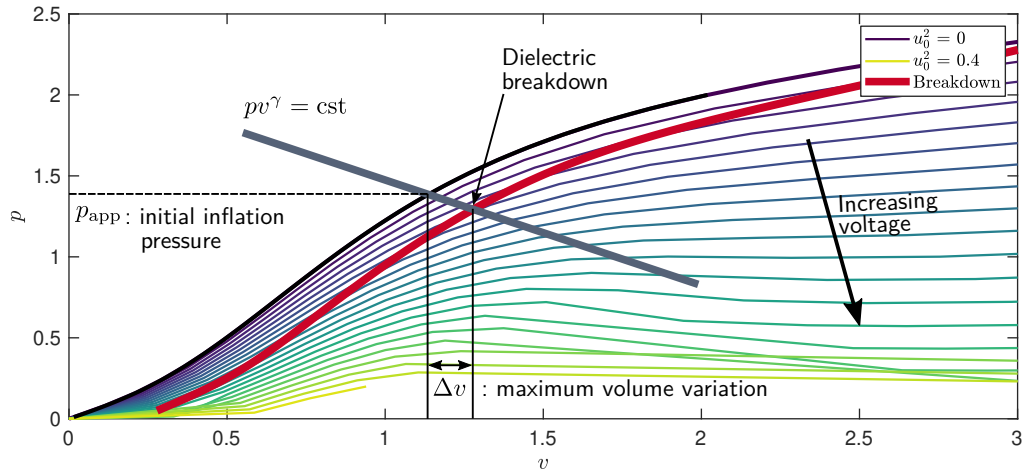


Fig. 5.2. Static characteristics of the inflated DE membrane. The horizontal axis is the non-dimensional volume of the inflated membrane, and the vertical axis is the non-dimensional pressure inside the cavity [see chapter 2 for the definition]. The red line corresponds to the breakdown conditions, when the maximal electric field in the membrane equals the breakdown electric field. The color lines correspond each to a value of the voltage applied between the electrodes, from null voltage $u_0^2 = 0$ for the black line at the top, to $u_0^2 = 0.4$ at the bottom.

The system evolution can be represented by a line on fig. 5.2, which describes a path in the $p - v$ plane. For an adiabatic evolution of the gas inside the cavity, the relation between the pressure and the volume changes reads:

$$\tilde{P} \approx -\gamma \frac{P_{\text{atm}}}{V_{\text{cav}}} \tilde{V}, \quad (5.1)$$

so the slope of this line can be adjusted by the the cavity volume V_{cav} .

An inflation pressure p_{app} is chosen, and the system will evolve on a straight line starting from that point when the voltage is increased. The maximum voltage is limited by the breakdown, represented by the red line in fig. 5.2. The maximum volume variation Δv is thus defined as the difference between the volume of the membrane at the starting point (no voltage), and at the end point (the breakdown).

This maximum volume variation depends on the inflation pressure p_{app} , so the inflation pressure that yields the largest volume variation is searched for.

The maximum volume variation depends also on the volume cavity v_{cav} , as a large cavity would yield a more horizontal evolution in the $p - v$ plane, and thus a larger volume variation before breakdown. The maximum volume variation is therefore plotted as a function of the inflation pressure p_{app} for several cavity volume v_{cav} in fig. 5.3.

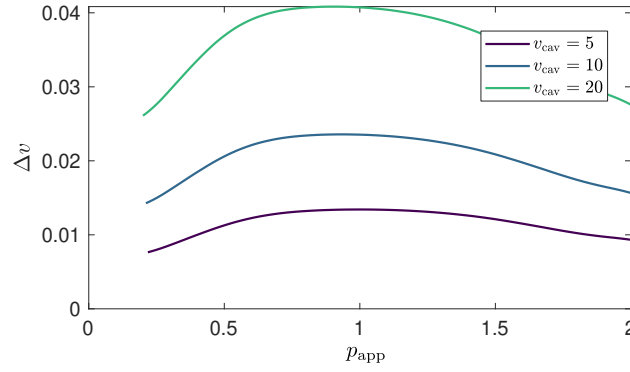


Fig. 5.3. Maximum volume variation before breakdown as a function of the inflation pressure, for several cavity volumes.

It appears that for each cavity volume v_{cav} there is an optimal inflation pressure for which the volume variation before breakdown is maximal. This optimal pressure seems to always lie close to $p = 1$: the pressure which approximately inflates the membrane into a hemisphere. The cavity volume is the key parameter that determines the volume variation, and its influence is studied in more details in fig. 5.4 where the maximal volume variation (for the optimal inflation pressure) is plotted as a function of the cavity volume.

Figure 5.4 shows clearly that large volume variations can only be obtained for large cavity volumes. As a reminder, the non-dimensional volume is $v = V/A^3$, so $\Delta v = 0.5$ means that the volume variation of the membrane is equal to half a cube of dimension A , the membrane radius.

Also, the optimal inflation pressure is close to 1 for small cavity volumes, but becomes larger (close to 2) for large volumes. This can be explained by fig. 5.2: for small volumes, the evolution line ($pv^\gamma = \text{cst}$ in grey) would be almost vertical. The optimal pressure would then be located where there is a large vertical distance between the curve without voltage, and the dielectric breakdown curve. On the other hand, for large volumes, the evolution line is almost horizontal, and the optimal pressure is then located where there is the largest horizontal distance between the no-voltage curve and the dielectric breakdown curve.

A last interesting point concerns the applied voltage u_0 . For large inflation pressures p_{app} , the membrane is very thin, so for a given voltage u_0 the electric field is larger. This means that the membrane can be actuated with lower voltages when the inflation pressure is large [see fig. 5.4c].

In practice, the size of the cavity is limited by practical considerations, so the design procedure would be the following:

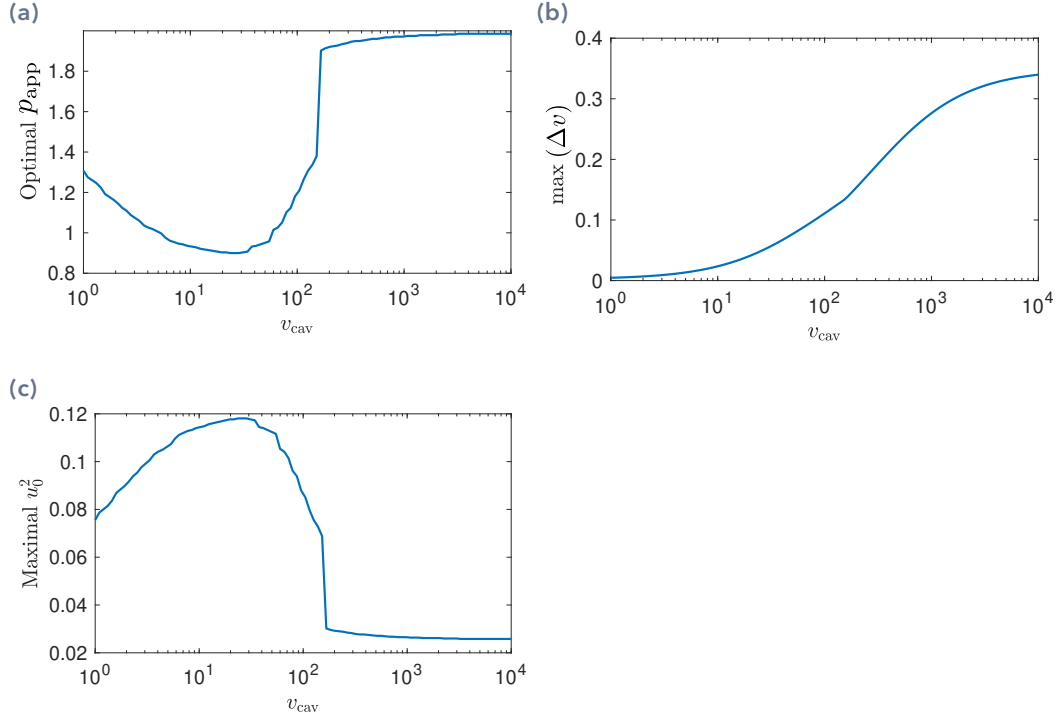


Fig. 5.4. (a) Optimal initial inflation pressure as a function of the cavity volume. (b) Maximal volume variation as a function of the cavity volume. (c) Maximal voltage before breakdown, for the optimal initial inflation pressure.

- Choose the device volume, by considering the balance between the size and the desired low-frequency behavior.
- Find the optimal inflation pressure using fig. 5.3.

5.1.3 Acoustic radiation with the optimal parameters

The study in the previous section is based on static considerations only. In the present section, the acoustic radiation of the prototype with the optimal parameters found in the previous section is computed, to demonstrate the relevance of the static study.

Electrical excitation signal

In the static analysis only a constant voltage u_0 was considered, whereas the signal to study dynamics is:

$$U(T) = \sqrt{U_0^2 + W_a(T)} , \quad (5.2)$$

which yields in non dimensional form:

$$u(t) = \sqrt{u_0^2 + w_a} , \quad (5.3)$$

where $w_a = \epsilon W_a / \mu \check{H}^2$. In order to study the maximal acoustic response, the maximal excitation is considered, for which $|w_a| = u_0^2$. The amplitude of the total excitation voltage must remain below the maximal voltage before breakdown $u_{0,\max}$ [see fig. 5.4c]. The maximal value of the static voltage is then:

$$u_0 = \frac{u_{0,\max}}{\sqrt{2}}. \quad (5.4)$$

The maximal acoustical response will therefore be computed in the following for $u_0^2 = u_{0,\max}^2/2$ and $|w_a| = u_{0,\max}^2/2$.

Influence of the cavity volume

The pressure radiated by the prototype, for the parameters used in fig. 5.3 is plotted in fig. 5.5 for two cavity volumes $v_{\text{cav}} = 5$ and $v_{\text{cav}} = 20$.

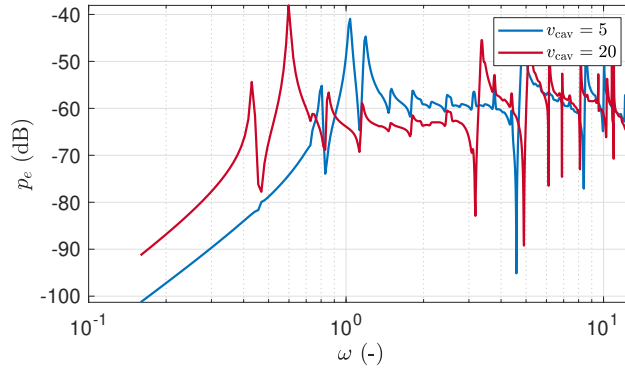


Fig. 5.5. Maximal radiated pressure on axis before breakdown at 1 m, for two different volumes of the cavity. The inflation pressure is $p_{\text{app}} = 0.9$.

Figure 5.5 shows that the volume cavity indeed has a large influence on the low frequency behavior of the loudspeaker. For frequencies below the first mode, where the response is stiffness-dominated, the prototype with the large cavity volume radiates about 10 dB louder, meaning its volume change during one oscillation period is $10 \text{ dB} = 3.2$ times larger. The maximum volume change with the large cavity is about 0.4 and 0.12 with the small cavity [see fig. 5.3], and $0.4/0.12 = 3.3$, so the static analysis directly reflects the low frequency behavior.

Influence of the inflation pressure

Once the cavity volume is fixed, the radiated pressure depends on the inflation pressure. A method was proposed in section 5.1.2 to choose the optimal inflation pressure in order to enhance the low frequency behavior. In fig. 5.6 for a cavity volume $v_{\text{cav}} = 20$, the acoustic response is plotted for two different pressures, at the maximum voltage before breakdown.

The membrane with the low inflation pressure appears to radiate the most at low frequencies. This is the result of the balance between two opposing phenomena. On the one

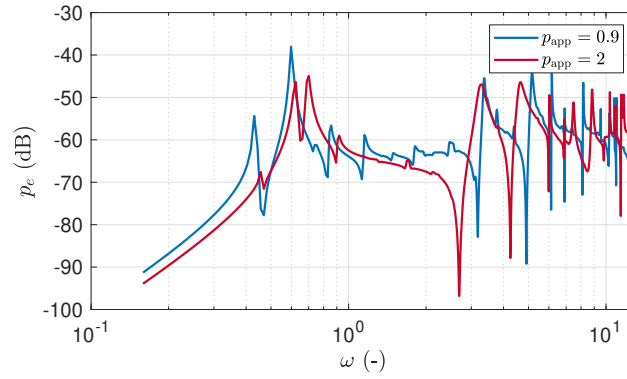


Fig. 5.6. Maximal radiated pressure on axis before breakdown at 1 m, for two inflation pressures. The cavity volume is $v_{\text{cav}} = 20$.

hand, the larger the inflation pressure, the larger the radiating surface of the membrane. Also, the larger the pressure, the thinner the membrane, so for a given voltage the electric field will be larger for large pressures, and the electrostatic excitation stronger. This should increase the radiation for the very inflated membrane ($p_{\text{app}} = 2$). On the other hand, for large inflation pressures, the maximum voltage that can be applied before breakdown is much lower as seen in fig. 5.2, and the membrane is stiffer so it deforms less. This appears to be the dominant effect here, and is directly related to the result that was found in section 5.1.2: the largest volume displacement before breakdown is obtained for $p_{\text{app}} = 0.9$.

5.1.4 Conclusion

The operation range of the dielectric membrane is limited by dielectric breakdown, which limits the maximal applicable voltage. The maximal voltage depends on the inflation pressure and on the cavity volume. Therefore, a deep understanding of the interplay of the inflation pressure, cavity volume, and dielectric breakdown is necessary to choose properly the value of these parameters for an optimal operation.

The static analysis of the inflation of a DE membrane provides guidelines to choose some of the main parameters of the loudspeaker to enhance the low frequency behavior. It has been verified on acoustic calculations that the conclusions drawn from the static analysis were valid to improve the low frequency behavior.

5.2 Optimization of the electrode shape

5.2.1 Introduction

The electrode shape is a parameter that can very easily be controlled, as the electrode is deposited on the membrane by pad-printing using a mask [see section 3.1.2].

The electrode shape has various effects: it locally adds mass and stiffens the membrane, and changes the excitation force. Indeed, the electrostatic pressure is applied only in areas where there is an electrode on both sides. As a consequence, changing the electrode shape is a way to control the modal forces, and therefore a way of controlling the frequency response, by exciting more or less the different modes.

The general idea in this section is to use numerical optimization procedures to find the optimal electrode shape to improve certain characteristics of the loudspeaker, like for example the frequency response, or the directivity.

Vibroacoustic optimization has been investigated mainly for sound reduction purposes, like for example by Rattle & Berry [91], where point masses are added on a vibrating plate, and their position optimized to reduce the radiation. A genetic algorithm is used to solve the highly non-linear optimization problem.

Optimization of the modal distribution has also been investigated on Distributed Mode Loudspeakers [74], where the objective was to evenly spread the modes of a radiating panel in frequency, in order to obtain the flattest frequency response as possible. The modal distribution was modified by adding local masses to the surface of the radiator.

The modal forces can also be optimized, as carried out by Clarck & Fuller [18]. A baffled vibrating plate is equipped with a piezoelectric sensor and a piezoelectric actuator, which are used to implement an active control of the plate sound radiation. The shape and size of the piezoelectric sensor actuator placed on a vibrating plate are optimized, in order to improve the active noise control performances.

In the context of loudspeakers, optimization has been carried out for structures excited with piezoelectric patches in order to improve the frequency response of flat loudspeakers by Doaré *et al.* [23]. A non-linear optimization algorithm is used as the optimization problem has many local minima, but with only a small number of parameters to optimize.

5.2.2 Definition of the optimization problem

The studied device is the same as in the rest of the thesis, namely a DE membrane inflated over a closed cavity. In this section, the inflation pressure P_{app} is fixed, as well as the static voltage U_0 . The only optimized parameter is the electrode shape. As the model is axisymmetric [see chapter 2], the optimized electrode must be axisymmetric too. Therefore, the electrode will consist in several rings, whose radii are the optimized parameters. The electrode shape is shown in fig. 5.7.

The electrode radii in the reference configuration are denoted \bar{r}_i , \bar{r}_1 being the inner radius of the first ring. The radii may vary between the two neighboring radii:

$$\bar{r}_{i-1} \leq \bar{r}_i \leq \bar{r}_{i+1} . \quad (5.5)$$

This definition of the optimization parameters is quite unpractical, as it defines a bounded optimization problem, where the bounds for one parameter depends on the values of

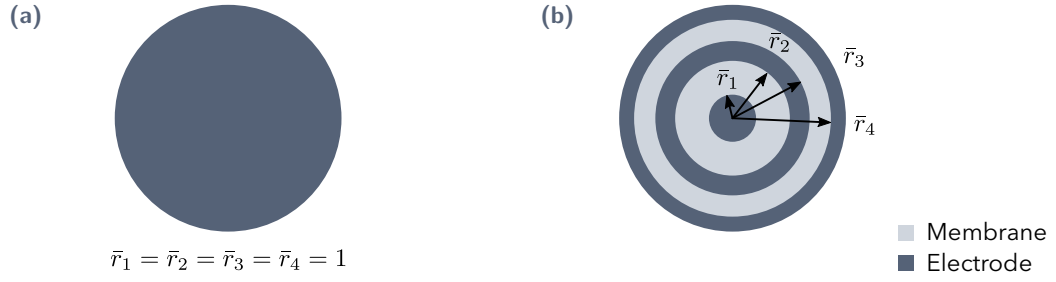


Fig. 5.7. (a) Initial electrode shape. (b) Optimal electrode shape, defined by the radii of the electrode in the **reference configuration** [see fig. 2.1].

the other parameters. In order to overcome this difficulty, relative radii are defined as:

$$\tilde{r}_i = \frac{\bar{r}_i}{\bar{r}_{i+1}}, \quad (5.6)$$

so all \tilde{r}_i vary between 0 and 1.

5.2.3 Objective functions

The objective (or cost) function is certainly the most important choice in the optimization procedure. Depending on the acoustic criteria that we want to improve, a scalar function should be build, that is minimal when the system behaves the best. In the present section the spectral balance (or flatness of the frequency response) will mainly be investigated. The ideal frequency response function that we wish to obtain is shown in fig. 5.8.

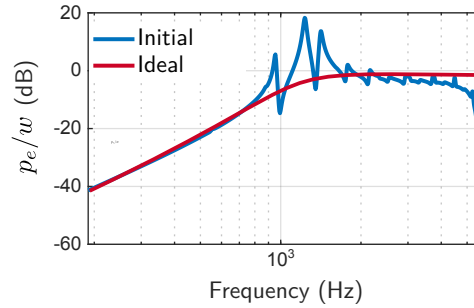


Fig. 5.8. Ideal frequency response that we wish to obtain, compared with the computed frequency response of the DE loudspeaker before optimization.

Maximisation of the contribution of one mode to the radiation

In standard electrodynamic loudspeakers, the acoustical response is dominated by the first mode of the speaker: the resonance of the moving mass (membrane and coil mainly) over the stiffness of the suspension. This mode occurs at frequencies which are much lower than the other modes, which arise due to the membrane dynamics. The contribution of the membrane modes to the radiation typically should be avoided, as it creates deviations from a flat frequency response.

In chapter 2, the pressure radiated by the membrane was expanded on a basis of coupled fluid-structure modes. The following expression was obtained for the non-dimensional radiated pressure [see eqs. (2.70) and (2.72a)]:

$$p_e = \sum_n \omega^2 \frac{F_n}{m_n(\omega_n^2 - \omega^2)} \Psi_{n,e}^R, \quad (5.7)$$

where it is recalled that F_n is the modal force, m_n the modal mass, and $\Psi_{n,e}^R$ the exterior acoustics part of mode n . The pressure at the resonance of mode n is thus proportional to :

$$p_e \sim \frac{F_n}{m_n} \Psi_{n,e}^R. \quad (5.8)$$

A cost function to improve the loudspeaker behavior by maximizing the contribution of mode k to the radiation would then be:

$$J_1 = \frac{\sum_{n \neq k} F_n \Psi_{n,e}^R / m_n}{F_k \Psi_{k,e}^R / m_k}. \quad (5.9)$$

A similar expression was used by Doaré *et al.* [23] who improved a flat loudspeaker by adding piezoelectric patches.

For standard loudspeakers, the first mode would be maximized, so $k = 1$. For the inflated DE membrane, the radiation is not dominated at all by the first mode, so maybe maximizing the radiation of another mode may be more useful. This will be investigated in the results section 5.2.5.

Minimizing the sound pressure level standard deviation

As the frequency response of the studied DE loudspeaker is very different from the frequency response of standard loudspeakers, the cost function J_1 defined in eq. (5.9) may not be the most appropriate. Another cost function will be tested, which is based on the standard deviation of the radiated sound pressure level. It has been used for Distributed Mode Loudspeakers to improve the frequency response [74].

The second cost-function is obtained by computing the standard deviation of the sound pressure level in a given frequency band, where we want to flatten the frequency response, and is thus defined as follows:

$$J_2 = \sqrt{\frac{\sum_n (\text{SPL}_n - \text{SPL}_0)^2}{N_f}}, \quad (5.10)$$

where N_f is the number of frequencies at which the sound pressure level is evaluated, SPL_n is the sound pressure level (in dB) at frequency ω_n , and SPL_0 the mean sound pressure level in the frequency range of interest.

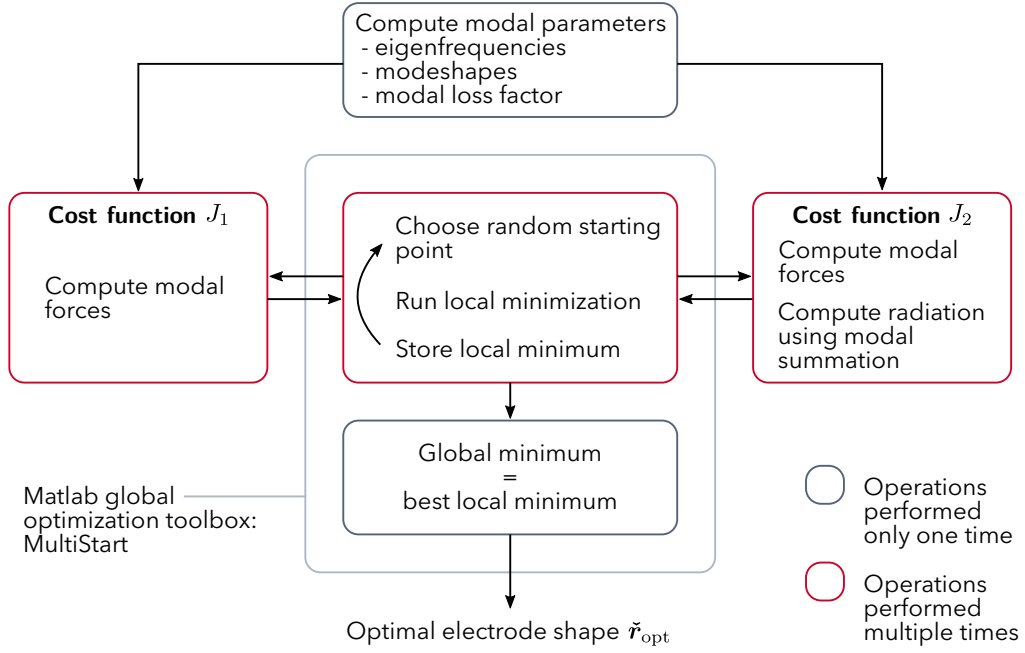


Fig. 5.9. Block diagram of the optimization procedure. Either the cost function J_1 is used, and then the left part of the diagram is followed, or J_2 is used, and the right part is followed.

5.2.4 Optimization procedure

The optimization procedure is summarized in fig. 5.9. The general idea of this procedure is that the time-consuming operations, namely computing the modal parameters (eigenfrequencies, eigenmodes and modal loss factor) should be performed only once. For this purpose, we assume that influence of the mass of the electrodes on the mode-shapes and eigenfrequencies can be neglected. As a result, the modal parameters do not change when the electrode shape is varied during the optimization process. The electrode shape only changes the modal forces, which can be computed very quickly using the following formula:

$$F_n = \int_0^1 \left(\bar{r} \frac{\Gamma}{h} \lambda_{20}^2 ((\Psi_{n,y}^L)' z_0' + (\Psi_{n,x}^L)' r_0') + \frac{\Gamma}{h} \lambda_{10}^2 \lambda_{20} \Psi_{n,x}^L \right) d\bar{r}, \quad (5.11)$$

which comes from eq. (2.71). The electrode shape is defined by the function Γ , which equals unity when an electrode is present, and zero otherwise. Calculating numerically this integral is performed by computing a single sum as all the terms are constant, and only the electrode shape needs to be re-evaluated at each iteration of the optimization.

The optimization is performed as follows:

1. Compute the modal parameters using the model of chapter 2.
2. Build a function that returns the cost as a function of the electrode radii.
3. Feed this function into a non-linear optimization routine, such as *MultiStart* in the Matlab Global Optimization Toolbox.

MultiStart is a routine that generates random starting points, and finds the local minima of the cost function by running a gradient descent algorithm from each starting point [see fig. 5.10]. The best local minimum is returned as an estimation of the global minimum. There is no evidence that the returned minimum is indeed the global minimum, but the more starting points are tested, the higher the chance that the global minimum is found. For the present study, finding the true global minimum may not be of primary importance, as a local minimum would already be an improvement of the frequency response compared to the initial geometry.

Still, for all the presented results, it has been checked that increasing the number of starting points did not change the outcome of *MultiStart*.

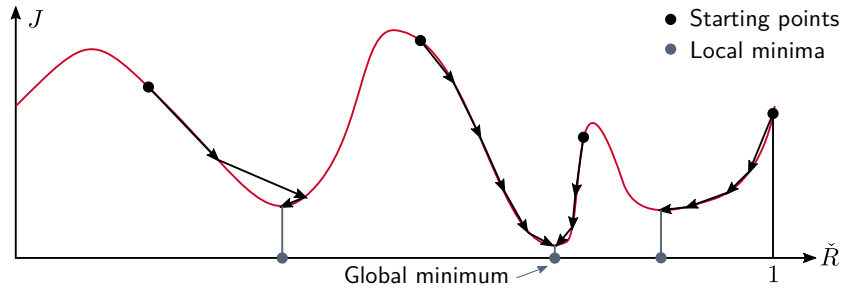


Fig. 5.10. Principle of the *MultiStart* algorithm, explained on a 1-parameter optimization problem.

5.2.5 Results

The following results are obtained for the parameters given in table 4.1 of the prototype that was measured in chapter 4. In all the following plots, the initial frequency response is obtained with an electrode occupying the whole membrane as shown in fig. 5.7a.

Optimization of the radiation of one mode

A first test is performed in which the radiation of the first mode is maximized compared to the other modes, and the results plotted in fig. 5.11. This would be the natural optimization if a standard loudspeaker is optimized.

This first test case [see fig. 5.11] shows that the optimization succeeds in modifying the frequency response in the desired way. Indeed, the radiation of the first mode is larger compared to the other modes after optimization. However, even though the optimization succeeded in minimizing the cost function, it appears that the optimal solution is not interesting from the acoustic point of view: the frequency response is not better after the optimization than before.

A second test is therefore performed, where the radiation of mode 5 is maximized, see fig. 5.12. Mode 5 is chosen because it dominates the frequency response.

Figure 5.12 shows again that the optimization procedure succeeds in maximizing the radiation of mode 5 compared to the others. Still, the optimized frequency response is not convincing in terms of spectral balance.

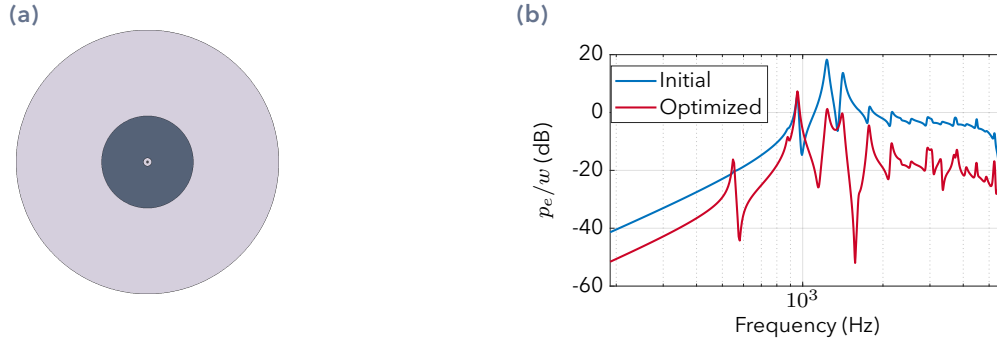


Fig. 5.11. Maximization of the radiation of mode 1. **(a)** Optimal electrode shape. **(b)** Pressure radiated on axis before and after optimization.

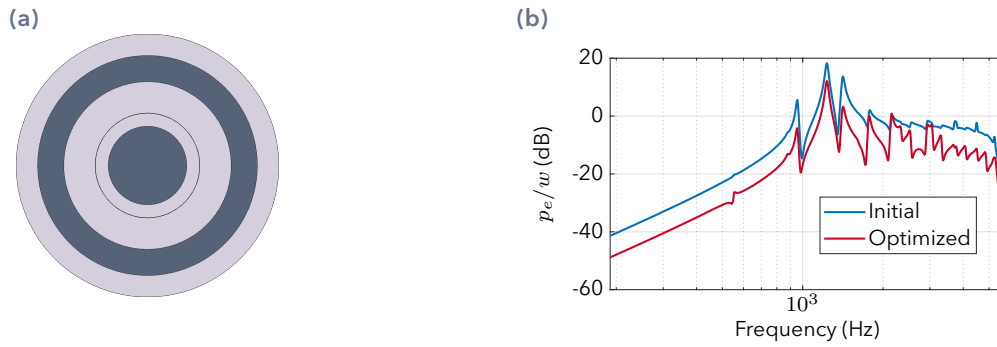


Fig. 5.12. Maximization of the radiation of the mode 5, which is the one that dominates the frequency response (at $f = 1230$ Hz). **(a)** Optimal electrode shape. **(b)** Pressure radiated on axis before and after optimization.

The problem with the optimization results shown in figs. 5.11 and 5.12 is that the frequency response of the DE loudspeaker is inherently multi-modal. Many modes contribute to the response, so trying to obtain a response dominated by a single mode is pointless. This means that the cost function J_1 which is used for figs. 5.11 and 5.12, is not adapted, and does not transcribe the desired frequency response correctly.

Optimization of the SPL standard deviation

Therefore, the second cost function J_2 is now used to try to improve the frequency response.

Two calculations are presented, one where the SPL deviation is minimized over a large frequency range [see fig. 5.13], and one where only the high-frequency range is optimized [see fig. 5.14].

When the large frequency range is optimized, it appears that the initial solution actually is the optimal solution, and that no improvement of the frequency response can be obtained by changing the shape of the electrodes. One possible explanation is that the frequency response is dominated by modes which have a relatively large number of

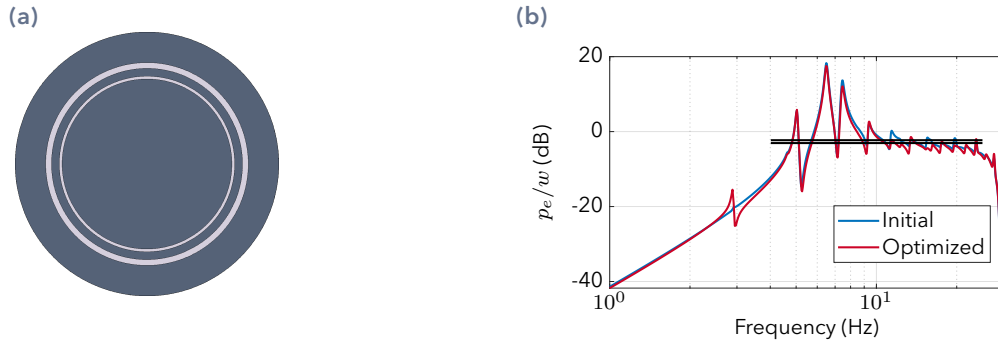


Fig. 5.13. Minimization of the SPL deviation between 760 Hz and 4740 Hz. **(a)** Optimal electrode shape. **(b)** Pressure radiated on axis before and after optimization. The black line is the mean value of the SPL in the optimized frequency range. Initial value of the cost function $J_2 = 18.6$, final value $J_2 = 18.0$.

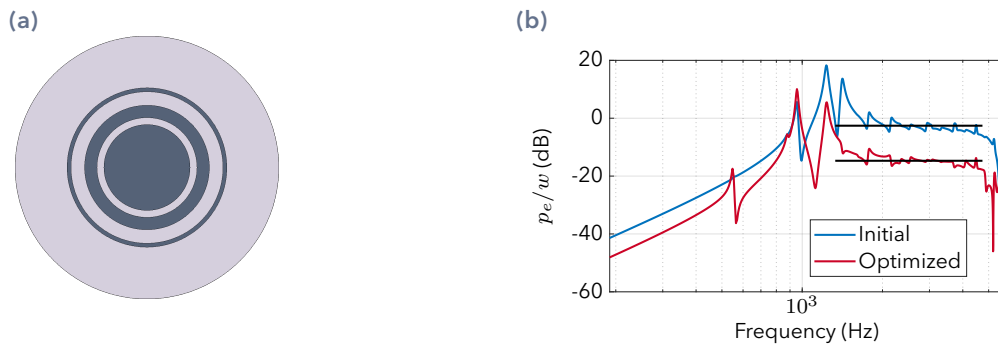


Fig. 5.14. Minimization of the SPL deviation between 1330 Hz and 4740 Hz. **(a)** Optimal electrode shape. **(b)** Pressure radiated on axis before and after optimization. The black line is the mean value of the SPL in the optimized frequency range. Initial value of the cost function $J_2 = 8.8$, final value $J_2 = 3.6$.

nodal lines. Controlling the modal force on these modes may therefore require very fine patterned electrodes, and 3 rings parametrized by 5 parameters may not be sufficient. Also, the modes 3, 4 and 5 which dominate the frequency response are hard to reduce in amplitude, because they correspond to a global resonance of the system (the resonance of the membrane mass over the stiffness cavity, see section 4.4). As a consequence, the membrane is easier to excite in this frequency range and naturally moves and thus radiates more. This global resonance can be decreased by increasing the cavity volume for example, as seen in section 4.4. A better option to reduce the amplitude of the modes 3, 4 and 5 would therefore be to damp this resonance, for example by adding porous material in the cavity. This option will be considered in section 5.3.

If the optimized frequency range does not contain the dominant modes, as in fig. 5.14, the results are slightly more convincing. The cost function decreases by a noticeable amount during the optimization (from 8.8 to 3.6), and the frequency response is flatter in the optimized frequency range. However, the spectral balance improvement must be balanced by the loss of amplitude. As the electrode surface is smaller, the electrostatic excitation is smaller, and the membrane radiates less. A loss of about 12 dB is observed,

which is quite important. The small gain in spectral balance may not be worth to loose 12 dB in amplitude.

This drawback could be taken into account in the optimization procedure, by adding a constraint on the electrode surface for example. This has been implemented and tested, but the results were not considered sufficiently convincing to be shown here.

5.2.6 Experimental investigation


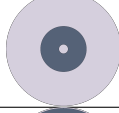
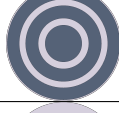

Description of the tested designs

Even though the optimization results presented in previous section 5.2.5 were not very convincing, the optimal geometries have been built and tested, in order to assess the global procedure consisting in adjusting the electrode shape to control the system's dynamics. This design method could have many other applications in other contexts than loudspeakers.

The practical electrode design, which connects the different rings to the power supply has been described in section 3.1.2, and an example of the electrode design shown in fig. 3.7.

The four tested electrodes are described in table 5.1. The first one (OP1) is obtained when the radiation of the third mode is maximized, with only one optimized electrode radius. The electrode is thus a disk. The second electrode is obtained when the radiation of modes 4 and 5 is minimized. The idea was to smoothen out the dominant peaks in the frequency response. Two radii are optimized. The third electrode is obtained when the SPL standard deviation is minimized in the frequency range 950-2800 Hz, and same for the fourth but in the frequency range 1200-2800 Hz.

Tab. 5.1. Definition of the experimentally tested electrode geometries.

Name	Label in fig. 5.15	Electrode	Optimization criteria
OP1	(a)		Maximization of mode 3
OP2	(b)		Minimize radiation of modes 4 and 5
OP3	(c)		Minimize SPL standard deviation in $F \in 950 - 2800$ Hz.
OP4	(d)		Minimize SPL standard deviation in $F \in 1200 - 2800$ Hz.

Results

The radiation on axis at one meter obtained with the electrodes described in table 5.1 is plotted in fig. 5.15.

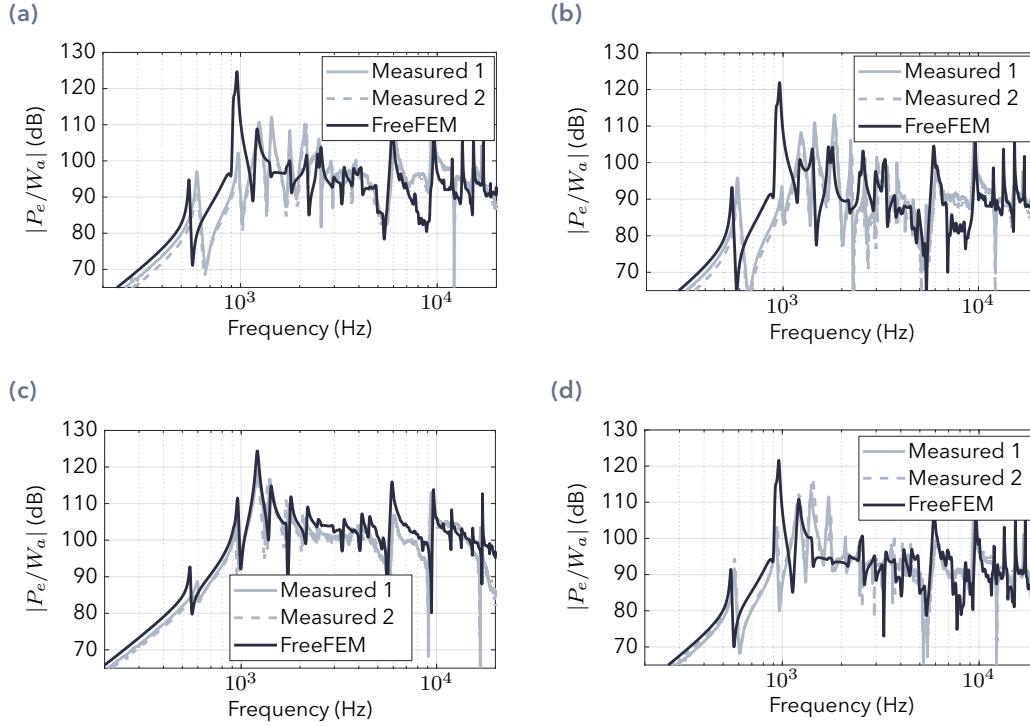


Fig. 5.15. Pressure radiated on axis, for different electrode patterns. For each electrode geometry, two membranes are measured, to demonstrate the measurement repeatability. **(a)** Electrode OP1. **(b)** Electrode OP2. **(c)** Electrode OP3. **(d)** Electrode OP4.

None of the tested designs is very convincing from the acoustical point of view, the frequency obtained with the optimized electrodes is not flatter than the initial frequency response. However, the effect of the electrode geometry on the frequency response was quite visible on these designs (at least on the numerical calculations), and corresponds well to the optimized criteria. This is the reason why these designs were tested, to investigate whether the frequency response could be designed in some extent by the shape of the electrodes.

For example, in the first optimization OP1, the radiation of mode 3 is maximized. This effect is very clear in fig. 5.15a on the numerical frequency response. Unfortunately, the maximization of mode 3 could not be observed experimentally.

Similar conclusions are drawn from fig. 5.15b, where the radiation of modes 4 and 5 is minimized. After the optimization, it is quite clear that these modes no longer dominate the frequency response in the calculation. Here again, this effect is not as clear on the measured frequency response.

The main limitation of the optimization of the electrode shape appears to be that the model no longer predicts correctly the system's dynamics and acoustic radiation when the electrode occupies only a portion of the membrane area. Indeed, there is a larger discrepancy between the measurements and the calculations for the plots of fig. 5.15 than with full electrodes [see fig. 4.18]. The amplitude of the first modes is no longer correctly predicted with partial electrodes [see fig. 5.15], but the global level of the frequency response is on the other hand well captured. For example, with electrode OP3, the mean level between 1500 Hz and 5000 Hz is about 100 dB, and only 90 dB with electrode OP4. This effect is both measured and computed, and is directly related to the surface of active area of the electrodes.

Conclusion

In brief:

- The model predicts correctly the global influence of the electrode shape on the frequency response. The global level is correct.
- The model fails in predicting the change in amplitude of the first modes due to the electrode shape.
- The model can therefore not be used to optimize the electrode shape to improve the frequency response at low frequencies.

The error between the model and the measurements are not due to measurement errors, as two different membranes with the same electrode geometry are found to have exactly the same frequency response [see fig. 5.15].

One possible explanation is related to the effect of the electrodes on the membrane. Indeed, as the electrodes are made of carbon black embedded in a silicone matrix, they locally stiffen the membrane. What is more, the elastomer membrane relaxes when the electrodes are applied. These effects are hard to quantify and are therefore not taken into account in the model. Only the global effect of the electrodes on the membrane behavior is accounted for, in other words the shear modulus is considered uniform in the membrane. This may not be valid for patterned electrodes.

5.2.7 Conclusion

In this section the model built in chapter 2 has been used to run optimization algorithms, in order to find the optimal electrode shape for improving certain acoustic criteria.

Two criteria have been considered, either maximizing the radiation of one membrane mode compared to others, or minimizing the radiated sound pressure level standard deviation in a given frequency range. It has been shown that optimizing the electrode shape according to the second criteria could help improving a little the frequency response on axis.

However, no significant improvement could be obtained just by modifying the electrode shape. The main limitation is related to the high number of modes that contribute to the

radiation in the frequency range of interest, making it hard to control precisely the modal force on each mode with an electrode consisting of only three rings.

Finally, the optimal designs found by optimizing the model have been tested experimentally. It is observed that the electrode shape changes the measured frequency response, but the model fails in capturing accurately these changes. Therefore, before the optimization for improving the loudspeaker frequency response can be used in practice, the model needs to be refined even further to take into account the local relaxation and stiffening effect of the electrodes. This requires an extensive study of the change of the membrane hyper-elastic parameters when the electrode is applied, and is not addressed in this thesis.

5.3 Acoustic damping

In this section, another possible way of improving the behavior of the inflated DE loudspeaker is tested: the cavity is filled with porous material as shown in fig. 5.16, in order to damp out the acoustic modes which distort the frequency response at high frequencies [see fig. 4.17]. As the first membrane modes are coupled to the acoustic cavity, it is also expected that adding foam will increase the damping of these modes.

In the following, the influence of foam in the cavity is investigated both experimentally and numerically.



Fig. 5.16. DE loudspeaker cavity with foam, for damping both the membrane modes and the acoustic cavity modes.

5.3.1 Theory

In order to optimize the behavior of the loudspeaker with foam in the cavity, it is interesting to be able to model the influence of the foam.

Porous material model

The most simple porous material models are equivalent fluids, among which the Delany-Bazley-Miki model is the most widely used [80]. The porous material is assumed to behave as an acoustic fluid, but with complex and frequency dependent density and speed of sound, or equivalently with complex and frequency dependent wavenumber K_c and characteristic impedance Z_c . Fitting on experimental data provided the coefficients in the following expressions [80]:

$$Z_c = \rho_f C_f \left[1 + 5.50 \left(10^3 \frac{F}{\sigma} \right)^{-0.632} - 8.43 i \left(10^3 \frac{F}{\sigma} \right)^{-0.632} \right], \quad (5.12a)$$

$$K_c = \frac{\Omega}{C_f} \left[1 + 7.81 \left(10^3 \frac{F}{\sigma} \right)^{-0.618} - 11.41 i \left(10^3 \frac{F}{\sigma} \right)^{-0.618} \right], \quad (5.12b)$$

where σ denotes here the static air flow resistivity, and F the frequency. This model is considered valid for frequencies in $0.01 < F/\sigma < 1$ [80].

Non-dimensional complex impedance and wavenumber are then defined as:

$$z_c = \frac{Z_c}{\rho_f C_f}, \quad k_c = \frac{K_c}{\Omega/C_f}. \quad (5.13)$$

As the solving method described in section 2.6 requires that the mass and stiffness matrices of the coupled vibroacoustic system are frequency independent, the above expressions are modified by removing the frequency dependence. The frequency F in eq. (5.12) is replaced by a fixed arbitrarily chosen reference frequency $F_{\text{ref}} = 1000$ Hz. This modification of the expressions of the complex wavenumber and impedance will be validated by measurements in the following section.

Acoustic equations with equivalent fluid model

The acoustic equations (2.40) which have been given in section 2.5.2 are re-written with the complex impedance and wavenumber:

$$\frac{k_c}{z_c} \Omega^2 (P_a + P_u) + C_f^2 \nabla \cdot \left(\frac{1}{z_c k_c} \nabla P_a \right) = 0, \quad (5.14a)$$

$$\int_{\Omega_i} P_a R dS = 0, \quad (5.14b)$$

$$P_u \int_{\Omega_i} \frac{k_c}{z_c} R dS + C_f^2 \frac{\rho_f}{V_0} 2\pi \int_{\Sigma} \frac{1}{\lambda_{10}} (-Y'_0 \tilde{X} + X'_0 \tilde{Y}) X_0 dL = 0, \quad (5.14c)$$

where z_c and k_c should be seen as functions of the position: they are equal to 1 if no foam is present, and to the values given in eq. (5.13) where there is porous material.

These equations are implemented in the coupled vibroacoustic model, and solved by the same algorithm as before. The same modal approach is used to compute the radiated pressure.

5.3.2 Results

Measurement of the acoustic properties of the porous material

In order to identify the acoustic behavior of the chosen porous material (grey acoustic foam of unknown properties), a sample is placed in a Brüel & Kjaer Kundt tube, and its reflection coefficient is measured [see fig. 5.17]. The tube diameter is 29 mm, so only plane waves can propagate up to the cut-on frequency of higher order modes at 6400 Hz. All following measurements are therefore valid only up to this frequency.

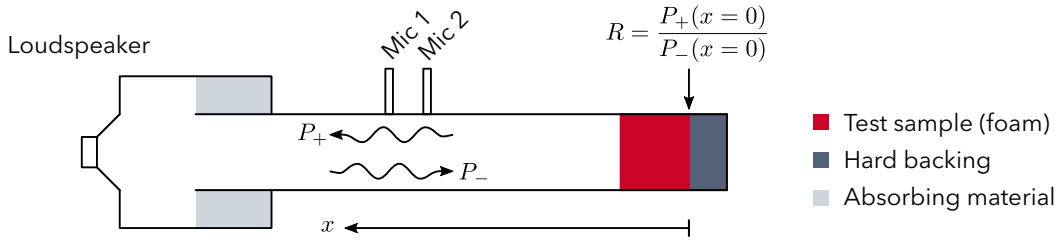


Fig. 5.17. Measurement of the reflection coefficient of a foam sample in a Kundt tube, in order to identify its flow resistivity σ .

The two-microphone method [8] is used to decompose the acoustic field in the tube into propagating waves, and the reflection coefficient of the foam on hard backing is obtained by computing their relative amplitudes.

The reflection coefficient is also computed analytically [3], and compared to the measurement in fig. 5.18.

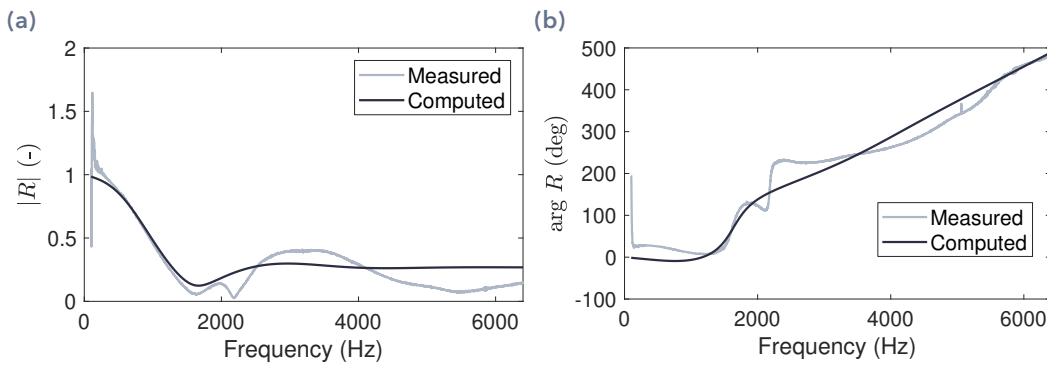


Fig. 5.18. Reflection coefficient of a 4 cm-thick sample of grey acoustic foam, measured in a Kundt tube, and computed analytically. **(a)** Amplitude, **(b)** Phase. The flow resistivity has been adjusted for the model to fit at best the measurement. The obtained value is $\sigma = 15 \times 10^3 \text{ Nsm}^{-4}$.

Figure 5.18 shows that the foam has absorbing properties, as the reflection coefficient is smaller than unity. The Delany-Bazley-Miki model modified to remove the frequency-dependence captures the global behavior of the reflection coefficient, both in amplitude and phase. There are oscillations in the measurements around 2000 Hz, which are not

observed in the computed reflection coefficient. This indicates small deviations of the behavior of the sample from the equivalent fluid model.

As the main goal here is to predict the global influence of the porous material on the radiated pressure, the accuracy observed in fig. 5.18 will be considered sufficient.

Influence of the porous material on the radiated acoustic pressure

The pressure radiated by the prototype is measured using the same protocol as for the previous measurements [see section 3.4.5], for two configurations:

- In configuration (a), the cavity is empty, as it was for all the measurements which have been shown up to this point.
- In configuration (b), the cavity is filled with acoustic foam, as shown in fig. 5.16.

The pressure radiated on axis is plotted in fig. 5.19 for the two configurations, together with the results of the model.

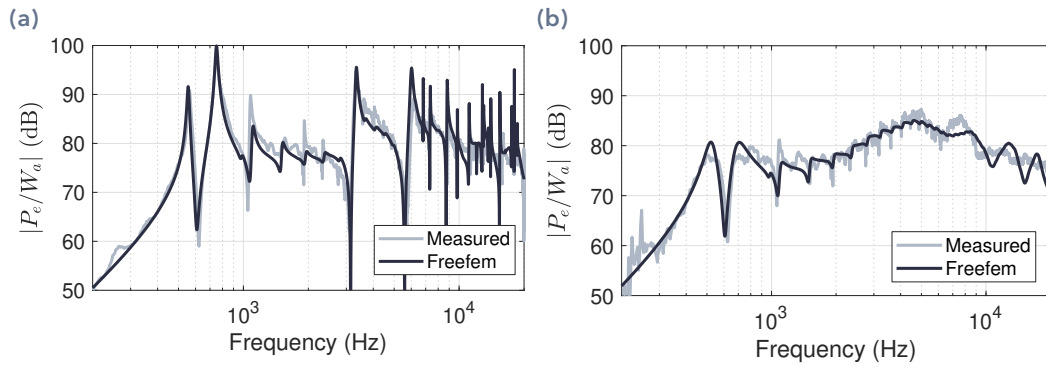


Fig. 5.19. Pressure radiated by the DE loudspeaker on axis at 14 cm, measured in the anechoic chamber at IMSIA, and computed using the model presented in chapter 2. (a) Empty cavity. (b) Cavity filled with 5 cm-thick foam.

Figure 5.19 shows that the porous material has a tremendous effect on the frequency response of the loudspeaker, both at low and high frequencies.

As expected, at high frequencies above 3 kHz, all acoustic cavity dominated modes are completely damped, and are no longer visible in the frequency response, which is rather flat between 2-10 kHz. The decrease of the amplitude above 10 kHz is due to electrical resistivity effects, as explained in section 2.4.

At low frequencies, the frequency response is dominated by *membrane modes* [see section 2.6.3 for the definition of *membrane modes*]. Comparing fig. 5.19a and fig. 5.19b reveals that even the first *membrane modes* have seen their modal loss factor increase when the porous material was added. This occurs because the *membrane modes* are strongly coupled with the acoustic cavity, as already observed in sections 4.5.1 and 4.5.2.

In the medium frequency range, where the frequency response is dominated by higher order *membrane modes*, between 800-3000 Hz, the acoustic behavior is less influenced

by the porous material. This happens because higher order *membrane modes* are less coupled to the cavity, so the acoustic damping has a smaller influence. It would be interesting to investigate complementary damping solutions in this frequency range, for example by damping directly the membrane, either by increasing the elastomer loss factor, or by adding some visco-elastic material. Adding porous material closer to the membrane could also increase the damping on the first modes.

The model captures correctly the influence of the porous material, especially below 6 kHz where it yields exactly the same level as the measurements. At higher frequencies, there is larger deviation from the measurements. Several reasons could explain this: errors in the identification of the flow resistivity, or deviations of the behavior of the foam from the equivalent fluid model. The Kundt tube which has been used to identify the porous material parameters is limited to 6 kHz, so we have no information on the behavior of the foam above that frequency, and it may thus deviate a lot from the equivalent fluid model.

5.3.3 Conclusion

To conclude, it appears that adding porous material in the cavity is an effective solution to flatten the frequency response of the DE loudspeaker, both in the low-frequency and high-frequency ranges.

A simple model based on equivalent fluids has been implemented to model the influence of the added porous material, and it captures accurately the influence of the foam on the radiated pressure.

Using this model, the acoustic and geometrical properties of the porous material could be optimized, in order to further improve the frequency response.

5.4 Control and filtering solutions

5.4.1 Introduction

In this section, signal processing solutions are investigated to improve the behavior of the loudspeaker, in terms of frequency response and directivity. The idea is to filter the audio signal before it is sent to the loudspeaker to compensate for the loudspeaker response. This problem is known in the audio-engineering world as equalization, and has been vastly studied for standard electrodynamic loudspeakers [64, 60]. From the signal processing point of view, it consists in a deconvolution: the audio signal is convolved by the speaker response, and we look for an inverse filter that deconvolves the speaker response, so that the pressure signal radiated by the speaker is identical to the original signal.

The most simple equalization problem is the on-axis equalization of a single loudspeaker, where a filter is designed to obtain a flat frequency response at a single position. This may overall reduce the sound quality because there is no control of what happens off axis

[60]. Therefore, the deconvolution problem should consider radiation at different angles in the definition of the optimal response. What is more, a sound reproduction system usually consists of several loudspeakers, and equalizing all the speakers together leads to more interesting results. The general equalization problem is therefore a multiple input multiple output problem. Tokuno *et al.* [110] proposed an Inverse Fourier transform method to compute the inverse filters for such a system, which is relatively simple and fast to implement.

In this section, the equalization method by Tokuno *et al.* [110] will be used to improve the response of the inflated DE loudspeaker with one and two electrodes, in terms of frequency response and directivity.

5.4.2 Description of the studied system

A modified prototype is considered, where two distinct electrodes can be excited by two different electrical signals. This enables a much larger freedom for control strategies, as two independent excitations can be used at the same time, in order to control the membrane dynamics. One electrode is a disk at the center of the membrane, and the second is an annulus around the first one. In order to allow electrical connections, the second electrode cannot be a full annulus, so the symmetry of the system is no longer exact. A picture of the manufactured membrane is shown in fig. 5.20, annotated to indicate the active areas and the connections.

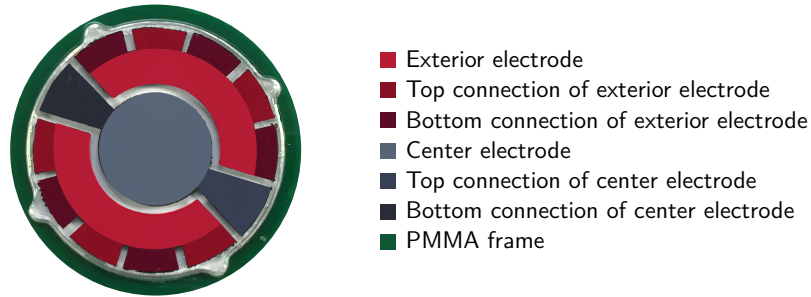


Fig. 5.20. Design of the electrodes and electrode connections for actuation with two different voltages. The active parts are denoted *Center electrode* and *Exterior electrode*.

5.4.3 Theory of the control strategy

In this section, the notations are adapted a little to be more consistent with signal processing conventions. The center electrode is referred to hereafter as electrode 1, and electrode 2 denotes the exterior electrode. They are excited with the following electrical signals:

$$U_1(T) = \sqrt{U_0^2 + W_1(T)} , \quad U_2(T) = \sqrt{U_0^2 + W_2(T)} . \quad (5.15)$$

As explained in section 2.4.2, the excitation of the DE membrane will be proportional to W_1 and W_2 .

The notations for the different signals and filters used in this section are given in fig. 5.21.

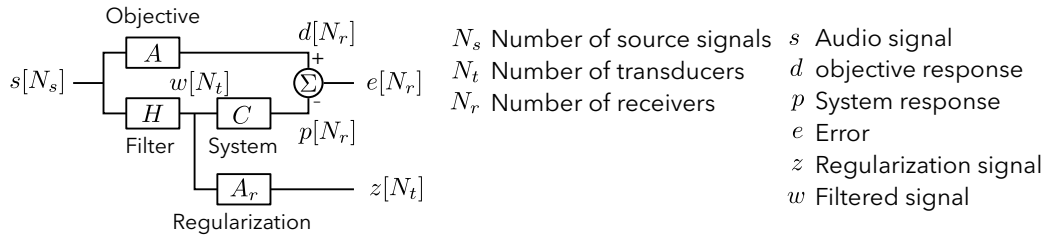


Fig. 5.21. Block-diagram of the system. The filters should be seen as matrices, and the signals as vectors. The size of each vector is written into brackets.

A vector of input signals (for example left and right channels) is fed into the system. The ideal response is defined by the matrix A , which gives the signal that is wanted at each receiver location. The input signal is first filtered by the filter H that we want to determine, and then by the system response C , which is known either from measurements or from the numerical model presented in chapter 2. An error is defined as the difference between the objective signal d and the system response p . The optimal H is obtained when the error e is minimal, in the least square sense. A regularization signal z is also defined, and will be used to improve the conditioning before the inverse filter is computed.

A cost function is defined as follows:

$$J = ee^* + \beta zz^*, \quad (5.16)$$

where the superscript $*$ denotes the hermitian transpose, and β is a regularization scalar parameter that will be adjusted.

Substituting e by $e = Aw - Cp$ in eq. (5.16), and minimizing the error in terms of w yields the optimal w_0 :

$$w_0 = (CC^* + \beta A_r A_r^*)^{-1} C^* A s. \quad (5.17)$$

Inserting the relation between s and w finally yields [110]:

$$H_0 = (CC^* + \beta A_r A_r^*)^{-1} C^* A, \quad (5.18)$$

where H_0 is the optimal inverse filter.

The most simple regularization is to take A_r equal to the identity matrix.

The method to obtain the optimal inverse filter is summarized as follows:

1. Compute $C(\omega)$ by taking the Fourier transform of the system impulse response.
2. Compute $H_0(\omega)$ using eq. (5.18).
3. Compute h_0 the impulse response of the filter by taking the inverse Fourier Transform of H_0 .
4. Perform a cyclic shift of the obtained impulse response by half of its length, to create a modelling delay [110].

The objective matrix A will depend on the desired response of the system, and several options will be studied in the following section.

5.4.4 Results

Equalization of a single channel loudspeaker

First, in order to validate the method on a simple test case, a single channel loudspeaker is considered. The number of input signals is therefore equal to $N_s = 1$. To simplify even further this preliminary test, the number of receivers is also set to $N_r = 1$, and only the acoustic pressure on axis is considered. The objective function is defined as follows:

$$A(\omega) = \begin{cases} 1 & \text{for } \omega \in [\omega_{\min}, \omega_{\max}] , \\ \varepsilon & \text{otherwise} , \end{cases} \quad (5.19)$$

where ε is a small parameter that can be adjusted. In the following, we use $\varepsilon = 1 \times 10^{-6}$. The frequency range in which the loudspeaker response is equalized is $[\omega_{\min}, \omega_{\max}]$. In this study we take $f_{\min} = 100 \text{ Hz}$, and $f_{\max} = 10\,000 \text{ Hz}$.

The impulse response is obtained from the computed frequency response function of the loudspeakers studied in chapter 4, with electrodes occupying the whole surface. The membrane is inflated to 1000 Pa, and the applied static voltage is $u_0 = 1000 \text{ V}$. The frequency response and the impulse response are plotted in fig. 5.22.

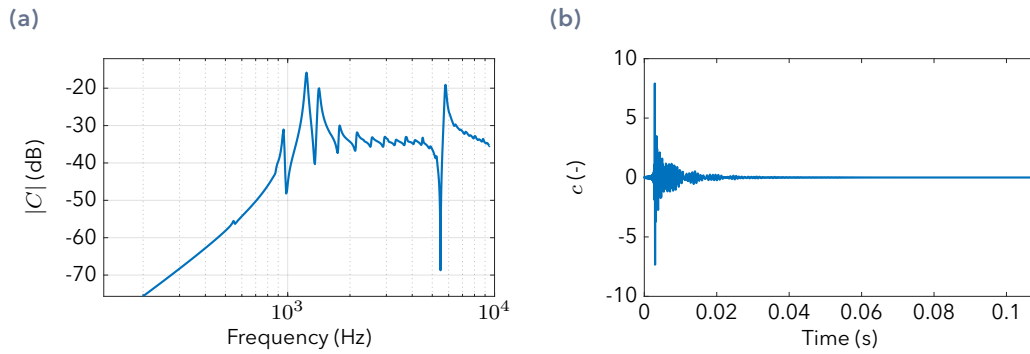


Fig. 5.22. (a) Frequency response and (b) impulse response of the studied prototype. This response is the ratio between the radiated pressure on axis at 1 m and the excitation signal s . The amplitude is non-dimensional here.

The frequency response of the loudspeaker exhibits many peaks and drops due to the membrane modes, and here we will try to flatten the frequency response using the equalization method by Tokuno et al.

Numerical validation To validate the method, and understand the influence of the regularization, the optimal inverse filter is tested on a trial signal: a pink noise s is generated,

filtered first by the filter H and then by the system response C to obtain p , as described in the block diagram in fig. 5.21. The transfer function between the obtained signal and the initial signal is then computed and plotted in fig. 5.23.

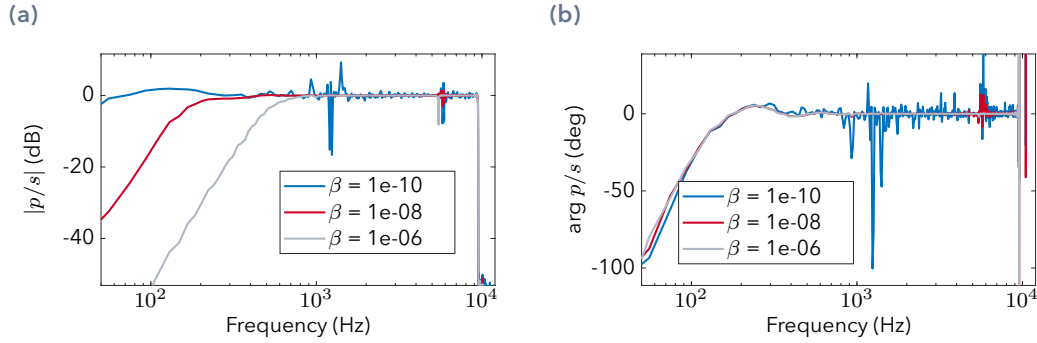


Fig. 5.23. Transfer function between the excitation signal s and the output signal of the system p with equalization, for three values of the regularization parameter β . **(a)** Amplitude. **(b)** Phase corrected by the modelling delay.

Figure 5.23 shows that a flat frequency response can be obtained by equalization if the regularization parameter is correctly chosen. For a too small β , the obtained response exhibits many drops and peaks that deviate from the flat response. For a too large β , the filter deviates from the ideal inverse filter (here at low frequencies), and the desired inversion is not observed any longer. The parameter β limits the power of the filter, which is why at low frequencies the response with the large β deviates from the flat response, as not enough power is added at low frequencies. For the optimal β , here around $\beta \approx 1 \times 10^{-8}$, both a flat frequency response and good low frequency behavior are obtained.

Experimental validation The control strategy is now tested experimentally on the prototype filled with porous material [see section 5.3]: a first measurement is carried out to obtain the transfer function between the excitation s and the pressure radiated on axis at 1 m P_e . The inverse filter is then computed using the method by Tokuno *et al.*, as explained above. Finally, the excitation signal is filtered by the inverse filter and sent to the loudspeaker. The transfer function between the original signal and the radiated pressure is computed, and plotted in fig. 5.24, together with the transfer function without filtering.

Figure 5.24 shows that the proposed inverse filtering method succeeds in flattening the frequency response of the DE loudspeaker over a large frequency range 400-15 000 Hz. Small oscillations remain, especially around 2 kHz where the original frequency response has a very sharp peak. This could be due to a slight evolution of the system between the moment when its transfer function was measured, and the moment when the measurement with the inverse filter was performed. To get rid of such troubles, adaptive filtering algorithms which track the system eigenfrequencies would be helpful.

Of course, there is a tradeoff between the quality of the frequency response and the radiated level: for a maximum excitation amplitude (to avoid dielectric breakdown), the

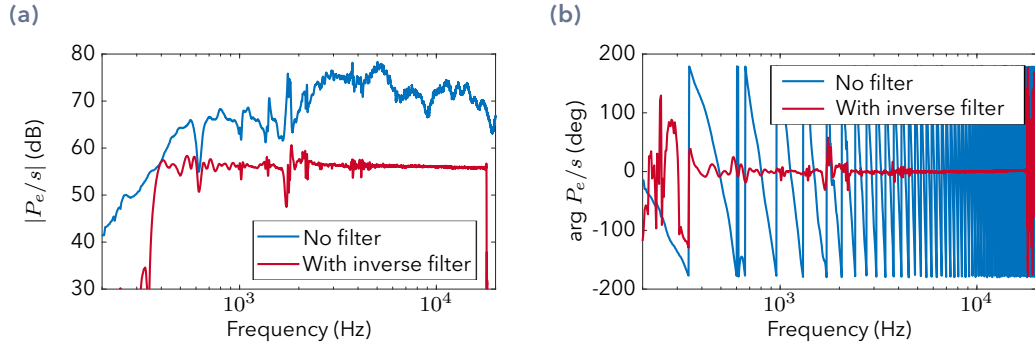


Fig. 5.24. Measured transfer function between the excitation signal s and the radiated pressure P_e [see fig. 2.1 for the definitions], with and without inverse filtering based on the measured frequency response. **(a)** Amplitude, **(b)** Phase.

filtered response will be lower in amplitude, as the maximum voltage will be determined by low frequencies where the original frequency response is small.

The same procedure can be followed, but using the response computed in FreeFEM instead of the measured response to compute the inverse filter. This is particularly interesting, as it opens adaptive control possibilities: the model can be run in real time to follow the evolution of the system, in order to adapt the filter. Only a preliminary test is shown here on the prototype without porous material: the model is used to compute the acoustic response of the prototype in given conditions, and the inverse filter is computed from the numerical results. It is then applied to the signal before it is sent to the speaker, and the frequency response is measured again. The results are shown in fig. 5.25.

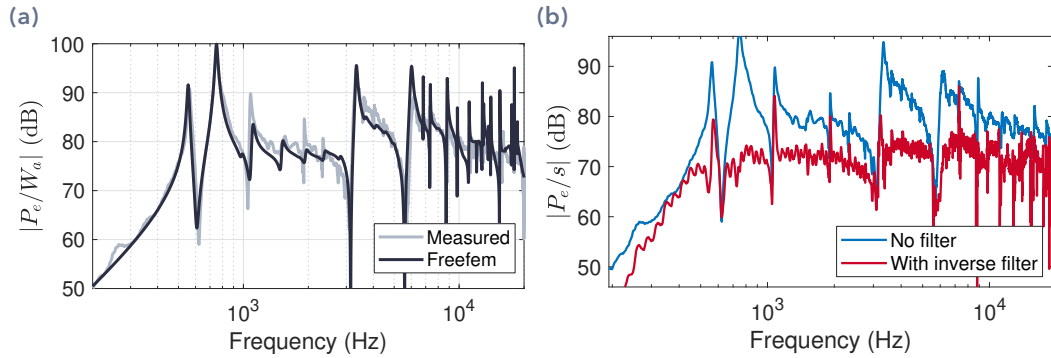


Fig. 5.25. **(a)** Pressure radiated on axis of a DE inflated loudspeaker, measured and computed. **(b)** Measured pressure radiated on axis of the same DE loudspeaker, when the signal is filtered by an inverse filter obtained from the response calculated in FreeFEM shown in **(a)**.

Figure 5.25 shows that the filter computed from FreeFEM succeeds in improving a little the frequency response, but large peaks remain at the system's eigenfrequencies. This is related to a small mismatch between the measured and computed eigenfrequencies, which for sharp resonances yields a large error between the model and the mea-

surements at a given frequency. Tuning the model with the measured eigenfrequencies would therefore be of primary interest. Ideas on self-sensing methods to measure the dominant eigenfrequencies will be discussed in chapter 6.

Equalization for several receiver locations As explained in [60], equalizing a loudspeaker only for the on-axis response may create problem for the off-axis response. Therefore, the method of Takuno *et al.* is now applied for several receivers (using the numerical results), located on a circle of radius 1 m around the loudspeaker. Five positions are considered, and the objective function for each of them is the same as for only one receiver: flat response in the frequency range 100-10 000 Hz [see eq. (5.19)]. The results are plotted in fig. 5.26.

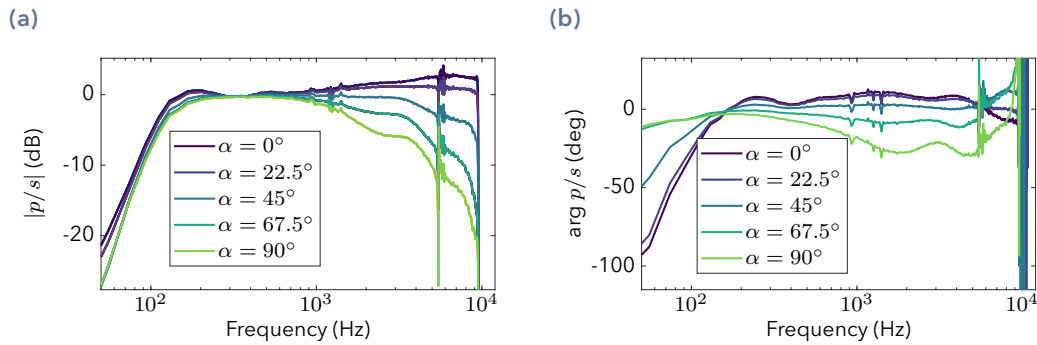


Fig. 5.26. Transfer function between the excitation signal s , and the output signal of the system P with equalization for several receiver locations, located on a circle of radius 1 m around the loudspeaker. The regularization parameter is set to $\beta = 1 \times 10^{-8}$. **(a)** Amplitude. **(b)** Phase.

Figure 5.26 shows that the equalization procedure is still useful for improving the frequency response of the loudspeaker even for several receiver locations. However, a perfectly flat frequency response can no longer be obtained, as the equalization is now a compromise between the different locations. Also, at high frequencies, the radiated pressure is larger on axis than off axis, and this is due to the inherent directivity of the loudspeaker. The equalization does not change the directivity, so the directivity pattern remains the same.

In order to improve the directivity of the loudspeaker, two different excitation channels can be used. Each of them has its own directivity pattern, and by combining them a desired directivity pattern can be approached. This is studied in the following section.

Equalization of a dual-channel loudspeaker

The loudspeaker with two channels (two electrodes) described in fig. 5.20 is now studied, for improvements of the frequency response using the method of Tokuno *et al.* [110].

The loudspeaker response to the excitation with each electrode is computed using the method of chapter 2. As the system is assumed to be linear, the response of the system

to a combined excitation by the two electrodes will be the sum of the system response to each excitation. Therefore, this system can be described by the block-diagram of fig. 5.21, where there is one source signal ($N_s = 1$), two transducers ($N_s = 2$), and as many receivers as desired. In the following the receivers will be distributed on a circle of radius 1 m around the loudspeaker [see fig. 5.27]. For each receiver, an objective frequency response is defined. Typically, a flat frequency response in a given frequency range is searched for, as defined by eq. (5.19). However, this objective function may vary for each receiver, for example, an objective could be to radiate only around the axis, and not on the sides. The objective function would then be set to zero for the receivers on the side, as represented in fig. 5.27.

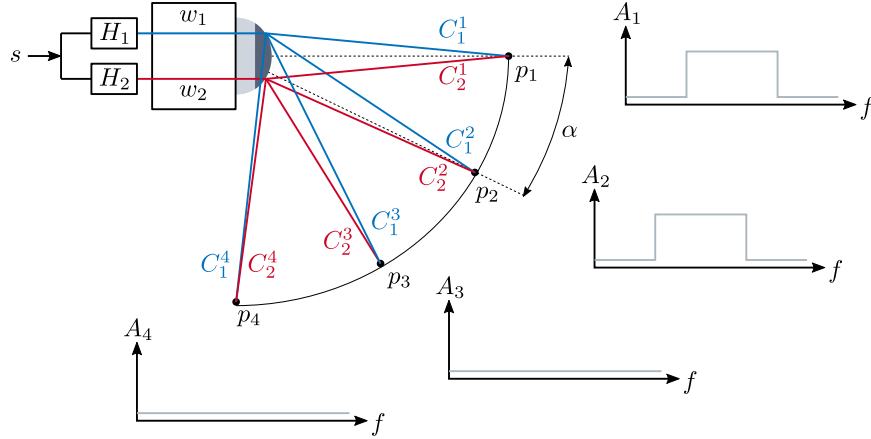


Fig. 5.27. Block-diagram of the loudspeaker with two electrodes, and definition of the objective response A . The transfer functions between the two excitation channels and the different microphone positions are denoted C_i^j .

A first equalization is performed, where a flat frequency-response in the range 100-10 000 Hz with omnidirectional radiation is searched for. This is obtained by setting all the objective functions A_i in fig. 5.27 equal to A defined in eq. (5.19). The transfer function between the source signal s and the pressure received by the different microphones is plotted in fig. 5.28 for the optimal filters H_1 and H_2 .

Figure 5.28 should be compared with fig. 5.26, indeed the equalization objective is the same for both results, but fig. 5.26 is obtained for a single excitation, and fig. 5.28 for two excitations. With only one excitation it was not possible to control the directivity, so a flat frequency response could only be obtained on axis. With two excitations, the relative level and phase between the two can be used to control the directivity. This is what is observed in fig. 5.28, where all the microphones have almost the same frequency response. Even at high frequencies, the deviation between the receivers is smaller than 5 dB, when 20 dB where observed with one excitation.

The equalization procedure can also be used to force a certain directivity pattern. For example, the radiation close the loudspeaker axis could be maximized compared to the off-axis radiation. The interesting thing here is that the directivity can be modified only by signal processing, it can be adjusted instantly depending on which radiation pattern is wanted. In fig. 5.29, the objective function is set to unity for the angles $\alpha < 45^\circ$, and zero for angles $\alpha > 45^\circ$.

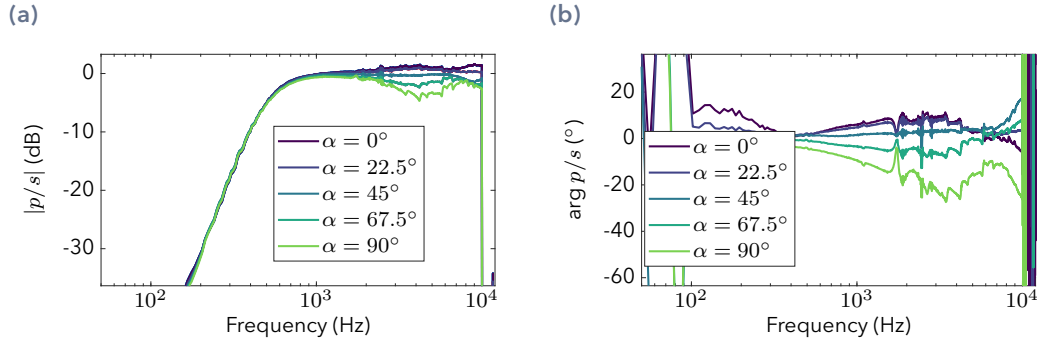


Fig. 5.28. Transfer function between the excitation signal s , and the pressure radiated at the different receiver locations p with equalization aiming at flat frequency response and omnidirectional radiation. The regularization parameter is set to $\beta = 1 \times 10^{-7}$. (a) Amplitude. (b) Phase.

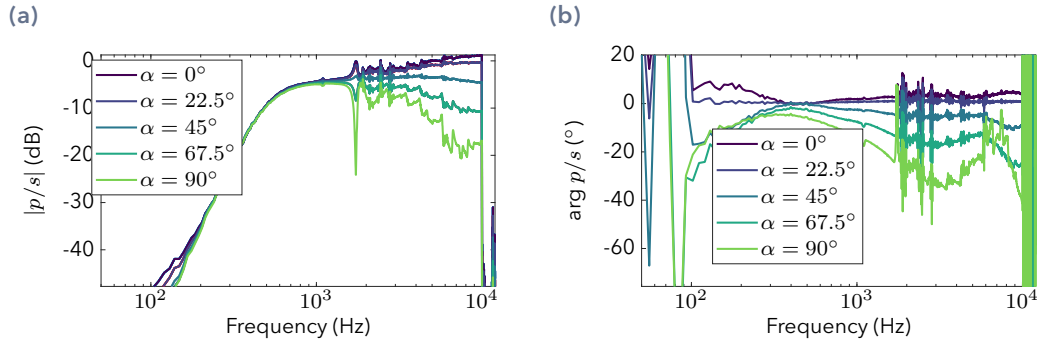


Fig. 5.29. Transfer function between the excitation signal s , and the pressure radiated at the different microphone locations p_i with equalization aiming at flat frequency response and radiation only for $\alpha < 45^\circ$. The regularization parameter is set to $\beta = 1 \times 10^{-7}$. (a) Amplitude. (b) Phase.

Figure 5.29 shows that the directivity can be controlled using the equalization procedure of Tokuno *et al.*. Indeed, above 1 kHz, a 20 dB difference is observed between the receivers with $\alpha < 45^\circ$ and those with $\alpha > 45^\circ$. Below 1 kHz, the loudspeaker is acoustically compact, so the radiation is omnidirectional, and cannot be changed. Also, it is interesting to note that the frequency response deviates more from the desired flat frequency response than in fig. 5.28 where an omnidirectional response is wanted. This is certainly due to the definition of the objective functions A , where for now the ideal off axis response is just null. Defining more clever objective functions might help improving the flatness of the frequency response, even off-axis.

The frequency response of the equalization filters for the omnidirectional [see fig. 5.28] and on-axis [see fig. 5.29] equalizations are plotted in fig. 5.30.

Figure 5.30 shows that it is really the interplay of the two channels that makes it possible to control the directivity. Indeed, the amplitudes of the two filters are in the same order

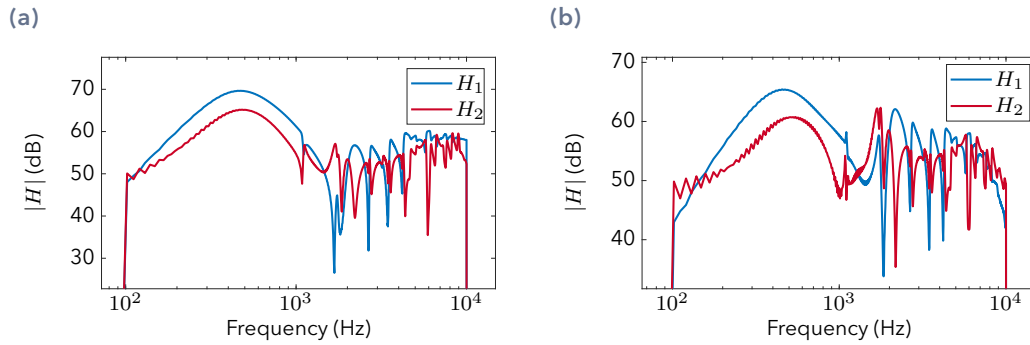


Fig. 5.30. Amplitude of the equalization filters for the two investigated cases. **(a)** omni-directional radiation [see fig. 5.28]. **(b)** On-axis radiation [see fig. 5.29].

of magnitude over the whole frequency range, meaning that both channels contribute to the total radiated pressure.

5.4.5 Conclusion

A method to improve the frequency response of the DE, based on digital signal processing and inverse filters has been proposed, and tested numerically on the results of the model presented in chapter 2. This method succeeds in flattening the frequency response over a large frequency-range, and if two different excitations are available, the directivity of the loudspeaker can also be controlled.

Moreover, the inverse filter can be computed from the results of the model, which opens adaptive control possibilities.

This method has some major limitations:

- The generated filters are quite long (2048 taps in the present study), and introduce a delay of about 50 ms. In some situations this is not acceptable, as the maximum audio/video delay should remain below 45 ms for television applications, and 20 ms for cinema [21]. Shorter filters can be used in order to reduce the modelling delay, at a cost of a decrease in performance.
- The filters are computed from the system frequency response (or impulse response). Therefore, the frequency response must either be measured, or computed using a numerical model. Using the numerical model to compute the inverse filter is quite delicate, as a perfect match between the model and the real prototype is needed. Indeed, a small error in the eigenfrequencies for example leads to large amplitude errors in the inverse filter at a given frequency.
- The system may evolve in time, at a timescale much larger than the audio-frequencies. This evolution could be due to visco-elastic relaxation, leakages in the cavity which would change the inflation pressure, softening of the membrane

due to heat created by the Joule effect in the electrodes, etc. The frequency response of the system could therefore change, and the filters would need to be re-computed regularly.

One interesting solution to cope with the evolution of the system problem would be to implement adaptive filters, whose parameters are adapted in order to follow the system evolution. This requires live knowledge of the system state, so either external sensors have to be used, or self-sensing possibilities offered by DEs can be used [98]. For example, the impedance can be measured during operation, and in chapter 6 we will show that the impedance contains information on the dominant eigenfrequencies. The inverse filter could then be adjusted to follow the evolution of the system eigenfrequencies.

5.5 Conclusion

In this chapter four options to improve the acoustical behavior of DE loudspeakers have been investigated:

- Choosing the right inflation pressure helps enhancing the low frequency radiation.
- Patterning the electrode to tune the modal forces may help improving the frequency response.
- Adding porous material in the cavity damps out acoustic cavity modes, but also increases the damping on coupled modes dominated by membrane vibrations, and yields a flatter frequency response.
- Finally, digital signal processing can be used to flatten the frequency response, and to control the directivity of the loudspeaker, especially if several electrodes can be excited independently.

Resistive effects

In this chapter the effects of electrode resistivity are investigated in greater details than in chapter 2.

It is found that for large resistivity the voltage is not uniform on the electrodes at high frequencies, and that the voltage distribution is coupled to the membrane vibrations. A model to describe this phenomenon is derived, and compared to experiments.

Possible applications of the coupling between the voltage distribution and the membrane vibrations are then discussed, in particular for self-sensing.

6.1 Literature review

When DEs are operated in high frequency applications (several kHz) such as loudspeakers [45, 51, 31], the resistivity of the electrodes starts to play a significant role. It decreases the actual actuation voltage, which gets lower than the voltage supplied by the high voltage source.

Different approaches have been used to model this effect, using either lumped models or more realistic distributed models, depending on the desired accuracy and on the system parameters.

6.1.1 Lumped models

The most simple model for the resistive effects is a lumped model, in which the electrical behavior of the whole membrane is modelled as a resistor in series with a capacitor [105, 37]. The equivalent resistor-capacitor RC circuit is characterized by its time constant $\tau_e = RC$ or its characteristic frequency $\Omega_{RC} = 1/RC$. For frequencies $\Omega > \Omega_{RC}$, the effective voltage which actuates the transducer is smaller than the supplied voltage, leading to a decrease in performance.

The lumped model has been extensively used to study self-sensing applications for one-degree-of-freedom systems [61, 98, 53]. The deformation of the actuator can be monitored during actuation without any added sensor: its deformation can be estimated from measurements of the supplied voltage and current. Self-sensing leads to huge improvement of the performance of DE actuators, as they can be operated in closed loop to compensate for their limitations, such as visco-elastic creep [98].

Most self-sensing methods are based on measurements of the capacitance, which is inversely proportional to the actuator area. The capacitance is either measured by superimposing a high frequency signal to the actuation voltage [56, 53, 98], or the actuation

signal can be directly used for sensing [36]. Other self-sensing methods based on measurements of the resistance of the DE have also been proposed, but appear to be less accurate [83].

Most of the time the influence of the mechanics on the electrical dynamics is neglected. It is assumed that the mechanical displacement occurs at time scales which are much larger than the electrical dynamics (at frequencies $\Omega \ll \Omega_{RC}$). Therefore, the electrical response can be computed assuming that the resistivity and the capacitance are constant.

One of the first study to take into account the strong influence of the mechanical dynamics on the electrical dynamics is the article by Rizzello *et al.* [93]. A one degree of freedom DE oscillator is investigated carefully, by taking into account among other phenomena the influence of the vibrations on the electrical dynamics, which is introduced by the dependence of the capacitance and resistance on the actuator position. This study is performed in the time domain, in order to compute all the non-linear effects, coming from the material behavior, the geometry or the visco-elasticity. Rizzello *et al.* show that the electrical dynamics do influence the mechanical displacement at high frequencies. This fully coupled model is then used for self-sensing control of a 1-DOF DE oscillator [94].

Another study which takes into account the couplings between the electrical and mechanical dynamics is the article by Hoffstadt and Maas [48], where a stacked dielectric transducer is studied, and a control strategy based on a Kalman filter is set up.

6.1.2 Transmission line models

It has then been noticed that at higher frequencies, the lumped RC model does not describe correctly the electrical behavior of DEs, and transmission line models which account for the spacial variation of the voltage on the electrode have been proposed as a refinement [58, 39, 38]. These models are built by assembling unit circuit cells which are themselves built with lumped resistive and capacitive elements [see fig. 6.2].

The transmission line models have been used to study the voltage distribution on DE membranes for actuator applications [58, 39, 38], where the position of the electrode connections is optimized to improve the actuation at high frequencies. Transmission line models have also been used to investigate stacked DE transducers where the resistivity of the electrodes connections is large [49].

However, in the above-mentioned studies the influence of the membrane displacement on the electric field is not taken into account in the electrical model, in which the geometry is considered static.

In most DE applications, resistivity is considered as a drawback because it limits the frequency bandwidth of actuation and sensing. A huge research effort has been made to manufacture thinner and more conductive electrodes, and this for now remains a major limitation for downsizing DE actuators and sensors [99]. Developing actuation and sensing methods that work with more resistive electrodes is another path, as manufacturing thinner but more resistive electrodes is relatively easy.

Recently, Xu *et al.* [117, 118, 119] developed a method that builds on the voltage drop across a DE membrane caused by resistivity to sense capacitance changes at different locations, using a single pair of connections. High frequency signals are quickly attenuated in the DE, so they sense only areas close to the electrode connections. Low frequency signals ($\Omega \ll \Omega_{RC}$) propagate on the whole membrane, so they can sense deformations far away from the connections. A transmission line model is used to model the electric field propagation in the resistive DE.

6.1.3 Goal of the present work

On the one hand the effect of electrode resistivity on the voltage distribution in DEs has been largely studied using transmission line models, for applications as actuators or sensors, but without taking into account the influence of the membrane vibrations on the voltage distribution. On the other hand, the coupling between the mechanical vibrations and the electrical dynamics has been studied in depth in a single-degree-of-freedom device, using lumped electrical models.

Therefore the goal of the present work is to combine these two approaches, by studying the influence of the DE vibrations on the spatial distribution of the voltage, and analyse the influence of the coupling in both directions between electrodynamics and mechanical dynamics. These couplings are likely to occur in large devices operated at high frequencies, which is typically the case for DE loudspeakers. Potential outcomes of this study are extended self-sensing possibilities at high frequencies, and the opportunity to design control methods based on self-sensing for DE actuators operated at high frequencies. Also, it could refine the estimation of the electrostatic excitation in resistive systems.

In all the forgoing, *high frequencies* are defined as frequencies above the electrical cut-off frequency $\Omega > \Omega_{RC}$. Therefore, the present work would also be useful to investigate DE devices with less conductive electrodes at relatively low frequencies. This is also of general interest because less conductive electrodes generally means thinner and more compliant electrodes, which are easier to manufacture.

6.2 Theory

The present section is divided into four parts. After a description of the studied system in section 6.2.1, the equations governing the dynamic voltage distribution are obtained using the transmission line theory in section 6.2.2, which is the method that is used by most authors. In section 6.2.3, a similar set of equations is derived starting from Maxwell's equations. The differences between the two methods are finally commented on in section 6.2.4.

6.2.1 Description of the studied system

We consider a DE membrane on which an electrode is deposited on both sides, on the surface Σ . This setup is described in fig. 6.1. The voltage on the top and bottom electrodes are denoted U_1 and U_2 respectively. The top electrode is connected to the voltage supply on the contour Γ_1 where the voltage is fixed at U_a . The bottom electrode is connected to the ground on Γ_2 . On the rest of the border $\Gamma = \partial\Sigma$, no current is flowing out.

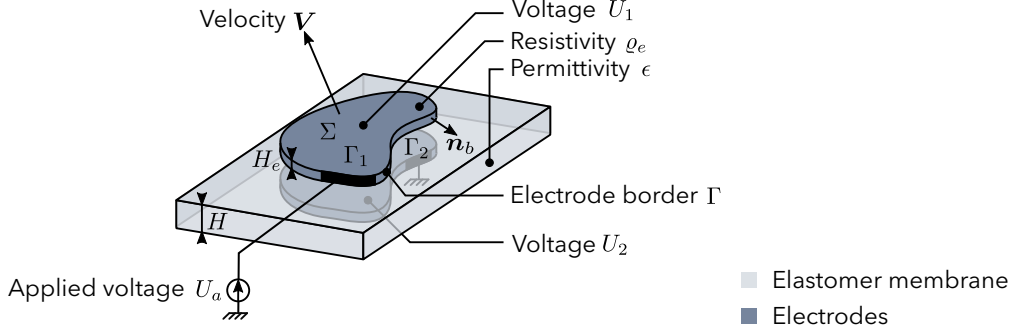


Fig. 6.1. Studied dielectric elastomer membrane, and definition of the variables.

6.2.2 Transmission line model

In section 6.2.2 only, small letters are used for the dimensional spatial coordinates x and y .

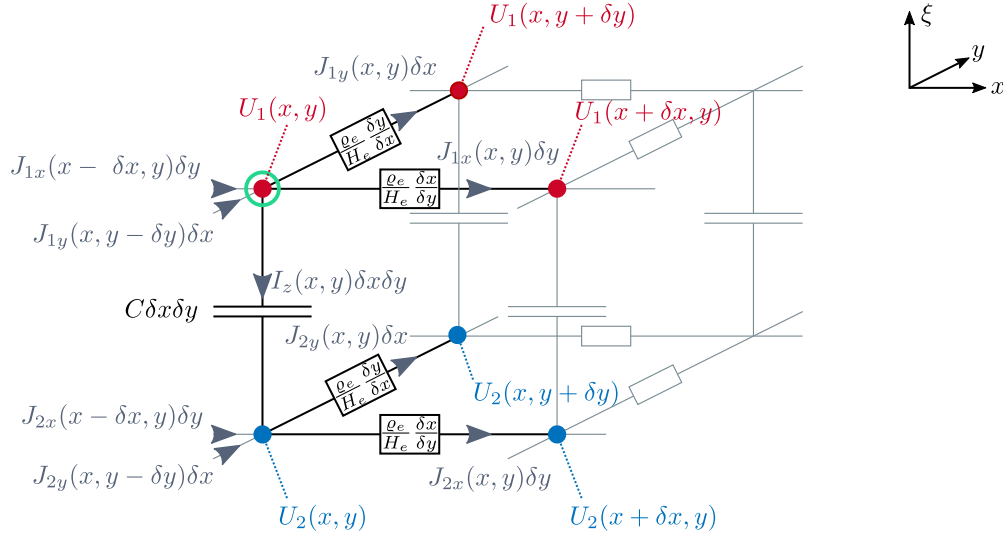


Fig. 6.2. Lumped model of the dielectric elastomer membrane. The black lines denote the considered unit cell, and grey lines correspond to the neighboring cells.

Transmission line theory is a intuitive way to derive the equations governing the charge and voltage distribution on a DE membrane [58]. It is here applied to the membrane

sketched in fig. 6.2. An element of the DE membrane is modelled as a capacitor, connected to resistors which stand for the electrode resistivity. The surface capacitance is denoted $C = \epsilon/H$ where ϵ is the membrane permittivity and H its thickness. The volume current density flowing from the top to the bottom electrode is I_z . The surface current densities on the top and bottom electrodes are \mathbf{J}_1 and \mathbf{J}_2 :

$$\mathbf{J}_1 = J_{1x}\mathbf{e}_x + J_{1y}\mathbf{e}_y, \quad \mathbf{J}_2 = J_{2x}\mathbf{e}_x + J_{2y}\mathbf{e}_y. \quad (6.1)$$

The current balance at the node marked by a green circle in fig. 6.2 reads:

$$I_z(x, y)\delta x\delta y = J_{1x}(x - \delta x, y)\delta y - J_{1x}(x, y)\delta y + J_{1y}(x, y - \delta y)\delta x - J_{1y}(x, y)\delta x. \quad (6.2)$$

Making δx and δy tend towards 0 and considering similarly the bottom electrode yields:

$$I_z = -\nabla_s \cdot \mathbf{J}_1, \quad I_z = \nabla_s \cdot \mathbf{J}_2, \quad (6.3)$$

where ∇_s denotes the surface del operator:

$$\nabla_s = \frac{\partial}{\partial x}\mathbf{e}_x + \frac{\partial}{\partial y}\mathbf{e}_y. \quad (6.4)$$

The constitutive law of the capacitor reads:

$$I_z = \frac{\partial}{\partial T} [C(U_1 - U_2)]. \quad (6.5)$$

The last needed equations are provided by Ohm's law, which reads, in the x -direction on the top electrode:

$$U_1(x, y) = U_1(x + \delta x, y) + \frac{\rho_e}{H_e} \frac{\delta x}{\delta y} J_{1x} \delta y. \quad (6.6)$$

Making δx tend towards 0 yields $\partial U_1 / \partial x = -J_{1x} \rho_e / H_e$. Using the same method in the y -direction and considering similarly the bottom electrode, we obtain:

$$\mathbf{J}_1 = -\frac{H_e}{\rho_e} \nabla_s U_1, \quad \mathbf{J}_2 = -\frac{H_e}{\rho_e} \nabla_s U_2. \quad (6.7)$$

Substituting in the current balance (6.3) the expressions of the surface current densities \mathbf{J}_1 and \mathbf{J}_2 given by Ohm's law (6.7) and the expression of the volume current density I_z given by the constitutive law (6.5) yields:

$$\nabla_s \cdot \left(\frac{H_e}{\rho_e} \nabla_s U_1 \right) = \frac{\partial}{\partial T} \left(\frac{\epsilon}{H} (U_1 - U_2) \right), \quad (6.8a)$$

$$-\nabla_s \cdot \left(\frac{H_e}{\rho_e} \nabla_s U_2 \right) = \frac{\partial}{\partial T} \left(\frac{\epsilon}{H} (U_1 - U_2) \right). \quad (6.8b)$$

These governing equations must be completed with the boundary conditions which read:

$$\begin{aligned} U_1 &= U_a & \text{on } \Gamma_1, & & U_2 &= 0 & \text{on } \Gamma_2, \\ \nabla_s U_1 \cdot \mathbf{n} &= 0 & \text{on } \Gamma/\Gamma_1, & & \nabla_s U_2 \cdot \mathbf{n} &= 0 & \text{on } \Gamma/\Gamma_2. \end{aligned} \quad (6.9)$$

Even if they are not always written in this partial differential equation form, eqs. (6.8) and (6.9) have been used by many researchers to study resistivity effects in DEs (see [58, 38, 118] for example). Most of the time they are used in a more simple form, which is obtained if the thickness and resistivity are assumed to be uniform, and if the membrane thickness does not depend on time:

$$\Delta \bar{U} = \frac{H_e \epsilon}{\rho_e H} \frac{\partial \bar{U}}{\partial T}, \quad (6.10)$$

where $\bar{U} = U_1 - U_2$. This is a diffusion equation which is easily solved by finite element methods for example. Although the governing equation is more compact in the form eq. (6.10), the form eq. (6.8) is more practical because the boundary conditions are much easier to implement when the two variables U_1 and U_2 are used.

6.2.3 Model based on Maxwell's equations

The assumptions that lie behind the transmission line theory must be clarified for a moving medium. A DE membrane under dynamic excitation will move and deform, and the motion could very likely interact with the charge diffusion. In this section we derive the equations governing the voltage distribution on the electrodes from Maxwell's equations written for a moving medium [69]. We will show that it leads to additional terms in the equations.

Maxwell's equations for electroquasistatics in a moving frame.

Maxwell's equations for a moving medium have been written thoroughly by Kovetz [69].

Two frames are defined: \mathcal{R} is a Galilean reference frame, and \mathcal{R}' is the frame of reference of the matter. The frame \mathcal{R}' moves relatively to \mathcal{R} in a motion defined by the velocity field $\mathbf{V}(\mathbf{X}, T)$. Quantities will be noted with an apostrophe when referring to the frame \mathcal{R}' and without when referring to the frame \mathcal{R} . In particular, the current density \mathbf{I} refers to the velocity of the charges with respect to the reference frame \mathcal{R} while the current density \mathbf{I}' refers to the velocity of the charges with respect to the matter. In the frame \mathcal{R} , Maxwell's equations read:

$$\nabla \cdot \mathbf{D} = \rho, \quad (6.11a)$$

$$\nabla \times \mathbf{H} = \mathbf{I} + \frac{\partial \mathbf{D}}{\partial T}, \quad (6.11b)$$

$$\nabla \cdot \mathbf{B} = 0, \quad (6.11c)$$

$$\nabla \times \mathbf{E} = -\frac{\partial \mathbf{B}}{\partial T}, \quad (6.11d)$$

where \mathbf{D} is the electric displacement, \mathbf{E} the electric field, \mathbf{H} the magnetic field strength, \mathbf{B} the magnetic flux density, and ρ the charge density. These equations must be completed by the aether relations:

$$\mathbf{D} = \epsilon_0 \mathbf{E} + \mathbf{P}, \quad \mathbf{H} = \frac{\mathbf{B}}{\mu_0} - \mathbf{M}, \quad (6.12)$$

where \mathbf{P} and \mathbf{M} are the material polarization and magnetization. The electromagnetic fields are transformed as follows in the moving frame \mathcal{R}' [69]:

$$\begin{aligned} \mathbf{B}' &= \mathbf{B}, & \mathbf{E}' &= \mathbf{E} + \mathbf{V} \times \mathbf{B}, \\ \mathbf{H}' &= \mathbf{H} - \mathbf{V} \times \mathbf{D}, & \mathbf{D}' &= \mathbf{D}, \\ \mathbf{M}' &= \mathbf{M} + \mathbf{V} \times \mathbf{P}, & \mathbf{P}' &= \mathbf{P}, \\ \mathbf{I}' &= \mathbf{I} - \rho \mathbf{V}, & \rho' &= \rho. \end{aligned} \quad (6.13)$$

The expressions of the polarization \mathbf{P}' and the magnetization \mathbf{M}' as functions of the electric field \mathbf{E}' and the magnetic field \mathbf{H}' are given by constitutive relations, written in the frame \mathcal{R}' attached to matter.

In the present application electromagnetic wave propagation can be neglected, and magnetic effects as well. We will therefore work within the framework of electro-quasistatics [112]. The time derivative of the magnetic flux is neglected ($\partial \mathbf{B} / \partial T \approx 0$), and induction effects are disregarded as well, which suppresses the terms in $\mathbf{V} \times \mathbf{B}$. Moreover, the divergence of the Maxwell-Ampère equation (the second one in Eqs. (6.11)) is taken, to obtain the charge balance equation. The fields \mathbf{B} , \mathbf{H} and \mathbf{M} are then removed from the formulation of the problem, and Maxwell's equations for electro-quasistatics are obtained:

$$\nabla \cdot \mathbf{D} = \rho, \quad (6.14a)$$

$$\nabla \cdot \mathbf{I} + \frac{\partial \rho}{\partial T} = 0, \quad (6.14b)$$

$$\mathbf{E} = -\nabla U, \quad (6.14c)$$

$$\mathbf{D} = \epsilon_0 \mathbf{E} + \mathbf{P}, \quad (6.14d)$$

where the scalar potential U from which the electric field \mathbf{E} derives has been introduced because of the Maxwell-Faraday equation (the last one in Eqs. (6.11)).

These equations have to be completed by constitutive relations. In the present case two types of materials are considered:

- The membrane is made of a linear dielectric material, which does not conduct free charges, that is $\mathbf{I}' = 0$, and in which the polarization \mathbf{P}' is proportional to the electric field \mathbf{E}' . Given that there are no free charges initially in the dielectric, and that there are no currents, the charge remains null at all times ($\forall T, \rho' = 0$). So in the dielectric membrane:

$$\mathbf{P} = \epsilon_0 \chi_e \mathbf{E}, \quad \mathbf{I} = 0, \quad (6.15)$$

where χ_e is the membrane electrical susceptibility.

- The electrodes are made of linear conductive material, which satisfies Ohm's law $\mathbf{I}' = \mathbf{E}'/\rho_e$, and is not polarizable, that is $\mathbf{P}' = 0$. Thus, in the electrodes:

$$\mathbf{P} = 0, \quad \mathbf{I} - \rho \mathbf{V} = \frac{1}{\rho_e} \mathbf{E}. \quad (6.16)$$

Simplification for a thin DE membrane

Modelling assumptions Maxwell's equations presented in the previous paragraph are now simplified in the case of a thin dielectric membrane between electrodes as described in section 6.2.1. Because of the thinness of the system, the aim is to describe

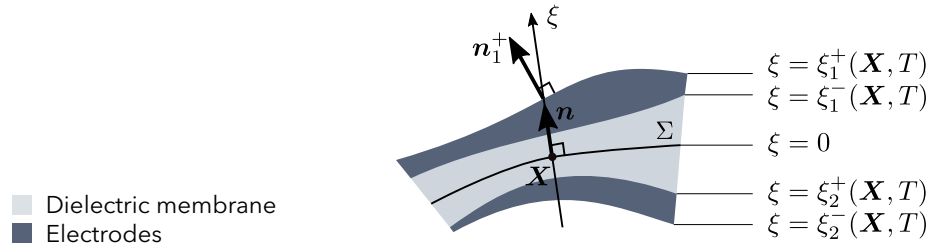


Fig. 6.3. Definition of the geometry of a thin membrane for the simplification of Maxwell's equations. A point of the system is identified by the location \mathbf{X} of its projection on the reference surface, and its coordinate ξ along the normal \mathbf{n} to the reference surface. The surfaces $\xi = \xi_i^\pm(\mathbf{X}, T)$ define the bottom and top sides of the electrodes, so that the thickness of the dielectric membrane is $h = \xi_1^- - \xi_2^+$, and the thicknesses of the top and bottom electrodes are $\xi_1^+ - \xi_1^-$ and $\xi_2^+ - \xi_2^-$ respectively, both supposed to be equal to h_e in the section 6.2.2.

the problem by planar equations written on a given reference surface Σ close to the membrane geometry, involving only two spatial variables. Each point in the volume of the membrane is identified by a point \mathbf{X} on the reference surface and an altitude ξ , see Fig. 6.3. For an arbitrary vector field $\mathbf{a}(\mathbf{X}, \xi)$ in this volume, $\mathbf{a}_\parallel(\mathbf{X}, \xi)$ denotes its projection on the tangent plane to the reference surface at location \mathbf{X} .

The equations will be expressed using surface operators: $\nabla_s a$ refers to the surface gradient of a scalar field a , defined as the projection of ∇a on the tangent plane to the reference surface, and $\nabla_s \cdot \mathbf{a}$ refers to the surface divergence of a vector field \mathbf{a} , defined as the divergence of \mathbf{a}_\parallel . Assuming that the thickness of the membrane is much smaller than the radius of curvature of the reference surface, these surface operators are simply expressed using the surface del operator defined by Eq. (6.4), where x and y denotes now curvilinear coordinates on the reference surface. Indeed, neglecting curvature effects, the following relation holds:

$$\nabla = \nabla_s + \frac{\partial}{\partial \xi} \mathbf{n}. \quad (6.17)$$

The construction of the 2D model is based on the following assumptions:

- In the electrodes the electric field is tangential (i.e. $\mathbf{E} \cdot \mathbf{n} = 0$).

- In the membrane the electric field is dominated by the normal component (fringe effects are neglected).
- Outside of the electrodes and of the membrane the electric field is null.

The first assumption amounts to assume that the potential U from which the electric field derives by Eq. (6.14c) does not depend on ξ in the electrodes. So we define the potentials U_1 and U_2 in the top and bottom electrodes respectively, by $U_1(\mathbf{X}, T) = U(\mathbf{X}, \xi, T)$ for $\xi_1^-(\mathbf{X}) \leq \xi \leq \xi_1^+(\mathbf{X})$ and $U_2(\mathbf{X}, T) = U(\mathbf{X}, \xi, T)$ for $\xi_2^-(\mathbf{X}) \leq \xi \leq \xi_2^+(\mathbf{X})$. The second assumption implies that in the membrane the electric field is expressed as a function of the electrode potentials as:

$$\mathbf{E} = -\frac{U_1 - U_2}{h} \mathbf{n} . \quad (6.18)$$

Indeed, due to the aether relation (6.14d) and the constitutive law (6.15), the electric field and the electric displacement are proportional:

$$\mathbf{D} = \epsilon \mathbf{E} , \quad (6.19)$$

where $\epsilon = \epsilon_0(1 + \chi_e)$ is the permittivity of the membrane's material. Therefore, as there are no free charges in the membrane ($\rho = 0$), Gauss's law (6.14a) implies that the dominant normal component of the electric field is uniform in the thickness of the membrane. From Eqs. (6.14c) and (6.17), this component is given by:

$$\mathbf{E} \cdot \mathbf{n} = \frac{\partial U}{\partial \xi} ,$$

which gives eq. (6.18).

Note that in this expression, the tangential component \mathbf{E}_{\parallel} of the electric field has been omitted because it is negligible compared to $\mathbf{E} \cdot \mathbf{n}$. The tangential component of the electric field is actually of the same order of magnitude in the membrane and in the electrodes, due to its continuity across the interface between the two materials. On the other hand, our assumptions violate the continuity of the normal component of the electric field (null in the electrodes and given by eq. (6.18) in the membrane). In practice, the charges will be mainly localized near the interface because of the discontinuity of the material properties, which justifies the jump of the electric field.

In the following paragraphs Maxwell's equations are integrated with respect to ξ in order to obtain surface equations.

Integration of Gauss's law Using eq. (6.17), the integration of Gauss's law eq. (6.14a) from the reference surface to the outer boundary of the top electrode reads:

$$\int_0^{\xi_1^+} \nabla_s \cdot \mathbf{D} d\xi + \int_0^{\xi_1^+} \frac{\partial \mathbf{D}}{\partial \xi} d\xi \cdot \mathbf{n} = \int_0^{\xi_1^+} \rho d\xi . \quad (6.20)$$

Note that the interval of integration includes the interface where $\mathbf{D} \cdot \mathbf{n}$ was assumed to be discontinuous. The jump of \mathbf{D} , related to the charge density ρ , is expressed by the

second member. Given that there are charges only in the electrode, and that the electric displacement is null for $\xi \geq \xi_1^+$, eq. (6.20) is then rewritten as:

$$\int_0^{\xi_1^+} \nabla_s \cdot \mathbf{D} d\xi - D_\perp = \sigma, \quad (6.21)$$

where σ is the surface charge density of the top electrode defined as:

$$\sigma = \int_{\xi_1^-}^{\xi_1^+} \rho d\xi, \quad (6.22)$$

and D_\perp is the normal component of the electric displacement in the membrane, which does not depend on ξ as seen in eqs. (6.18) and (6.19).

The normal component of the electric field in the membrane is much larger than its tangential component both in the electrode and in the membrane and, in addition, the membrane radius is much larger than its thickness so the first term of eq. (6.21) is negligible compared to the second one.

Finally, combining eqs. (6.18), (6.19) and (6.21) gives the expression of the surface charge density as a function of the electrode potentials:

$$\sigma = \frac{\epsilon}{h} (U_1 - U_2). \quad (6.23)$$

The same procedure applied to the bottom electrode shows that its surface charge density is $-\sigma$.

Integration of the charge balance Integrating the charge balance equation (6.14b) over the thickness of the top electrode reads:

$$\int_{\xi_1^-}^{\xi_1^+} \nabla_s \cdot \mathbf{I} d\xi + \left(\int_{\xi_1^-}^{\xi_1^+} \frac{\partial \mathbf{I}}{\partial \xi} d\xi \right) \cdot \mathbf{n} + \int_{\xi_1^-}^{\xi_1^+} \frac{\partial \rho}{\partial T} d\xi = 0. \quad (6.24)$$

Using the Leigniz integral rule to express the terms of this equation yields:

$$\begin{aligned} \nabla_s \cdot \left(\int_{\xi_1^-}^{\xi_1^+} \mathbf{I} d\xi \right) - \mathbf{I}(\xi_1^+) \cdot (\nabla_s \xi_1^+ - \mathbf{n}) + \mathbf{I}(\xi_1^-) \cdot (\nabla_s \xi_1^- - \mathbf{n}) \\ + \frac{\partial}{\partial T} \left(\int_{\xi_1^-}^{\xi_1^+} \rho d\xi \right) - \rho(\xi_1^+) \frac{\partial \xi_1^+}{\partial T} + \rho(\xi_1^-) \frac{\partial \xi_1^-}{\partial T} = 0. \end{aligned} \quad (6.25)$$

As neither the dielectric membrane nor the surrounding air can conduct free charges, the boundary conditions for the current on the top and bottom surfaces of the electrode read $\mathbf{I}'(\xi_1^\pm) \cdot \mathbf{n}_1^\pm = 0$, that is:

$$[\mathbf{I}(\xi_1^\pm) - \rho(\xi_1^\pm) \mathbf{V}(\xi_1^\pm)] \cdot (\mathbf{n} - \nabla_s \xi_1^\pm) = 0. \quad (6.26)$$

Moreover, the normal velocity of the interfaces reads:

$$\mathbf{V}(\xi_1^\pm) \cdot \mathbf{n} = \frac{\partial \xi_1^\pm}{\partial T} + \mathbf{V}(\xi_1^\pm) \cdot \nabla_s \xi_1^\pm, \quad (6.27)$$

so the boundary conditions eq. (6.26) become:

$$\mathbf{I}(\xi_1^\pm) \cdot (\mathbf{n} - \nabla_s \xi_1^\pm) - \rho(\xi_1^\pm) \frac{\partial \xi_1^\pm}{\partial T} = 0. \quad (6.28)$$

Introducing these boundary conditions in the charge balance eq. (6.25) cancels all the boundary terms, so this equation finally reads:

$$\nabla_s \cdot \mathbf{J}_1 + \frac{\partial \sigma}{\partial T} = 0, \quad (6.29)$$

where σ is the surface charge density defined by eq. (6.22), and the surface current density on the top and bottom electrodes

$$\mathbf{J}_1 = \int_{\xi_1^-}^{\xi_1^+} \mathbf{I}_\parallel d\xi, \quad \mathbf{J}_2 = \int_{\xi_2^-}^{\xi_2^+} \mathbf{I}_\parallel d\xi, \quad (6.30)$$

have been introduced.

Integration of Ohm's law In this work, we are interested in the voltage distribution on the electrodes, which is related to the charges' in-plane motion. The slowing down of this motion, due to the resistivity of the electrodes, is described by Ohm's law. Since the significant component of the charges' motion is the tangential one, Ohm's law (6.16) is projected on the tangent plane to the reference surface:

$$\mathbf{I}_\parallel - \rho \mathbf{V}_\parallel = \frac{1}{\varrho_e} \mathbf{E}_\parallel. \quad (6.31)$$

As in the previous paragraphs, let us examine the case of the top electrode. The electric field is there given by the surface gradient of the potential U_1 and is uniform in the electrode thickness. Integrating Ohm's law eq. (6.31) over the electrode thickness yields:

$$\int_{\xi_1^-}^{\xi_1^+} \mathbf{I}_\parallel d\xi - \int_{\xi_1^-}^{\xi_1^+} \rho \mathbf{V}_\parallel d\xi = -\nabla_s U_1 \int_{\xi_1^-}^{\xi_1^+} \frac{1}{\varrho_e} d\xi. \quad (6.32)$$

In order to recognize in the second term the surface charge σ defined by eq. (6.22), we further assume that the tangential velocity \mathbf{V}_\parallel does not depend on ξ in the electrodes. This tangential velocity is denoted by $\mathbf{V}_{1\parallel}$ and $\mathbf{V}_{2\parallel}$ in the top and bottom electrodes respectively. The surface Ohm's law eq. (6.32) is then simplified as follows:

$$\mathbf{J}_1 - \mathbf{V}_{1\parallel} \sigma + \gamma_1 \nabla_s U_1 = 0, \quad (6.33)$$

where \mathbf{J}_1 is the surface current defined by eq. (6.30) and the surface conductivity of the top and bottom electrodes

$$\gamma_1 = \int_{\xi_1^-}^{\xi_1^+} \frac{1}{\varrho_e} d\xi, \quad \gamma_2 = \int_{\xi_2^-}^{\xi_2^+} \frac{1}{\varrho_e} d\xi, \quad (6.34)$$

have been introduced.

Diffusion equations By introducing in the charge balance eq. (6.29) the expression of the surface current \mathbf{J}_1 given by Ohm's law eq. (6.33) and the expression of the surface charge σ given by eq. (6.23), a diffusion equation governing the voltage distribution on the top electrode is obtained, and this procedure is repeated for the bottom electrode, yielding:

$$\nabla_s \cdot (\gamma_1 \nabla_s U_1) = \frac{\partial}{\partial T} \left(\frac{\epsilon}{H} (U_1 - U_2) \right) + \nabla_s \cdot \left(\frac{\epsilon}{H} (U_1 - U_2) \mathbf{V}_{1\parallel} \right), \quad (6.35a)$$

$$-\nabla_s \cdot (\gamma_2 \nabla_s U_2) = \frac{\partial}{\partial T} \left(\frac{\epsilon}{H} (U_1 - U_2) \right) + \nabla_s \cdot \left(\frac{\epsilon}{H} (U_1 - U_2) \mathbf{V}_{2\parallel} \right). \quad (6.35b)$$

In the following, given the small thickness of the electrodes and of the membrane, it is assumed that the tangential velocity is the same in the whole membrane, meaning that $\mathbf{V}_{1\parallel} = \mathbf{V}_{2\parallel} = \mathbf{V}_{\parallel}$. Also, the top and bottom electrode thicknesses and resistivity are assumed to be identical and uniform, which yields $\gamma_1 = \gamma_2 = H_e/\varrho_e$.

The diffusion equations obtained from Maxwell's equations in a moving frame are therefore simplified to:

$$\nabla_s \cdot \left(\frac{H_e}{\varrho_e} \nabla_s U_1 \right) = \frac{\partial}{\partial T} \left(\frac{\epsilon}{H} (U_1 - U_2) \right) + \nabla_s \cdot \left(\frac{\epsilon}{H} (U_1 - U_2) \mathbf{V}_{\parallel} \right), \quad (6.36a)$$

$$-\nabla_s \cdot \left(\frac{H_e}{\varrho_e} \nabla_s U_2 \right) = \frac{\partial}{\partial T} \left(\frac{\epsilon}{H} (U_1 - U_2) \right) + \nabla_s \cdot \left(\frac{\epsilon}{H} (U_1 - U_2) \mathbf{V}_{\parallel} \right). \quad (6.36b)$$

On the portion of the top electrode border where there is no connection, the boundary condition reads $\mathbf{I}' \cdot \mathbf{n}_b = 0$, that is:

$$\mathbf{I} \cdot \mathbf{n}_b = \rho \mathbf{V} \cdot \mathbf{n}_b \quad \text{for } \mathbf{X} \in \Gamma \setminus \Gamma_1 \text{ and } \xi \in [\xi_1^-(\mathbf{X}), \xi_1^+(\mathbf{X})]. \quad (6.37)$$

Integrating this condition over the thickness of the top electrode and using Ohm's law eq. (6.33) yields:

$$\nabla_s U_1 \cdot \mathbf{n}_b = 0 \quad \text{on } \Gamma \setminus \Gamma_1. \quad (6.38)$$

The same holds for the bottom electrode, and the full set of boundary conditions is finally the same as in the case of the model based on transmission line theory, namely eq. (6.9).

6.2.4 Comparison of transmission line and Maxwell models

The governing equations obtained using the transmission line theory are eq. (6.8) with the boundary conditions eq. (6.9). The equations obtained using Maxwell's equations are eq. (6.36) with the boundary conditions eq. (6.9).

First, the boundary conditions obtained using both approaches are identical.

Second, if the dielectric membrane is at rest, $\mathbf{V} = 0$, and ϵ/H can be moved out of the derivative in eq. (6.36), and eq. (6.36) is then identical to eq. (6.8).

However, if the membrane moves and deforms, eqs. (6.8) and (6.36) differ by the convective term $\nabla_s \cdot (\epsilon/H(U_1 - U_2)\mathbf{V}_{\parallel})$ in eq. (6.36), which matters when there is an in-plane movement of the membrane.

6.2.5 Linearized coupled equations

For small actuation voltage compared to the static voltage ($\tilde{U}_a \ll U_0$), eq. (6.36) can be linearized around a steady state:

$$\begin{aligned} U_1 &= U_0 + \tilde{U}_1(T), & U_2 &= 0 + \tilde{U}_2(T), \\ H &= H_0 + \tilde{H}(T), & H_e &= H_{e0} + \tilde{H}_e(T). \end{aligned}$$

The linearized version of eq. (6.36) is:

$$\begin{aligned} \frac{\epsilon}{H_0} \frac{\partial}{\partial T} (\tilde{U}_1 - \tilde{U}_2) - \frac{\epsilon U_0}{H_0^2} \frac{\partial \tilde{H}}{\partial T} &= \nabla_s \cdot \left(\frac{H_{e0}}{\rho_e} \nabla_s \tilde{U}_1 \right) - U_0 \nabla_s \cdot \left(\frac{\epsilon}{H_0} \mathbf{V}_{\parallel} \right), \\ \frac{\epsilon}{H_0} \frac{\partial}{\partial T} (\tilde{U}_1 - \tilde{U}_2) - \frac{\epsilon U_0}{H_0^2} \frac{\partial \tilde{H}}{\partial T} &= -\nabla_s \cdot \left(\frac{H_{e0}}{\rho_e} \nabla_s \tilde{U}_2 \right) - U_0 \nabla_s \cdot \left(\frac{\epsilon}{H_0} \mathbf{V}_{\parallel} \right). \end{aligned} \quad (6.39)$$

Equation (6.39) shows that even at the linear order, the voltage distribution is coupled to the mechanical vibrations, through the time derivative of the membrane thickness and through the membrane velocity \mathbf{V} . Note that the coupling terms are proportional to the bias voltage U_0 .

6.3 Application

As emphasized here-above, the system of electrical equations (6.39) is coupled to the mechanical equations.

For now in chapter 6, the equations have been derived in a general case for an arbitrary geometry. In order to further investigate the influence of the coupling terms, a given mechanical design should be chosen.

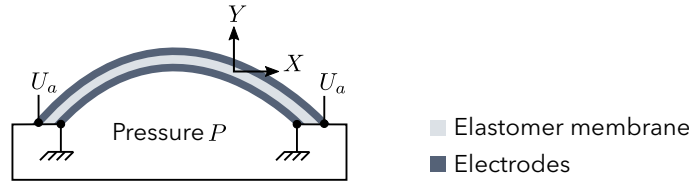


Fig. 6.4. Schematics of the device used for the experimental validation of the electromechanical coupling model.

Here as an application, the same system as in the rest of the thesis is considered, namely an inflated DE membrane, as shown in fig. 6.4. This system enables high frequency actuation, as no additional mass apart from the DE membrane is moving. It has been investigated by several researchers for use as loudspeakers [52, 46, 30, 34] or pumps [90].

6.3.1 Coupled equations

Weak form of the coupled electromechanical system

The equations governing the dynamics of this membrane have already been derived in chapter 2 and linearized around an inflated configuration. We showed in chapter 4 that acoustics have a strong influence on the membrane dynamics, and must therefore be taken into account to compute correctly the dynamics of the system. Thus, vibro-acoustic coupling is modelled here by the equations derived in chapter 2, but in the following we omit writing them for clarity reasons. The equations for acoustics can be considered included in the mechanical variables \tilde{x}, \tilde{y} .

The complete system of mechanical and electrical linearized equations can be written in the following weak form:

$$\begin{aligned}
 & \mathfrak{R}_K([\mathcal{X}, \mathcal{Y}, \mathcal{U}_1, \mathcal{U}_2]) , [\tilde{x}, \tilde{y}, \tilde{u}_1, \tilde{u}_2] \\
 & + \mathfrak{R}_C([\mathcal{X}, \mathcal{Y}, \mathcal{U}_1, \mathcal{U}_2]) , [\dot{\tilde{x}}, \dot{\tilde{y}}, \dot{\tilde{u}}_1, \dot{\tilde{u}}_2] \\
 & + \mathfrak{R}_M([\mathcal{X}, \mathcal{Y}, \mathcal{U}_1, \mathcal{U}_2]) , [\ddot{\tilde{x}}, \ddot{\tilde{y}}, \ddot{\tilde{u}}_1, \ddot{\tilde{u}}_2] \\
 & = \mathfrak{R}_F([\mathcal{X}, \mathcal{Y}, \mathcal{U}_1, \mathcal{U}_2], u_a) , \quad \forall [\mathcal{X}, \mathcal{Y}, \mathcal{U}_1, \mathcal{U}_2] , \quad (6.40)
 \end{aligned}$$

where $(\tilde{x}(t), \tilde{y}(t))$ is the position of the membrane [see fig. 2.1], $\tilde{u}_1 = \tilde{U}_1/U_0$ and $\tilde{u}_2 = \tilde{U}_2/U_0$ the non-dimensional voltages on the top and bottom electrodes. The force term \mathfrak{R}_F contains only the boundary condition on the top electrode ($\tilde{u}_1 = \tilde{u}_a$ on a portion of the border). We emphasize that eq. (6.40) is linear, but strongly couples electrical and mechanical dynamics.

Solving using finite elements

The linearized weak form for the voltage distribution and mechanical vibrations eq. (6.40) is discretized on the same mesh as the weak form for the mechanical vibrations eq. (2.27) in chapter 2. There are now four variables $(\tilde{x}, \tilde{y}, \tilde{u}_1, \tilde{u}_2)$ instead of two in chapter 2 to describe the membrane state.

Equation (6.40) is solved in the frequency domain, by inverting the discretized finite element matrix system for all frequencies of interest.

6.3.2 Experimental setup

High voltage probe

In order to measure the voltage on the membrane, a Testec TT-HVP15 HF high voltage probe has been used. A high voltage probe behaves electrically like a large resistor, which builds together with the input impedance of an oscilloscope a voltage divider [see fig. 6.5].

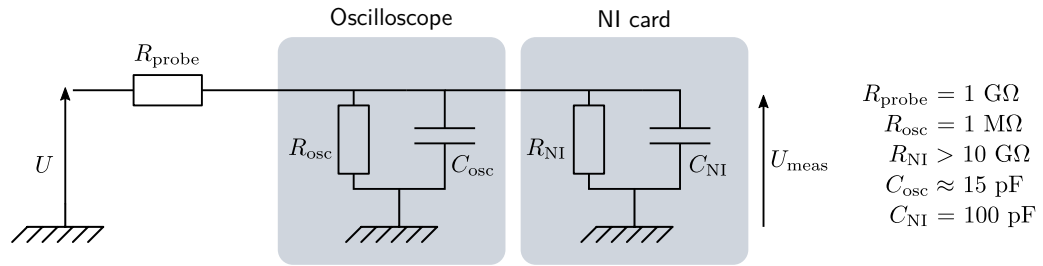


Fig. 6.5. Electrical schematics of the high voltage probe, and connection to the measurement devices.

In order to obtain an attenuation of the measured voltage by a factor of 1000, the high voltage probe must be connected to an oscilloscope of input impedance $1 \text{ M}\Omega$, it is not possible to connect it directly to the acquisition card, whose input impedance is too high ($R_{\text{NI}} > 10 \text{ G}\Omega$). Unfortunately, both the oscilloscope and the NI card have an input capacitance, which forms an RC circuit together with the input resistance [see fig. 6.5]. The measured voltage then reads in the frequency domain:

$$U_{\text{meas}} = \frac{\left(\frac{1}{R_{\text{osc}}} + \frac{1}{R_{\text{NI}}} + iC_{\text{osc}}\Omega + iC_{\text{NI}}\Omega \right)^{-1}}{R_{\text{probe}}} U. \quad (6.41)$$

At low frequency, the capacitive terms are negligible, and as the resistance of the oscilloscope is much smaller than the NI card resistance, the measured voltage reads:

$$U_{\text{meas}} \approx \frac{R_{\text{osc}}}{R_{\text{probe}}} U \approx \frac{U}{1000}, \quad (6.42)$$

so the high voltage probe behaves as expected, as a $1000 \times$ voltage divider. At high frequencies, capacitive effects start to play a role, and it is then interesting to define the cut-off frequency of the probe as:

$$\Omega_{\text{cut}} = \frac{1}{R_{\text{osc}}(C_{\text{NI}} + C_{\text{osc}})}, \quad (6.43)$$

where the resistance of the NI card has been neglected compared to the resistance of the oscilloscope. With the parameters of fig. 6.5, eq. (6.43) yields $f_{\text{cut}} \approx 1400 \text{ Hz}$. Therefore

above the cut-off frequency f_{cut} , the measured voltage is not equal to $U/1000$, and this limits the measurement frequency range. The capacitive effects can be compensated for, by applying the inverse transfer function of the electrical circuit shown in fig. 6.5, which is done in the following. However, the measurement accuracy decreases at high frequencies, so measurements above the cut-off frequency may not be very reliable.

Voltage spatial distribution measurements

The goal is to measure the spatial distribution of the voltage on the electrode surface, during actuation. This means that the membrane is moving while the voltage is measured. This cannot be avoided, as we are here interested in the coupling between the membrane vibrations and the voltage distribution. Therefore, special care must be taken to ensure the connection of the high voltage probe to the electrode surface even when it moves.

The best found solution was to use a very thin wire ($\approx 100 \mu\text{m}$), pressed against the electrode surface as shown in figs. 6.6 and 6.7. A small droplet of conductive grease is deposited between the membrane and the wire, to ensure the connection during the movement. The viscosity of the grease also helps to avoid the wire bouncing on the membrane during actuation. To minimize the influence of the probe on membrane vibrations, the amount of conductive grease should be minimal.

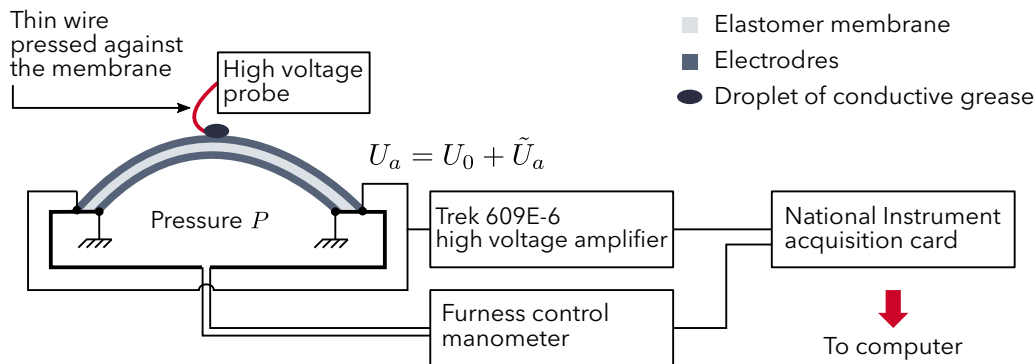


Fig. 6.6. Measurement setup to measure the local voltage on the membrane. The top electrode is connected on its whole outer perimeter to the high voltage source, and the bottom electrode is Similarly connected on its whole outer perimeter to the ground. See fig. 3.6 for the details of the connections on the prototype.

The first membrane eigenfrequencies have been measured with and without applying the wire, to estimate its influence on the membrane vibrations. The first eigenfrequencies changed by only a few percent when the wire was pressed against the membrane, showing its limited influence.

Parameters of the tested prototype

The parameters of the prototype used in this chapter are given in table 6.1.

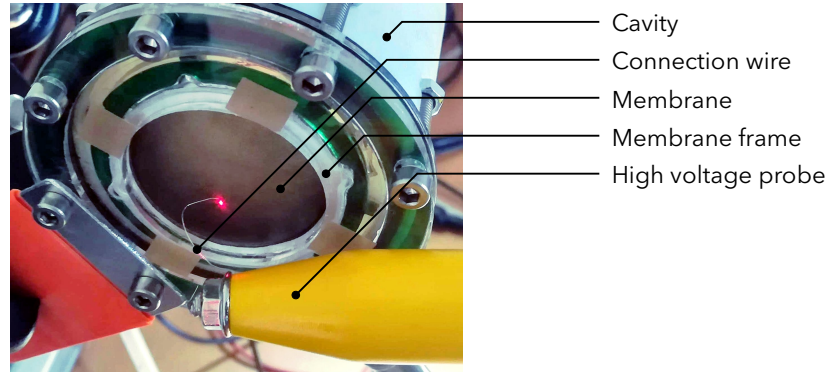


Fig. 6.7. Picture of the measurement setup to measure the voltage distribution on the electrode surface during actuation.

Tab. 6.1. List of all experimental dimensional parameters (Dim.) and non-dimensional parameters (Non-dim.). These parameters are used in all experiments and numerical results presented in the present chapter.

Dimensional	Value	Non-dimensional	Value
\check{H}	48 μm	-	-
V_{cav}	125 mL	$v_{\text{cav}} = V_{\text{cav}}/A^3$	23.4
\bar{R}_E	1.75 cm	\bar{r}_E	1
μ	$4.5 \times 10^5 \text{ Pa}$	-	-
P_{app}	1500 Pa	p_{app}	1.2
ρ_s	1042 kg m^{-3}	-	-
J_m	100	J_m	100
U_0	1500 V	u_0^2	0.052
ρ_{elec}	0.0036 kg m^{-2}	ρ_{ratio}	0.07
\bar{A}	1.75 cm	-	-
A	1.9 cm	a	1.085
W	$2 \times 10^5 \text{ V}^2$	-	-
ϵ_r	2.8	-	-
η	2 %	η	2 %
C_f	343 ms^{-2}	c^2	272
ρ_f	1.2 Kg m^{-3}	m	0.41
L_{cav}	5 cm	$l_{\text{cav}} = L_{\text{cav}}/A$	2.8
R_{cav}	3 cm	$r_{\text{cav}} = R_{\text{cav}}/A$	1.18

6.4 Results

For the interpretation of the results, the characteristic time for the mechanics is defined as:

$$\tau_m = \frac{A}{\sqrt{\frac{\mu}{\rho}}} \approx 800 \mu\text{s} , \quad (6.44)$$

where μ is the shear modulus of the membrane, ρ its density, and A its radius. A characteristic time scale for the charge diffusion effects is also built from eq. (6.39):

$$\tau_e = \frac{\epsilon A^2 \rho_e}{H H_e} \approx 80 \mu\text{s} . \quad (6.45)$$

6.4.1 Membrane dynamics

First, the transfer function between the membrane velocity at $r = 0.1$ and the applied voltage is plotted in fig. 6.8. The model predicts correctly the dynamics of the inflated membrane, which validates the mechanical model and the electrostatic excitation.

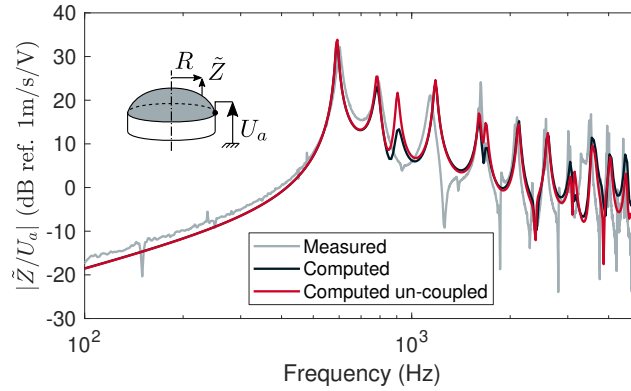


Fig. 6.8. Transfer function between the membrane vibrations and the applied voltage, measured and computed at radius $r = 0.1$. *Computed* is the velocity computed using the coupled electrodynamics/mechanics model, using the electrical equations derived from Maxwell's equations in a moving frame [see eq. (6.36)], and *Computed un-coupled* is the velocity computed by a weakly coupled model: the voltage on the electrodes is computed assuming the membrane is at rest, and the resulting voltage is used as the excitation for the membrane dynamics.

There is a slight difference between the coupled and un-coupled calculations in fig. 6.8, the coupled calculation seems to have a slightly higher damping than the un-coupled one. This may be due to resistivity effects, for example the third mechanical mode may strongly couple to resistivity effects, which increases its damping. The amplitude of this mode appears to be closer to the measurements with the coupled model.

6.4.2 Impedance

The impedance of the membrane $Z = U_a/I$ can be obtained from the numerical results, as the current flowing through the membrane reads:

$$I = \int_{\Sigma} \frac{\epsilon}{H_0} \frac{\partial}{\partial T} (\tilde{U}_1 - \tilde{U}_2) dS + \int_{\Sigma} \epsilon U_0 \frac{\partial}{\partial T} \left(\frac{1}{\tilde{H}} \right) dS . \quad (6.46)$$

If membrane dynamics are neglected, the current reads:

$$I_{\text{static}} = \int_{\Sigma} \frac{\epsilon}{H_0} \frac{\partial}{\partial T} (\tilde{U}_1 - \tilde{U}_2) dS . \quad (6.47)$$

The impedance is measured using a shunt resistor for the current, and the voltage monitor output of the used Trek 609-E amplifier. It is plotted in fig. 6.9, together with the impedance computed by the fully coupled model [see eq. (6.46)], and the impedance computed by the model neglecting the influence of the membrane vibrations [see eq. (6.47)].

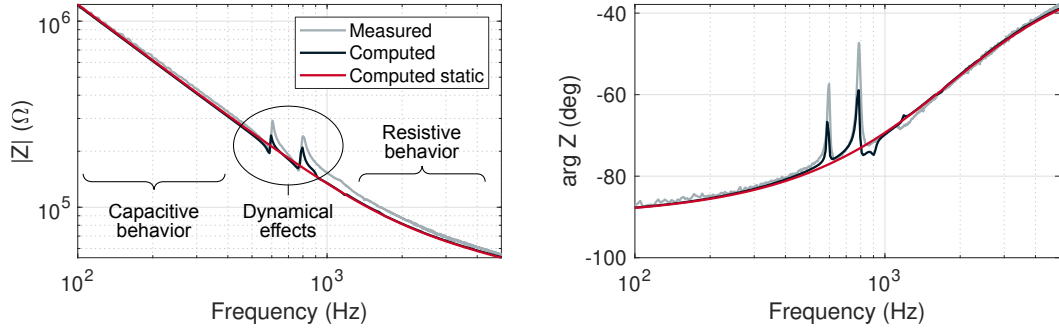


Fig. 6.9. Membrane impedance, measured on a prototype, computed with the coupled model, and computed omitting membrane displacement effect (Computed static).

The general shape of the impedance is characteristic of a capacitor at low frequencies (below 800 Hz), and resistive effects make it deviate from the purely capacitive behavior at high frequencies. This resistive effect is correctly captured by the static impedance calculation using eq. (6.47).

As the frequency of the excitation passes one of the first eigenfrequencies of the membrane, a large displacement of the membrane will be caused by the applied voltage U_a . As a consequence, the membrane thickness will oscillate, and the second term in eq. (6.46) results in peaks in the impedance. This effect is visible in the measured impedance and correctly captured by the coupled model eq. (6.46).

Physically, if the membrane vibrations are in phase with the voltage oscillations (a maximum of the voltage corresponds to a maximum of the thickness), then a smaller amount of charges are needed on the membrane to satisfy Gauss's law $(U_1 - U_2)/H = H_e \rho / \epsilon$. Therefore the required current is smaller than if the membrane were at rest, and the impedance is larger. Such a situation where the thickness oscillates in phase with the voltage is a dynamical effect. Indeed the opposite effect occurs in the quasi-static case: an increase of the voltage decreases the thickness.

The impedance reveals coupling effects between the electrodynamic loading of the membrane and its vibrations. However, the coupling mechanism analysed above is not related to the electrode resistivity, but to capacitance changes during actuation.

6.4.3 Voltage on the membrane

The voltage on the electrodes is now investigated. It has been measured using a high voltage probe, which is connected by a very thin wire to the electrode surface, as described in section 6.3.2. The electrode voltage can thus be measured at different radius, and is plotted in fig. 6.10, together with the results of the coupled model. The voltage distribution is also plotted as a function of the membrane non-dimensional radius r in fig. 6.11 for three arbitrary chosen frequencies.

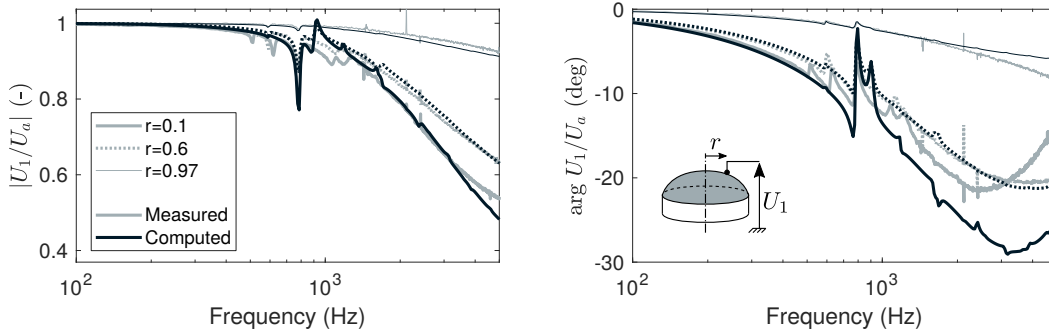


Fig. 6.10. Voltage on the membrane during actuation, measured at different radius.

Figure 6.10 exhibits several interesting phenomena. First, the voltage on the electrodes decreases at high frequencies, down to half of the applied voltage. Also, the farther away from the connections, the fastest the voltage decreases, as observed clearly in fig. 6.11. This is a consequence of the resistivity, and has already been analysed [58, 38]. However, this is to the author's knowledge the first experimental results validating the numerical predictions.

More interesting is the behavior of the voltage around 1 kHz, at the first membrane eigen-frequencies (see fig. 6.8): clear peaks and drops are visible in fig. 6.10. This highlights a coupling between the membrane vibrations and the voltage distribution, which arises because of the electrode resistivity. Indeed, with perfectly conductive electrodes, the voltage would be equal to U_a on the whole electrode. This coupling phenomenon can be explained by the schematics in fig. 6.12.

This coupling phenomenon can be explained by the schematics in fig. 6.12.

- **Stage 1** Consider a DE membrane at rest, charged by a static voltage at its edge.
- **Stage 2** Suppose that, under external action, the membrane deforms during a mechanical response time τ_m . This deformation induces local changes in thickness. Before the charges move on the membrane, due to Gauss's law $(U_1 - U_2)/H = H_e \rho / \epsilon$, the voltage on the membrane will increase where it is thicker, and decrease where it is thinner.
- **Stage 3** Charges will be supplied by the generator, and they will move on the membrane so that the voltage equals the applied voltage everywhere. This diffusion occurs during the timescale τ_e .

In practice, the membrane is actuated by a non stationary input voltage $U_a(t)$, which vibrates the system at the period τ_m . The deformation is most significant at system's

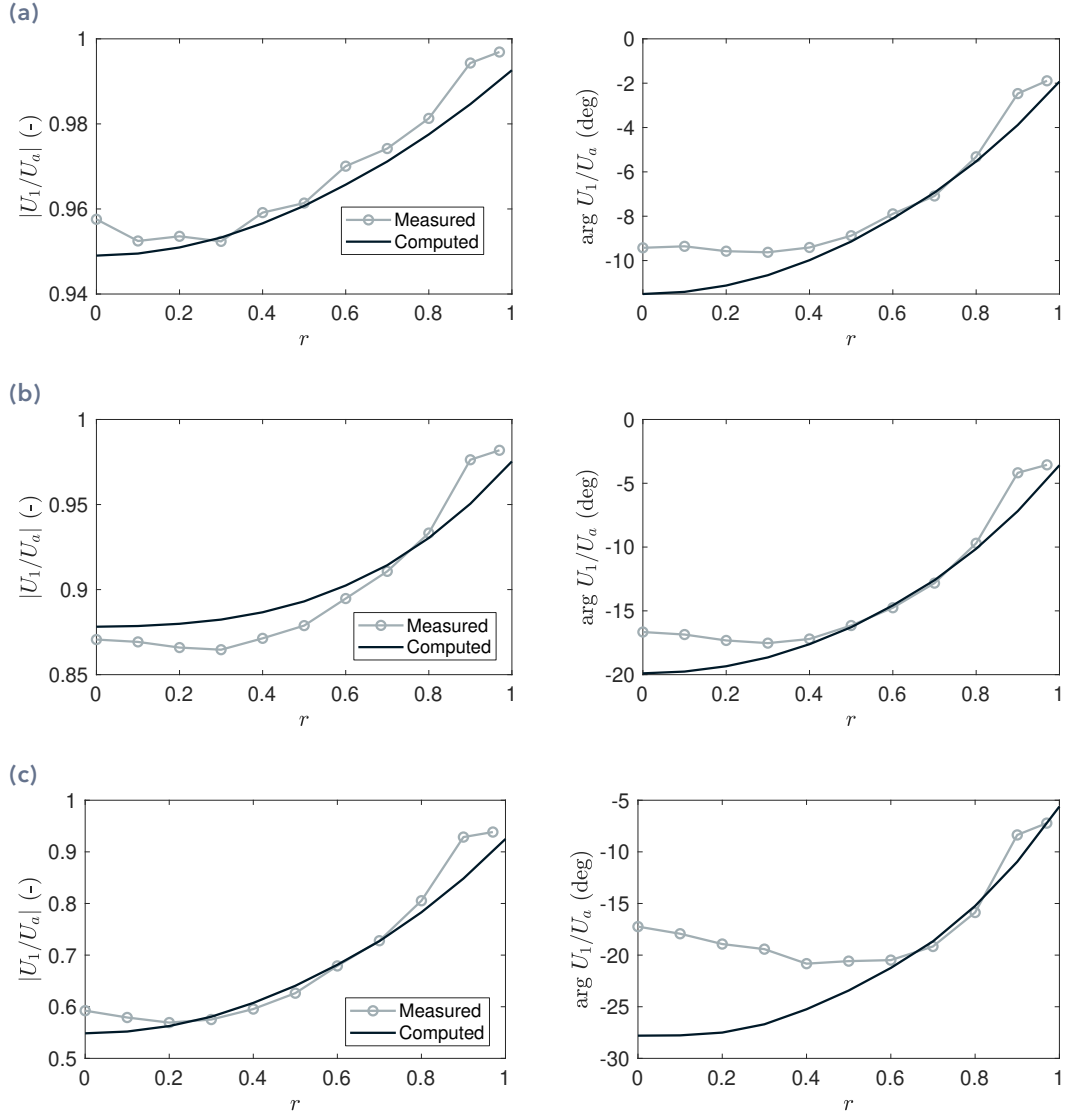


Fig. 6.11. Voltage on the membrane as a function of the radius, measure and computed. **(a)** at 674 Hz, **(b)** at 1348 Hz, **(c)** at 4000 Hz.

eigenmodes, thus, we now examine the case where the excitation frequency matches one of the eigenfrequencies. The electromechanical behavior of the system is governed by the ratio of the mechanical timescale τ_m and the electrical timescale τ_e :

- If $\tau_e \ll \tau_m$, the electrodynamic equilibrium is satisfied at all times, the voltage is uniform on the membrane, and equal to the applied voltage $U_a(t)$.
- If $\tau_e \approx \tau_m$, the charge diffusion takes approximately one period of oscillation, and the coupling phenomenon described in Fig. 6.12 then occurs.
- If $\tau_e \gg \tau_m$, the charges do not have the time to spread on the membrane, so the electrostatic excitation is small, and the membrane does not move. If the mem-

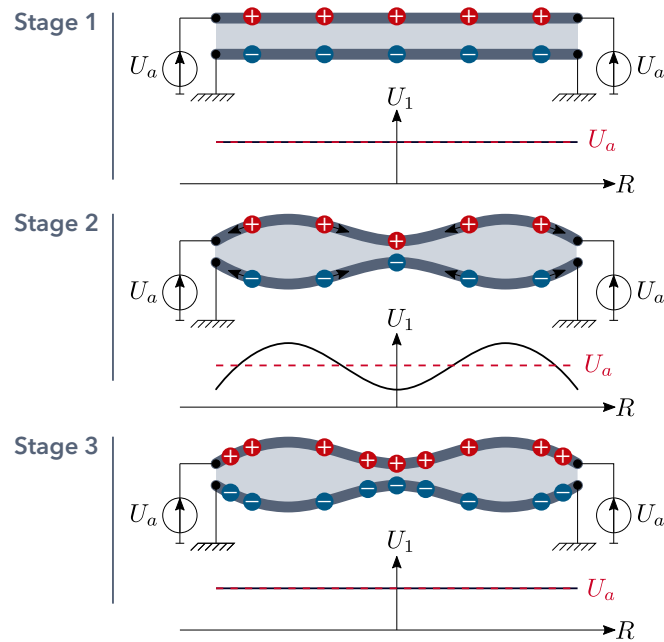


Fig. 6.12. Coupling between the electrodynamics of a resistive capacitor and its vibrations.

brane is vibrated by another excitation of period τ_m , the voltage will still locally vary on the electrodes because the charges are 'fixed' by the high resistivity.

The coupling exhibited in fig. 6.10 also highlights that for resistive DE actuators operated at high frequencies, as the actuation depends on the voltage which itself depends on the vibrations, the voltage and the vibrations must be computed together using a coupled model.

6.5 Conclusion

In this chapter, resistivity effects on DE actuators are investigated, with a special focus on the high frequency behavior. It has been shown that for a certain set of parameters, when the timescale for electrodynamics is similar to the mechanical timescale, a coupling between the voltage distribution and the vibrations occurs. A model has been presented to explain this phenomenon and is validated experimentally.

We believe that the model developed in this section may have two different uses.

Refined modelling of the electromechanic excitation at high frequencies

The calculation of the electromechanical excitation of DE devices is refined at high frequencies. The response of DE actuators can thus be computed with increased accuracy.

Adaptive filtering

The other consequence of the study presented in this chapter concerns self-sensing. We see two possible applications:

- The first membrane eigenfrequencies can be estimated from impedance measurements [see fig. 6.9]. This can be useful to implement adaptive filtering techniques, such as adapting the control method proposed in section 5.4 to changes of the dynamics of the DE membrane. The filters could be adjusted to follow the change of the membrane eigenfrequencies.
- The voltage on the membrane could also be monitored, maybe at different locations. More complete information on the membrane state could then be obtained, and exploited to design adaptive control methods too.

Conclusion

7.1 Summary of the main results

In this thesis, we studied the dynamics and sound radiation of dielectric elastomer loudspeakers. A specific geometry was chosen, namely a DE membrane inflated over a closed cavity, to identify the different physics that are coupled in these devices, and to set up the modelling methods.

In chapter 2, a model of this inflated DE loudspeaker is set up, by studying the different physics that matter. The coupled electromechanical behavior of dielectric elastomers is obtained from thermodynamics considerations. Strong vibroacoustic coupling is taken into account, and a modal method for solving exterior acoustic radiation problems is proposed. The system of coupled equations is solved by finite elements, implemented in the open source software FreeFEM.

Chapter 3 presents the experimental procedure to design, manufacture and test DE loudspeakers. Set-ups for measuring the static deformation, the linear dynamics and acoustical radiation are presented, as well as the experiments required to identify the material parameters of the membrane.

The experimental and numerical results of the first two chapters are compared to each other in chapter 4, in terms of static deformation, free and forced dynamics, acoustic radiation and directivity. It is shown that electrostatics, large-deformations mechanics, and acoustics must all be taken into account to yield an accurate prediction of the loudspeaker behavior. The model is validated, and is capable of predicting the acoustical radiation.

In chapter 5, the validated model is used to try to improve the loudspeaker behavior, in terms of frequency response (spectral balance), low frequency cut-off, and directivity. Four options are considered: choosing properly the inflation pressure to maximize the low frequency radiation, patterning the electrode to control the modal response, filling the cavity with porous material to damp out acoustic modes, and filtering the excitation signal to achieve a flatter frequency response as well as a more omni-directional directivity.

Chapter 6 departs a little from the main goal of the thesis which is to model and improve DE loudspeakers, as it focuses on resistivity effects at high frequencies. These effects have little influence on the speaker behavior, but are interesting from an academic point of view, and may open self-sensing possibilities. It is found that the voltage spatial distribution on the electrodes of DE membranes is coupled to the membrane vibrations, when the timescale for electrodynamic effects is similar to the mechanical timescale. To my knowledge, these effects had not been observed before, nor described by models.

7.2 Perspectives

7.2.1 Model improvement

From the modelling point of view, several points could be improved.

The model, which predicted very accurately the sound radiation when the electrode occupied the whole surface of the membrane, gave less accurate predictions for electrodes covering only partially the membrane. This limited the use of the model to optimize the electrode shape, so further investigations should be carried out to analyse and correct these errors.

The losses inherent to the elastomer material were taken into account by a simple structural damping model. This model seemed to be sufficient to capture the behavior of the system, but for other materials the losses could have a larger role. Increasing the damping of the membrane would improve the acoustical response, by flattening the frequency response. The electrode material could maybe be tuned to have a high loss factor, in order to increase the damping of the whole sandwich.

Acoustical radiation was computed on a reduced modal basis, made of coupled vibroacoustic modes. This type of modal methods for exterior acoustics has not been used a lot in the literature, so there are still no clear guidelines on how truncate the modal basis. This deserves further work to improve the efficiency of these modal methods.

7.2.2 Optimization

The main focus of this thesis was on refining the models for dielectric elastomer loudspeakers, in order to enable more efficient design of these devices. We started using the developed models to improve the acoustical behavior, with more or less convincing results depending on the chosen optimization strategy.

This part of the work would require further work, especially on the following points:

- The whole study presented in thesis concerns linear dynamics. Harmonic distortion is rather high in DE loudspeakers, because of the large deformations of the membrane, and models capable of computing the distortion would therefore be useful to improve this point. I believe that reduced order models (see [111] for example) would be of particular interest, for computing quickly the response and use the model in automatic optimization routines.
- The results obtained in chapter 6 are promising in terms of self-sensing possibilities. Information on the membrane dynamics at high frequencies can be retrieved from impedance measurements. For example, the first membrane eigenfrequencies can then be monitored in real time, while music is played on the loudspeaker. This type of information could then be used in adaptive filtering methods to improve the frequency response, the harmonic distortion or the directivity.

- As soon as several electrodes can be excited with different signals, a great freedom is available to improve the response by signal processing. Combined with the self-sensing capabilities of dielectric elastomers, large improvement of the frequency response, distortion and directivity may be possible. Adaptive control algorithms are particularly promising as they could follow the evolution of the system, due to relaxation of the elastomer, loss of inflation pressure, aging of the material, etc.
- In the present thesis, we focused on a single geometry, namely the inflated membrane. This geometry was particularly suited to develop the models, but other may be more interesting from an acoustical point of view.

Bibliography

- [1] Ahmed Abbad, Kanty Rabenorosoa, Morvan Ouisse, and Nouredine Atalla. "Adaptive Helmholtz Resonator Based on Electroactive Polymers: Modeling, Characterization, and Control". en. In: *Smart Materials and Structures* 27.10 (Oct. 2018), p. 105029 (cit. on p. 9).
- [2] J. E. Adkins and R. S. Rivlin. "Large Elastic Deformations of Isotropic Materials IX. The Deformation of Thin Shells". en. In: *Phil. Trans. R. Soc. Lond. A* 244.888 (May 1952), pp. 505-531 (cit. on pp. 20, 24-26).
- [3] Jean Allard and Nouredine Atalla. *Propagation of Sound in Porous Media: Modelling Sound Absorbing Materials* 2e. John Wiley & Sons, 2009 (cit. on p. 106).
- [4] Iain A. Anderson, Todd A. Gisby, Thomas G. McKay, Benjamin M. O'Brien, and Emilio P. Calius. "Multi-Functional Dielectric Elastomer Artificial Muscles for Soft and Smart Machines". In: *Journal of Applied Physics* 112.4 (Aug. 2012), p. 041101 (cit. on p. 5).
- [5] George L. Augspurger. "Theory, Ingenuity, and Wishful Wizardry in Loudspeaker Design—A Half-century of Progress?" en. In: *The Journal of the Acoustical Society of America* 77.4 (June 1998), p. 1303 (cit. on p. 3).
- [6] Fabio Beco Albuquerque and Herbert Shea. "Influence of Humidity, Temperature and Prestretch on the Dielectric Breakdown Strength of Silicone Elastomer Membranes for DEAs". en. In: *Smart Materials and Structures* (July 2020) (cit. on p. 87).
- [7] Jean-Pierre Berenger. "A Perfectly Matched Layer for the Absorption of Electromagnetic Waves". In: *Journal of Computational Physics* 114.2 (Oct. 1994), pp. 185-200 (cit. on p. 31).
- [8] Hans Bodén and Mats Åbom. "Influence of Errors on the Two-microphone Method for Measuring Acoustic Properties in Ducts". In: *The Journal of the Acoustical Society of America* 79.2 (Feb. 1986), pp. 541-549 (cit. on p. 106).
- [9] Giorgio V. Borgiotti. "The Power Radiated by a Vibrating Body in an Acoustic Fluid and Its Determination from Boundary Measurements". In: *The Journal of the Acoustical Society of America* 88.4 (Oct. 1990), pp. 1884-1893 (cit. on p. 31).
- [10] Mary C. Boyce and Ellen M. Arruda. "Constitutive Models of Rubber Elasticity: A Review". en. In: *Rubber Chemistry and Technology* 73.3 (July 2000), pp. 504-523 (cit. on p. 55).
- [11] Anders Brandt. "The ABRAVIBE Toolbox for Teaching Vibration Analysis and Structural Dynamics". In: *Special Topics in Structural Dynamics, Volume 6*. Springer, 2013, pp. 131-141 (cit. on p. 65).
- [12] R. Bustamante, A. Dorfmann, and R. W. Ogden. "Nonlinear Electroelastostatics: A Variational Framework". en. In: *Zeitschrift für angewandte Mathematik und Physik* 60.1 (Jan. 2009), pp. 154-177 (cit. on p. 21).
- [13] Chongjing Cao, Thomas L. Hill, Bo Li, Lei Wang, and Xing Gao. "Nonlinear Dynamics of a Conical Dielectric Elastomer Oscillator with Switchable Mono to Bi-Stability". en. In: *International Journal of Solids and Structures* (Feb. 2020), S0020768320300512 (cit. on p. 11).
- [14] Chongjing Cao, Thomas L Hill, and A T Conn. "On the Nonlinear Dynamics of a Circular Dielectric Elastomer Oscillator". en. In: *Smart Materials and Structures* (Apr. 2019) (cit. on p. 11).

- [15] Federico Carpi, Iain Anderson, Siegfried Bauer, et al. "Standards for Dielectric Elastomer Transducers". en. In: *Smart Materials and Structures* 24.10 (Oct. 2015), p. 105025 (cit. on pp. 55, 87).
- [16] Uttam Kumar Chakravarty. "On the Resonance Frequencies of a Membrane of a Dielectric Elastomer". In: *Mechanics Research Communications* 55 (Jan. 2014), pp. 72-76 (cit. on p. 9).
- [17] Choon Chiang Foo, Shengqiang Cai, Soo Jin Adrian Koh, Siegfried Bauer, and Zhigang Suo. "Model of Dissipative Dielectric Elastomers". en. In: *Journal of Applied Physics* 111.3 (Feb. 2012), p. 034102 (cit. on p. 12).
- [18] Robert L. Clark and Chris R. Fuller. "Optimal Placement of Piezoelectric Actuators and Polyvinylidene Fluoride Error Sensors in Active Structural Acoustic Control Approaches". In: *The Journal of the Acoustical Society of America* 92.3 (Sept. 1992), pp. 1521-1533 (cit. on p. 94).
- [19] Bernard D Coleman and Walter Noll. "The Thermodynamics of Elastic Materials with Heat Conduction and Viscosity". In: *Archive for rational mechanics and analysis* 13.1 (1963), pp. 167-178 (cit. on pp. 21, 157).
- [20] Francis Collino and Peter Monk. "The Perfectly Matched Layer in Curvilinear Coordinates". en. In: *SIAM Journal on Scientific Computing* 19.6 (Nov. 1998), pp. 2061-2090 (cit. on pp. 31, 34).
- [21] Advanced Television Systems Committee et al. "ATSC Implementation Subcommittee Finding: Relative Timing of Sound and Vision for Broadcast Operations". In: *IS-191* 26 (2003) (cit. on p. 117).
- [22] Kenneth A. Cunefare and M. Noelle Currey. "On the Exterior Acoustic Radiation Modes of Structures". In: *The Journal of the Acoustical Society of America* 96.4 (Oct. 1994), pp. 2302-2312 (cit. on p. 31).
- [23] Olivier Doaré, Gérald Kergourlay, and Clément Sambuc. "Design of a Circular Clamped Plate Excited by a Voice Coil and Piezoelectric Patches Used as a Loudspeaker". In: *Journal of Vibration and Acoustics* 135.5 (June 2013), p. 051025 (cit. on pp. 94, 96).
- [24] Luis Dorfmann and Ray W. Ogden. *Nonlinear Theory of Electroelastic and Magnetoelastic Interactions*. en. Boston, MA: Springer US, 2014 (cit. on p. 21).
- [25] P. Dubois, S. Rosset, M. Niklaus, M. Dadras, and H. Shea. "Voltage Control of the Resonance Frequency of Dielectric Electroactive Polymer (DEAP) Membranes". In: *Journal of Microelectromechanical Systems* 17.5 (Oct. 2008), pp. 1072-1081 (cit. on p. 7).
- [26] John Edmiston and David Steigmann. "Analysis of Nonlinear Electrostatic Membranes". en. In: *Mechanics and Electrodynamics of Magneto- and Electro-Elastic Materials*. CISM International Centre for Mechanical Sciences. Springer, Vienna, 2011, pp. 153-180 (cit. on pp. 21, 22, 157, 159).
- [27] David J Ewins. *Modal Testing: Theory and Practice*. Vol. 15. Research studies press Letchworth, 1984 (cit. on pp. 64, 65).
- [28] Angelo Farina. "Simultaneous Measurement of Impulse Response and Distortion with a Swept-Sine Technique". English. In: *Audio Engineering Society Convention 108*. Audio Engineering Society, Feb. 2000 (cit. on p. 83).
- [29] P.J.T. Filippi, D. Habault, P.-O. Mattei, and C. Maury. "The Role of the Resonance Modes in the Response of a Fluid-Loaded Structure". en. In: *Journal of Sound and Vibration* 239.4 (Jan. 2001), pp. 639-663 (cit. on p. 31).
- [30] J. W. Fox and N. C. Goulbourne. "Electric Field-Induced Surface Transformations and Experimental Dynamic Characteristics of Dielectric Elastomer Membranes". In: *Journal of the Mechanics and Physics of Solids* 57.8 (Aug. 2009), pp. 1417-1435 (cit. on pp. 7, 14, 132).
- [31] J. W. Fox and N. C. Goulbourne. "On the Dynamic Electromechanical Loading of Dielectric Elastomer Membranes". In: *Journal of the Mechanics and Physics of Solids* 56.8 (Aug. 2008), pp. 2669-2686 (cit. on pp. 7, 27, 119).

- [32] Jason William Fox. "Electromechanical Characterization of the Static and Dynamic Response of Dielectric Elastomer Membranes". Thesis. Virginia Tech, Aug. 2007 (cit. on p. 7).
- [33] Emil Garnell, Olivier Doaré, and Corinne Rouby. "Coupled Vibro-Acoustic Modeling of a Dielectric Elastomer Loudspeaker". en. In: *The Journal of the Acoustical Society of America* 147.3 (Mar. 2020), pp. 1812-1821 (cit. on pp. 169, 170).
- [34] Emil Garnell, Corinne Rouby, and Olivier Doaré. "Dynamics and Sound Radiation of a Dielectric Elastomer Membrane". In: *Journal of Sound and Vibration* 459 (Oct. 2019), p. 114836 (cit. on p. 132).
- [35] A. N. Gent. "A New Constitutive Relation for Rubber". In: *Rubber Chemistry and Technology* 69.1 (Mar. 1996), pp. 59-61 (cit. on pp. 23, 55).
- [36] Todd A. Gisby, Benjamin M. O'Brien, and Iain A. Anderson. "Self Sensing Feedback for Dielectric Elastomer Actuators". en. In: *Applied Physics Letters* 102.19 (May 2013), p. 193703 (cit. on p. 120).
- [37] N. C. Goulbourne, E. M. Mockensturm, and M. I. Frecker. "Electro-Elastomers: Large Deformation Analysis of Silicone Membranes". In: *International Journal of Solids and Structures* 44.9 (May 2007), pp. 2609-2626 (cit. on p. 119).
- [38] C Graf and J Maas. "A Model of the Electrodynamical Field Distribution for Optimized Electrode Design for Dielectric Electroactive Polymer Transducers". en. In: *Smart Materials and Structures* 21.9 (Sept. 2012), p. 094001 (cit. on pp. 120, 124, 138).
- [39] Christian Graf and Jürgen Maas. "In-Plane Field Propagation in EAP Transducers Based on the Equivalent Network Method". en. In: *Volume 1: Development and Characterization of Multifunctional Materials; Modeling, Simulation and Control of Adaptive Systems; Structural Health Monitoring*. Stone Mountain, Georgia, USA: ASME, Sept. 2012, p. 207 (cit. on pp. 28, 120).
- [40] Guo-Ying Gu, Jian Zhu, Li-Min Zhu, and Xiangyang Zhu. "A Survey on Dielectric Elastomer Actuators for Soft Robots". en. In: *Bioinspiration & Biomimetics* 12.1 (Jan. 2017), p. 011003 (cit. on pp. 5, 13).
- [41] F. Hecht. "New Development in Freefem++". In: *Journal of Numerical Mathematics* 20.3-4 (2013), pp. 251-266 (cit. on p. 38).
- [42] O. Heuss, W. Kaal, T. B. Klaus, and et al. "Design Approach for an Active Double-Glazed Window". In: *ISMA 2014, International Conference on Noise and Vibration Engineering. Proceedings. CD-ROM*. 2014, pp. 77-91 (cit. on p. 9).
- [43] R. Heydt, R. Kornbluh, R. Pelrine, and V. Mason. "Design and Performance of an Electrostrictive Polymer-Film Acoustic Actuator". In: *Journal of Sound and Vibration* 215.2 (Aug. 1998), pp. 297-311 (cit. on pp. 5, 6).
- [44] R.P. Heydt, R.E. Pelrine, R.D. Kornbluh, N.A. Bonwit, and J.S. Eckerle. *Compliant Electroactive Polymer Transducers for Sonic Applications*. Google Patents, Oct. 2009 (cit. on pp. 6, 8).
- [45] Richard Heydt, Roy Kornbluh, Joseph Eckerle, and Ron Pelrine. "Sound Radiation Properties of Dielectric Elastomer Electroactive Polymer Loudspeakers". In: *Smart Structures and Materials 2006: Electroactive Polymer Actuators and Devices (EAPAD)*. Vol. 6168. San Diego, California, USA: International Society for Optics and Photonics, Mar. 2006, p. 61681M (cit. on pp. 6, 12, 14, 27, 119).
- [46] Richard Heydt, Ron Pelrine, Jose Joseph, Joseph Eckerle, and Roy Kornbluh. "Acoustical Performance of an Electrostrictive Polymer Film Loudspeaker". In: *The Journal of the Acoustical Society of America* 107.2 (2000), pp. 833-839 (cit. on pp. 6, 10, 28, 132).
- [47] K. Hochradel, S. J. Rupitsch, A. Sutor, et al. "Dynamic Performance of Dielectric Elastomers Utilized as Acoustic Actuators". en. In: *Applied Physics A* 107.3 (June 2012), pp. 531-538 (cit. on p. 7).

- [48] Thorben Hoffstadt and Jürgen Maas. "Self-Sensing Control for Soft-Material Actuators Based on Dielectric Elastomers". English. In: *Frontiers in Robotics and AI* 6 (2019) (cit. on pp. 28, 120).
- [49] Thorben Hoffstadt, Philip Meier, and Jürgen Maas. "Modeling Approach for the Electrodynamics of Multilayer DE Stack-Transducers". en. In: *Volume 1: Multifunctional Materials; Mechanics and Behavior of Active Materials; Integrated System Design and Implementation; Structural Health Monitoring*. Stowe, Vermont, USA: ASME, Sept. 2016, V001T02A015 (cit. on pp. 28, 120).
- [50] Wei Hong. "Modeling Viscoelastic Dielectrics". In: *Journal of the Mechanics and Physics of Solids* 59.3 (Mar. 2011), pp. 637–650 (cit. on p. 12).
- [51] Naoki Hosoya, Shun Baba, and Shingo Maeda. "Hemispherical Breathing Mode Speaker Using a Dielectric Elastomer Actuator". In: *The Journal of the Acoustical Society of America* 138.4 (Oct. 2015), EL424–EL428 (cit. on pp. 8, 14, 27, 119).
- [52] Naoki Hosoya, Hiroaki Masuda, and Shingo Maeda. "Balloon Dielectric Elastomer Actuator Speaker". In: *Applied Acoustics* 148 (May 2019), pp. 238–245 (cit. on pp. 8, 132).
- [53] Weili Hu, Xiaofan Niu, Ran Zhao, and Qibing Pei. "Elastomeric Transparent Capacitive Sensors Based on an Interpenetrating Composite of Silver Nanowires and Polyurethane". In: *Applied Physics Letters* 102.8 (Feb. 2013), p. 083303 (cit. on p. 119).
- [54] Jiangshui Huang, Samuel Shian, Roger M. Diebold, Zhigang Suo, and David R. Clarke. "The Thickness and Stretch Dependence of the Electrical Breakdown Strength of an Acrylic Dielectric Elastomer". In: *Applied Physics Letters* 101.12 (Sept. 2012), p. 122905 (cit. on p. 87).
- [55] Arthur A. Janszen. "Electrostatic Loud-Speaker". US2631196A. Mar. 1953 (cit. on p. 3).
- [56] Kwangmok Jung, Kwang J. Kim, and Hyouk Ryeol Choi. "A Self-Sensing Dielectric Elastomer Actuator". en. In: *Sensors and Actuators A: Physical* 143.2 (May 2008), pp. 343–351 (cit. on p. 119).
- [57] W. Kaal and S. Herold. "Electroactive Polymer Actuators in Dynamic Applications". In: *IEEE/ASME Transactions on Mechatronics* 16.1 (Feb. 2011), pp. 24–32 (cit. on p. 28).
- [58] W. Kaal, S. Herold, and T. Melz. "Modeling Approaches for Electroactive Polymers". en. In: *SPIE Smart Structures and Materials + Nondestructive Evaluation and Health Monitoring*. Ed. by Yoseph Bar-Cohen. San Diego, California, USA, Mar. 2010, p. 764211 (cit. on pp. 28, 120, 122, 124, 138).
- [59] William Kaal and Sven Herold. *Numerical Investigations on Dielectric Stack Actuators with Perforated Electrodes*. Vol. 22. Sept. 2013 (cit. on p. 9).
- [60] Matti Karjalainen, Esa Piirilä, Antti Järvinen, and Jyri Huopaniemi. "Comparison of Loudspeaker Equalization Methods Based on DSP Techniques". In: *J. Audio Eng. Soc* 47.1/2 (1999), pp. 14–31 (cit. on pp. 108, 109, 114).
- [61] Christoph Keplinger, Martin Kaltenbrunner, Nikita Arnold, and Siegfried Bauer. "Capacitive Extensometry for Transient Strain Analysis of Dielectric Elastomer Actuators". In: *Applied Physics Letters* 92.19 (May 2008), p. 192903 (cit. on p. 119).
- [62] Christoph Keplinger, Tiefeng Li, Richard Baumgartner, Zhigang Suo, and Siegfried Bauer. "Harnessing Snap-through Instability in Soft Dielectrics to Achieve Giant Voltage-Triggered Deformation". en. In: *Soft Matter* 8.2 (2012), pp. 285–288 (cit. on p. 88).
- [63] Christoph Keplinger, Jeong-Yun Sun, Choon Chiang Foo, et al. "Stretchable, Transparent, Ionic Conductors". en. In: *Science* 341.6149 (Aug. 2013), pp. 984–987 (cit. on p. 12).
- [64] O Kirkeby, F Orduna, P A Nelson, and H Hamed. "Inverse Filtering in Sound Reproduction". en. In: *Measurement and Control* 26.9 (Nov. 1993), pp. 261–266 (cit. on p. 108).
- [65] Paul W. Klipsch. "A High Quality Loudspeaker of Small Dimensions". In: *The Journal of the Acoustical Society of America* 17.3 (Jan. 1946), pp. 254–258 (cit. on p. 3).

- [66] Florian Klug, Christian Endl, Susana Solano-Arana, and Helmut F. Schlaak. "Design, Fabrication, and Customized Driving of Dielectric Loudspeaker Arrays". en. In: *Electroactive Polymer Actuators and Devices (EAPAD) XXI*. Ed. by Yoseph Bar-Cohen and Iain A. Anderson. Denver, United States: SPIE, Mar. 2019, p. 73 (cit. on pp. 10, 12, 14).
- [67] Guggi Kofod, Peter Sommer-Larsen, Roy Kornbluh, and Ron Pelrine. "Actuation Response of Polyacrylate Dielectric Elastomers". en. In: *Journal of Intelligent Material Systems and Structures* 14.12 (Dec. 2003), pp. 787-793 (cit. on p. 87).
- [68] Matthias Kollosche and Guggi Kofod. "Electrical Failure in Blends of Chemically Identical, Soft Thermoplastic Elastomers with Different Elastic Stiffness". en. In: *Applied Physics Letters* 96.7 (Feb. 2010), p. 071904 (cit. on p. 87).
- [69] A. Kovetz. *Electromagnetic Theory*. Oxford, New York: Oxford University Press, Mar. 2000 (cit. on pp. 21, 124, 125, 157, 159).
- [70] Philippe Lalanne, Wei Yan, Kevin Vynck, Christophe Sauvan, and Jean-Paul Hugonin. "Light Interaction with Photonic and Plasmonic Resonances". en. In: *Laser & Photonics Reviews* 12.5 (May 2018), p. 1700113 (cit. on pp. 32, 42).
- [71] B. Lassen. "Modelling of Dielectric Elastomer Loudspeakers Including Dissipative Effects". In: *Electroactive Polymer Actuators and Devices (EAPAD) 2013*. Vol. 8687. International Society for Optics and Photonics, Apr. 2013, 86871E (cit. on p. 9).
- [72] Yunlong Li, Inkyu Oh, Jiehao Chen, Haohui Zhang, and Yuhang Hu. "Nonlinear Dynamic Analysis and Active Control of Visco-Hyperelastic Dielectric Elastomer Membrane". In: *International Journal of Solids and Structures* (May 2018) (cit. on p. 11).
- [73] Avinoam Libai and James G Simmonds. *The Nonlinear Theory of Elastic Shells*. Cambridge, UK: Cambridge university press, 2005 (cit. on pp. 25, 26).
- [74] Guochao Lu, Yong Shen, and Ziyun Liu. "Optimization of Orthotropic Distributed-Mode Loudspeaker Using Attached Masses and Multi-Exciters". In: *The Journal of the Acoustical Society of America* 131.2 (Jan. 2012), EL93-EL98 (cit. on pp. 94, 96).
- [75] F. Ma and T. K. Caughey. "Analysis of Linear Nonconservative Vibrations". In: *Journal of Applied Mechanics* 62.3 (Sept. 1995), pp. 685-691 (cit. on p. 175).
- [76] Frederikke B. Madsen, Anders E. Daugaard, Søren Hvilsted, and Anne L. Skov. "The Current State of Silicone-Based Dielectric Elastomer Transducers". en. In: *Macromolecular Rapid Communications* 37.5 (Mar. 2016), pp. 378-413 (cit. on p. 87).
- [77] Steffen Marburg. "Normal Modes in External Acoustics. Part I: Investigation of the One-Dimensional Duct Problem". en. In: *Acta acustica united with acustica* 91 (2005), p. 17 (cit. on pp. 32, 44, 180).
- [78] Steffen Marburg. "Normal Modes in External Acoustics. Part III: Sound Power Evaluation Based on Superposition of Frequency-Independent Modes". In: *Acta acustica united with acustica* 92.2 (2006), pp. 296-311 (cit. on pp. 32, 180).
- [79] Steffen Marburg, Frank Dienerowitz, Thomas Horst, and Stefan Schneider. "Normal Modes in External Acoustics. Part II: Eigenvalues and Eigenvectors in 2D". In: *Acta acustica united with acustica* 92.1 (2006), pp. 97-111 (cit. on pp. 32, 180).
- [80] Yasushi Miki. "Acoustical Properties of Porous Materials-Modifications of Delany-Bazley Models-". In: *Journal of the Acoustical Society of Japan (E)* 11.1 (1990), pp. 19-24 (cit. on p. 105).
- [81] Eric M. Mockensturm and Nakhiah Goulbourne. "Dynamic Response of Dielectric Elastomers". In: *International Journal of Non-Linear Mechanics* 41.3 (Apr. 2006), pp. 388-395 (cit. on pp. 7, 26).
- [82] Henri J.-P. MORAND and Roger OHAYON. "Fluid Structure Interaction - Applied Numerical Methods". In: (1995), 212 p. : ill., 25 cm (cit. on pp. 30, 33).

- [83] Benjamin O'Brien, Justin Thode, Iain Anderson, et al. "Integrated Extension Sensor Based on Resistance and Voltage Measurement for a Dielectric Elastomer". en. In: *The 14th International Symposium on: Smart Structures and Materials & Nondestructive Evaluation and Health Monitoring*. Ed. by Yoseph Bar-Cohen. San Diego, California, Apr. 2007, p. 652415 (cit. on p. 120).
- [84] Roger Ohayon and Jean-Sébastien Schotté. "Fluid-Structure Interaction Problems". en. In: *Encyclopedia of Computational Mechanics Second Edition*. Ed. by Erwin Stein, René de Borst, and Thomas J R Hughes. Chichester, UK: John Wiley & Sons, Ltd, Dec. 2017, pp. 1-12 (cit. on p. 30).
- [85] Roger Ohayon and Christian Soize. "Computational Vibroacoustics in Low- and Medium-Frequency Bands: Damping, ROM, and UQ Modeling". en. In: *Applied Sciences* 7.6 (June 2017), p. 586 (cit. on p. 30).
- [86] R.E. Pelrine, R.D. Kornbluh, and J.S. Eckerle. *Elastomeric Dielectric Polymer Film Sonic Actuator*. Google Patents, Jan. 2002 (cit. on pp. 6, 10).
- [87] Ron Pelrine, Roy Kornbluh, Qibing Pei, and Jose Joseph. "High-Speed Electrically Actuated Elastomers with Strain Greater Than 100%". en. In: *Science* 287.5454 (Feb. 2000), pp. 836-839 (cit. on pp. 4, 18).
- [88] Ronald E. Pelrine, Roy D. Kornbluh, and Jose P. Joseph. "Electrostriction of Polymer Dielectrics with Compliant Electrodes as a Means of Actuation". In: *Sensors and Actuators A: Physical*. Tenth IEEE International Workshop on Micro Electro Mechanical Systems 64.1 (Jan. 1998), pp. 77-85 (cit. on pp. 12, 18, 19).
- [89] Douglas M. Photiadis. "The Relationship of Singular Value Decomposition to Wave-vector Filtering in Sound Radiation Problems". In: *The Journal of the Acoustical Society of America* 88.2 (Aug. 1990), pp. 1152-1159 (cit. on p. 31).
- [90] Kimberly Pope, Alyson Tews, Mary I. Frecker, et al. "Dielectric Elastomer Laminates for Active Membrane Pump Applications". In: *Smart Structures and Materials 2004: Electroactive Polymer Actuators and Devices (EAPAD)*. Vol. 5385. International Society for Optics and Photonics, July 2004, pp. 60-68 (cit. on p. 132).
- [91] Alain Ratle and Alain Berry. "Use of Genetic Algorithms for the Vibroacoustic Optimization of a Plate Carrying Point-Masses". en. In: *The Journal of the Acoustical Society of America* 104.6 (Dec. 1998), pp. 3385-3397 (cit. on p. 94).
- [92] Chester W Rice and Edward W Kellogg. "Notes on the Development of a New Type of Hornless Loud Speaker". In: *Transactions of the American Institute of Electrical Engineers* 44 (1925), pp. 461-480 (cit. on p. 3).
- [93] G Rizzello, M Hodgins, D Naso, A York, and S Seelecke. "Modeling of the Effects of the Electrical Dynamics on the Electromechanical Response of a DEAP Circular Actuator with a Mass-Spring Load". en. In: *Smart Materials and Structures* 24.9 (Sept. 2015), p. 094003 (cit. on p. 120).
- [94] G Rizzello, D Naso, A York, and S Seelecke. "Closed Loop Control of Dielectric Elastomer Actuators Based on Self-Sensing Displacement Feedback". en. In: *Smart Materials and Structures* 25.3 (Mar. 2016), p. 035034 (cit. on p. 120).
- [95] Samuel Rosset, Oluwaseun A. Araromi, Samuel Schlatter, and Herbert R. Shea. "Fabrication Process of Silicone-Based Dielectric Elastomer Actuators". In: *Journal of Visualized Experiments : JoVE* 108 (Feb. 2016) (cit. on pp. 48, 49).
- [96] Samuel Rosset, Pit Gebbers, Benjamin M. O'Brien, and Herbert R. Shea. "The Need for Speed". In: *Electroactive Polymer Actuators and Devices (EAPAD) 2012*. Vol. 8340. International Society for Optics and Photonics, Apr. 2012, p. 834004 (cit. on p. 12).
- [97] Samuel Rosset, Luc Maffli, Simon Houis, and Herbert R. Shea. "An Instrument to Obtain the Correct Biaxial Hyperelastic Parameters of Silicones for Accurate DEA Modelling". In: *Proc. SPIE* 9056. San Diego, California, USA, Mar. 2014, p. 90560M (cit. on pp. 55, 57).

- [98] Samuel Rosset, Benjamin M O'Brien, Todd Gisby, et al. "Self-Sensing Dielectric Elastomer Actuators in Closed-Loop Operation". en. In: *Smart Materials and Structures* 22.10 (Oct. 2013), p. 104018 (cit. on pp. 118, 119).
- [99] Samuel Rosset and Herbert R. Shea. "Small, Fast, and Tough: Shrinking down Integrated Elastomer Transducers". en. In: *Applied Physics Reviews* 3.3 (Sept. 2016), p. 031105 (cit. on pp. 5, 120).
- [100] Philipp Rothmund, Xavier P. Morelle, Kun Jia, George M. Whitesides, and Zhigang Suo. "A Transparent Membrane for Active Noise Cancelation". en. In: *Advanced Functional Materials* (May 2018), p. 1800653 (cit. on p. 10).
- [101] Lucie Rouleau, Jean-François Deü, and Antoine Legay. "A Comparison of Model Reduction Techniques Based on Modal Projection for Structures with Frequency-Dependent Damping". en. In: *Mechanical Systems and Signal Processing* 90 (June 2017), pp. 110-125 (cit. on p. 32).
- [102] Emiliano Rustighi, William Kaal, Sven Herold, and Ahmed Kubbara. "Experimental Characterisation of a Flat Dielectric Elastomer Loudspeaker". en. In: *Actuators* 7.2 (June 2018), p. 28 (cit. on pp. 9, 12).
- [103] Junjie Sheng, Hualing Chen, Lei Liu, et al. "Dynamic Electromechanical Performance of Viscoelastic Dielectric Elastomers". In: *Journal of Applied Physics* 114.13 (Oct. 2013), p. 134101 (cit. on p. 12).
- [104] Jean-François Sigrist. *Fluid-Structure Interaction: An Introduction to Finite Element Coupling*. John Wiley & Sons, 2015 (cit. on p. 30).
- [105] Peter Sommer-Larsen, Jacob C. Hooker, Guggi Kofod, et al. "Response of Dielectric Elastomer Actuators". en. In: *SPIE's 8th Annual International Symposium on Smart Structures and Materials*. Ed. by Yoseph Bar-Cohen. Newport Beach, CA, USA, July 2001, p. 157 (cit. on p. 119).
- [106] Takehiro Sugimoto, Akio Ando, Kazuho Ono, et al. "A Lightweight Push-Pull Acoustic Transducer Composed of a Pair of Dielectric Elastomer Films". In: *The Journal of the Acoustical Society of America* 134.5 (Oct. 2013), EL432-EL437 (cit. on p. 8).
- [107] Takehiro Sugimoto, Kazuho Ono, Akio Ando, et al. "Efficiency of Semicylindrical Acoustic Transducer from a Dielectric Elastomer Film". In: *Acoustical Science and Technology* 33.3 (2012), pp. 208-210 (cit. on p. 8).
- [108] Zhigang Suo. "Theory of Dielectric Elastomers". In: *Acta Mechanica Sinica* 23.6 (Dec. 2010), pp. 549-578 (cit. on pp. 21, 159).
- [109] Zhigang Suo, Xuanhe Zhao, and William H. Greene. "A Nonlinear Field Theory of Deformable Dielectrics". In: *Journal of the Mechanics and Physics of Solids* 56.2 (2008), pp. 467-486 (cit. on p. 21).
- [110] Hironori Tokuno, Ole Kirkeby, Philip A Nelson, and Hareo Hamada. "Inverse Filter of Sound Reproduction Systems Using Regularization". In: *IEICE transactions on fundamentals of electronics, communications and computer sciences* 80.5 (1997), pp. 809-820 (cit. on pp. 109, 110, 114).
- [111] C. Touzé and M. Amabili. "Nonlinear Normal Modes for Damped Geometrically Nonlinear Systems: Application to Reduced-Order Modelling of Harmonically Forced Structures". en. In: *Journal of Sound and Vibration* 298.4 (Dec. 2006), pp. 958-981 (cit. on p. 144).
- [112] Ursula van Rienen, Jürgen Flehr, Ute Schreiber, and Victor Motrescu. "Modeling and Simulation of Electro-Quasistatic Fields". en. In: *Modeling, Simulation, and Optimization of Integrated Circuits*. Ed. by Kurt Antreich, Roland Bulirsch, Albert Gilg, and Peter Rentrop. ISNM International Series of Numerical Mathematics. Birkhäuser Basel, 2003, pp. 17-31 (cit. on p. 125).
- [113] W. Kaal, S. Herold, and T. Melz. "Design and Modeling of Dielectric Elastomer Actuators". In: vol. 8340. 2012, pp. 83402D-8340-10 (cit. on p. 9).

- [114] Chih-Ta Wang and Shi-Chern Yen. "Theoretical Analysis of Film Uniformity in Spinning Processes". In: *Chemical Engineering Science* 50.6 (Mar. 1995), pp. 989-999 (cit. on p. 46).
- [115] Michael Wissler and Edoardo Mazza. "Electromechanical Coupling in Dielectric Elastomer Actuators". In: *Sensors and Actuators A: Physical* 138.2 (Aug. 2007), pp. 384-393 (cit. on p. 19).
- [116] Bai-Xiang Xu, Ralf Mueller, Anika Theis, Markus Klassen, and Dietmar Gross. "Dynamic Analysis of Dielectric Elastomer Actuators". In: *Applied Physics Letters* 100.11 (Mar. 2012), p. 112903 (cit. on p. 11).
- [117] Daniel Xu, Silvain Michel, Thomas McKay, et al. "Sensing Frequency Design for Capacitance Feedback of Dielectric Elastomers". en. In: *Sensors and Actuators A: Physical* 232 (Aug. 2015), pp. 195-201 (cit. on pp. 28, 121).
- [118] Daniel Xu, Andreas Tairych, and Iain A Anderson. "Stretch Not Flex: Programmable Rubber Keyboard". en. In: *Smart Materials and Structures* 25.1 (Jan. 2016), p. 015012 (cit. on pp. 121, 124).
- [119] Daniel Xu, Andreas Tairych, and Iain A. Anderson. "Where the Rubber Meets the Hand: Unlocking the Sensing Potential of Dielectric Elastomers". en. In: *Journal of Polymer Science Part B: Polymer Physics* 54.4 (2016), pp. 465-472 (cit. on p. 121).
- [120] S. C. Xu, B. Y. Man, S. Z. Jiang, et al. "Flexible and Transparent Graphene-Based Loudspeakers". In: *Applied Physics Letters* 102.15 (Apr. 2013), p. 151902 (cit. on pp. 7, 12).
- [121] Wei Yan, Rémi Faggiani, and Philippe Lalanne. "Rigorous Modal Analysis of Plasmonic Nanoresonators". en. In: *Physical Review B* 97.20 (May 2018) (cit. on p. 32).
- [122] X. Yu, R. Rajamani, K. A. Stelson, and T. Cui. "Carbon Nanotube-Based Transparent Thin Film Acoustic Actuators and Sensors". In: *Sensors and Actuators A: Physical* 132.2 (Nov. 2006), pp. 626-631 (cit. on pp. 7, 12).
- [123] Junshi Zhang, Hualing Chen, Junjie Sheng, et al. "Dynamic Performance of Dissipative Dielectric Elastomers under Alternating Mechanical Load". en. In: *Applied Physics A* 116.1 (July 2014), pp. 59-67 (cit. on p. 12).
- [124] Xuanhe Zhao, Soo Jin Adrian Koh, and Zhigang Suo. "Nonequilibrium Thermodynamics of Dielectric Elastomers". In: *International Journal of Applied Mechanics* 03.02 (June 2011), pp. 203-217 (cit. on p. 12).
- [125] Jian Zhu, Shengqiang Cai, and Zhigang Suo. "Nonlinear Oscillation of a Dielectric Elastomer Balloon". en. In: *Polymer International* 59.3 (Mar. 2010), pp. 378-383 (cit. on p. 10).
- [126] Jian Zhu, Shengqiang Cai, and Zhigang Suo. "Resonant Behavior of a Membrane of a Dielectric Elastomer". In: *International Journal of Solids and Structures* 47.24 (Dec. 2010), pp. 3254-3262 (cit. on pp. 8, 11, 14, 26, 69, 70, 73).

Appendix

Constitutive equations of dielectric elastomers

In this appendix, the constitutive relations of DEs are derived, following the method of Coleman and Noll [19], applied to dielectric elastomers by Kovetz [69], and simplified for DE membranes by Edmiston & Steigmann [26].

We consider a dielectric body partially covered by electrodes on its surface.

In the absence of any electric charge or mechanical load, the body occupies a reference configuration, where each material particle is identified by its position $\bar{\mathbf{X}}$. Under electrical and mechanical loading, the body is transformed to a deformed configuration: the material point initially in $\bar{\mathbf{X}}$ moves to the position \mathbf{X} .

The deformation gradient tensor is defined by $\mathbf{F} = \partial \mathbf{X} / \partial \bar{\mathbf{X}}$. In the deformed configuration, body forces per unit mass \mathbf{T}_v and surface forces \mathbf{T}_b are applied to the body, as well as electric surface charges σ_b . It is assumed that there is no electric body charge.

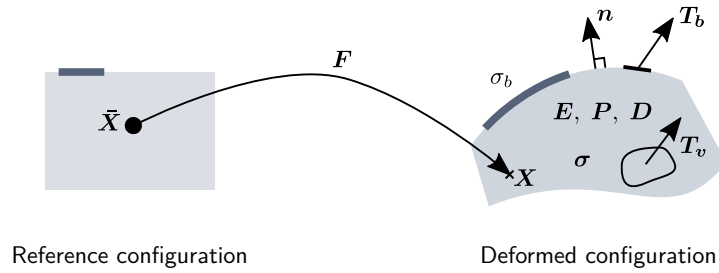


Fig. A.1. Description of a material sample and definition of external loads

The problem is sketched in fig. A.1. The mass density is denoted by ρ_s , the Cauchy stress tensor by $\boldsymbol{\sigma}$, and the electric displacement by $\mathbf{D} = \epsilon_0 \mathbf{E} + \mathbf{P}$, where ϵ_0 is the vacuum permittivity, \mathbf{E} the electric field and \mathbf{P} the electric polarization density, all in the deformed configuration. The Lagrangian time derivative d/dT is written $(\dot{})$, and the notation $\boldsymbol{\nabla} = \partial/\partial \bar{\mathbf{X}}$ is introduced.

If the resistivity of the electrodes is low enough, the time scale for electrodynamic effects is much shorter than that for mechanics. It is therefore assumed that Maxwell's equations for electrostatics hold.

The local electrostatic equations (Gauss and Faraday), linear momentum balance and mass conservation are thus:

$$\boldsymbol{\nabla} \cdot \mathbf{D} = 0, \quad \boldsymbol{\nabla} \times \mathbf{E} = \mathbf{0}, \quad \rho_s \ddot{\mathbf{X}} = \boldsymbol{\nabla} \cdot \boldsymbol{\sigma} + \rho_s \mathbf{T}_v, \quad \dot{\rho}_s + \rho_s \boldsymbol{\nabla} \cdot \dot{\mathbf{X}} = 0. \quad (\text{A.1})$$

The related jump conditions on the boundaries are:

$$\mathbf{n} \cdot \llbracket \mathbf{D} \rrbracket = \sigma_b, \quad \mathbf{n} \times \llbracket \mathbf{E} \rrbracket = \mathbf{0}, \quad \mathbf{n} \cdot \llbracket \boldsymbol{\sigma} \rrbracket + \mathbf{T}_b = \mathbf{0}, \quad (\text{A.2})$$

where \mathbf{n} denotes the normal to the surface and $\llbracket a \rrbracket = a(\mathbf{X}^+) - a(\mathbf{X}^-)$, \mathbf{X}^+ and \mathbf{X}^- being points just outside and inside of the surface respectively.

In the following, we search for a constitutive relation compatible with the local balance equations (A.1) and (A.2). Thermodynamic principles will restrict the expression of the constitutive relation: the global energy balance and entropy imbalance need to be satisfied. They read, for any arbitrary region $\Omega \subset \mathbb{R}^3$ of boundary $\partial\Omega$:

$$\begin{aligned} \frac{d}{dt} \left(\int_{\Omega} \rho_s \varepsilon d\Omega \right) &= \int_{\Omega} \mathbf{T}_v \cdot \dot{\mathbf{X}} \rho_s d\Omega - \int_{\partial\Omega} (\boldsymbol{\sigma} \cdot \mathbf{n}) \cdot \dot{\mathbf{X}} dA \\ &\quad + \int_{\Omega} \rho_s \vartheta d\Omega + \int_{\partial\Omega} -\mathbf{Q} \cdot \mathbf{n} dA - \int_{\partial\Omega} \mathbf{E} \times (\dot{\mathbf{X}} \times \mathbf{D}) \cdot \mathbf{n} dA, \end{aligned} \quad (\text{A.3})$$

$$\frac{d}{dt} \left(\int_{\Omega} \rho_s \eta d\Omega \right) \geq \int_{\Omega} \rho_s \vartheta \theta_T^{-1} d\Omega + \int_{\partial\Omega} -\mathbf{Q} \cdot \mathbf{n} \theta_T^{-1} dA, \quad (\text{A.4})$$

where ε is the total energy per unit mass, \mathbf{Q} the heat flux, ϑ the volume heat source, η the entropy, and θ_T the temperature. The two first terms on the right hand side of eq. (A.3) are the mechanical power, the two next ones the thermal power, and the last one the electrostatic power.

Using eq. (A.1) in eqs. (A.3) and (A.4), applying the divergence theorem and using vector identities yields the local energy balance and entropy imbalance:

$$\rho_s \dot{\varepsilon} = \rho_s (\dot{\mathbf{X}} \cdot \ddot{\mathbf{X}} + \vartheta) + [\boldsymbol{\sigma} - \mathbf{D} \otimes \mathbf{E} + (\mathbf{E} \cdot \mathbf{D}) \mathbf{I}] : \dot{\mathbf{F}} + \mathbf{E} \cdot \dot{\mathbf{D}} - \nabla \cdot \mathbf{Q}, \quad (\text{A.5})$$

$$\rho_s \dot{\eta} \geq \rho_s \vartheta \theta_T^{-1} - \nabla \cdot (\mathbf{Q} \theta_T^{-1}). \quad (\text{A.6})$$

Replacing the heat source ϑ in eq. (A.6) using eq. (A.5) yields:

$$\begin{aligned} -\rho_s \dot{\varepsilon} + \rho_s (\theta_T \dot{\eta} + \dot{\mathbf{X}} \cdot \ddot{\mathbf{X}}) + [\boldsymbol{\sigma} - \mathbf{D} \otimes \mathbf{E} + (\mathbf{E} \cdot \mathbf{D}) \mathbf{I}] : \dot{\mathbf{F}} + \mathbf{E} \cdot (\epsilon_0 \dot{\mathbf{E}} + \dot{\mathbf{P}}) \\ - \theta_T^{-1} \mathbf{Q} \cdot (\nabla \theta_T) \geq 0. \end{aligned} \quad (\text{A.7})$$

This equation shows that variations of the internal energy ε are related to variations of $\dot{\mathbf{X}}$, $\dot{\mathbf{F}}$, $\dot{\mathbf{E}}$, $\dot{\mathbf{P}}$ and η .

Therefore, ε must be a function of those five variables only, or of five independent combinations of them. Computing the derivatives of ε and inserting into the entropy imbalance eq. (A.7) yields:

$$\begin{aligned} \rho_s \left[\left(\theta_T - \frac{\partial \varepsilon}{\partial \eta} \right) \dot{\eta} + \dot{\mathbf{X}} \cdot \left(\dot{\mathbf{X}} - \frac{\partial \varepsilon}{\partial \dot{\mathbf{X}}} \right) \right] + \left[-\rho_s \left(\frac{\partial \varepsilon}{\partial \mathbf{F}} \cdot \mathbf{F}^T \right)^T + \boldsymbol{\sigma} - \mathbf{D} \otimes \mathbf{E} + (\mathbf{E} \cdot \mathbf{D}) \mathbf{I} \right] : \dot{\mathbf{F}} \\ + \left(\epsilon_0 \mathbf{E} - \rho_s \frac{\partial \varepsilon}{\partial \mathbf{E}} \right) \cdot \dot{\mathbf{E}} + \left(\mathbf{E} - \rho_s \frac{\partial \varepsilon}{\partial \mathbf{P}} \right) \cdot \dot{\mathbf{P}} - \theta_T^{-1} \mathbf{Q} \cdot (\nabla \theta_T) \geq 0. \end{aligned} \quad (\text{A.8})$$

As $\dot{\mathbf{X}}, \mathbf{F}, \mathbf{E}, \mathbf{P}$ and η are independent variables that can take arbitrary values, the internal energy ε must satisfy the following equations:

$$\begin{aligned} \frac{\partial \varepsilon}{\partial \eta} &= \theta_T, & \frac{\partial \varepsilon}{\partial \dot{\mathbf{X}}} &= \dot{\mathbf{X}}, & \rho_s \left(\frac{\partial \varepsilon}{\partial \mathbf{F}} \cdot \mathbf{F}^T \right)^T &= \boldsymbol{\sigma} - \mathbf{D} \otimes \mathbf{E} + (\mathbf{E} \cdot \mathbf{D}) \mathbf{I}, \\ \rho_s \frac{\partial \varepsilon}{\partial \mathbf{E}} &= \epsilon_0 \mathbf{E}, & \rho_s \frac{\partial \varepsilon}{\partial \mathbf{P}} &= \mathbf{E}, \end{aligned} \quad (\text{A.9})$$

and the heat flux \mathbf{Q} is restricted by the condition $\theta_T^{-1} \mathbf{Q} \cdot (\nabla \theta_T) \leq 0$. For a given expression of ε in terms of $\dot{\mathbf{X}}, \mathbf{F}, \mathbf{E}, \mathbf{P}$ and η , eq. (A.9) specify the constitutive relations of the coupled system. These equations can be simplified, by defining the free energy ψ :

$$\psi = \varepsilon - \frac{1}{2} \dot{\mathbf{X}} \cdot \dot{\mathbf{X}} - \eta \theta_T - \frac{\epsilon_0}{2 \rho_s} \mathbf{E} \cdot \mathbf{E} - \frac{1}{\rho_s} \mathbf{E} \cdot \mathbf{P}. \quad (\text{A.10})$$

Computing the derivatives of ψ in terms of the derivatives of ε , and using eq. (A.9) shows that ψ is a function of \mathbf{F}, \mathbf{E} , and θ_T only. Finally the expression of ε in terms of ψ can be substituted into eq. (A.7), yielding:

$$\begin{aligned} \rho_s \left[- \left(\frac{\partial \psi}{\partial \mathbf{E}} + \frac{\mathbf{P}}{\rho_s} \right) \cdot \dot{\mathbf{E}} - \left(\frac{\partial \psi}{\partial \theta_T} + \eta \right) \dot{\theta}_T \right] \\ + \left[- \rho_s \left(\frac{\partial \psi}{\partial \mathbf{F}} \cdot \mathbf{F}^T \right)^T + \boldsymbol{\sigma} - \mathbf{D} \otimes \mathbf{E} + \frac{\epsilon_0}{2} (\mathbf{E} \cdot \mathbf{E}) \mathbf{I} \right] : \dot{\mathbf{F}} - \theta_T^{-1} \mathbf{Q} \cdot (\nabla \theta_T) \geq 0. \end{aligned} \quad (\text{A.11})$$

And again for the energy imbalance eq. (A.11) to hold for any arbitrary evolution, the following equations need to be satisfied:

$$\frac{\partial \psi}{\partial \mathbf{E}} = - \frac{\mathbf{P}}{\rho_s}, \quad \frac{\partial \psi}{\partial \theta_T} = - \eta, \quad \boldsymbol{\sigma} = \rho_s \left(\frac{\partial \psi}{\partial \mathbf{F}} \cdot \mathbf{F}^T \right)^T + \mathbf{D} \otimes \mathbf{E} - \frac{\epsilon_0}{2} (\mathbf{E} \cdot \mathbf{E}) \mathbf{I}. \quad (\text{A.12})$$

We now assume that the transformation is isotherm, which removes the dependence on θ_T of the free energy. The principle of material frame invariance [69] implies that the free energy should depend only on the Cauchy-Green tensor $\mathbf{C} = \mathbf{F}^T \cdot \mathbf{F}$ and on the electric field in reference configuration $\bar{\mathbf{E}} = \mathbf{F}^T \cdot \mathbf{E}$, that is to say $\psi(\mathbf{F}, \mathbf{E}) = \phi(\mathbf{C}, \bar{\mathbf{E}})$. Equating variations of ψ and ϕ yields :

$$\boldsymbol{\sigma} = 2 \rho_s \mathbf{F} \cdot \frac{\partial \phi}{\partial \mathbf{C}} \cdot \mathbf{F}^T + \epsilon_0 \mathbf{E} \otimes \mathbf{E} - \frac{\epsilon_0}{2} (\mathbf{E} \cdot \mathbf{E}) \mathbf{I}, \quad \mathbf{P} = - \rho_s \mathbf{F} \cdot \frac{\partial \phi}{\partial \bar{\mathbf{E}}}. \quad (\text{A.13})$$

Equations (A.13) are the two constitutive equations giving the material behavior, which is fully described by the specification of the free energy function ϕ . The first resembles the classical mechanical equation relating the Cauchy stress tensor to the free energy, but with added terms that depend on electrostatics.

Following the method of Edminton and Steigmann [26], a realistic free energy function is now searched for. In this step, we aim at reproducing behaviors that have been observed experimentally.

Typical DEs have been shown to be linear for the electrostatics (the material polarization \mathbf{P} is proportional to the electric field \mathbf{E} , meaning that the permittivity ϵ does not depend on the deformation). This class of materials is called *ideal DEs* by Suo [108]. Also,

when no electric field is applied, the material should behave as a standard hyperelastic material. Therefore, a free energy function that satisfies the two following conditions is searched for:

$$\mathbf{P} = \epsilon_0 \chi_e \mathbf{E} , \quad (\text{A.14a})$$

$$\boldsymbol{\sigma} = \rho_s \left(2\mathbf{F} \cdot \frac{\partial \phi_0}{\partial \mathbf{C}} \cdot \mathbf{F}^T \right)^T \quad \text{when } \bar{\mathbf{E}} = 0 , \quad (\text{A.14b})$$

where ϕ_0 is a purely mechanical free energy, and χ_e the electrical susceptibility. We suggest the following form of the free energy, which fulfills the two conditions:

$$\phi(\mathbf{C}, \bar{\mathbf{E}}, \Pi) = \phi_0(\mathbf{C}) - \frac{\epsilon_0 \chi_e J}{2\rho_s} \bar{\mathbf{E}} \cdot \mathbf{C}^{-1} \cdot \bar{\mathbf{E}} . \quad (\text{A.15})$$

For this specific form of the free energy, eq. (A.13) implies that the total stress is the sum of a purely mechanical stress $\boldsymbol{\sigma}_0$ and a Maxwell stress:

$$\boldsymbol{\sigma} = \boldsymbol{\sigma}_0 + \boldsymbol{\sigma}_{\text{Maxwell}} , \quad (\text{A.16a})$$

$$\text{with } \boldsymbol{\sigma}_0 = 2\rho_s \mathbf{F} \cdot \frac{\partial \phi_0}{\partial \mathbf{C}} \cdot \mathbf{F}^T , \quad \text{and } \boldsymbol{\sigma}_{\text{Maxwell}} = \epsilon \left(\mathbf{E} \otimes \mathbf{E} - \frac{1}{2} \mathbf{E} \cdot \mathbf{E} \mathbf{I} \right) , \quad (\text{A.16b})$$

where $\epsilon = \epsilon_0(1 + \chi_e)$. Equation (A.16) is a well known equation that is used by most people working with DEs. They have here been thoroughly derived starting from general equilibrium equations, making clear the assumptions that have been made to obtain these equations. The distinction between the mechanical and the Maxwell stress appears to have no importance, as all equilibrium equations depend on the total stress $\boldsymbol{\sigma}$.

Linearized weak forms

B.1 Static deformation

B.1.1 Solving **step 1**

In the first step (**step 1**, see Figure 2.1 the definition of the different calculation steps), the membrane is inflated with the pressure p_{app} , and the resulting non-linear static deformation is computed.

The weak form of the equations governing the static evolution of the membrane is eq. (2.56):

$$\int_{\Sigma} \mathcal{Y}' \frac{\bar{r} \bar{h} s_1 y'}{\lambda_1^2} dl + \int_{\Sigma} \mathcal{X}' \frac{\bar{r} \bar{h} s_1 x'}{\lambda_1^2} dl + \int_{\Sigma} \frac{1}{\lambda_1} s_2 \bar{h} \mathcal{X} dl - \int_{\Sigma} \frac{1}{\lambda_1} (p_{\text{app}}) (-y' \mathcal{X} + x' \mathcal{Y}) x dl = 0 ,$$

$$\forall \mathcal{X}, \mathcal{Y}, \quad |\mathcal{X}(\bar{r} = 1) = \mathcal{Y}(\bar{r} = 1) = 0 , \quad (\text{B.1})$$

where the nominal non-dimensional stresses are defined by (2.55):

$$s_1 = \frac{J_m(1 + i\eta)}{J_m - I_1 + 3} (\lambda_1 - \lambda_1^{-3} \lambda_2^{-2}) - u_0^2 \frac{\Gamma}{h^2} \lambda_1 \lambda_2^2 \quad (\text{B.2a})$$

$$s_2 = \frac{J_m(1 + i\eta)}{J_m - I_1 + 3} (\lambda_2 - \lambda_1^{-2} \lambda_2^{-3}) - u_0^2 \frac{\Gamma}{h^2} \lambda_1^2 \lambda_2 \quad (\text{B.2b})$$

These equations need to be linearized, to provide the gradient for Newton-Raphson's method.

An initial state is defined, and written with zero subscripts (x_0, y_0) . We stress that the initial state (x_0, y_0) is not the **static configuration** defined in fig. 2.1. Small perturbations this initial state are introduced, and written with tildes:

$$\begin{aligned} x &= x_0 + \tilde{x} , & y &= y_0 + \tilde{y} , & s_1 &= s_{10} + \tilde{s}_1 , & s_2 &= s_{20} + \tilde{s}_2 , \\ I_1 &= I_{10} + \tilde{I}_1 , & \lambda_1 &= \lambda_{10} + \tilde{\lambda}_1 , & \lambda_2 &= \lambda_{20} + \tilde{\lambda}_2 . \end{aligned} \quad (\text{B.3})$$

All quantities that appear in eq. (B.2) need to be linearized. Writing only the first order terms, the strains read:

$$\lambda_1 = \sqrt{\left(\frac{\partial x_0}{\partial \bar{r}}\right)^2 + \left(\frac{\partial y_0}{\partial \bar{y}}\right)^2} + \frac{1}{\lambda_{10}} (x'_0 \tilde{x}' + y'_0 \tilde{y}') ,$$

$$\lambda_2 = \frac{x_0}{\bar{r}} + \frac{\tilde{x}}{\bar{r}} ,$$

and the first invariant of the deformation tensor reads:

$$I_1 = \lambda_{10}^2 + \lambda_{20}^2 + \lambda_{10}^{-2} \lambda_{20}^{-2} \\ + 2\lambda_{10} \tilde{\lambda}_1 + 2\lambda_{20} \tilde{\lambda}_2 - 2\lambda_{10}^{-3} \lambda_{20}^{-2} \tilde{\lambda}_1 - 2\lambda_{10}^{-2} \lambda_{20}^{-3} \tilde{\lambda}_2 .$$

The linearized stresses are obtained:

$$s_1 = \frac{J_m(1+i\eta)}{J_m - I_{10} + 3} (\lambda_{10} - \lambda_{10}^{-3} \lambda_{20}^{-2}) - u_0^2 \frac{\Gamma}{\bar{h}^2} \lambda_{10} \lambda_{20}^2 \\ + \frac{J_m(1+i\eta)}{(J_m - I_{10} + 3)^2} \tilde{I}_1 (\lambda_{10} - \lambda_{10}^{-3} \lambda_{20}^{-2}) \\ + \frac{J_m(1+i\eta)}{J_m - I_{10} + 3} (\tilde{\lambda}_1 + 3\lambda_{10}^{-4} \lambda_{20}^{-2} \tilde{\lambda}_1 + 2\lambda_{10}^{-3} \lambda_{20}^{-3} \tilde{\lambda}_2) \\ - u_0^2 \frac{\Gamma}{\bar{h}^2} (\lambda_{20}^2 \tilde{\lambda}_1 + 2\lambda_{10} \lambda_{20} \tilde{\lambda}_2) \\ s_2 = \frac{J_m(1+i\eta)}{J_m - I_{10} + 3} (\lambda_{20} - \lambda_{10}^{-2} \lambda_{20}^{-3}) - u_0^2 \frac{\Gamma}{\bar{h}^2} \lambda_{10}^2 \lambda_{20} \\ + \frac{J_m(1+i\eta)}{(J_m - I_{10} + 3)^2} \tilde{I}_1 (\lambda_{20} - \lambda_{10}^{-2} \lambda_{20}^{-3}) \\ + \frac{J_m(1+i\eta)}{J_m - I_{10} + 3} (\tilde{\lambda}_2 + 3\lambda_{10}^{-2} \lambda_{20}^{-4} \tilde{\lambda}_2 + 2\lambda_{10}^{-3} \lambda_{20}^{-3} \tilde{\lambda}_1) \\ - u_0^2 \frac{\Gamma}{\bar{h}^2} (\lambda_{10}^2 \tilde{\lambda}_2 + 2\lambda_{10} \lambda_{20} \tilde{\lambda}_1)$$

Inserting the linearized quantities in the weak form eq. (B.1) defines the residual for Newton-Raphson's method:

$$\begin{aligned} \Re([x_0 + \tilde{x}, y_0 + \tilde{y}], [\mathcal{X}, \mathcal{Y}]) = \\ (V_s) \quad & \int_{\Sigma} \mathcal{Y}' \frac{\bar{r} \bar{h} s_{10} y'_0}{\lambda_{10}} d\bar{r} + \int_{\Sigma} \mathcal{X}' \frac{\bar{r} \bar{h} s_{10} x'_0}{\lambda_{10}} d\bar{r} + \int_{\Sigma} s_{20} \bar{h} \mathcal{X} d\bar{r} - \int_{\Sigma} p_0 (-y'_0 \mathcal{X} + x'_0 \mathcal{Y}) x_0 d\bar{r} \\ (K_s) \quad & + \int_{\Sigma} \mathcal{Y}' \frac{r \bar{h} \tilde{s}_1}{\lambda_{10}} y'_0 d\bar{r} - \int_{\Sigma} \mathcal{Y}' \frac{r \bar{h} s_{10}}{\lambda_{10}^2} y'_0 \tilde{\lambda}_1 d\bar{r} + \int_{\Sigma} \mathcal{Y}' \frac{r \bar{h} s_{10}}{\lambda_{10}} \tilde{y}' d\bar{r} \\ (K_s) \quad & + \int_{\Sigma} \mathcal{X}' \frac{r \bar{h} \tilde{s}_1}{\lambda_{10}} x'_0 d\bar{r} - \int_{\Sigma} \mathcal{X}' \frac{r \bar{h} s_{10}}{\lambda_{10}^2} x'_0 \tilde{\lambda}_1 d\bar{r} + \int_{\Sigma} \mathcal{X}' \frac{r \bar{h} s_{10}}{\lambda_{10}} \tilde{x}' d\bar{r} \\ (K_s) \quad & + \int_{\Sigma} \tilde{s}_2 \bar{h} \mathcal{X} d\bar{r} \\ (K_s) \quad & - \int_{\Sigma} p_{\text{app}} (\tilde{x} x'_0 + x_0 \tilde{x}') \mathcal{Y} d\bar{r} + \int_{\Sigma} p_{\text{app}} (\tilde{x} y'_0 + x_0 \tilde{y}') \mathcal{X} d\bar{r} . \end{aligned} \quad (\text{B.4})$$

Equation (B.4) defines a linear form, and a bilinear form. These forms are discretized in the finite element software FreeFEM++, to build the vector V_s and the matrix K_s . A mesh of the membrane in the reference configuration is used, with 100 P2 Lagrange elements along the radius.

The matrix equation solved at each step of Newton-Raphson's algorithm is:

$$K_s \begin{bmatrix} \tilde{x} \\ \tilde{y} \end{bmatrix} + V_s = 0 \quad (\text{B.5})$$

At each step of the Newton Raphson algorithm, the initial guess of the solution is updated by:

$$\begin{bmatrix} x_0 \\ y_0 \end{bmatrix} = \begin{bmatrix} x_0 \\ y_0 \end{bmatrix} + \begin{bmatrix} \tilde{x} \\ \tilde{y} \end{bmatrix}, \quad (\text{B.6})$$

where $[\tilde{x}, \tilde{y}]$ is the solution of eq. (B.5). This loop is stopped when the L2 norm of $[\tilde{x}, \tilde{y}]$ is smaller than a chosen value, typically 1×10^{-8} .

B.1.2 Solving **step 2**

In step 2, the cavity is closed, so the amount of air that it contains is fixed. The pressure will drop as the voltage is increased, because the volume of the membrane increases.

The weak form of the equations governing the static evolution of the membrane is eq. (2.56):

$$\int_{\Sigma} \mathcal{Y}' \frac{\bar{r} \bar{h} s_1 y'}{\lambda_1^2} dl + \int_{\Sigma} \mathcal{X}' \frac{\bar{r} \bar{h} s_1 x'}{\lambda_1^2} dl + \int_{\Sigma} \frac{1}{\lambda_1} s_2 \bar{h} \mathcal{X} dl - \int_{\Sigma} \frac{1}{\lambda_1} p_i (-y' \mathcal{X} + x' \mathcal{Y}) x dl$$

$$\forall \mathcal{X}, \mathcal{Y} \mid \mathcal{X}(\bar{r} = 1) = \mathcal{Y}(\bar{r} = 1) = 0, \quad (\text{B.7})$$

where p_i is the pressure inside the cavity.

Similarly to **step 1**, small perturbations are introduced around the initial guess of the solution (the result of **step 1** is used as initial guess):

$$x = x_0 + \tilde{x}, \quad \tilde{y} = y_0 + \tilde{y}, \quad p_i = p_0 + p_u. \quad (\text{B.8})$$

The perturbation of the pressure is written p_u instead of \tilde{p} because it obeys an adiabatic evolution, as p_u in eq. (2.52):

$$\mathcal{P}_u p_u + \mathcal{P}_u \frac{mc^2}{v_0} 2\pi \int_{\Sigma} \frac{1}{\lambda_{10}} (-y'_0 \tilde{x} + x'_0 \tilde{y}) x_0 dl = 0, \quad \forall \mathcal{P}_u. \quad (\text{B.9})$$

Equation (B.9) is the linearized form of the adiabatic evolution $PV^\gamma = \text{cst}$, but is sufficient because the pressure variations inside the cavity will remain small compared to the atmospheric pressure.

The linearized weak form governing the evolution of the system in **step 2** is:

$$\begin{aligned}
& \Re([x_0 + \tilde{x}, y_0 + \tilde{y}, p_0 + p_u], [\mathcal{X}, \mathcal{Y}, \mathcal{P}_u]) = \\
(V_s) \quad & \int_{\Sigma} \mathcal{Y}' \frac{\bar{r} \bar{h} s_{10} y'}{\lambda_{10}} d\bar{r} + \int_{\Sigma} \mathcal{X}' \frac{\bar{r} \bar{h} s_{10} x'}{\lambda_{10}} d\bar{r} + \int_{\Sigma} s_{20} \bar{h} \mathcal{X} d\bar{r} - \int_{\Sigma} p_0 (-y'_0 \mathcal{X} + x'_0 \mathcal{Y}) x_0 d\bar{r} \\
(K_s) \quad & + \int_{\Sigma} \mathcal{Y}' \frac{r \bar{h} \tilde{s}_1}{\lambda_{10}} y'_0 d\bar{r} - \int_{\Sigma} \mathcal{Y}' \frac{r \bar{h} s_{10}}{\lambda_{10}^2} y'_0 \tilde{\lambda}_1 d\bar{r} + \int_{\Sigma} \mathcal{Y}' \frac{r \bar{h} s_{10}}{\lambda_{10}} \tilde{y}' d\bar{r} \\
(K_s) \quad & + \int_{\Sigma} \mathcal{X}' \frac{r \bar{h} \tilde{s}_1}{\lambda_{10}} x'_0 d\bar{r} - \int_{\Sigma} \mathcal{X}' \frac{r \bar{h} s_{10}}{\lambda_{10}^2} x'_0 \tilde{\lambda}_1 d\bar{r} + \int_{\Sigma} \mathcal{X}' \frac{r \bar{h} s_{10}}{\lambda_{10}} \tilde{x}' d\bar{r} \\
(K_s) \quad & + \int_{\Sigma} \tilde{s}_2 \bar{h} \mathcal{X} d\bar{r} \\
(K_s) \quad & - \int_{\Sigma} p_0 (\tilde{x} x'_0 + x_0 \tilde{x}') \mathcal{Y} d\bar{r} + \int_{\Sigma} p_0 (\tilde{x} y'_0 + x_0 \tilde{y}') \mathcal{X} d\bar{r} \\
(K_u^s) \quad & + p_u \int_{\Sigma} x_0 (-x'_0 \mathcal{Y} + y'_0 \mathcal{X}) d\bar{r} \\
(K_s^u) \quad & + \mathcal{P}_u \int_{\Sigma} x_0 (-x'_0 \tilde{y} + y'_0 \tilde{x}) d\bar{r} \\
(K_u) \quad & - p_u \mathcal{P}_u \frac{v_0}{2\pi m c^2}, \tag{B.10}
\end{aligned}$$

which is then discretized in FreeFEM on the same mesh as for **step 1**, to obtain the following matrix system:

$$\begin{bmatrix} K_u & K_u^s \\ K_s^u & K_s \end{bmatrix} \begin{bmatrix} p_u \\ \tilde{\mathbf{x}} \end{bmatrix} + \begin{bmatrix} 0 \\ V_s \end{bmatrix} = 0, \tag{B.11}$$

where the different matrices are defined in eq. (B.10), and $\tilde{\mathbf{x}} = [\tilde{x}, \tilde{y}]$. The same Newton-Raphson algorithm as for **step 1** is used, and the loop is stopped when the norm of the increment $[\tilde{x}, \tilde{y}, p_u]$ is sufficiently small.

At the end of this step, the **static configuration** is known, and in the following the subscript zero refers to the **static configuration**.

B.2 Dynamics

The third calculation step (**step 3**) consists of computing the linear dynamics of the system around the **static configuration**. This time the couplings with the acoustics must be taken into account. To this end, the membrane is meshed this time in the **static configuration** and not in the **reference configuration** as in **step 1** and **step 2**.

The linear weak form of the equations governing the coupled problem is obtained by summing the weak forms of the different physics eqs. (2.56) to (2.59). The weak forms for acoustics are already linearized, weak form for the membrane is linearized in a similar manner as for **step 1** and **step 2**. The linearized coupled weak form finally reads:

$$\begin{aligned}
(K_s) & + \int_{\Sigma} \mathcal{Y}' \frac{\bar{r}\bar{h}\tilde{s}_1}{\lambda_{10}^2} y'_0 dl - \int_{\Sigma} \mathcal{Y}' \frac{\bar{r}\bar{h}s_{10}}{\lambda_{10}^3} y'_0 \tilde{\lambda}_1 dl + \int_{\Sigma} \mathcal{Y}' \frac{\bar{r}\bar{h}s_{10}}{\lambda_{10}^2} \tilde{y}' dl \\
(K_s) & + \int_{\Sigma} \mathcal{X}' \frac{\bar{r}\bar{h}\tilde{s}_1}{\lambda_{10}^2} x'_0 dl - \int_{\Sigma} \mathcal{X}' \frac{\bar{r}\bar{h}s_{10}}{\lambda_{10}^3} x'_0 \tilde{\lambda}_1 dl + \int_{\Sigma} \mathcal{X}' \frac{\bar{r}\bar{h}s_{10}}{\lambda_{10}^2} \tilde{x}' dl \\
(K_s) & + \int_{\Sigma} \frac{\tilde{s}_2}{\lambda_{10}} \bar{h} \mathcal{X} dl \\
(K_s) & - \int_{\Sigma} p_0 (\tilde{x} x'_0 + x_0 \tilde{x}') \mathcal{Y} \frac{1}{\lambda_{10}} dl + \int_{\Sigma} p_0 (\tilde{x} y'_0 + x_0 \tilde{y}') \mathcal{X} \frac{1}{\lambda_{10}} dl \\
(K_s^u) & + p_u \int_{\Sigma} x_0 (-x'_0 \mathcal{Y} + y'_0 \mathcal{X}) \frac{1}{\lambda_{10}} dl \\
(K_s^u) & + \mathcal{P}_u \int_{\Sigma} x_0 (-x'_0 \tilde{y} + y'_0 \tilde{x}) \frac{1}{\lambda_{10}} dl \\
(K_u) & - p_u \mathcal{P}_u \frac{v_0}{2\pi m c^2} \\
(K_a) & + c^2 \int_{\Omega_i} \nabla q_a \cdot \nabla \mathcal{Q}_a r ds \\
(K_a^u) & - \int_{\Omega_i} p_u \mathcal{Q}_a r ds \\
(K_a^s) & - m c^2 \int_{\Sigma} \frac{1}{\lambda_{10}} (-y'_0 \tilde{x} + x'_0 \tilde{y}) \mathcal{Q}_a x_0 dl \\
(K_a^{\kappa}) & + \kappa_i \int_{\Omega_i} \mathcal{Q}_a r ds \\
(K_{\kappa}^a) & + \mathcal{K}_i \int_{\Omega_i} q_a r ds \\
(K_e) & + c^2 \int_{\Omega_e} \left(\frac{\gamma_z}{\gamma_r} \frac{\partial q_e}{\partial r} \frac{\partial \mathcal{Q}_e}{\partial r} + \frac{\gamma_r}{\gamma_z} \frac{\partial q_e}{\partial z} \frac{\partial \mathcal{Q}_e}{\partial z} \right) \hat{r} ds \\
(K_e^s) & + m c^2 \int_{\Sigma} \frac{1}{\lambda_{10}} (-y'_0 \tilde{x} + x'_0 \tilde{y}) \mathcal{Q}_e x_0 dl = 0 \\
(M_s) & - \omega^2 \int_{\Sigma} \frac{1}{\lambda_{10} \lambda_{20}} (1 + \Gamma \rho_{\text{ratio}}) (\mathcal{Y} \tilde{y} + \mathcal{X} \tilde{x}) x_0 dl \\
(M_a) & - \omega^2 \int_{\Omega_i} q_a \mathcal{Q}_a r ds \\
(M_e) & - \omega^2 \int_{\Omega_e} q_e \mathcal{Q}_e \hat{r} ds \\
(M_e^e) & + \omega^2 \int_{\Sigma} \frac{1}{\lambda_{10}} q_e (-y'_0 \mathcal{X} + x'_0 \mathcal{Y}) x_0 dl \\
(M_s^a) & - \omega^2 \int_{\Sigma} \frac{1}{\lambda_{10}} q_a (-y'_0 \mathcal{X} + x'_0 \mathcal{Y}) x_0 dl \\
& = \\
(Fs) & w \left(\int_{\Sigma} x_0 \frac{\Gamma}{h} \frac{\lambda_{20}}{\lambda_{10}} (\mathcal{Y}' y'_0 + \mathcal{X}' x'_0) dl + \int_{\Sigma} \mathcal{X}' \frac{\Gamma}{h} \lambda_{10} \lambda_{20} dl \right) , \\
& \quad \forall \mathcal{X}, \mathcal{Y}, \mathcal{P}_u, \mathcal{Q}_a, \mathcal{Q}_e, \mathcal{K}_i . \quad (\text{B.12})
\end{aligned}$$

The coupled finite element matrices are assembled as follows:

$$\mathbf{M}_{\text{tot}} = \begin{bmatrix} M_a & 0 & 0 & 0 & 0 \\ 0 & 0 & 0 & 0 & 0 \\ 0 & 0 & 0 & 0 & 0 \\ 0 & 0 & 0 & M_e & 0 \\ M_s^a & 0 & 0 & M_s^e & M_s \end{bmatrix}, \quad \mathbf{K}_{\text{tot}} = \begin{bmatrix} K_a & K_a^\kappa & K_a^u & 0 & K_a^s \\ K_\kappa^a & 0 & 0 & 0 & 0 \\ 0 & 0 & K_u & 0 & K_u^s \\ 0 & 0 & 0 & K_e & K_e^s \\ 0 & 0 & K_s^u & 0 & K_s \end{bmatrix}, \quad \mathbf{F}_{\text{tot}} = \begin{bmatrix} 0 \\ 0 \\ 0 \\ 0 \\ F_s \end{bmatrix}, \quad (\text{B.13})$$

where all sub-matrices are defined in eq. (B.12).

Validation of the axisymmetric perfectly matched layers implementation

This appendix has been published as Supplementary Material to Garnell, E., Doaré, O., & Rouby, C., (2020). Coupled vibroacoustic modeling of a dielectric elastomer loudspeaker. Journal of the Acoustical Society of America.

In this supplementary material, axisymmetric perfectly matched layers (PMLs) for acoustical radiation in free field are implemented in the open source finite element software FreeFEM. The theory of frequency-independent PMLs is detailed, and an example code is provided to show how they can be implemented in practice. To validate the implementation, a simple system for which a semi-analytical solution for the radiation is available is considered: a moving surface is embedded in an infinite baffle, and radiates into the half space. The finite element solution is compared to the Rayleigh integral, which is exact for the considered system.

C.1 Description of the studied system

A circular moving surface Σ located in an infinite baffle is considered. We are interested in the acoustic pressure P radiated in the half space Ω by the harmonic motion of Σ at the frequency ω . The acceleration of the surface is written $G = g e^{i\omega t}$.

In the following, the pressure is written $P = p e^{i\omega t}$. The non dimensional equations governing the acoustic radiation are:

$$\Delta p + \omega^2 p = 0, \quad \text{in } \Omega, \quad (\text{C.1a})$$

$$\nabla p \cdot \mathbf{n} = g, \quad \text{on } \Sigma, \quad (\text{C.1b})$$

$$\lim_{|\mathbf{x}| \rightarrow \infty} |\mathbf{x}| \left(\frac{\partial p}{\partial |\mathbf{x}|} + i\omega \right) p = 0, \quad (\text{Sommerfeld radiation condition}), \quad (\text{C.1c})$$

where the lengths have been scaled by the radius A of the membrane, and the time by A/C_s where C_s is the speed of sound.

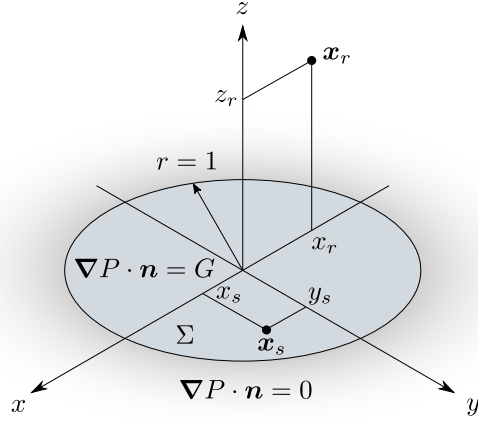


Fig. C.1. Schematics of the studied system, and definition of the geometrical parameters.

C.2 Theory

C.2.1 Weak form of the governing equation

The weak form of the system eq. (C.1) is the following:

$$-\omega^2 \int_{\Omega} p q + \int_{\Omega} \nabla p \cdot \nabla q = \int_{\Sigma} g q, \quad \forall q,$$

and the Sommerfeld radiation condition must also be satisfied. To implement this radiation condition, PMLs are added at the outer boundary of the domain.

C.2.2 PML definition

Attenuation functions Θ_i are defined:

$$\Theta_r(r) = \Theta_0(r - r_{\text{in}})^2, \quad \Theta_z(z) = \Theta_0(z - z_{\text{in}})^2,$$

where Θ_0 is a parameter that should be adjusted, and r_{in} and z_{in} the coordinates of the inner boundary of the PMLs (see fig. C.2). The following changes of variables are considered:

$$\hat{r} = \begin{cases} r - i \int_{r_{\text{in}}}^r \Theta_r(r) ds & \text{for } |r| > |r_{\text{in}}| \\ r & \text{otherwise} \end{cases}, \quad \hat{z} = \begin{cases} z - i \int_{z_{\text{in}}}^z \Theta_z(z) ds & \text{for } |z| > |z_{\text{in}}| \\ z & \text{otherwise} \end{cases}, \quad (\text{C.2})$$

which imply the following changes of the partials derivatives:

$$\frac{\partial}{\partial \hat{r}} = \frac{1}{\gamma_r(r)} \frac{\partial}{\partial r}, \quad \frac{\partial}{\partial \hat{z}} = \frac{1}{\gamma_z(z)} \frac{\partial}{\partial z},$$

where the functions γ_i are defined as:

$$\gamma_r(r) = \begin{cases} 1 - i\Theta_r(r) & \text{for } |r| > |r_{\text{in}}| \\ 1 & \text{otherwise} \end{cases}, \quad \gamma_z(z) = \begin{cases} 1 - i\Theta_z(z) & \text{for } |z| > |z_{\text{in}}| \\ 1 & \text{otherwise} \end{cases}.$$

The change of variables eq. (C.2) are inserted in the weak form:

$$-\omega^2 \int_{\Omega} pq + \int_{\Omega} \hat{\nabla} p \cdot \hat{\nabla} q = \int_{\Sigma} gq.$$

In axisymmetric coordinates this yields:

$$-\omega^2 \int_{\Omega} pqrdrdz + \int_{\Omega} \hat{\nabla} p \cdot \hat{\nabla} q rdrdz = \int_{\Sigma} gqrdrdz.$$

Finally by substituting the expressions for \hat{r} , \hat{z} and their derivatives, we get:

$$-\omega^2 \int_{\Omega} pq\gamma_r\gamma_z rdrdz + \int_{\Omega} \left(\frac{\gamma_z}{\gamma_r} \frac{\partial p}{\partial r} \frac{\partial q}{\partial r} + \frac{\gamma_r}{\gamma_z} \frac{\partial p}{\partial z} \frac{\partial q}{\partial z} \right) rdrdz = \int_{\Sigma} gqrdrdz.$$

There is no PML on the boundary Σ where the acceleration is prescribed, so the force term is the same as it would be without PMLs.

C.2.3 Pressure computation using the Rayleigh integral

As the radiating surface is flat and embedded in a infinite baffle, the radiated pressure can be computed using the Rayleigh integral:

$$p(\mathbf{x}_r) = \int_{\Sigma} g \frac{e^{-i\omega d}}{2\pi d} dS,$$

where \mathbf{x}_r is the receiver location, and d the distance between the receiver and the source element location \mathbf{x}_s (defined in fig. C.1):

$$d = \sqrt{(x_s - x_r)^2 + y_s^2 + z_r^2}.$$

C.3 Results

All the following results are obtained using the example code which is provided as supplementary material to the article mentioned at the beginning of the appendix [33]. The reader is encouraged to run this code using the open source software FreeFEM, and test the influence of the different parameters.

The results shown here are obtained with a uniform prescribed acceleration $g = 1$ on Σ .

C.3.1 Frequency range of interest

For the application considered in the article, the frequency range of interest is 100 Hz to 5 kHz. For a membrane radius of approximately 4 cm and a speed of sound $C_s = 340$ m/s this corresponds to non-dimensional angular frequencies:

$$\omega \in [0.04, 2] .$$

The efficiency of the PMLs are therefore tested for these two extreme frequencies. If there are no reflections at either of these frequencies, it can be assumed that the PML behave correctly over the whole frequency range of interest.

The PML attenuation parameter is set to $\Theta_0 = 400$.

C.3.2 Mesh

The mesh which is used for the following results is shown in fig. C.2. The pressure computed using the FreeFEM code and the Rayleigh integral are plotted for the two frequencies $\omega = 0.04$ and $\omega = 2$ in figs. C.3 and C.4.

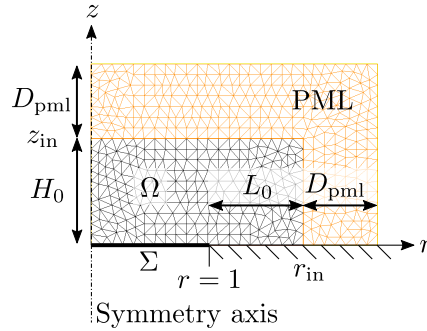


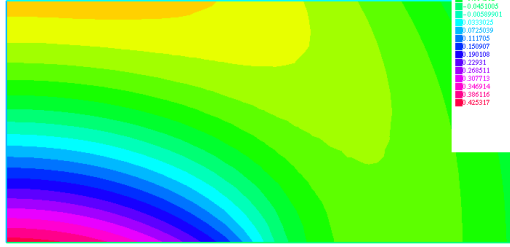
Fig. C.2. Mesh used for the following numerical results. The PML thickness is $D_{\text{pml}} = 0.7$, the height of the acoustical domain is $H_0 = 1$, the distance between the membrane and the PML is $L_0 = 1$.

C.3.3 Convergence analysis

The FreeFEM code given in supplementary material to [33] can be used to compute the convergence of the FEM solution to the analytical solution, when the size of the PML mesh decreases. It is expected that for a fixed attenuation parameter Ψ_0 , if the number of elements in the PML mesh is increased, the numerical solution should converge to the analytical one.

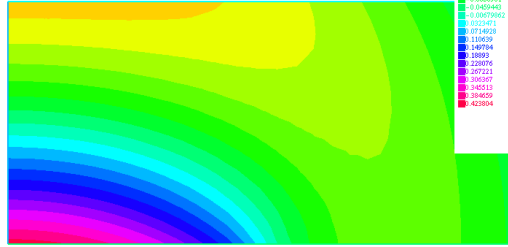
(a) FreeFEM solution

FreeFEM solution



(b) Rayleigh integral solution

Rayleigh integral solution



(c) Relative error (%)

Relative error (%)

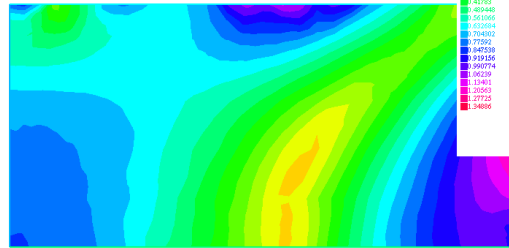


Fig. C.4. Real part of the pressure radiated by the moving surface Σ . Comparison of FreeFEM calculation with PMLs, and Rayleigh integral, for $\omega = 2$. The maximum relative error is 1.3%.

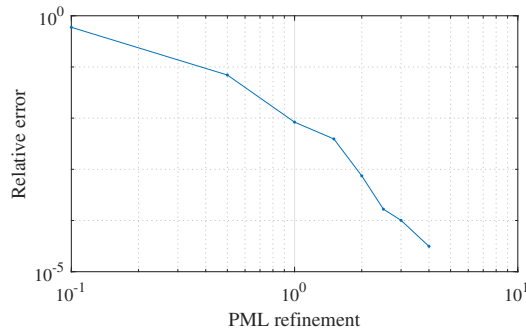


Fig. C.5. Convergence of the numerical solution to the analytical solution in L^2 sense, when the mesh is refined in the PML. The relative error is defined as $\sqrt{\int_{\Omega} |P_{\text{FEM}} - P_{\text{Rayleigh}}|^2 / \int_{\Omega} |P_{\text{Rayleigh}}|^2}$. The refinement parameter equals 1 when the mesh is the same as in fig. C.2, and defines how many elements there are on the PML borders compared to the mesh in fig. C.2. For example if the PML refinement equals 2, there are twice as many elements on the PML borders than in fig. C.2. In the PML domain there would then be approximately 4 times more elements.

Validation of modal methods for exterior vibroacoustic problems

In this appendix a simple exterior coupled vibroacoustic problem is studied using modal methods. The goal is to present the modal method used throughout this thesis to compute the acoustic radiation of the inflated DE membrane on a test case which contains only the necessary ingredients to understand the key problems and limitations.

This appendix is organized as follows. First the system is described and the governing equations are derived. The numerical method to solve the equations using modal methods is presented, and finally the performance of the modal method is evaluated, in terms of modal summation convergence.

D.1 Description of the studied system

The studied system consists in a flat circular tensioned membrane embedded in an infinite baffle. The membrane vibrations are strongly coupled to the surrounding air. The system is similar to the one studied in appendix C, but this time the piston is replaced by a membrane. The membrane is excited by an exterior pressure g , applied on the whole membrane surface.

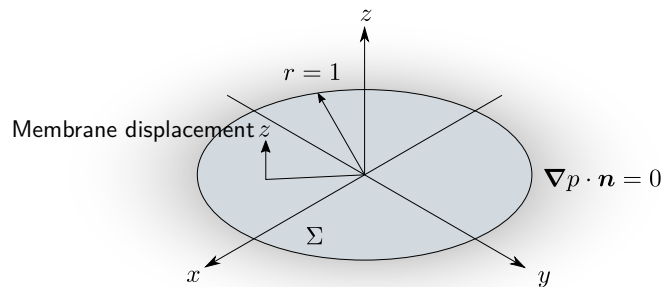


Fig. D.1. Schematics of the studied system

D.2 Governing equations

In this whole appendix section, all equations are written in non-dimensional form.

The governing equations for the membrane dynamics are:

$$\frac{\partial z}{\partial t^2} - (1 + i\eta) \frac{\partial z}{\partial r^2} + p = g \quad \text{on } \Sigma, \quad (\text{D.1})$$

$$\frac{\partial z}{\partial r}(r = 0) = 0, \quad (\text{D.2})$$

$$z(r = 1) = 0 \quad (\text{D.3})$$

where η is a constant structural loss factor. The governing equations for acoustics are:

$$\frac{\partial p}{\partial t^2} - m \Delta p = 0 \quad \text{in } \Omega, \quad (\text{D.4a})$$

$$\nabla p \cdot \mathbf{n} = -c^2 \omega^2 z \quad \text{on } \Sigma, \quad (\text{D.4b})$$

$$\lim_{|\mathbf{x}| \rightarrow \infty} |\mathbf{x}| \left(\frac{\partial p}{\partial |\mathbf{x}|} + i\omega \right) p = 0, \quad (\text{Sommerfeld radiation condition}), \quad (\text{D.4c})$$

$$\nabla p \cdot \mathbf{n} = 0 \quad \text{on the other boundaries.} \quad (\text{D.4d})$$

where $m = \frac{\rho_F}{\rho_s}$ and $c^2 = \frac{c_F^2}{c_s^2}$. $g(r)$ is an external pressure applied to the membrane.

The weak forms of the governing equations are obtained by multiplying eqs. (D.1) and (D.4a) by the test functions \mathcal{Z} and \mathcal{P} and integrating by parts:

$$-\omega^2 \int_{\Sigma} z \mathcal{Z} r dr + \int_{\Sigma} z' \mathcal{Z}' r dr + \int_{\Sigma} p \mathcal{Z} r dr = \int_{\Sigma} g \mathcal{Z} r dr, \quad (\text{D.5a})$$

$$-\omega^2 \int_{\Omega} p \mathcal{P} \gamma_r \gamma_z \hat{r} dr dz + m \int_{\Omega} \left(\frac{\gamma_z}{\gamma_r} \frac{\partial p}{\partial r} \frac{\partial \mathcal{P}}{\partial r} + \frac{\gamma_r}{\gamma_z} \frac{\partial p}{\partial z} \frac{\partial \mathcal{P}}{\partial z} \right) \hat{r} dr dz + m c^2 \omega^2 \int_{\Sigma} z \mathcal{P} r dr = 0. \quad (\text{D.5b})$$

where the PML complex change of coordinates introduced in appendix C has been applied to account for the Sommerfeld radiation condition at the outer limit of the computational domain.

A different set of equations is obtained if the displacement potential $q = \frac{p}{i\omega}$ is used as the state variable for the fluid instead of the pressure:

$$-\omega^2 \int_{\Sigma} z \mathcal{Z} r dr + \int_{\Sigma} z' \mathcal{Z}' r dr + \omega^2 \int_{\Sigma} q \mathcal{Z} r dr = \int_{\Sigma} g \mathcal{Z} r dr, \quad (\text{D.6a})$$

$$-\omega^2 \int_{\Omega} q \mathcal{P} \gamma_r \gamma_z \hat{r} dr dz + m \int_{\Omega} \left(\frac{\gamma_z}{\gamma_r} \frac{\partial q}{\partial r} \frac{\partial \mathcal{P}}{\partial r} + \frac{\gamma_r}{\gamma_z} \frac{\partial q}{\partial z} \frac{\partial \mathcal{P}}{\partial z} \right) \hat{r} dr dz + m c^2 \int_{\Sigma} z \mathcal{P} r dr = 0. \quad (\text{D.6b})$$

D.3 Numerical solving

D.3.1 Finite element discretization

Equations (D.5) and (D.6) are discretized using finite elements, in the software FreeFEM. Two different matrix equations are obtained, depending on the state variable that is used for the fluid. If the pressure is used, the following system is obtained, and referred to hereafter as the ***p*-formulation**:

$$\left(-\omega^2 \begin{bmatrix} M_F & -mc^2 R \\ 0 & M_s \end{bmatrix} + \begin{bmatrix} mK_F & 0 \\ R & K_s \end{bmatrix} \right) \begin{bmatrix} p \\ z \end{bmatrix} = \begin{bmatrix} 0 \\ F_s \end{bmatrix}, \quad (\text{D.7})$$

where M_F and K_f are the mass and stiffness matrices of the fluid, M_s and K_s those of the structure, R is the coupling matrix, and F_s the force vector on the structure.

If the displacement potential is used, the following system is obtained and referred to as the ***q*-formulation**:

$$\left(-\omega^2 \begin{bmatrix} M_F & 0 \\ -R & M_s \end{bmatrix} + \begin{bmatrix} mK_F & mc^2 R \\ 0 & K_s \end{bmatrix} \right) \begin{bmatrix} q \\ z \end{bmatrix} = \begin{bmatrix} 0 \\ F_s \end{bmatrix}. \quad (\text{D.8})$$

The systems eqs. (D.7) and (D.8) differ only by the extra-diagonal terms. The sub-matrices are the same, but coupling mass and stiffness appear either on the first or on the second lines of the matrices. We will see that this has a major importance for the convergence of the modal summation.

For both the ***p*-** and the ***q*-formulation**, the full system can be re-written as:

$$(-\omega^2 \mathbf{M}_{\text{tot}} + \mathbf{K}_{\text{tot}}) \mathbf{X}_{\text{tot}} = \mathbf{F}_{\text{tot}}, \quad (\text{D.9})$$

where \mathbf{M}_{tot} and \mathbf{K}_{tot} are frequency-independent matrices, because of the choice of frequency-independent PMLs that has been made [see appendix C]. Of course, the matrices \mathbf{M}_{tot} and \mathbf{K}_{tot} depend on the formulation that is chosen (*p* or *q*), but as the solving method does not depend on the formulation, this generic writing is kept in the following.

D.3.2 Modal analysis

As the mass and stiffness matrices are not symmetric, left and right modes need to be computed to diagonalize the system [75], we call them Ψ_n^R and Ψ_n^L :

$$\Psi_n^L (-\omega_n^2 \mathbf{M}_{\text{tot}} + \mathbf{K}_{\text{tot}}) = 0, \quad (\text{D.10})$$

$$(-\omega_n^2 \mathbf{M}_{\text{tot}} + \mathbf{K}_{\text{tot}}) \Psi_n^R = 0. \quad (\text{D.11})$$

The total displacement vector is expanded on the right modeshapes:

$$\mathbf{X}_{\text{tot}} = \mathbf{\Psi}^R \mathbf{d} \quad (\text{D.12})$$

where \mathbf{d} is a vector of modal amplitudes, and $\mathbf{\Psi}^R$ the matrix containing the right modeshapes.

If all eigenvalues are of order one, the bi-orthogonality relations between the left and right modeshapes hold:

$$\mathbf{\Psi}^L \mathbf{M}_{\text{tot}} \mathbf{\Psi}^R = \text{diag}(\mu_n), \quad \mathbf{\Psi}^L \mathbf{K}_{\text{tot}} \mathbf{\Psi}^R = \text{diag}(\kappa_n). \quad (\text{D.13})$$

The modal mass and stiffness matrices are plotted in fig. D.2 to check the bi-orthogonality relations. Figure D.2 confirms that the modal mass and stiffness are diagonal.

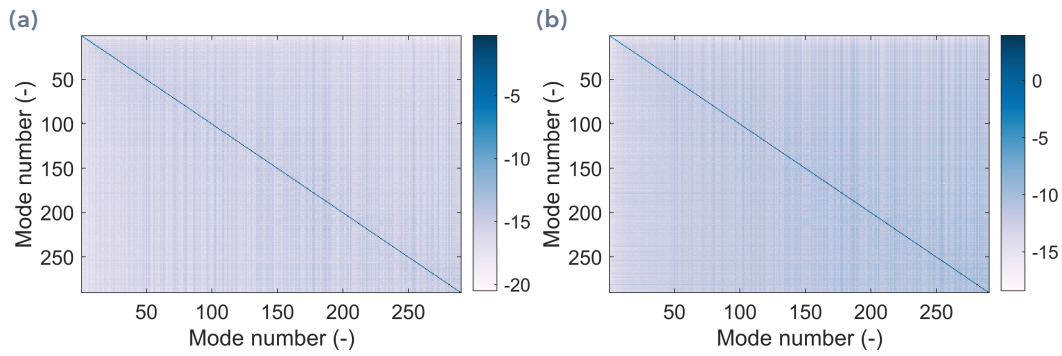


Fig. D.2. (a) Modal mass matrix. (b) Modal stiffness matrix. A quantitative indicator I_{qual} of how close the matrices are to diagonal matrices can be defined, by computing the ratio between the smallest diagonal element over the largest non-diagonal element. It yields $I_{\text{qual}} = 9 \times 10^6$ for the modal mass, and $I_{\text{qual}} = 6 \times 10^4$ for the modal stiffness. These values can be considered very large, close to the numeric precision of the data exported from FreeFEM.

Left multiplying eq. (D.9) by the left eigenvectors $\mathbf{\Psi}^L$, inserting the modal expansion of the displacement vector eq. (D.12), and using the orthogonality relations yields:

$$(-\omega^2 \mu_n + \kappa_n) d_n = F_n, \quad (\text{D.14})$$

where $F_n = \mathbf{\Psi}_L^n \mathbf{F}_{\text{tot}}$, and d_n is the modal amplitude which thus reads:

$$d_n(\omega) = \frac{F_n}{\mu_n(\omega_n^2 - \omega^2)}, \quad (\text{D.15})$$

where $\omega_n^2 = \kappa_n / \mu_n$.

The modal summation for the total displacement is finally obtained:

$$\mathbf{X}_{\text{tot}} = \sum_n d_n(\omega) \mathbf{\Psi}_n^R. \quad (\text{D.16})$$

The modal summation for the pressure and for the membrane displacement now depend on the chosen formulation (pressure or displacement potential).

Pressure fomulation In the *p-formulation*, the total displacement contains the pressure and the membrane displacement. Thus, the modal expansion yields:

$$\mathbf{X}_{\text{tot}} = \begin{bmatrix} p \\ z \end{bmatrix} = \sum_n d_n(\omega) \Psi_n^R = \sum_n d_n(\omega) \begin{bmatrix} \Psi_{n,p}^R \\ \Psi_{n,z}^R \end{bmatrix}, \quad (\text{D.17})$$

where $\Phi_{n,z}^R$ contains the structural degrees of freedom of mode n , and $\Phi_{n,p}^R$ the acoustical degrees of freedom. The modal expansions for the membrane displacement and the radiated pressure are:

$$z = \sum_n d_n(\omega) \Psi_{n,z}^R, \quad p = \sum_n d_n(\omega) \Psi_{n,p}^R. \quad (\text{D.18})$$

Here, one may notice that the pressure and the membrane displacement have the same frequency dependence. This is surprising as the pressure radiated from a vibrating surface is proportional to the surface acceleration, and not proportional to its displacement. This will cause a poor convergence of the modal summation for the pressure, as seen in next section.

Displacement potential fomulation In the *q-formulation*, the total displacement contains the displacement potential and the membrane displacement. Thus, the modal expansion yields:

$$\mathbf{X}_{\text{tot}} = \begin{bmatrix} q \\ z \end{bmatrix} = \begin{bmatrix} \frac{p}{\omega^2} \\ z \end{bmatrix} = \sum_n d_n(\omega) \Psi_n^R = \sum_n d_n(\omega) \begin{bmatrix} \Psi_{n,p}^R \\ \Psi_{n,z}^R \end{bmatrix}, \quad (\text{D.19})$$

where $\Phi_{n,z}^R$ contains the structural degrees of freedom of mode n , and $\Phi_{n,p}^R$ the acoustical degrees of freedom. The modal expansions for the membrane displacement and the radiated pressure are:

$$z = \sum_n d_n(\omega) \Psi_{n,z}^R, \quad p = \sum_n \omega^2 d_n(\omega) \Psi_{n,p}^R. \quad (\text{D.20})$$

This time, the pressure has the same frequency dependence as the membrane acceleration, which will improve the modal summation convergence.

The convergence of the two formulations is studied in the following section D.4.

D.4 Results

All the following results are obtained with the parameters given in table D.1.

The perfectly matched layers attenuation parameter Θ_0 is defined in appendix C.

Tab. D.1. Non-dimensional parameters used for the results in appendix D.4.

Parameter	m	c^2	Θ_0	η
Value	1	100	100	0.01

The mesh used for the numerical results is shown in fig. D.3.

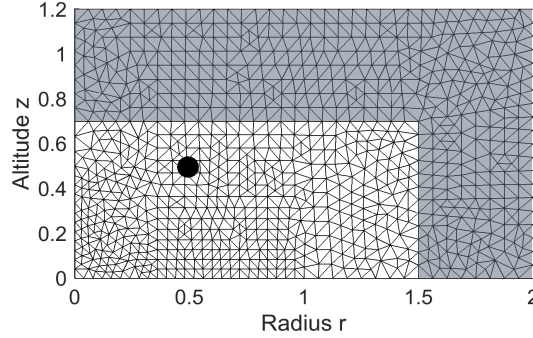


Fig. D.3. Mesh used for the numerical results. The black dot is the point where the pressure is computed, and the grey area corresponds to the perfectly matched layers. The membrane mesh is too thin to be visible, but is located at the bottom, from radius $r = 0$ to $r = 1$.

D.4.1 Modal parameters

First, the modal parameters are studied. The two formulations behave similarly here, so only the results for the ***q*-formulation** are given. The first computed modes are plotted in fig. D.4.

Figure D.4 highlights that two different types of modes are computed. The membrane modes are dominated by the membrane dynamics, the structural part of the mode resemble classical modes of a flat circular tensioned membrane, and the pressure is created by the membrane displacement. The PML modes on the other hand are created by reflections in the PMLs themselves, and have no physical interpretation. They depend on the shape and size of the PMLs, and cannot be defined for a infinite domain. They exist just because the computational domain for the exterior was truncated.

The eigenfrequencies are plotted in the complex plane in fig. D.5a to provide further explanation. There is a clear distinction between membrane modes and PML modes: the membrane modes lie on the real axis, and have a very small imaginary part. This means their damping is low, and can be confirmed by fig. D.5b. The PML modes have a large displacement in the PML part of the computational domain, and as a numerical damping is introduced in this region, the PML modes have a larger damping.

In order to distinguish PML modes from membrane modes, a simple damping threshold is sufficient, as seen in fig. D.5b. All modes with a modal loss factor over the threshold are considered to be PML modes, and all modes below to be membrane modes. Other authors studied the variations eigenfrequencies when the PML parameters (size, attenuation, distance from the surface) are varied, and tracked the modes which are not affected by these parameters. The obtained modes are the membrane modes, and the rest the

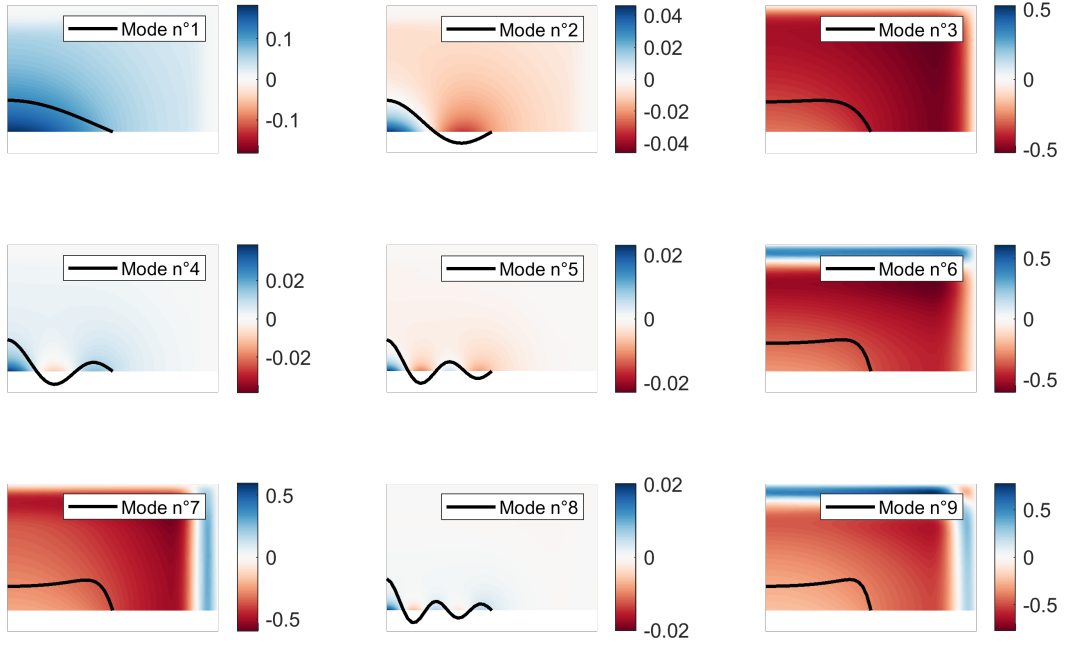


Fig. D.4. First nine computed coupled modes, $c^2 = 100$, $m = 1$, $\Theta_0 = 100$. The black line — is the membrane displacement, and the color represents the displacement potential in the fluid domain. All modes are scaled (both the structural and the acoustical parts) so that the membrane maximum displacement is 0.2.

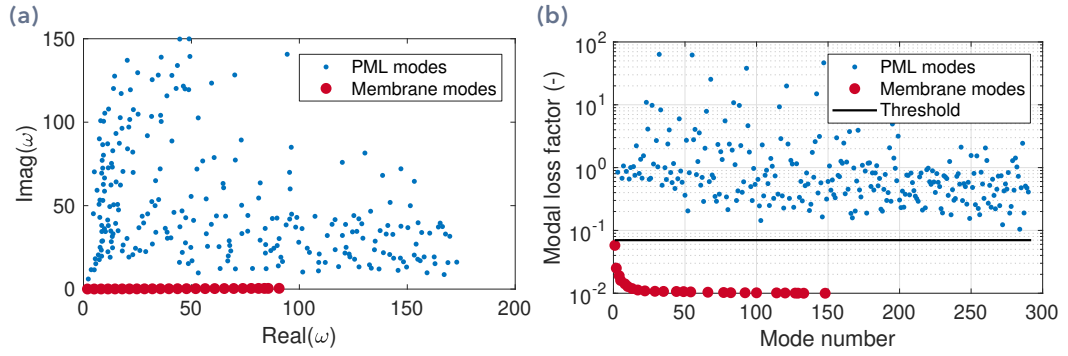


Fig. D.5. Eigenfrequencies of the coupled vibroacoustic system. **(a)** Frequencies in the complex plane. **(b)** Modal loss factor, and threshold to distinguish membrane modes from PML modes.

PML modes. This has been checked, and yields the same results in terms of distinction between PML and membrane modes.

D.4.2 Convergence of the modal summation

The two formulations (pressure and displacement potential) are now compared in terms of convergence of the modal summation. First, the membrane displacement is analysed, and plotted in fig. D.6.

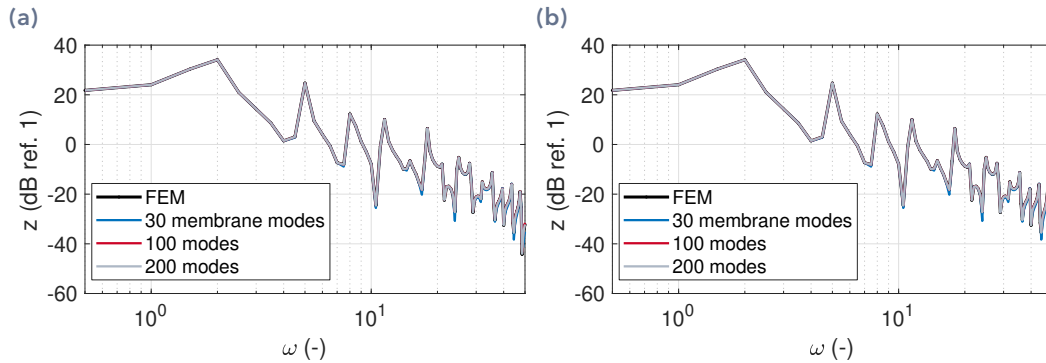


Fig. D.6. Convergence of the modal summation for the membrane displacement, at an arbitrary chosen point. **(a)** Pressure formulation. **(b)** Displacement potential formulation. The FEM calculation — is obtained by inverting the system eq. (D.9) for all frequencies of interest.

The modal method is evaluated by comparing to the FEM method, in which the system eq. (D.9) is inverted for all frequencies of interest. As the implementation of the perfectly matched layers has been validated in appendix C, the FEM solution is a reference. Figure D.6 shows that the modal method converges to the FEM solution for a small number of modes. All presented modal truncations have converged to the FEM solution. Interestingly, only membrane modes are necessary to describe the membrane displacement, meaning that the basis formed by only membrane modes is a complete basis for the membrane displacement. The contribution of the PML modes to the membrane displacement is negligible. Both formulations yield the same results.

On the other hand, the modal summation for the radiated pressure yields different results, and is plotted in fig. D.7.

Figure D.7a shows that the convergence of the modal summation to the FEM solution for the **p-formulation** is poor. Many modes (200) are needed to describe correctly the radiated pressure. Keeping only the membrane modes in the modal basis is clearly not sufficient to capture the radiated pressure, which demonstrates that all types of modes should be included in the summation, as found by Marburg [77, 79, 78]. This poor convergence is directly related to the frequency dependence of the modal amplitude for the **p-formulation** eq. (D.18). Indeed the amplitude for each mode behaves like a constant value at low frequencies, when the FEM solution behaves like ω^2 .

On the other hand the **q-formulation** yields a much better convergence, as seen in fig. D.7b. A satisfying approximation of the pressure is obtained even if only membrane modes are used, especially at low frequencies. This may be useful if a rough estimation of the pressure only is needed, as the calculation can be very fast with only a few modes. With 200 modes, the modal solution converged completely to the reference solution. Even if 200

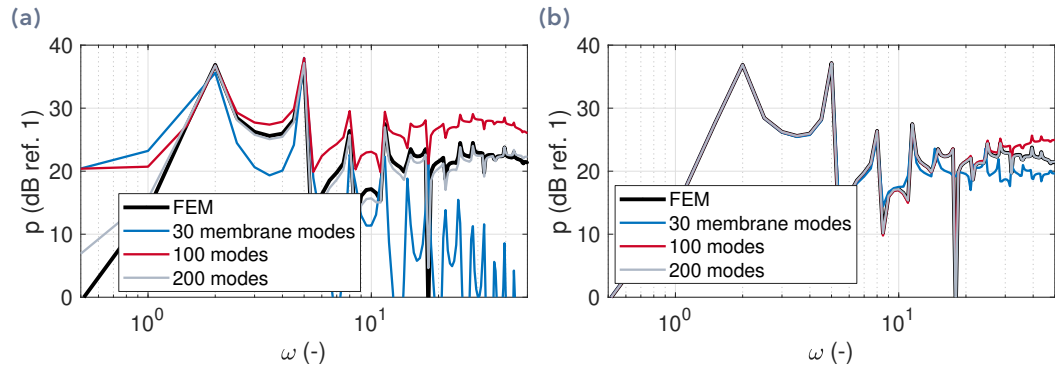


Fig. D.7. Convergence of the modal summation for the radiated pressure, at an arbitrary chosen point. **(a)** Pressure formulation. **(b)** Displacement potential formulation.

may seem to be a large number compared to the number of membrane eigenfrequencies in the frequency range of interest, it is still much lower than the number of finite element degrees of freedom, in the order of 10000, and thus provide a large model order reduction.

Figure D.7 showed the pressure and the membrane displacement at only one point. The pressure and displacement are also plotted in the whole domain in fig. D.8 to show that the modal solution is identical to the reference solution on the whole computational domain.

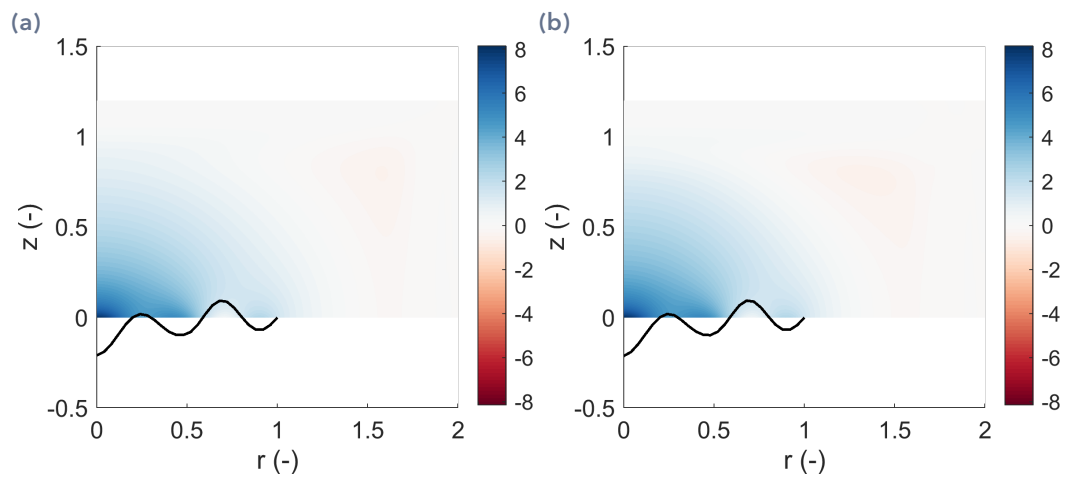


Fig. D.8. Pressure and membrane displacement plotted at $\omega = 15$. **(a)** FEM solution. **(b)** Modal summation using the *q*-formulation and 200 modes.

D.5 Conclusion

Modal methods for exterior vibroacoustic problems have been investigated on a simple test case, consisting in a flat tensioned membrane embedded in an infinite baffle. It has been shown that the pressure radiated by the membrane can be expanded on a basis of coupled fluid/structure modes, that are obtained by solving a linear eigenvalue problem. Frequency-independent PMLs appear to be a convenient solution to model the Sommerfeld radiation condition, as frequency-independent mass and stiffness matrix can be obtained.

The methods developed in this thesis are limited to frequency-independent systems. As soon as more complex damping models are used, the system matrices are likely to depend on frequency, and the eigenvalue problem becomes non-linear. The orthogonality relations that are used to obtain the modal summation formula may not be valid for non-linear eigenvalue problems.

Titre : Haut-parleurs en élastomères diélectriques: modèles, expériences et optimisation

Mots clés : Élastomères diélectriques, haut-parleurs, couplages vibroacoustiques

Résumé : Les élastomères diélectriques sont des matériaux actifs souples capables de grandes déformations sous chargement électrique. Ils sont constitués d'une fine membrane d'élastomère (en général en silicone ou acrylique), recouverte de chaque côté par des électrodes souples et étirables. L'ensemble a une épaisseur de l'ordre de 100 microns. Lorsqu'une tension électrique est appliquée entre les électrodes, la membrane se comprime et sa surface peut augmenter de plus de 100%.

Ce principe de conversion électromécanique peut être utilisé pour réaliser des haut-parleurs. Des prototypes ont été développés par plusieurs groupes de recherche, et des modèles ont été proposés pour évaluer leurs performances.

Une caractéristique intrinsèque des haut-parleurs en élastomères diélectriques est leur nature multiphysique. En effet, le mécanisme d'actuation est lui-même un couplage entre électrostatique et mécanique; la membrane est très fine et légère, et

se couple ainsi fortement à l'acoustique car l'air est lourd par rapport à la membrane; et enfin la résistivité des électrodes génère un couplage entre l'électrodynamique et la mécanique.

Les modèles proposés jusqu'alors ne considéraient pas l'ensemble de ces couplages, limitant leur utilisation à des estimations qualitatives. Dans cette thèse, un modèle multiphysique de haut-parleurs en élastomères diélectriques est mis en place, afin de permettre l'optimisation de leurs performances acoustiques, en terme de réponse en fréquence, niveau rayonné, et directivité. Les couplages forts entre électrostatique, dynamique membranaire, acoustique, et électrodynamique sont étudiés à l'aide d'un modèle par éléments finis dans FreeFEM. Ce modèle est validé par des comparaisons avec des mesures dynamiques et acoustiques, et ensuite utilisé pour améliorer les performances du prototype, en travaillant sur plusieurs plans : optimisation de l'excitation, filtrage, amortissement, et contrôle.

Title : Dielectric elastomer loudspeakers: models, experiments and optimization

Keywords : Dielectric elastomers, loudspeakers, vibroacoustic coupling

Abstract :

Dielectric elastomers are soft active materials capable of large deformations when activated by a high voltage. They consist of a thin elastomer membrane (generally made of silicone or acrylic), sandwiched between compliant electrodes. The thickness of the assembly is about 100 microns. When a high voltage is applied between the electrodes, the membrane is squeezed between the electrodes, and increases in area by up to 100%.

This electromechanical conversion principle can be used to build loudspeakers. Prototypes have been developed and tested by several research groups, and models have been proposed to estimate their performance.

An intrinsic characteristic of dielectric elastomer loudspeakers is their multi-physic nature. Indeed, the actuation mechanism is itself a coupling between electrostatics and mechanics; the membrane is very thin

and light, and couples therefore strongly with the surrounding air which is comparatively heavy; and finally the electrode electrical resistivity induces a coupling between electrodynamics and mechanics.

The models proposed so far did not consider all of these couplings together, which limited their use to qualitative estimations. In this thesis, a multi-physic model of dielectric elastomer loudspeakers is set-up, in order to optimize their acoustic performances, in terms of frequency response, radiated level, and directivity. The strong couplings between electrostatics, membrane dynamics, acoustics and electrodynamics are studied with a finite element model in FreeFEM. This model is validated by dynamical and acoustical measurements, and then used to improve the performances of the prototype, by working on several levels : optimization of the excitation, filtering, damping and control.